# Circuit Quantum Electrodynamics with Single Electron Spins in Silicon

**Important note**
To cite this publication, please use the final published version (if applicable).
Please check the document version above.

# Circuit Quantum Electrodynamics with Single Electron Spins in Silicon

# Circuit Quantum Electrodynamics with Single Electron Spins in Silicon

**Proefschrift**

ter verkrijging van de graad van doctor
aan de Technische Universiteit Delft,
op gezag van de Rector Magnificus Prof. dr. ir. T.H.J.J. van der Hagen,
voorzitter van het College voor Promoties,
in het openbaar te verdedigen op
vrijdag 12 februari 2021 om 12:30 uur

door

**Guoji ZHENG**

Master of Science in Applied Physics,
Technische Universiteit Delft, Nederland
geboren te Ruian, China.

Dit proefschrift is goedgekeurd door de promotoren.

Samenstelling promotiecommissie bestaat uit:

| | |
|---|---|
| Rector Magnificus | voorzitter |
| Prof. dr. ir. L.M.K. Vandersypen | Technische Universiteit Delft, promotor |
| Dr. G. Scappucci | Technische Universiteit Delft, copromotor |

Onafhankelijke leden/Independent members:

| | |
|---|---|
| Prof. dr. A. Wallraff | ETH Zürich, Zwitserland |
| Prof. dr. T. Kontos | ENS Paris, Frankrijk |
| Prof. dr. ir. T. H. Oosterkamp | Universiteit Leiden |
| Prof. dr. G. A. Steele | Technische Universiteit Delft |
| Prof. dr. L. DiCarlo | Technische Universiteit Delft, reservelid |

*If I have seen further,*
*it is by standing on the shoulders of giants.*

Isaac Newton

# Contents

# Summary

This dissertation describes a set of experiments with the goal of creating a super-conductor-semiconductor hybrid circuit quantum electrodynamics architecture with single electron spins. Single spins in silicon quantum dots have emerged as attractive qubits for quantum computation. However, how to scale up spin qubit systems remains an open question. The hybrid architecture considered here could provide a route to realizing large networks of quantum dot–based spin qubit registers.

The first experiment in this thesis is aimed at achieving strong coupling between a single electron spin and a single microwave photon. The electron is trapped in a gate-defined double quantum dot in a Si/SiGe heterostructure and the photon is stored in an on-chip superconducting high-impedance ($>1\,\mathrm{k\Omega}$) NbTiN cavity. The photon is coupled directly to the electron charge, and indirectly to the electron spin, mediated through a synthetic spin-orbit field. We observe a vacuum Rabi splitting that depends on the spin-charge hybridization. The ratio of spin-photon coupling strength to decoherence rates of the spin and cavity combined is larger than unity, confirming the strong coupling regime has been reached. In addition, we find an optimal degree of spin-charge hybridization for which this ratio is maximized. The demonstration of strong spin-photon coupling not only opens a new range of physics experiments, but fulfills also a crucial requirement for coupling spin qubits at a distance via a cavity.

The second experiment is focused on spin readout with the on-chip cavity. Instead of the direct dispersive readout of a single spin, we use the cavity to detect whether the electron is allowed to tunnel between the two dots or not. We benchmark the charge sensitivity and bandwidth of the detector and find that rapid detection of the electron charge with high SNR is possible. In the two-electron regime, electron tunneling is contingent on the total spin state (Pauli spin blockade). This spin-to-charge conversion scheme enables single-shot detection of singlet states with high-fidelity. The demonstration of single-shot spin readout with a cavity is an essential step towards readout in dense spin qubit arrays, such as the cross-bar network, where it is not possible to integrate electrometers and accompanying reservoirs adjacent to the qubit dots.

In the third experiment, we develop on-chip microwave filters to suppress microwave photon leakage from the cavity through the gate electrodes that are necessary to form quantum dots. We introduce a new cavity design that is compatible with long-distance connectivity between spins, but is also more susceptible to microwave leakage. We test and compare two low-pass filter variations in terms of performance, footprint and integrability. They use the same nanowire inductor, but different implementations of the capacitor: one with a planar interdigitated capacitor and one novel design with an overlapping thin-film capacitor. We find that both approaches are effective against microwave leakage. However, the large footprint

of the interdigitated capacitor makes this solution inconvenient as the number of gate lines increases. The thin-film capacitor, with its much smaller footprint, is better suited for our devices.

The final part of this dissertation contains concluding remarks and possible future directions are proposed.

*Guoji Zheng*

# Samenvatting

Dit proefschrift beschrijft een aantal experimenten met als doel het ontwikkelen van een supergeleider-halfgeleider hybride circuit-quantumelektrodynamica architectuur met enkele elektronspins. Enkele spins in silicium quantumdots zijn veelbelovende qubits voor quantumcomputers gebleken. Hoe spinqubitsystemen opgeschaald moeten worden blijft echter een open vraag. De hybride architectuur die hier wordt beschreven kan dienen als een eerste stap naar netwerken van quantumdot-gebaseerde spinqubitregisters.

Het eerste experiment in deze scriptie is gericht op het bereiken van een sterke koppeling tussen een enkele elektronspin en een enkel microgolffoton. Het elektron is gevangen in een door elektrodes gedefinieerde dubbelquantumdot in een Si/SiGe heterostructuur, en het foton is opgeslagen in een supergeleidende hoge-impedantie (>1 kΩ) NbTiN resonator op de chip. Het foton is direct gekoppeld aan de elektronlading, en indirect aan de elektronspin door middel van een kunstmatig spin-baanveld. We observeren een vacuüm Rabisplitsing die afhangt van de spin-ladingshybridisatie. De verhouding van spin-fotonkoppelingssterkte en mate van incoherentie van de spin en resonator samen is groter dan één, wat bevestigt dat het sterke koppelingsregime is bereikt. Verder vinden we de optimale mate van spin-ladingshybridisatie voor welke deze verhouding maximaal is. Het aantonen van sterke spin-fotonkoppeling baant niet alleen de weg naar nieuwe natuurkundeexperimenten, maar beantwoordt ook aan een cruciale vereiste voor het koppelen van spinqubits op afstand via een resonator.

Het tweede experiment richt zich op het uitlezen van spins met behulp van de resonator op de chip. In plaats van een directe dispersieve uitlezing van een enkele spin, wordt de resonator gebruikt om te detecteren of een elektron in staat is om tussen de twee dots te tunnelen. We peilen de ladingsgevoeligheid en bandbreedte van de detector, en vinden dat snelle detectie van elektronlading met hoge signaal-ruisverhouding mogelijk is. In het twee-elektronregime is het tunnelen van een elektron afhankelijk van de totale spinstoestand (Pauli-spinblokkade). Deze methode van conversie van spin naar lading maakt detectie van singlettoestanden in een enkele meting met hoge betrouwbaarheid mogelijk. De demonstratie van uitlezing in een enkele meting met een resonator is een essentiële stap richting het uitlezen van hoge-dichtheid spinqubitroosters, zoals het crossbar-netwerk, waarbij het niet mogelijk is elektrometers en de hiermee gepaarde reservoirs naast de qubitdots te integreren.

In het derde experiment ontwikkelen we microgolffilters op de chip, waarmee microgolffotonverlies door de electrodes, die noodzakelijk zijn voor de quantumdots, wordt onderdrukt. We introduceren een nieuw ontwerp van de resonator welke compatibel is met lange-afstandsconnectiviteit tussen spins. Deze resonator is echter ook vatbaarder voor microgolfverlies. We testen en vergelijken de presta-

tie, voetafdruk en integreerbaarheid van twee laagdoorlaatfilters. Deze gebruiken dezelfde nanodraadspoel, maar verschillende implementaties van de condensator: één met een planaire in elkaar grijpende condensator, en één nieuw ontwerp met een overlappende dunne-laagcondensator. We zien dat beide varianten effectief zijn tegen microgolfverlies. De grote voetafdruk van de in elkaar grijpende condensator maakt deze echter ongeschikt als het aantal elektrodes toeneemt. De dunne-laagcondensator, met een aanzienlijk kleinere voetafdruk, is geschikter voor onze apparaten.

Het laatste stuk van dit proefschrift bevat conclusies, en mogelijke onderzoeksrichtingen worden voorgesteld.

*Guoji Zheng*

# 1

## Introduction

*We never experiment with just one electron or (small) molecule.
In thought-experiments we sometimes assume that we do;
this invariably entails ridiculous consequences...*

Erwin Schrödinger

**1**

## **1.1.** The first quantum revolution

### **1.1.1.** Since the ancient Greeks

Ancient Greek philosophers Democritus and his mentor Leucippus theoretized, already in the 5th century BCE, that all matter was composed of small indivisible particles called atoms [1]. Despite the fact that they differ from the atoms as we know them today, it was still one of the first formulations of the atomic theory. The atomic theory remained controversial throughout history. Even when John Dalton, in the early 19th century, introduced the modern atomic theory by assimilating the known experimental work of many scientists before him to summarize the empirical evidence on the composition of matter [2]. It was not until the beginning of the 20th century, when Albert Einstein[1] explained in precise details how the motion that Robert Brown observed (now known as "Brownian motion") was a result of the pollen being moved by individual water molecules [3], and after this was further verified experimentally by Jean Perrin a few years later, that the existence of atoms and molecules became the scientific mainstream. Science and technology have advanced at a tremendous pace to the present day, where scientists are able to manipulate individual atoms and electrons literally at the push of a button.

### **1.1.2.** Quantum mechanics

For a complete understanding of the behaviour of particles at the atomic scale, one needs to employ quantum mechanics [4]. Historically, quantum physics started as a collection of phenomenological theories to explain several experimental observations which could not be reconciled with classical physics. Among the first to start the first quantum revolution and establish the foundations of quantum mechanics was Max Planck, who proposed that light could only be absorbed or emitted in discrete energy packets called "quanta". This strange assumption at the time led him to the correct formula of the blackbody radiation spectrum in 1900, thereby resolving the problem of the ultraviolet catastrophe predicted by classical physics. Soon after, Einstein[2] postulated that Planck's quanta were not just a mathematical construct as Planck himself insisted, but real physical particles (later called photons), and applied it to explain the photoelectric effect in 1905 [5]. This observation proved that light, which was until then thought of as electromagnetic waves governed by the Maxwell equations, showed particle-like properties as well. This is a fundamental concept in quantum mechanics and it is called the wave-particle duality. Louis de Broglie extended this concept in 1924 by proposing that, not only light, but also all matter exhibit wave-particle duality.

The modern quantum theory as we know it today came to be in the mid-1920s when more mathematically sophisticated formalisms were developed by Erwin Schrödinger, Werner Heisenberg, Max Born and many other famous scientists. Schrödinger came up with the complex-valued wave function $\Psi(\vec{r}, t)$ to describe a particle. In the Schrödinger picture, the particle is delocalized in space and, accord-

---

[1]This is one of his four groundbreaking papers published in 1905, his Annus Mirabilis ("miracle year"), that radically changed the views on space, time, mass en energy.
[2]Also one of his Annus Mirabilis papers.

ing to Born, the probability density of finding the particle at position $\vec{r}$ at time $t$ is given by the absolute square of the wave function $|\Psi(\vec{r}, t)|^2$. So it is no longer possible to tell with certainty where the particle was before observing it, pointing out the probabilistic nature of a measurement in quantum mechanics. The wave function, however, evolves in time in a deterministic way according to the Schrödinger equation:

$$i\hbar \frac{\partial}{\partial t} \Psi(\vec{r}, t) = \hat{H} \Psi(\vec{r}, t), \tag{1.1}$$

where $\hat{H}$ is the Hamiltonian operator that describes the kinetic and potential energies of the particle.

Quantum mechanics makes some counter-intuitive, yet very interesting, predictions. For instance, a particle can be, loosely speaking, at two different locations at the same time. The phenomenon that a particle can be in two (or more) distinct states is called quantum superposition. When measuring the state (in this case the position) of the particle, the wave function is said to collapse to give a single position. Another prediction according to quantum mechanics is quantum tunneling, where a particle has a finite probability of crossing a potential barrier, even though the particle has insufficient energy to pass over the barrier. This is a scenario that is strictly forbidden according to classical mechanics. Entanglement is one more example of a quantum effect with no classical counterpart, where two or more particles are described by a wave function that cannot be separated into a product of the individual wave functions. This means that the state of one particle cannot be described independently of the state of the other particle. We will see in the next sections how these quantum phenomena are actively used to create new technology.

### 1.1.3. Cavity quantum electrodynamics

The aforementioned wave-particle duality leads to a strange reality in which atoms and light can together exist in a quantum superposition state. The founding fathers of quantum mechanics described thought experiments in which they could control and observe single atoms and photons to reveal some of the counter-intuitive behaviour of nature. The direct observations of said behaviour remained elusive for a long time though, because the technology was not sufficiently advanced yet. In particular, scientists had to wait for the development of lasers, superconducting materials and fast computers. By using these technologies and harnessing coherent light-matter interaction, the teams led by David Wineland [6] and Serge Haroche [7] were among the first to manipulate and detect single atoms and photons, while preserving and exploiting their quantum properties. Their experiments explored the boundaries between quantum and classical mechanics, providing deep insights on how quantum systems lose their quantum information due to interactions with the environment, which is a process called quantum decoherence.

In the field of cavity quantum electrodynamics (QED) [8], pioneered by Haroche and Kimble among others, photons are trapped in a cavity made of highly reflecting superconducting mirrors and beams of atoms crossing the cavity are used to
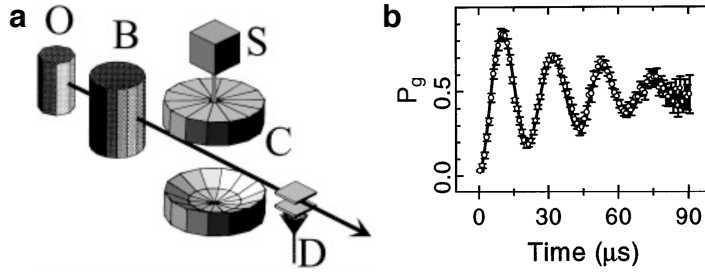
Figure 1.1: **Cavity quantum electrodynamics**. **a** Sketch of the experimental setup. A thermal beam of Rubidium atoms originating from the oven $O$ is promoted to highly excited circular Rydberg states in box $B$. The atoms cross a 3D superconducting cavity $C$ with resonance frequency $\sim$50 GHz. Source $S$ injects continuously a small coherent field into the cavity with energy varying from zero to a few photons. The atoms are detected after passing the cavity at $D$. **b** First experimental observation of vacuum Rabi oscillation with Rydberg atoms (no field injected). The probability of finding the initially excited atom in its ground state $P_g$ depends on the time spent in the cavity. The cavity is tuned into resonance with the transition frequency of the atom here. Adapted from Ref. [10].

manipulate and detect these photons, and to study their evolution (Fig. 1.1a). A theoretical model, introduced by Jaynes and Cummings in 1963 [9], predicted that an initially excited two-level atom in an empty cavity would coherently emit and absorb a single photon, provided that the cavity resonance frequency matches the atom's transition frequency and the rate at which this energy quantum is lost is sufficiently small (so-called strong coupling regime). This process, stimulated by the vacuum fluctuations, is called a vacuum Rabi oscillation and was first observed in 1996 with Rydberg atoms [10] (Fig. 1.1b). The cavity QED framework plays a central role in this thesis, and as will be discussed in the next sections, it can be a useful tool for quantum information processing.

## 1.2. The second quantum revolution

### 1.2.1. From quantum surprises to quantum devices

Some say we are now in the midst of a second quantum revolution [11]. The first quantum revolution furthered our knowledge of physics with quantum science and gave us a new set of rules that governs nature at the microscopic scale. While quantum theory is of fundamental scientific interest, it also led to practical applications. Many important technological inventions were made in the last century which are reliant on the laws of quantum mechanics. These include nuclear energy, laser systems, transistors and MRI scanners, just to name a few. The second quantum revolution will exploit quantum mechanics even further to develop new quantum technologies that actively create, manipulate and read out quantum states of matter, often making use of quantum superposition and entanglement. As Dowling and Milburn phrased it nicely: "The hallmark of this second quantum revolution is the realization that we humans are no longer passive observers of the quantum world that nature has given us" [11]. Quantum technology is expected to have far-reaching implications for society with applications in quantum information pro-

cessing, quantum communication, sensing, imaging and metrology among others.

Quantum technology is driven by mainly two imperatives. The first one is practical. We will soon end up with devices on the nanometer scale due to miniaturization, at which point designs need to be based on quantum mechanics. The second one is more fundamental. Quantum mechanics seems to offer a significantly better performance in certain cases compared to what can be achieved based on the classical framework.

### 1.2.2. Quantum computation and simulation

Building a quantum computer is one of the most daunting technological challenges in the second quantum revolution [12, 13]. Quantum computing is a new computing paradigm which promises to solve certain computational problems intractable for even the best 'classical' supercomputers now [14]. It will have applications across a broad range of disciplines, from fundamental science to industry to artificial intelligence. To name a few: designing more effective drugs and new materials, and factoring large numbers.

The idea of quantum computing is often credited to Richard Feynman, who gave a talk in 1981 arguing that quantum mechanical systems could be used to efficiently solve complex computational problems or to simulate other quantum systems in a way that classical computers cannot [15]. A decade later, the first algorithms for quantum computers were devised which showed a significant quantum speedup for certain tasks. Famous quantum algorithms include Shor's factoring algorithm [16] and Grover's search algorithm [17]. However, there were serious doubts about the feasibility of quantum computing since a single error could ruin the whole computation. In response, Peter Shor [18] and Andrew Steane [19, 20] came up independently around the same time with the first quantum error correction codes. It was not until Shor's work on fault-tolerant quantum computation [21] and subsequent work by others on quantum threshold theorem that convinced scientists that quantum computing with imperfect components was feasible, provided that the error rate is not too high, and started major experimental efforts in this direction. More specifically, the error rate has to be below $1\%$ to achieve fault-tolerant quantum computing, i.e. errors are corrected faster than they are created, using the surface code quantum error-correcting scheme [22]. It has now become a global race to build the first, useful, large-scale quantum computer.

At the heart of a quantum computation lie the principles of superposition and entanglement, which enable computations to be done in parallel. The computation is performed with quantum bits (qubits), which are the building blocks of a quantum processor. Like a normal (classical) bit, one can assign the bit values $|0\rangle$[3] and $|1\rangle$ to the two levels of a qubit. The difference is that a qubit can be prepared in an arbitrary superposition state $|\psi\rangle = a\,|0\rangle + b\,|1\rangle$, with $|a|^2$ ($|b|^2$) the probability of finding the qubit in state $|0\rangle$ ($|1\rangle$), and $|a|^2 + |b|^2 = 1$. When a computation $f(\psi)$ is performed on a qubit in superposition, the result will be a superposition of $f(0)$ and $f(1)$. This means that a single computation can evaluate multiple input values simultaneously. This becomes more rewarding as the number of qubits increases,

---

[3]The $|.\rangle$ is called a ket and physically it represents a quantum state.
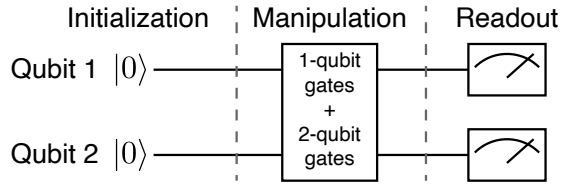
Figure 1.2: **Quantum circuit diagram**. Example of a basic quantum computation circuit diagram for two qubits showing the three stages of a quantum computation: initialization, manipulation and readout of qubits. Time flows from left to right.

i.e. a system comprising $N$ qubits allows for the evaluation of $2^N$ input states simultaneously. To emphasize the difference with classical computers: to double the computational power of a classical computer, one needs the double the number of bits, whereas for a quantum computer, one only needs to add one more qubit.

However, the moment we measure the final superposition state of the system, it collapses randomly to a single state, which is not so useful if that is not the answer we are looking for. Therefore, the purpose of a quantum algorithm is to increase the probability of finding the correct outcome and cancel out the undesired outcomes.

Fig. 1.2 illustrates an example of a circuit diagram of a quantum computation in the case of two qubits (each row represents a qubit). It shows the three stages of a computation: (1) During the initialization stage the qubits are usually prepared in the ground state $|0\rangle$. (2) During the manipulation stage a quantum algorithm is executed using single-qubit gate operations to modify the quantum state of a single qubit and two-qubit gate operations to entangle various qubits. (3) The final qubit states are measured during the readout stage.

Besides representing $|0\rangle$'s and $|1\rangle$'s for quantum computation, qubits can also be used for quantum simulation. Such a system is appropriately called a quantum simulator [23]. It makes use of the high degree of control we have over the intrinsic properties of a quantum system to mimic interactions that underlie a less accessible system.

### 1.2.3. Quantum bits

Various quantum mechanical two-level systems can be used as qubits. In this thesis, the two spin states of an electron in a magnetic field are used to store quantum information. The spin is an intrinsic form of angular momentum and it can be viewed as a tiny magnetic dipole moment that can align parallel or anti-parallel with the magnetic field. Other promising physical implementations include superconducting circuits [24], nitrogen-vacancy centers in diamond [25], trapped ions [26], Majorana fermions [27] and many others. Each type of qubit has its advantages and disadvantages, so it is still unclear which one is going to be the most suited for a quantum computer.

Nevertheless, for a quantum two-level system to function as a proper qubit for quantum computation, it needs to satisfy the five DiVincenzo criteria [28]:

1. A scalable physical system with well-characterized qubits
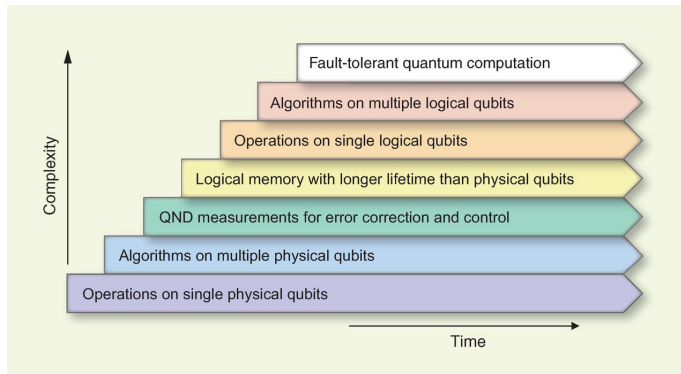
Figure 1.3: **Seven development stages towards a fault-tolerant quantum computer**. Every stage requires full control over the lower stages. Si spin qubits are currently at the third stage (from the bottom) and continuous efforts are being made to bring them to the next level. Adapted from Ref. [24].

2. The ability to initialize the system into a well-defined and determinate initial state, such as |000...⟩

3. Qubit decoherence times much longer than the gate operation times

4. A universal set of quantum gates

5. The ability to read out the qubit state with high fidelity

The above criteria have often been used for assessing the viability of different physical implementations as qubits.

It takes more than a few proper qubits to form a quantum computer. Michel Devoret and Robert Schoelkopf laid out guiding steps towards fault-tolerant quantum computing [24] (see Fig. 1.3). With each step the complexity of the total system increases. The first three stages concern physical qubits. The subsequent steps concern logical qubits. Each logical qubit consists of many physical qubits and is protected by active quantum error correction protocols. Currently, all quantum systems fall in the lower half of this graph.

Despite the fact that we are still a few (big) steps away from achieving a fault-tolerant quantum computer, there will be useful applications along the way in the near future. John Preskill described this as the Noisy Intermediate-Scale Quantum (NISQ) era [29], where devices containing 50-100 physical qubits can perform tasks that cannot be performed with today's best supercomputer.

### 1.2.4. Spin qubits in silicon
The qubit of our choice in this thesis is the spin of a single electron trapped in a semiconductor gate-defined quantum dot, as proposed by Daniel Loss and David DiVincenzo in 1998 [30]. We focus on silicon as the host material for the quantum dots. There are several reasons why the spin degree of freedom is an attractive option for a qubit [31, 32]. First of all, with high-fidelity initialization, readout,
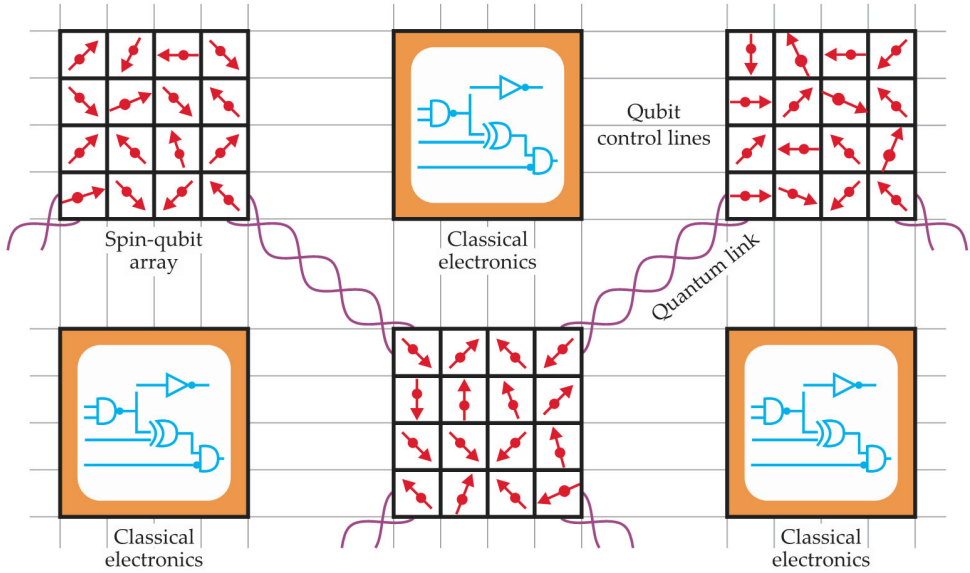
Figure 1.4:  **Vision of a future solid-state, spin-based quantum processor**.  Adapted from Ref. [42].

single- and two-qubit gates, Si spin qubits satisfy the aforementioned DiVincenzo criteria, providing an adequate starting point. Secondly, the small magnetic dipole moment of a spin couples weakly to the noisy solid-state environment. This leads to exceptionally long coherence times, which is an indication of how long a quantum superposition state is preserved. Thirdly, the resemblance of quantum dots to MOSFETs (metal–oxide–semiconductor field-effect transistors) make them compatible with the current highly advanced semiconductor microelectronics technology, especially when silicon is used as the host material [33–37].

As with any qubit platform, increasing the number of qubits while maintaining sufficient control and quality over each one of them is an extremely challenging task. Spin qubits are no exception in that regard. However, spin qubits have the additional advantage of a very small footprint, in comparison to other solid-state qubits (e.g. superconducting qubits), which offers the prospect of high-density integration, similar to classical integrated circuits. There are several proposals on the architecture of a future solid-state quantum processor based on spin qubits [38–41]. One of them, see Fig. 1.4, involves a sparse 2D array of dense spin qubit clusters [39]. Each cluster consists of spin qubits in a 1D linear array or 2D $N \times M$ array with only nearest-neighbour coupling. The 2D array can for instance be implemented using a crossbar design [40], where multiple qubits share the same gate electrode. Neighbouring clusters are connected via coherent quantum links. The long-range interaction between clusters creates space for potential classical electronics.

### 1.2.5. Hybrid superconductor-semiconductor circuit QED

Coherent links, that transfer quantum information from one location to another on the chip, come in different shapes and sizes. For example, the link can consist of a series of coupled quantum dots through which an electron can be shuttled while preserving its spin state [43]. Or transferring the electron spin coherently via surface acoustic waves (SAWs) [44]. Here, we opt for on-chip superconducting microwave resonators [45, 46], which are, to date, one of the most successful quantum links between various solid-state quantum systems, such as superconducting qubits [47–50], and offer long-range coupling over a millimeter distance. Furthermore, high quality factor resonators can act as quantum memories [48, 51]. In circuit QED [52], in analogy to cavity QED (Sec. 1.1.3), quantum devices are engineered using well-developed nanofabrication techniques in order to observe cavity QED behaviour between qubits and photons confined in on-chip superconducting resonators. Techniques inspired by cavity QED are used to manipulate and read out the quantum states of qubits and photons for quantum information processing. Circuit QED offers better scalability due to the compactness of a chip, compared to bulky cavity QED setups (see Fig. 1.1a). In addition, while solid-state qubits 'decohere' much faster than real atoms due to their constant interaction with the noisy environment, the coherent coupling strengths can be cleverly engineered to be much larger than what can be achieved in cavity QED and larger than the qubit loss rates. As a result, circuit QED devices routinely reach the strong coupling regime and beyond.

   In this thesis, we combine semiconductor quantum dots with superconducting resonators in a single device. This brings us into the active field of hybrid superconductor-semiconductor circuit QED [53]. The goal of our research is to build a hybrid circuit QED architecture with single electron spins in silicon, and investigate the feasibility of using superconducting resonators as coherent quantum links between distant spins and as a tool for readout of spin states. The year 2018 was an exciting year in this field as the strong spin-photon coupling regime was reached independently and nearly simultaneously in three labs around the world [54–56], including ours [54]. More amazing experiments are expected to come in this field.

### 1.2.6. Growing interest from outside academia

Both theoretical and experimental research in quantum computing has been conducted for several decades now. Recently, it started gaining traction from parties outside academia. Entities like national governments, institutes, tech and non-tech companies are showing increasing interest in this new quantum technology. And not to mention the numerous quantum startups. Big tech companies are investing directly in quantum computing research. For instance, Google, IBM, Rigetti and Alibaba are developing superconducting qubits. Whereas Intel, CEA-Leti, STMicroelectronics, Imec and HRL are developing spin qubits. Microsoft decided to develop topological qubits. With the help of these parties, progress in quantum computing is advancing at a tremendous pace. Indeed, an important milestone was reached in 2019, when Google claimed that they achieved quantum supremacy [57]. Google used 53 qubits to perform a quantum computation in 200 seconds that would oth-

erwise take a classical supercomputer 10,000 years to complete[4]. Though the computation had no practical use, this remains an amazing technological feat. Now is the time to make full use of the impulse and take quantum technology to the next level.

## **1.3.** Thesis outline

Finally, this thesis is outlined as follows:

- **Chapter 2** reviews the essential theoretical concepts and past experimental work in the field to help us understand and appreciate the experimental results in the later chapters. We begin by describing the general cavity and circuit QED framework in more details. Then, we discuss the physics of superconducting coplanar waveguide resonators and show the two variations measured in this thesis. We proceed by explaining the physics of gate-defined quantum dots in silicon and how they form a good foundation for electron spin qubits. Different types of spin readout will be elaborated on. The chapter ends by describing circuit QED specifically for single spins in double quantum dots and how a spin-photon coupling mechanism can be engineered.

- **Chapter 3** introduces the design and fabrication of the devices measured in Chap. 4 and 5. The remainder of the the chapter describes the room temperature and cryogenic experimental setups and measurement techniques used to obtain the experimental results.

- **Chapter 4** reports the strong coupling between a single electron spin and a single microwave photon, which is an essential step towards long-range spin-spin coupling. The electron spin is trapped in a silicon double quantum dot and the microwave photon is stored in an on-chip high-impedance superconducting cavity. The electric field component of the cavity photon couples directly to the charge dipole of the electron in the double dot, and indirectly to the electron spin, through a strong local magnetic field gradient from nearby micromagnets. Furthermore, we find the charge and spin qubits in the dispersive regime through two-tone spectroscopy. Finally, we demonstrate a fine control over the spin-charge and charge-photon hybridization by tuning the interdot tunnel coupling.

- **Chapter 5** reports the gate-based single-shot readout of singlet-triplet spin states. The on-chip high-impedance cavity is used as a very sensitive detector for the charge susceptibility of a two-electron double quantum dot, which depends on the electron spin configuration due to Pauli's exclusion principle. We characterize the charge sensitivity and bandwidth of this detector, and we subsequently analyze the readout fidelity taking into account spin relaxation.

---

[4]In response to Google's claim, IBM claimed that it would take a supercomputer 2.5 days to complete [58].

- **Chapter 6** reports the new generation of device design that allows for long-distance spin-spin entanglement. The cavity decay rate is dominated by microwave photon leakage to gate electrodes in the new design, so we are forced to develop countermeasures. To combat this loss channel, we develop and test on-chip filters on simplified test devices to isolate the photon loss due to leakage from other loss mechanisms. The on-chip filter comprises a nanowire inductor and an interdigitated or thin-film capacitor.

- **Chapter 7** summarizes the research progress reported in this thesis and draws conclusions based on the key findings. Finally, in the outlook we take our time discussing various possible directions for future research.

## References

[1] C. Taylor, *The Atomists, Leucippus and Democritus: Fragments* (University of Toronto Press, 2010).

[2] J. Dalton, *A New System of Chemical Philosophy* (S. Russell, 1808).

[3] A. Einstein, *Über die von der molekularkinetischen theorie der wärme geforderte bewegung von in ruhenden flüssigkeiten suspendierten teilchen,* Annalen der Physik **322**, 549 (1905).

[4] D. Griffiths and D. Schroeter, *Introduction to Quantum Mechanics* (Cambridge University Press, 2019).

[5] A. Einstein, *Über einen die erzeugung und verwandlung des lichtes betreffenden heuristischen gesichtspunkt,* Annalen der Physik **322**, 132 (1905).

[6] D. J. Wineland, *Nobel lecture: Superposition, entanglement, and raising schrödinger's cat,* Rev. Mod. Phys. **85**, 1103 (2013).

[7] S. Haroche, *Nobel lecture: Controlling photons in a box and exploring the quantum to classical boundary,* Rev. Mod. Phys. **85**, 1083 (2013).

[8] S. Haroche and J. M. Raimond, *Exploring the Quantum: Atoms, Cavities, and Photons* (Oxford Univ. Press, Oxford, 2006).

[9] E. T. Jaynes and F. W. Cummings, *Comparison of quantum and semiclassical radiation theories with application to the beam maser,* Proceedings of the IEEE **51**, 89 (1963).

[10] M. Brune, F. Schmidt-Kaler, A. Maali, J. Dreyer, E. Hagley, J. M. Raimond, and S. Haroche, *Quantum rabi oscillation: A direct test of field quantization in a cavity,* Phys. Rev. Lett. **76**, 1800 (1996).

[11] J. P. Dowling and G. J. Milburn, *Quantum technology: the second quantum revolution,* Philosophical Transactions of the Royal Society of London. Series A: Mathematical, Physical and Engineering Sciences **361**, 1655 (2003).

[12] T. D. Ladd, F. Jelezko, R. Laflamme, Y. Nakamura, C. Monroe,  and J. L. O'Brien, *Quantum computers,* Nature **464**, 45 (2010).

[13] M. Nielsen and I. Chuang, *Quantum Computation and Quantum Information: 10th Anniversary Edition* (Cambridge University Press, 2010).

[14] C. H. Bennett and D. P. DiVincenzo, *Quantum information and computation,* Nature **404**, 247 (2000).

[15] R. P. Feynman, *Simulating physics with computers,* International Journal of Theoretical Physics **21**, 467 (1982).

[16] P. W. Shor, *Algorithms for quantum computation: discrete logarithms and factoring,* in *Proceedings 35th Annual Symposium on Foundations of Computer Science* (1994) pp. 124–134.

[17] L. K. Grover, *A fast quantum mechanical algorithm for database search,* in *Proceedings of the Twenty-Eighth Annual ACM Symposium on Theory of Computing*, STOC '96 (Association for Computing Machinery, New York, NY, USA, 1996) p. 212–219.

[18] P. W. Shor, *Scheme for reducing decoherence in quantum computer memory,* Phys. Rev. A **52**, R2493 (1995).

[19] A. M. Steane, *Error correcting codes in quantum theory,* Phys. Rev. Lett. **77**, 793 (1996).

[20] A. Steane, *Multiple-particle interference and quantum error correction,* Proceedings of the Royal Society of London. Series A: Mathematical, Physical and Engineering Sciences **452**, 2551 (1996).

[21] P. W. Shor, *Fault-tolerant quantum computation,* in *Proceedings of 37th Conference on Foundations of Computer Science* (1996) pp. 56–65.

[22] A. G. Fowler, M. Mariantoni, J. M. Martinis,  and A. N. Cleland, *Surface codes: Towards practical large-scale quantum computation,* Phys. Rev. A **86**, 032324 (2012).

[23] I. Buluta and F. Nori, *Quantum simulators,* Science **326**, 108 (2009).

[24] M. H. Devoret and R. J. Schoelkopf, *Superconducting circuits for quantum information: An outlook,* Science **339**, 1169 (2013).

[25] F. Jelezko, T. Gaebel, I. Popa, M. Domhan, A. Gruber,  and J. Wrachtrup, *Observation of coherent oscillation of a single nuclear spin and realization of a two-qubit conditional quantum gate,* Phys. Rev. Lett. **93**, 130501 (2004).

[26] C. D. Bruzewicz, J. Chiaverini, R. McConnell,  and J. M. Sage, *Trapped-ion quantum computing: Progress and challenges,* Applied Physics Reviews **6**, 021314 (2019).

[27] V. Mourik, K. Zuo, S. M. Frolov, S. R. Plissard, E. P. A. M. Bakkers, and L. P. Kouwenhoven, *Signatures of majorana fermions in hybrid superconductor-semiconductor nanowire devices,* Science **336**, 1003 (2012).

[28] D. P. DiVincenzo, *The physical implementation of quantum computation,* Fortschritte der Physik **48**, 771 (2000).

[29] J. Preskill, *Quantum Computing in the NISQ era and beyond,* Quantum **2**, 79 (2018).

[30] D. Loss and D. P. DiVincenzo, *Quantum computation with quantum dots,* Phys. Rev. A **57**, 120 (1998).

[31] R. Hanson, L. P. Kouwenhoven, J. R. Petta, S. Tarucha, and L. M. K. Vandersypen, *Spins in few-electron quantum dots,* Rev. Mod. Phys. **79**, 1217 (2007).

[32] F. A. Zwanenburg, A. S. Dzurak, A. Morello, M. Y. Simmons, L. C. L. Hollenberg, G. Klimeck, S. Rogge, S. N. Coppersmith, and M. A. Eriksson, *Silicon quantum electronics,* Rev. Mod. Phys. **85**, 961 (2013).

[33] R. Pillarisetty, N. Thomas, H. C. George, K. Singh, J. Roberts, L. Lampert, P. Amin, T. F. Watson, G. Zheng, J. Torres, M. Metz, R. Kotlyar, P. Keys, J. M. Boter, J. P. Dehollain, G. Droulers, G. Eenink, R. Li, L. Massa, D. Sabbagh, N. Samkharadze, C. Volk, B. P. Wuetz, A. M. J. Zwerver, M. Veldhorst, G. Scappucci, L. M. K. Vandersypen, and J. S. Clarke, *Qubit device integration using advanced semiconductor manufacturing process technology,* in *2018 IEEE International Electron Devices Meeting (IEDM)* (2018) pp. 6.3.1–6.3.4.

[34] R. Pillarisetty, H. C. George, T. F. Watson, L. Lampert, N. Thomas, S. Bojarski, P. Amin, R. Caudillo, E. Henry, N. Kashani, P. Keys, R. Kotlyar, F. Luthi, D. Michalak, K. Millard, J. Roberts, J. Torres, O. Zietz, T. Krähenmann, A. M. J. Zwerver, M. Veldhorst, G. Scappucci, L. M. K. Vandersypen, and J. S. Clarke, *High volume electrical characterization of semiconductor qubits,* in *2019 IEEE International Electron Devices Meeting (IEDM)* (2019) pp. 31.5.1–31.5.4.

[35] L. Hutin, R. Maurand, D. Kotekar-Patil, A. Corna, H. Bohuslavskyi, X. Jehl, S. Barraud, S. De Franceschi, M. Sanquer, and M. Vinet, *Si cmos platform for quantum information processing,* in *2016 IEEE Symposium on VLSI Technology* (2016) pp. 1–2.

[36] M. Vinet, L. Hutin, B. Bertrand, S. Barraud, J. . Hartmann, Y. . Kim, V. Mazzocchi, A. Amisse, H. Bohuslavskyi, L. Bourdet, A. Crippa, X. Jehl, R. Maurand, Y. . Niquet, M. Sanquer, B. Venitucci, B. Jadot, E. Chanrion, P. . Mortemousque, C. Spence, M. Urdampilleta, S. De Franceschi, and T. Meunier, *Towards scalable silicon quantum computing,* in *2018 IEEE International Electron Devices Meeting (IEDM)* (2018) pp. 6.5.1–6.5.4.

[37] L. Bourdet, L. Hutin, B. Bertrand, A. Corna, H. Bohuslavskyi, A. Amisse, A. Crippa, R. Maurand, S. Barraud, M. Urdampilleta, C. Bäuerle, T. Meunier,

M. Sanquer, X. Jehl, S. De Franceschi, Y. Niquet, and M. Vinet, *All-electrical control of a hybrid electron spin/valley quantum bit in soi cmos technology,* IEEE Transactions on Electron Devices **65**, 5151 (2018).

[38] M. Veldhorst, H. G. J. Eenink, C. H. Yang, and A. S. Dzurak, *Silicon cmos architecture for a spin-based quantum computer,* Nature Communications **8**, 1766 (2017).

[39] L. M. K. Vandersypen, H. Bluhm, J. S. Clarke, A. S. Dzurak, R. Ishihara, A. Morello, D. J. Reilly, L. R. Schreiber, and M. Veldhorst, *Interfacing spin qubits in quantum dots and donors–hot, dense, and coherent,* npj Quantum Information **3**, 34 (2017).

[40] R. Li, L. Petit, D. P. Franke, J. P. Dehollain, J. Helsen, M. Steudtner, N. K. Thomas, Z. R. Yoscovits, K. J. Singh, S. Wehner, L. M. K. Vandersypen, J. S. Clarke, and M. Veldhorst, *A crossbar network for silicon quantum dot qubits,* Science Advances **4** (2018), 10.1126/sciadv.aar3960.

[41] J. M. Boter, J. P. Dehollain, J. P. G. van Dijk, T. Hensgens, R. Versluis, J. S. Clarke, M. Veldhorst, F. Sebastiano, and L. M. K. Vandersypen, *A sparse spin qubit array with integrated control electronics,* in *2019 IEEE International Electron Devices Meeting (IEDM)* (2019) pp. 31.4.1–31.4.4.

[42] L. M. K. Vandersypen and M. A. Eriksson, *Quantum computing with semiconductor spins,* Physics Today **71**, 38 (2019).

[43] T. Fujita, T. A. Baart, C. Reichl, W. Wegscheider, and L. M. K. Vandersypen, *Coherent shuttle of electron-spin states,* npj Quantum Information **3**, 22 (2017).

[44] B. Jadot, P.-A. Mortemousque, E. Chanrion, V. Thiney, A. Ludwig, A. D. Wieck, M. Urdampilleta, C. Bäuerle, and T. Meunier, *Distant spin entanglement via fast and coherent electron shuttling,* (2020), arXiv:2004.02727 [cond-mat.mes-hall] .

[45] K. D. Petersson, L. W. McFaul, M. D. Schroer, M. Jung, J. M. Taylor, A. A. Houck, and J. R. Petta, *Circuit quantum electrodynamics with a spin qubit,* Nature **490**, 380 (2012).

[46] T. Frey, P. J. Leek, M. Beck, A. Blais, T. Ihn, K. Ensslin, and A. Wallraff, *Dipole coupling of a double quantum dot to a microwave resonator,* Phys. Rev. Lett. **108**, 046807 (2012).

[47] J. Majer, J. M. Chow, J. M. Gambetta, J. Koch, B. R. Johnson, J. A. Schreier, L. Frunzio, D. I. Schuster, A. A. Houck, A. Wallraff, A. Blais, M. H. Devoret, S. M. Girvin, and R. J. Schoelkopf, *Coupling superconducting qubits via a cavity bus,* Nature **449**, 443 (2007).

[48] M. A. Sillanpää, J. I. Park, and R. W. Simmonds, *Coherent quantum state storage and transfer between two phase qubits via a resonant cavity,* Nature **449**, 438 (2007).

[49] L. DiCarlo, J. M. Chow, J. M. Gambetta, L. S. Bishop, B. R. Johnson, D. I. Schuster, J. Majer, A. Blais, L. Frunzio, S. M. Girvin, and R. J. Schoelkopf, *Demonstration of two-qubit algorithms with a superconducting quantum processor,* Nature **460**, 240 (2009).

[50] L. DiCarlo, M. D. Reed, L. Sun, B. R. Johnson, J. M. Chow, J. M. Gambetta, L. Frunzio, S. M. Girvin, M. H. Devoret, and R. J. Schoelkopf, *Preparation and measurement of three-qubit entanglement in a superconducting circuit,* Nature **467**, 574 (2010).

[51] W. Pfaff, C. J. Axline, L. D. Burkhart, U. Vool, P. Reinhold, L. Frunzio, L. Jiang, M. H. Devoret, and R. J. Schoelkopf, *Controlled release of multiphoton quantum states from a microwave cavity memory,* Nature Physics **13**, 882 (2017).

[52] A. Blais, A. L. Grimsmo, S. M. Girvin, and A. Wallraff, *Circuit quantum electrodynamics,* (2020), arXiv:2005.12667 [quant-ph] .

[53] G. Burkard, M. J. Gullans, X. Mi, and J. R. Petta, *Superconductor-semiconductor hybrid-circuit quantum electrodynamics,* Nature Reviews Physics (2020), 10.1038/s42254-019-0135-2.

[54] N. Samkharadze, G. Zheng, N. Kalhor, D. Brousse, A. Sammak, U. C. Mendes, A. Blais, G. Scappucci, and L. M. K. Vandersypen, *Strong spin-photon coupling in silicon,* Science **359**, 1123 (2018).

[55] X. Mi, M. Benito, S. Putz, D. M. Zajac, J. M. Taylor, G. Burkard, and J. R. Petta, *A coherent spin-photon interface in silicon,* Nature **555**, 599 (2018).

[56] A. J. Landig, J. V. Koski, P. Scarlino, U. C. Mendes, A. Blais, C. Reichl, W. Wegscheider, A. Wallraff, K. Ensslin, and T. Ihn, *Coherent spin-photon coupling using a resonant exchange qubit,* Nature **560**, 179 (2018).

[57] F. Arute *et al.*, *Quantum supremacy using a programmable superconducting processor,* Nature **574**, 505 (2019).

[58] E. Pednault, J. A. Gunnels, G. Nannicini, L. Horesh, and R. Wisnieff, *Leveraging secondary storage to simulate deep 54-qubit sycamore circuits,* (2019), arXiv:1910.09534 [quant-ph] .

# 2

# Theoretical and experimental background

*I think I can safely say that nobody understands quantum mechanics.*

Richard P. Feynman

*This chapter reviews the essential theoretical concepts and past experimental work in the field of hybrid superconductor-semiconductor circuit QED in order to help us understand and appreciate the experimental results in the later chapters. We begin by describing the general cavity and circuit QED framework. Next, the constituents are explained in more detail: a superconducting coplanar waveguide resonator as the cavity, and an electron spin in a semiconductor double quantum dot as the two-level system. The chapter ends with the results of the input-output theory for circuit QED with an electron charge and spin, which can be used to gain more insight into the measurement results. Many references to earlier work for further reading will be shared throughout the chapter.*

## **2.1.** Circuit quantum electrodynamics

Cavity quantum electrodynamics (QED) describes the physics between light and matter at the single-particle level [1, 2]. The most basic system for studying this physics is a two-level atom interacting via a dipole coupling with a cavity, which can be described by a quantum harmonic oscillator with photons as excitations. Early experiments were performed with real atoms and microwave or optical photons trapped in high quality 3D cavities (Fig. 2.1a). More recently, cavity QED has been reproduced in solid-state systems [3–6]. An artificial atom or qubit is used instead of a real atom, and an on-chip resonant circuit takes the place of a 3D cavity to confine microwave photons (Fig. 2.1b). The term circuit QED was aptly adopted to distinguish the latter from cavity QED. In both cavity and circuit QED the behaviour of the coupled system is captured by the quantum Rabi model [7–9]:

$$H_{\mathrm{Rabi}} = \hbar\omega_r \left( a^\dagger a + \frac{1}{2} \right) + \frac{1}{2}\hbar\omega_q \sigma_z + \hbar g \left( a^\dagger + a \right)\left( \sigma^- + \sigma^+ \right). \qquad (2.1)$$

The first term represents the energy of a single mode of the electromagnetic field, with $\omega_r$ the frequency of the photons, $a$ ($a^\dagger$) the photon annihilation (creation) operator, $a^\dagger a = n$ the photon number operator and $\hbar$ the reduced Planck constant. The second term represents the (artificial) atom as an effective two-level system, with $\omega_q$ the frequency difference between the two levels and $\sigma_z$ the Pauli-$z$ operator. The last term describes the dipole interaction between the two-level system and the cavity field, with $g$ the coupling strength and $\sigma^-$ ($\sigma^+$) the lowering (raising) operator acting on the two-level system.

The quantum Rabi model can be simplified by applying the rotating wave ap-poximation (RWA) to eliminate the fast-rotating terms $\left( a^\dagger\sigma^+ + a\sigma^- \right)$ that describes the simultaneous excitation and relaxation of the two-level system and cavity. This approximation is valid for $g \ll \omega_r, \omega_q$ and $|\omega_r - \omega_q| \ll |\omega_r + \omega_q|$, which turns out to be the case for many experiments. The result is the well-known Jaynes-Cummings Hamiltonian [10]:

$$H_{\mathrm{JC}} = \hbar\omega_r \left( a^\dagger a + \frac{1}{2} \right) + \frac{1}{2}\hbar\omega_q \sigma_z + \hbar g \left( a^\dagger\sigma^- + a\sigma^+ \right). \qquad (2.2)$$

The third term here describes the absorption ($a\sigma^+$) and emission ($a^\dagger\sigma^-$) of a photon by the two-level system from and to the cavity at a rate $2g$, respectively. Generally, the coupling strength $g = E^0_{\mathrm{rms}}d/\hbar$ is determined by the transition dipole moment $d$ and the rms vacuum electric field $E^0_{\mathrm{rms}}$. In circuit QED, $g$ can be much larger than in cavity QED in the microwave domain due to a physically large artificial atom (larger $d$) and small cavity design (larger $E^0_{\mathrm{rms}}$) [4]. The exact expression for $g$, however, will depend on the details of the two-level system and its underlying coupling mechanism to the magnetic or electric part of the cavity field. This will be worked out for a single charge and spin in Sec. 2.6.

The Jaynes-Cummings Hamiltonian above describes only coherent behaviour, but in reality there are also incoherent processes that obscure the dynamics of the coupled system. On the one hand, photons leak out of or are absorbed by the
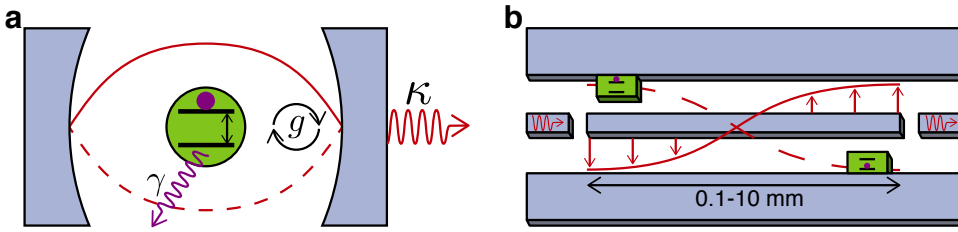
Figure 2.1: **Cavity and circuit quantum electrodynamics**. **a** An atom going through a 3D cavity and interacting with the cavity field at rate $g$. Photons are lost at rate $\kappa$, and the atom decays into modes not captured by the cavity at rate $\gamma$. The strong coupling regime is reached when the coherent interaction rate is larger than the decoherence rates: $g > \kappa, \gamma$. **b** Solid-state equivalent system to **a**, with an on-chip electromagnetic resonator coupled to artificial atoms or qubits. These qubits can be separated by a distance set by the length of the resonator and still interact with each other through the resonator.

cavity, resulting in a photon decay rate $\kappa$. This can also be expressed in terms of the quality factor of the resonator $Q = \omega_r/\kappa$. However, not all leakages are undesired since photons that are leaked into the detector allow us to probe the system. On the other hand, the (artificial) atom decays at a rate $\gamma$ into channels not captured by the cavity.

Exact diagonalization of $H_{\mathrm{JC}}$ yields the ground state $|g, 0\rangle$ and excited eigenstates [4]:

$$|+, n\rangle = \sin \theta_n |g, n+1\rangle + \cos \theta_n |e, n\rangle, \tag{2.3}$$
$$|-, n\rangle = \cos \theta_n |g, n+1\rangle - \sin \theta_n |e, n\rangle, \tag{2.4}$$

with

$$\theta_n = \frac{1}{2} \arctan\left(\frac{2g\sqrt{n+1}}{\Delta}\right). \tag{2.5}$$

The corresponding eigenenergies are:

$$E_{g,0} = -\frac{\hbar\Delta}{2}, \tag{2.6}$$

$$E_{\pm,n} = (n+1)\,\hbar\omega_r \pm \frac{\hbar}{2}\sqrt{4g^2\,(n+1) + \Delta^2}, \tag{2.7}$$

with atom-cavity detuning $\Delta = \omega_q - \omega_r$.

When considering only a single excitation at resonance, $\Delta = 0$, the eigenstates of the coupled system reduce to $|\pm, 0\rangle = (|g, 1\rangle \pm |e, 0\rangle)/\sqrt{2}$. The two-level system and cavity are maximally hybridized, and an initially excited two-level system in an empty cavity ($|e, 0\rangle$) will exhibit a coherent oscillation between $|e, 0\rangle$ and $|g, 1\rangle$ at the vacuum Rabi frequency $2g$. This phenomenon is called the vacuum Rabi oscillation because it can be interpreted as the vacuum fluctuations stimulating the

**2**
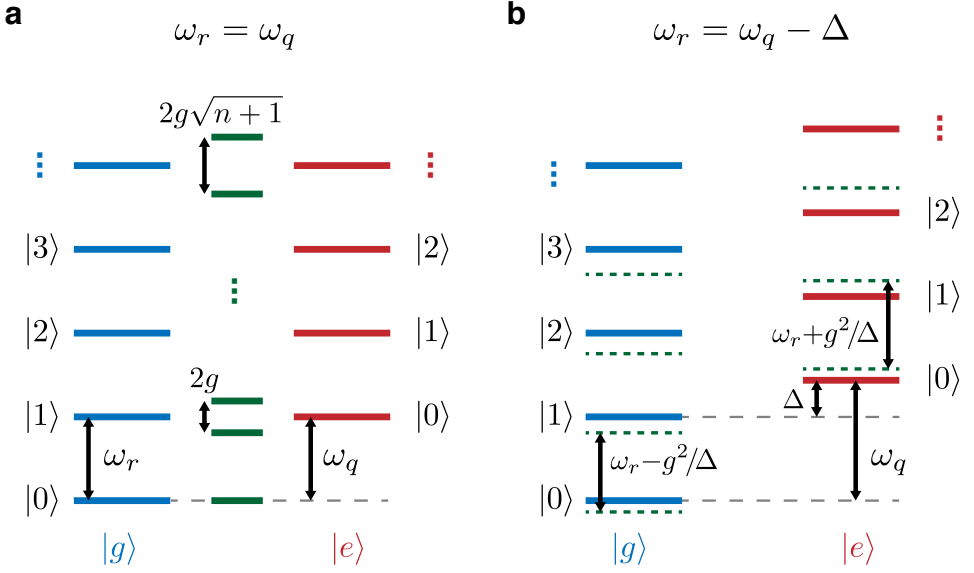


Figure 2.2: **Energy level diagrams of the Jaynes-Cummings Hamiltonian**. **a** Resonant regime: $|\Delta| \ll g$. The blue and red energy levels are the eigenstates of the uncoupled Hamiltonian, with left the qubit in the ground state $|g\rangle$ and right in the excited state $|e\rangle$, and $|n\rangle$ the photon number state with $n$ photons. The green levels in the middle include the dipole coupling, and are split by $2g\sqrt{n+1}$ to form new hybridized eigenstates. **b** Dispersive regime: $|\Delta| \gg g$. The cavity frequency shifts by $\pm g^2/\Delta$, depending on the state of the qubit. The qubit frequency shifts by $(2n+1)\,g^2/\Delta$, depending on the number of photons $n$ in the cavity. Adapted from Ref. [4].

emission and absorption of a photon by the two-level system. There is always a competition between coherent and incoherent processes. When many oscillations can take place before the excitation is lost, the system reaches the so-called strong coupling regime $g > \kappa, \gamma$.

Another way to view the strong coupling regime is to look at the energy levels of the hybridized system (Fig. 2.2a). The lowest levels at resonance are split by $2g$, the vacuum Rabi splitting. The finite lifetime of the individual systems contribute to the broadening of these energy levels, which will be a combination of $\kappa$ and $\gamma$. When the two-level system or photon decays before a single oscillation has completed, the splitting is obscured by the broadening of the levels. In the strong coupling limit these levels are well resolved. Only in this regime the full benefits of circuit QED can be reaped for quantum information processing.

### 2.1.1. Dispersive limit

In the dispersive limit, $|\Delta| > 10g$, no energy is exchanged between the two-level system and cavity. The Jaynes-Cummings Hamiltonian can be approximated in this limit as:

$$H_{\text{JC}}^{\text{disp}} \approx \hbar \left( \omega_r + \frac{g^2}{\Delta} \sigma_z \right) \left( a^\dagger a + \frac{1}{2} \right) + \frac{1}{2} \hbar \omega_q \sigma_z, \tag{2.8}$$

where the bare cavity frequency $\omega_r$ is shifted by $\pm g^2/\Delta$, conditional on the state of the two-level system. This effect allows us to use the cavity for dispersive readout of the two-level system. This type of measurement is quantum nondemolition (QND), which projects the two-level system into the state that is being measured and leaves it in that state after the measurement.

The terms in $H_{\text{JC}}^{\text{disp}}$ can be grouped differently to highlight the effect on the two-level system:

$$H_{\text{JC}}^{\text{disp}} \approx \hbar \omega_r \left( a^\dagger a + \frac{1}{2} \right) + \frac{1}{2} \hbar \left( \omega_q + \frac{2g^2}{\Delta} a^\dagger a + \frac{g^2}{\Delta} \right) \sigma_z, \tag{2.9}$$

where the two-level system gets an AC-stark shift ($2ng^2/\Delta$) depending on the photon number $n$, and a Lamb shift ($g^2/\Delta$) due to the vacuum energy fluctuations [11]. By probing the frequency of the two-level system, one can perform a QND measurement of the photon number. The AC-Stark shift effect can be conveniently used to calibrate the average photon number. When the cavity shift is larger than the cavity linewidth $\kappa$ and qubit linewidth $\gamma$, $2g^2/|\Delta| > \kappa, \gamma$, the system reaches the strong dispersive regime. The hallmark of this regime is that the qubit spectrum reveals well-resolved photon number peaks.

### 2.1.2. The cavity as a quantum bus

The cavity can be used as a quantum bus, which is a tool used to store and transfer quantum information between distant qubits coupled to the same cavity (see Fig. 2.1b). This was successfully accomplished for the first time using superconducting transmon qubits [12] and phase qubits [13]. The system of multiple qubits interacting with a single cavity mode can be described by the Tavis-Cummings Hamiltonian [14, 15]:

$$H_{\text{TC}} = \hbar \omega_r a^\dagger a + \sum_i \frac{1}{2} \hbar \omega_{q_i} \sigma_z^i + \sum_i g_i \left( a^\dagger \sigma_i^- + a \sigma_i^+ \right), \tag{2.10}$$

where the constant term $\hbar \omega_r/2$ is left out. This Hamiltonian simply reduces to $H_{\text{JC}}$ for a single qubit.

One way to transfer quantum information from one qubit to another is via a mapping onto a Fock state (photon number state) of the cavity using vacuum Rabi oscillations sequentially. However, this method suffers from photon decay since a real photon is used in the process, and forms a disadvantage when $\kappa$ is the dominant loss rate.

Alternatively, virtual photons can be used to transfer quantum information. In this scheme both qubits are dispersively coupled to the cavity, $|\Delta_i| = |\omega_{q_i} - \omega_r| \gg g_i$. Here, the qubit states contain a small photon component, but remain mostly qubit. When multiple qubits are strongly coupled to the same cavity, the photonic part of

**2**
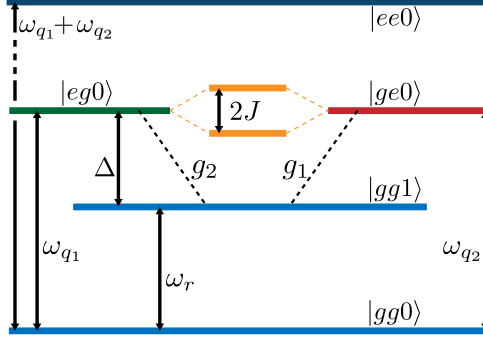


Figure 2.3: **Energy level diagram of the dispersive Tavis-Cummings Hamiltonian in the case of two qubits**. Possible scheme for dispersive qubit-qubit coupling. The qubit-state-dependent shifts of the resonator and AC Stark shift of the qubits are not shown. When the qubits are in resonance ($\omega_{q_1} = \omega_{q_2}$), they interact with each other via the exchange of a virtual photon $|gg1\rangle$ in the cavity at a rate $2J$. Adapted from Ref. [12].

the qubits overlap, creating a non-local coupling. The Hamiltonian for two qubits in the dispersive limit can be approximated as:

$$H_{\text{TC}}^{\text{disp}} \approx \hbar \left( \omega_r + \text{X}_1 \sigma_z^1 + \text{X}_2 \sigma_z^2 \right) a^\dagger a + \sum_{i=1}^{2} \frac{1}{2} \hbar \omega_{q_i} \sigma_z^i + \hbar J \left( \sigma_1^- \sigma_2^+ + \sigma_2^- \sigma_1^+ \right), \quad (2.11)$$

where $\text{X}_i = g_i^2/\Delta_i$ is the dispersive shift due to qubit $i$. Fig. 2.3 shows a simplified diagram of the lowest energy levels. The last term in $H_{\text{TC}}^{\text{disp}}$ describes the cavity-mediated interaction between the two qubits, characterized by the transverse exchange interaction:

$$J = \frac{g_1 g_2}{2} \left( \frac{1}{\Delta_1} + \frac{1}{\Delta_2} \right). \quad (2.12)$$

This interaction allows one to perform the $i\text{SWAP}$ and $\sqrt{i\text{SWAP}}$ gates. This method nicely circumvents cavity-induced loss as no real photons are used in the process, but it requires $J > \gamma_1, \gamma_2$ to work efficiently.

## 2.2. Superconducting resonators

Superconducting resonators are ubiquitous in science and technology due to their very high quality factors and relative ease of fabrication. They are important in a variety of applications ranging from (single-)photon detection [16–18] to parametric amplification [19, 20], to narrow-band filtering [21] and quantum information processing [3, 4, 22, 23]. In the latter, they are utilized as interconnect, readout and memory elements in quantum processors. The superconducting part assures that the losses are small, allowing resonators to reach quality factors $Q > 10^6$. This means that a photon can resonate about $10^6$ times inside the cavity before

**a**

**b**
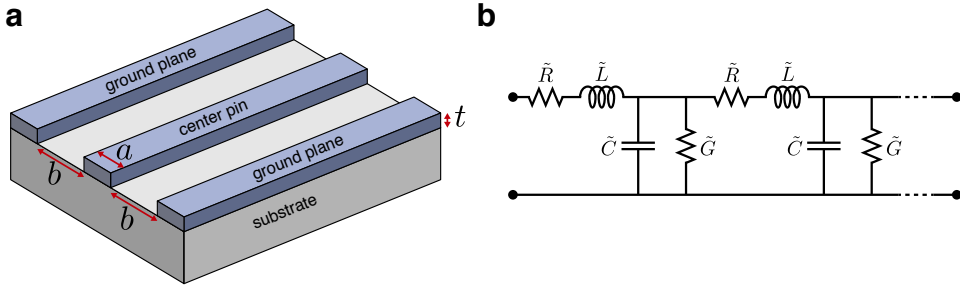


Figure 2.4: **Coplanar waveguide geometry**. **a** Schematic of a CPW segment showing the key length scales $a$, $b$ and $t$ to consider in a design. The conductors are usually deposited on a low-loss dielectric substrate with a thickness much larger than the dimensions $a$, $b$ and $t$. **b** The planar transmission line can be modelled as an infinite series of lumped-element inductors, capacitors and resistors. The symbols are explained in the text.

decaying, and corresponds to an average photon lifetime of a few hundred microseconds, in which the photon can travel an equivalent distance of hundreds of kilometers before decaying!

The resonators considered here are designed to be in the microwave-frequency range 4-10 GHz. On the one hand, this is high enough in frequency to sit in the photonic ground state at thermal equilibrium, $\hbar\omega_r \gg k_B T$, using dilution refrigerators that can easily reach temperatures of $T \approx 10$ mK. On the other hand, this is low enough in frequency to use low-noise, high-performance and affordable microwave electronics developed for the telecommunication and (military) satellite industries, such as high-electron-mobility transistor (HEMT) amplifiers, isolators, mixers, and fast measurement instruments.

## 2.2.1. Coplanar waveguides

A popular type of superconducting resonator is the coplanar waveguide (CPW) resonator. This is a distributed resonant circuit, meaning that the voltage and current varies in magnitude and phase over its length. Due to their large size (millimeter scale) and distributed nature, they are highly controllable in terms of resonance frequency, impedance and coupling to other transmission lines. The CPW is a planar transmission line that can be viewed as the 2D variant of a coaxial line (Fig. 2.4a), and is well suited for transmitting radio- and microwave-frequency signals. The center pin sits between ground planes. As signal propagates through the CPW, the current flows at the edges of the center pin and ground planes. The current in the center pin is equal and antiparallel to the currents in the ground planes. The currents in the ground planes are in the ideal case equal and in phase (even mode).

The physics of CPWs and CPW resonators have been studied extensively in the literature [23–27]. Here, we review only the theory relevant to the work presented in this thesis. The characteristic impedance of a transmission line is given by (Fig. 2.4b):

**2**

$$Z = \sqrt{\frac{\tilde{R} + i\omega\tilde{L}}{\tilde{G} + i\omega\tilde{C}}} \approx \sqrt{\frac{\tilde{L}}{\tilde{C}}}, \tag{2.13}$$

with $\tilde{R}$, $\tilde{G}$, $\tilde{L}$ and $\tilde{C}$ the resistance, conductance, inductance and capacitance per unit length. The resistance $\tilde{R}$ is responsible for the resistive loss in the conductor, whereas the conductance $\tilde{G}$ accounts for the leakage through the dielectric. Both losses are negligible in practice for superconducting resonators, justifying the approximation to $Z = \sqrt{\tilde{L}/\tilde{C}}$. CPWs are usually designed to have a characteristic impedance of $Z_0 = 50\,\Omega$ in order to efficiently interface with commercially available hardware, thereby minimizing signal reflections and distortions. The inductance $\tilde{L}$ can be broken down into $\tilde{L} = \tilde{L}_g + \tilde{L}_k$, with $\tilde{L}_g$ the geometric (magnetic) inductance and $\tilde{L}_k$ the kinetic inductance. The latter can be quite sizable in thin superconducting films. The kinetic inductance is an essential parameter in this thesis, and will be elaborated in Sec. 2.2.4. The geometric inductance and capacitance per unit length are given by the following expressions:

$$\tilde{L}_g = \frac{\mu_0}{4} \frac{K(k')}{K(k)}, \tag{2.14}$$

$$\tilde{C} = 4\mu_0 \epsilon_{\text{eff}} \frac{K(k)}{K(k')}, \tag{2.15}$$

where $\mu_0$ and $\epsilon_0$ are the vacuum permeability and permittivity, respectively, $K$ is the complete elliptic integral of the first kind, $k = a/(a+2b)$, $k' = \sqrt{1-k^2}$, $a$ is the center conductor width and $b$ is the gap width with the ground plane (Fig. 2.4a). Typically for $50\,\Omega$ CPWs, $a$ and $b$ are a few microns wide while $t$ is an order of magnitude smaller. The effective dielectric constant is approximately $\epsilon_{\text{eff}} \approx (1 + \epsilon_{\text{substrate}})/2$ as roughly half of the electric field lines are in vacuum and the other half in the substrate.

## 2.2.2. Coplanar waveguide resonators

A CPW can be made into a resonator by introducing impedance mismatches at the ends of a CPW strip of length $l$. An open end boundary condition imposes a voltage antinode (and a current node), whereas a shorted end boundary condition imposes a voltage node (and a current antinode). A resonator with two open ends has a fundamental mode of wavelength $\lambda/2$ with angular resonance frequency:

$$\omega_r = 2\pi f_r = \frac{2\pi}{2l\sqrt{\tilde{L}\tilde{C}}}. \tag{2.16}$$

Alternatively, one open end and one end shorted to ground creates a resonator with fundamental mode of wavelength $\lambda/4$ and angular resonance frequency $\omega_r/2$. Higher order modes $n\lambda/2$ and $m\lambda/4$ exist with resonances occurring at $n\omega_r$ ($n = 1, 2, 3, ...$; $n = 1$ for the fundamental mode) and $m\omega_r/2$ ($m = 1, 3, 5, ...$; $m = 1$ for the fundamental mode), respectively.

Often in the literature, CPW resonators are approximated by parallel lumped-element $LCR$ circuits around the resonance frequency. Care has to be taken when making this comparison as the lumped inductance $L^{\mathrm{LCR}}$ and capacitance $C^{\mathrm{LCR}}$ differ from their distributed counterparts [5]. This can be intuitively understood by realizing that at the location of the voltage (current) nodes in the distributed resonant circuit there is no contribution to the AC capacitance (inductance). More precisely, the angular resonance frequency of the lumped-element model is given by $\omega_{r,n}^{\mathrm{LCR}} = 1/\sqrt{L_n^{\mathrm{LCR}}C^{\mathrm{LCR}}}$. Compared to a distributed $\lambda/2$-resonator, the lumped-element capacitance and inductance are $C^{\mathrm{LCR}} = \frac{1}{2}\tilde{C}l$ and $L_n^{\mathrm{LCR}} = \frac{2}{n^2\pi^2}\tilde{L}l$, respectively. The impedance of the $LCR$ oscillator relates to the CPW resonator impedance according to $Z_n^{\mathrm{LCR}} = \frac{2}{n\pi}Z_r$.

Two distinct designs, related to the way CPW resonators are coupled to the outside world, are typically realized in the lab and will be discussed next (Fig. 2.5). Note that both implementations concern transmission line resonators and that the naming below is just for the sake of distinguishing between the two alternatives.

**Transmission style resonator**: In this design the CPW is interrupted at two locations separated by a distance $l$, defining the boundary conditions of the resonator (Fig. 2.5a). The gaps form capacitors at the ends of the resonator, which have a function analogous to mirrors in cavity QED with the transparency to photons fixed by the capacitance. The electrical behavior of this two-port system can be described using scattering parameters ($S$-parameters). The complex $S_{ij}$ parameter is defined as the ratio between the voltage wave originating from port $j$ and voltage wave arriving at port $i$. For example, $S_{21}$ is the complex transmission coefficient and describes how the signal from port 1 propagates through the resonator and arrives at port 2. The signal from port 1 (left) can only reach port 2 (right) when its frequency matches one of the resonance frequencies of the resonator. This naturally leads to a peak in the power of the transmitted signal $|S_{21}|^2$ and a phase shift of $\pi$ around $\omega_r$ (Fig. 2.5c). The resonance profile in the power spectrum follows a Lorentzian lineshape:

$$F_T(\omega) = A\frac{\kappa}{\left(\omega - \omega_r\right)^2 + \left(\frac{\kappa}{2}\right)^2}, \tag{2.17}$$

where $A$ is a scaling parameter and $\kappa$ is the full width at half maximum (FWHM), which quantifies the photon decay rate. This is because an exponentially damped oscillation in the time domain gives rise to a Lorentzian shape in the frequency domain. The phase change across resonance is given by:

$$\phi_T(\omega) = \arctan\left(\frac{2(\omega - \omega_r)}{\kappa}\right). \tag{2.18}$$

Transmission style resonators are experimentally characterized in Chap. 6.

**Hanger style resonator**: In this case the CPW resonator is placed adjacent to a transmission line called the feedline and coupled capacitively or inductively to it (Fig. 2.5b). In order to fully describe the electrical behavior of this system,

**2**
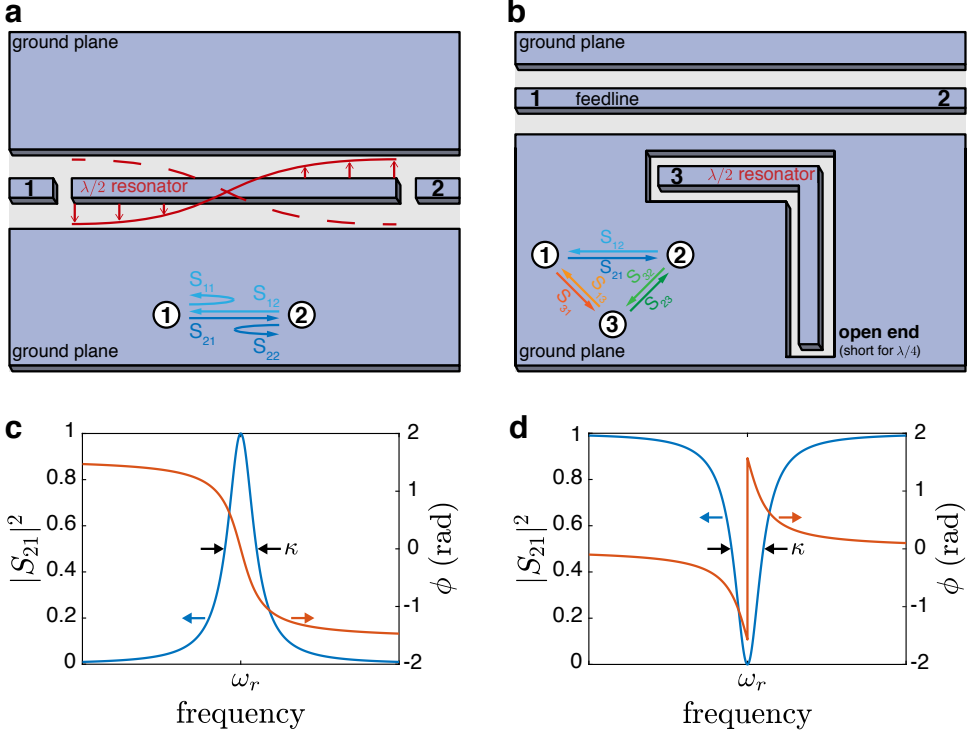


Figure 2.5:  **Two ways of probing CPW resonators and their corresponding frequency response**.  **a** Drawing of a typical transmission style resonator. The boundary conditions are set by the two discontinuities in the center conductor. The voltage distribution of the fundamental mode ($\lambda/2$) along the length of the resonator is shown by the solid and dashed red lines. The scattering parameters $S_{ij}$ describe how the resonator modifies a signal that is transmitted ($S_{21}$, $S_{12}$) or reflected ($S_{11}$, $S_{22}$) at each port.  **b** Drawing of a typical hanger style resonator. The resonator is capacitively coupled to the feedline (or inductively if the current antinode is placed parallel to the feedline). The fundamental mode here is $\lambda/2$, but it can be $\lambda/4$ when one of the ends is shorted to ground. This system can be modeled as a three-port network.  **c** Simulated power and phase spectrum of a resonator in **a** with signal input from port 1 and measured at port 2. The FWHM of the transmitted power is the cavity decay rate $\kappa$.  **d** Simulated power and phase spectrum of a resonator in **b** with signal input from port 1 and measured at port 2.

the $S$-matrix needs to take three ports into account. Again, we look at the signal propagating from port 1 to port 2, $S_{21}$, which depends on $S_{31}$ and $S_{23}$ as the signal interacts with the resonator. The transmitted power through the feedline shows an opposite response compared to the previous design, i.e. a dip instead of a peak near $\omega_r$ (Fig. 2.5d):

$$F_H(\omega) = 1 - F_T(\omega). \tag{2.19}$$

This can be intuitively seen as photons from the resonator destructively interfering with the photons in the feedline after acquiring a $\pi$ phase shift in the resonator. The phase of the transmitted signal near the resonance frequency for the hanger style resonator is described by:

$$\phi_H(\omega) = \arctan\left(\frac{\kappa}{2(\omega - \omega_r)}\right). \tag{2.20}$$

An advantage of this design is the ability to frequency multiplex resonators, i.e. multiple resonators with different resonance frequencies can be coupled to the same feedline. A single measurement can then characterize multiple resonators without additional hardware. Another advantage is the possibility to extract, from a single power or phase spectrum, besides the total cavity decay rate $\kappa$, also the external and internal decay rates $\kappa_{\text{ext}}$ and $\kappa_{\text{int}}$, respectively. This is possible because the power spectrum contains information about the maximum transmission through the feedline (i.e. the transmission away from $\omega_r$), but more on this in the next section. The hanger style resonator is used in Chap. 4 and 5.

### 2.2.3. Resonator loss mechanisms

A commonly used figure of merit for the performance of a resonator is the quality factor and relates to $\kappa$ as follows:

$$Q = \frac{\omega_r E}{P} = \frac{\omega_r}{\kappa}, \tag{2.21}$$

with $E$ the energy stored in the resonator and $P$ the power loss. The finite resonator linewidth $\kappa$ in the power spectrum is caused by a finite photon lifetime $\tau$: $\kappa = 2\pi/\tau$. In the previous section we assumed the ideal situation in which $\tau$ was solely due to leakage of photons into the transmission line. In reality, the resonator couples electrically and magnetically to its surrounding, and loses part of its energy unintentionally through unwanted channels. The total cavity decay rate $\kappa$ can be decomposed into:

$$\kappa = \kappa_{\text{ext}} + \kappa_{\text{int}}, \tag{2.22}$$

with $\kappa_{\text{ext}}$ being the external cavity decay rate due to a finite capacitive coupling with capacitance $C_{\text{ext}}$ to a transmission line, and is given by [18]:

$$\kappa_{\text{ext}} = \frac{2}{\pi} \omega_r^3 Z_r Z_0 C_{\text{ext}}^2. \tag{2.23}$$

**2**

where $Z_r$ is the resonator impedance and $Z_0$ is the impedance of the adjacent transmission line. For the transmission style resonator, $\kappa_{\text{ext}} = \kappa_1 + \kappa_2$ since there are separate input and output lines. The expression is modified accordingly with input $C_1$ and output $C_2$ capacitances: $\kappa_{\text{ext}} = \frac{2}{\pi}\omega_r^3 Z_r Z_0 (C_1^2 + C_2^2)$. Any additional loss falls under the internal loss rate $\kappa_{\text{int}}$. The total or loaded quality factor $Q$ is decomposed in a similar fashion:

$$\frac{1}{Q} = \frac{1}{Q_{\text{ext}}} + \frac{1}{Q_{\text{int}}}, \tag{2.24}$$

with $Q_{\text{ext}}$ the external or coupling quality factor and $Q_{\text{int}}$ the internal or intrinsic quality factor. In the context of this thesis, there are three major loss channels that contribute to $Q_{\text{int}}$ and will be discussed next.

- Resistive losses $Q_{\text{res}}$: Although a superconductor has zero DC resistance, it does have a finite AC resistance. A superconductor consists of a mixture of Cooper pairs and quasiparticles at nonzero temperature below the critical temperature $T_c$. A simple yet very useful model used for understanding the AC properties of a superconductor is the so-called two-fluid model. This can be thought of as the superconductor hosting two different types of fluids, which are modeled as an inductor (Cooper pairs) and a resistor (quasiparticles) in parallel. The resistance here is inversely proportional to the quasiparticle density, which depends exponentially on $T/T_c$. The DC current flows entirely through the inductor, i.e. via Cooper pairs, so the DC resistance is zero, independent of the quasiparticle density. In contrast, AC currents will partially flow through the lossy resistor, i.e. via quasiparticles, because of the nonzero impedance of the inductor. Resistive losses due to quasiparticles limit the maximum $Q_{\text{res}}$. These losses can be dramatically reduced at very low temperatures, $T \ll T_c$, when the resistance becomes very large and most of the current is forced to flow through the inductor. This can be achieved in a dilution refrigerator, where a temperature of ~10 mK can be reached. We use NbTiN superconducting films with $T_c \approx 5 - 10$ K (depends on the film thickness). Care has to be taken when part of the resonator is made of a normal conductor. For example, when the resonator is connected to metallic quantum dot gates. This could become the bottleneck for $Q_{\text{int}}$, which is why superconducting quantum dot gates are preferred in this regard.

- Dielectric losses $Q_{\text{diel}}$: At sufficiently low temperatures dielectric losses can start to dominate over the resistive losses. These are losses from parasitic two-level systems (TLSs) mostly in the dielectric [28, 29]. TLSs can reside in the bulk substrate, gate oxide and in various interfaces such as the superconductor-vacuum interface. Interface TLSs are often byproducts of fabrication processes, which is why good surface treatments are important for achieving high $Q_{\text{diel}}$. A good indication of when $Q_{\text{int}}$ is limited by dielectric losses is when $Q_{\text{int}}$ increases at higher temperatures or average photon numbers (input powers). This can be thought of as saturating the TLSs. Superconducting CPW resonators on silicon substrates routinely achieve

$Q_{\text{int}} \approx 10^5 - 10^6$, and even $Q_{\text{int}} > 10^6$ when the exposed substrate is etched away deeply [30].

- Microwave leakage $Q_{\text{leak}}$: This loss channel is absent for bare resonators. It starts to play a role when other conducting structures, that are not ground planes, are placed in the vicinity of the resonator's voltage antinodes. In our case, gate electrodes for forming quantum dots are placed nearby the resonator. The mere presence of these structures result in a parasitic capacitance through which microwave photons can leak and dissipate at a rate according to Eq. 2.23. This loss mechanism can be countered using on-chip filters [31, 32] and will be the topic of Chap. 6.

The loss channels simply add up to the internal quality factor in the following way:

$$\frac{1}{Q_{\text{int}}} = \frac{1}{Q_{\text{res}}} + \frac{1}{Q_{\text{diel}}} + \frac{1}{Q_{\text{leak}}} + \frac{1}{Q_{\text{other}}}. \tag{2.25}$$

### Resonator coupling regimes

The internal loss rate $\kappa_{\text{int}}$ dampens and broadens the resonance. The complex transmission that takes this effect into account is expressed as follows for the transmission style ($S_{21}^T$) and hanger style resonators ($S_{21}^H$):

$$S_{21}^T = \frac{-i\sqrt{\kappa_1 \kappa_2}}{\Delta_0 - i\frac{\kappa}{2}}, \tag{2.26}$$

$$S_{21}^H = \frac{\Delta_0 - i\frac{\kappa_{\text{int}}}{2}}{\Delta_0 - i\frac{\kappa}{2}}, \tag{2.27}$$

with $\Delta_0 = \omega - \omega_r$. The ratio $r = \frac{\kappa_{\text{ext}}}{\kappa_{\text{int}}} = \frac{Q_{\text{int}}}{Q_{\text{ext}}}$ can be divided into three coupling regimes:

$$\kappa_{\text{ext}}/\kappa_{\text{int}} > 1 \quad \text{(overcoupled)}, \tag{2.28}$$
$$\kappa_{\text{ext}}/\kappa_{\text{int}} = 1 \quad \text{(critically coupled)}, \tag{2.29}$$
$$\kappa_{\text{ext}}/\kappa_{\text{int}} < 1 \quad \text{(undercoupled)}. \tag{2.30}$$

The power $|S_{21}|^2$ and phase $\phi = \arg(S_{21})$ of the complex transmission in the three regimes are shown in Fig. 2.6. Note that for critical coupling the magnitude (power) is $|S_{21}| = 0.5$ ($|S_{21}|^2 = 0.25$) at $\omega_r$. For the transmission style resonator (Fig. 2.6a), the deviation of the peak power transmission from unity is called the insertion loss (in dB):

$$IL = 20 \log\left(\frac{r}{r+1}\right). \tag{2.31}$$

Which coupling regime is desired depends on the application of the resonator. For example, for readout it is advantageous to be overcoupled in terms of bandwidth

**2**
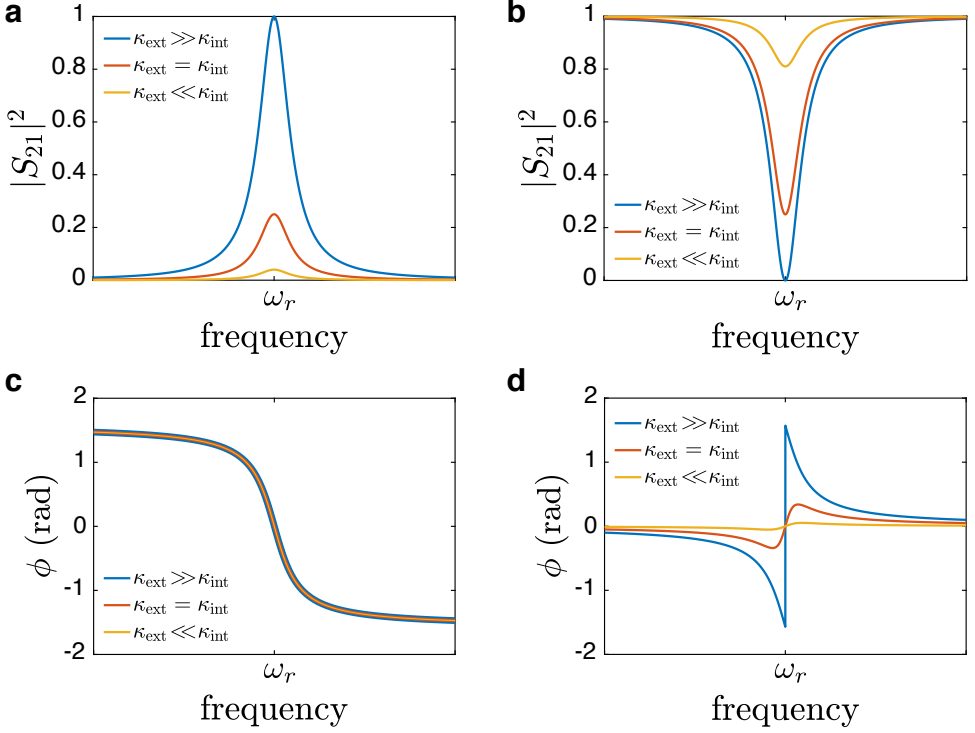


Figure 2.6: **Resonator coupling regimes**. **a** Simulated transmission power spectrum of a transmission style resonator for the three different coupling ratios. The external cavity decay rate is composed of $\kappa_\mathrm{ext} = \kappa_1 + \kappa_2$. Here, we consider symmetric couplers, i.e. $\kappa_1 = \kappa_2$. **b** Simulated transmission power spectrum of a hanger style resonator in the three different coupling regimes. **c** The corresponding phase responses of **a**. Note that the three curves fall on top of each other. **d** The corresponding phase responses of **b**. In these simulations the total cavity decay rate $\kappa$ is kept constant, while only the ratio $\frac{\kappa_\mathrm{ext}}{\kappa_\mathrm{int}}$ is varied.

**2**

and signal-to-noise ratio (SNR). As quantum bus or memory, it might be better to be undercoupled instead in order to maximize the photon lifetime.

### Asymmetric resonance shapes

In practice, the resonance shape deviates from an ideal symmetric Lorentzian profile. Several factors could cause this asymmetry and it is often not easy to pinpoint. Examples of sources that could give rise to a so-called asymmetric Fano lineshape include: a parasitic transmission channel between the input and output ports in parallel to the cavity transmission, spurious wide resonances in nearby ground planes or other structures that couple to the resonance mode, an impedance mismatch between resonator and input/output lines, or an coupling that is not purely capacitive, but also contains a small inductive part. The asymmetry can be modeled by adding a complex term. For the transmission style resonator the complex transmission coefficient becomes (Fig. 2.7a):

$$S_{21}^T = \frac{-i\left(\sqrt{\kappa_1\kappa_2} + \frac{\Delta_0}{q}\right)}{\Delta_0 - i\frac{\kappa}{2}} e^{-i(\omega t_v + \phi_0)}, \tag{2.32}$$

with $q = |q|e^{-i\theta_q}$ a complex-valued quantity causing the Fano lineshape [33]. The parasitic power transmission $1/|q|^2$ leads to an offset in the power spectrum and the Fano phase $\theta_q$ accounts for the asymmetry. Note that this expression reduces to the Eq. 2.26 for $|q| \to \infty$. Eq. 2.32 contains an additional phase factor at the end, which accounts for the frequency-dependent phase shift with $t_v$ the propagation delay for frequency $\omega$ and offset $\phi_0$ in a real experiment.

For the hanger style resonator the complex transmission coefficient in terms of $\kappa$ or $Q$ becomes (Fig. 2.7b):

$$S_{21}^H = \left(1 + \eta\frac{\Delta_0}{\omega_r}\right)\left(1 - \frac{-i\frac{\kappa_c}{2}}{\Delta_0 - i\frac{\kappa}{2}}\right) e^{-i(\omega t_v + \phi_0)} \tag{2.33}$$

$$= \left(1 + \eta\frac{\Delta_0}{\omega_r}\right)\left(1 - \frac{\frac{Q}{Q_c}}{1 + 2iQ\frac{\Delta_0}{\omega_r}}\right) e^{-i(\omega t_v + \phi_0)}, \tag{2.34}$$

with $\kappa_c = |\kappa_c|e^{i\theta_c}$ and $Q_c = |Q_c|e^{-i\theta_c}$ the complex-valued linewidth and quality factor, respectively, and related to the external linewidth and external quality factor according to $\kappa_{\text{ext}} = |\kappa_c|\cos\theta_c$ and $Q_{\text{ext}} = |Q_c|/\cos\theta_c$ [30, 34]. A prefactor has been added to account for a linear variation with slope $\eta$ in the overall transmission chain in the narrow range around the resonance. This could be due to the frequency-dependent attenuation of the lines for instance.

### Average photon number estimation

When $Q_{\text{int}}$ and $Q_{\text{ext}}$ are known, the average photon number $\langle n \rangle$ in the resonator for a given input power $P_{\text{in}}$ (at the sample) can be estimated using the following
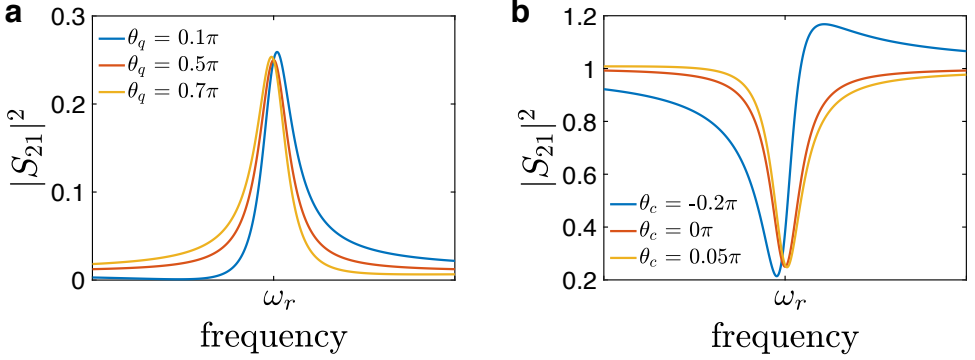
Figure 2.7: **Asymmetric Fano resonances**. **a** Simulated power spectra of a transmission style resonator with $\kappa_1 = \kappa_2 = \kappa/4$ (critical coupling) for three values of $\theta_q$ while the other parameters are kept constant (Eq. 2.32). The resonance shape is symmetric for $\theta_q = 0.5\pi$. **b** Simulated power spectra of a hanger style resonator at critical coupling for three values of $\theta_c$ while the other parameters are kept constant (Eq. 2.33). The resonance shape is symmetric for $\theta_c = 0$. Here, $\eta = 0$. Note that $|S_{21}|^2$ exceeds 1 for the asymmetric resonances, which is due to the choice of normalization and not because the resonator is producing more power.

relation [27]:

$$\langle n \rangle = \frac{2}{\pi \hbar \omega_r^2} \frac{Q^2}{Q_{\text{ext}}} \frac{Z_{\text{TL}}}{Z_r} P_{\text{in}}, \tag{2.35}$$

with $Z_{\text{TL}}$ the impedance of the transmission line. It is important to note that this equation provides only an upper limit for $\langle n \rangle$ because it does not take into account impedance mismatches in the lines from the microwave source to the resonator, which would otherwise reduce the amount of power reaching the resonator.

## 2.2.4. High-impedance resonators

Superconducting CPW resonators in circuit QED are traditionally designed to have an impedance of 50 Ω. However, depending on the application it could be beneficial to design a resonator with a much lower or higher impedance. By increasing (decreasing) the impedance, it is possible to enhance the zero-point fluctuations (ZPFs) of voltage (current), optimizing the resonator for electric [35] (magnetic [36]) dipole coupling to two-level systems. High-impedance resonators ($Z_r > 1 \text{ k}\Omega$) play a central role in this thesis.

The ZPFs of voltage relate to the resonator impedance according to $V_{\text{rms}}^0 \propto \omega_r \sqrt{Z_r}$. To increase $Z_r$, the capacitance of the CPW resonator can be reduced by retracting the ground planes from the center conductor. To increase the inductance of the resonator, one can take advantage of the high kinetic inductance of strongly disordered superconducting nanowires such as Nb, NbN, TiN or NbTiN [37]. The kinetic inductance arises from the kinetic energy stored in the motion of the charge carriers and is expressed as:

$$L_k = \frac{m_e}{2 n_s e^2} \frac{l}{wd}, \tag{2.36}$$

with $m_e$ the electron mass, $e$ the electron charge, $n_s$ the Cooper pair density, and $l$, $w$ and $d$ the length, width and thickness, respectively. Note that $L_k$ scales inversely with the wire cross section, so very high kinetic inductance can be achieved with a millimeterscale nanowire with nanoscale cross section. In normal nanowires the impedance is dominated by the resistive component up to ~THz, masking the effect from the kinetic inductance. However, in superconducting nanowires the resistive component is much smaller and the impedance can be dominated by the kinetic inductance of the supercurrent up to microwave frequencies. When designed properly, the kinetic inductance $\tilde{L}_k$ can be several orders of magnitude larger than the geometric inductance $\tilde{L}_g$.

A more practical relation for estimating $L_k$ is given by:

$$L_k = L_S \frac{l}{w}, \tag{2.37}$$

where $L_S$ is the sheet inductance of the film and depends on the film thickness. Both $L_k$ and $L_S$ can be deduced by matching an EM simulation to the data of a simple reference resonator. EM simulation softwares such as Sonnet [38] are very powerful for this purpose.

High-impedance resonators with $Z_r \approx 4\,\mathrm{k\Omega}$ and $Q_{\mathrm{int}} > 10^5$ have been demonstrated [35]. The corresponding $V_{\mathrm{rms}}^0 \approx 20\,\mu\mathrm{V}$ make these resonators well suited for coupling to systems with relatively small electric dipole moments, such as an electron in a double quantum dot. Furthermore, the small cross section of the nanowire strongly suppresses vortex generation in a magnetic field, making them compatible with in-plane magnetic fields up to (at least) $6\,\mathrm{T}$. This means that $Q_{\mathrm{int}}$ does not degrade in parallel magnetic fields up to $6\,\mathrm{T}$, and $\omega_r$ has been observed to stay relatively constant up to ~$200\,\mathrm{mT}$.

Due to the minimized total capacitance of a high-impedance resonator, it couples capacitively more easily to objects in its vicinity, also to quantum dot gates. This means that the microwave leakage increases with impedance, as can be seen in Eq. 2.23 as well. This issue will be addressed thoroughly in Chap. 6.

High-impedance resonators can also be made from a series of superconducting quantum interference devices (SQUIDs) [20], but they are extremely sensitive to magnetic fields. This makes SQUID array resonators difficult to work with spin qubits that require external magnetic fields.

## 2.3. Semiconductor quantum dots

We now turn our attention to the semiconductor part of the hybrid superconductor-semiconductor circuit QED system. Semiconductor quantum dots (QDs) contain a wealth of physics accumulated over the past decades. Several types of quantum dots have been developed and in various materials. The work in this thesis concerns only lateral, gate-defined quantum dots in silicon. In what follows, we will touch upon only a few concepts that are most relevant for our experiments. We refer the reader to review articles [39–41] or a book [42] for more in-depth information.

**a**



**b**
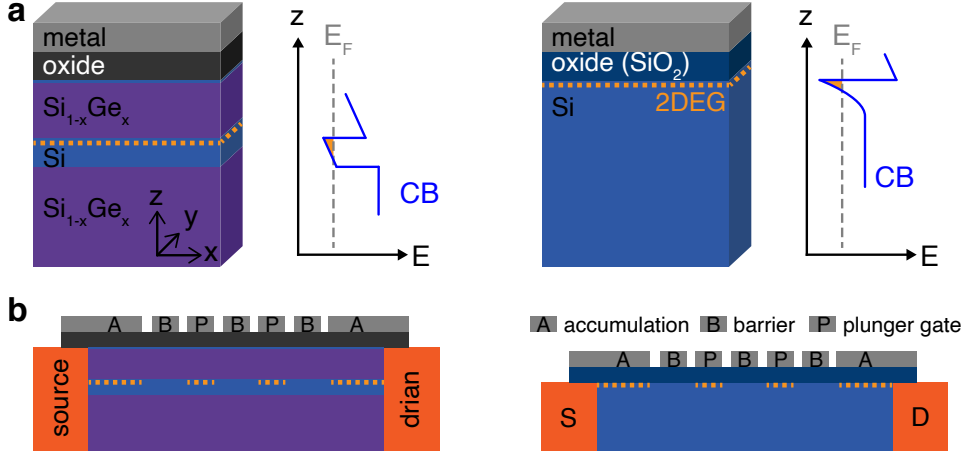


Figure 2.8:   **From 2DEGs to QDs**. **a** Schematic material stacks for a planar strained Si/Si$_{1-x}$Ge$_x$ heterostructure (left), where $x = 0.3$ in our experiments, and a Si-MOS structure (right). The schematic energy diagrams show the minimum of the conduction band (CB) along the $z$-direction when a positive voltage is applied to the metal. At the location where CB falls below the Fermi level, $E_F$, a 2DEG is formed. The orange dashed lines indicate the locations of the 2DEGs. **b** Schematics of transistorlike nanostructures integrated into transport devices with source, drain and gate electrodes. The lateral electrostatic confinements of QDs are defined by applying appropriate voltages to the gates. Ohmic contacts to the buried 2DEGs are achieved via highly doped regions (orange).

## 2.3.1. Creation of lateral quantum dots from 2DEGs

Quantum dots are man-made nanoscale objects that confine electrons[1] in all three spatial dimensions. The number of electrons in a QD can be very precisely controlled. To create lateral QDs, we start from a two-dimensional electron gas (2DEG) system. Fig. 2.8a depicts two commonly used material stacks for silicon QD devices[2]. We work with Si/Si$_{1-x}$Ge$_x$ heterostructures, where $x$ is typically 0.3 in our experiments. A thin silicon layer ($\sim$10 nm), often referred to as the quantum well (QW), is placed in between layers of SiGe. It is essential to have the conduction band minimum (CB) of the QW much lower than those of the neighbouring SiGe layers, as sketched in the energy diagram. The SiGe layer on top of the QW has a typical thickness of 30-50 nm. Due to the slight lattice constant mismatch of Si and Si$_{0.7}$Ge$_{0.3}$, the thin Si QW experiences an in-plane strain that allows for a dislocation-free growth on the SiGe layer below. A positive voltage applied to the metal on top of the stack tilts the CB and a 2DEG (orange dotted line) is formed at the location where the CB is pulled below the Fermi level ($E_F$). The electrons in the 2DEG are confined in the $z$-direction by a triangular potential well against the top of the quantum well, but are free to move in the $x$-$y$ plane. As a reference, the right

---

[1]Depending on the host material, holes can be used instead of electrons. See Ref. [43] for an extensive review on holes in germanium QDs. We restrict ourselves to electrons in this thesis.

[2]More variations of silicon-based QD devices exist, e.g. silicon-on-insulator (SOI) devices. Other silicon-based nanodevices, besides QD devices, have been explored, such as donors in silicon. See Ref. [41] for a thorough review. Here, we choose the options that are currently pursued in our lab.

side of Fig. 2.8a shows a planar Si-MOS (metal–oxide–semiconductor) structure, along with its energy diagram when a positive voltage is applied to the metal. The 2DEG is separated from the top gate by a thin layer of $SiO_2$ (typically 5-15 nm). Fig. 2.8b depicts schematics of QD devices based on the aforementioned material stacks, showing the relevant components for charge transport measurements. The confinement potentials in the $x$- and $y$-directions necessary to form QDs are defined by the top-gate electrodes. The QDs are formed under the plunger (P) gates. The barrier (B) gates control the tunnel barriers between neighbouring dots, and between dot and source or drain reservoir underneath the accumulation gate. Those reservoirs are connected to the outside world via ohmic contacts.

Historically, GaAs/AlGaAs heterostructures have been the workhorse of many groundbreaking mesoscopic physics experiments. Owing to the more advanced epitaxial growth techniques of lattice-matched group III-V materials, GaAs/AlGaAs heterostructures with very low defect density could be grown and 2DEG mobilities well above $10^6\,cm^2\,V^{-1}\,s^{-1}$ were and are still routinely achieved. The mobility is a commonly used metric for the quality of the material stack, with a high mobility indicating a low degree of disorder in the material. GaAs/AlGaAs proved to be an excellent platform for QDs as well, and the first proof-of-concept spin qubit experiments were performed in GaAs [40]. However, the main drawback slowing down the progress of GaAs-based spin qubits is the unavoidable abundance of nuclear spins, resulting in short dephasing times on the order of 10 ns [44]. Now, the developments in silicon-based material stacks, that contain fewer nuclear spins, are catching up quickly. High 2DEG mobilities have been observed in Si/SiGe heterostructures, with a record mobility of $6.5 \times 10^5\,cm^2\,V^{-1}\,s^{-1}$ reported for 50 nm deep quantum wells[3] [31]. For the work presented in this thesis, locally grown Si/SiGe heterostructures with 30 nm deep quantum wells and mobilities above $8 \times 10^4\,cm^2\,V^{-1}\,s^{-1}$ were used[4].

### 2.3.2. Single quantum dots

Fig. 2.9a shows a simplified electric circuit representation of a single QD modeled as an island connected to the source and drain contacts via tunnel barriers, which are represented by resistors and capacitors in parallel and allow the exchange of electrons. Adding an electron to the QD costs energy due to the small dimensions of a QD (10-100 nm). This is because of Coulomb repulsion between electrons. The energy that an additional electron has to pay for this is called the charging energy $E_C = \frac{e^2}{C_\Sigma}$, where $e$ is the elementary charge of an electron and $C_\Sigma$ the total capacitance of the QD. In addition to this classical effect, there is also a quantum effect associated with the small QD dimensions. An electron trapped in a QD can be treated as a particle in a box, which leads to the quantization of the orbital energy levels on the order of $E_{\mathrm{orb}} \sim \frac{\hbar^2}{m^* l^2}$, where $m^*$ is the effective mass of the electron and $l$ is the physical size of the QD. The total energy that an electron has to pay to get into the QD is called the addition energy:

---

[3]Grown by HRL Laboratories.
[4]Grown by A. Sammak at EKL, under the supervision of G. Scappucci.

**2**
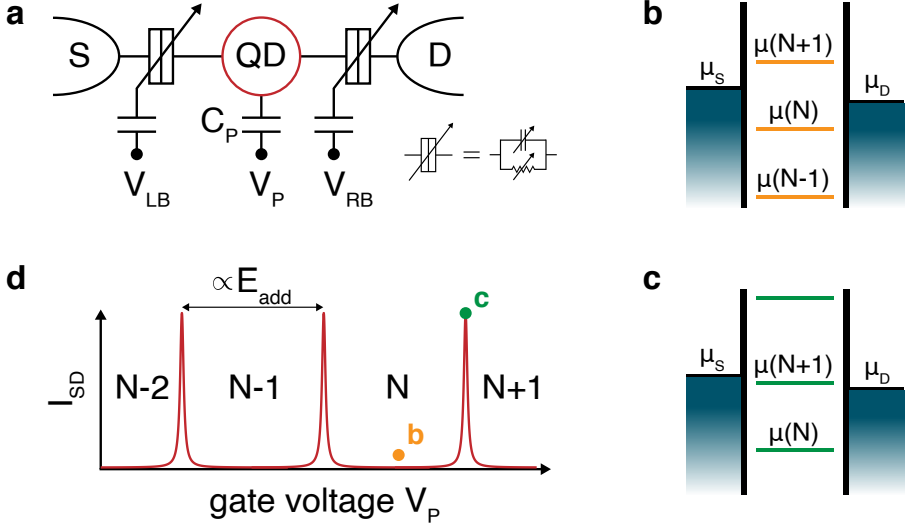


Figure 2.9: **Single quantum dot and Coulomb peaks**. **a** Electric circuit representation of a single QD. Tunable tunnel barriers between QD and electron reservoirs (S and D) are modeled using resistors and capacitors tunable with barrier gate voltages $V_{\mathrm{LB}}$ and $V_{\mathrm{RB}}$. Plunger gate P is capacitively coupled to the QD with capacitance $C_{\mathrm{P}}$ and regulates the number of electrons. In reality, P also affects the tunnel barriers via capacitive crosstalk. Source (S) and drain (D) contacts enable current measurements through the QD. **b, c** Schematic diagrams of the electrochemical potential levels of a QD and reservoirs in the low-bias regime, i.e. with a small source-drain bias voltage, $-|e|V_{\mathrm{SD}} = \mu_{\mathrm{S}} - \mu_{\mathrm{D}}$, applied. The resulting energy window is often called the bias window. By changing $V_{\mathrm{P}}$ the levels in the dot can be moved up or down. If there is no level inside the bias window (**b**), then there is no electron transport through the dot and the electron number is fixed at $N$. When the level $\mu(N + 1)$ falls within the bias window, the electron number can fluctuate between $N$ and $N + 1$, leading to a single-electron tunneling current. **d** Schematic plot of the source-drain current through the dot as function of the plunger gate voltage, which moves the levels in the dot and thereby gives rise to an alternating pattern of current and no current. The voltage different between Coulomb peaks is proportional to the addition energy $E_{\mathrm{add}}$.

$$E_{\mathrm{add}} = E_C + E_{\mathrm{orb}}. \tag{2.38}$$

Both $E_C$ and $E_{\mathrm{orb}}$ depend on the size of the dot, and they increase as the dot size decreases. We typically work in the regime $E_C > E_{\mathrm{orb}}$. Note that $E_{\mathrm{orb}}$ can be zero when two consecutive electrons are added to the same orbital level. Symmetrically-shaped quantum dots exhibit shell filling when electrons are added one by one [45]. For this reason, quantum dots are often referred to as artificial atoms.

A convenient quantity used to describe QDs is the electrochemical potential $\mu(N)$, which is defined as the energy needed to add the $N$th electron to the dot. Fig. 2.9b,c show the electrochemical potential levels of a QD. When $\mu(N)$ is below the electrochemical potentials of the source $\mu_S$ and drain $\mu_D$, there are exactly $N$ electrons trapped in the dot. Electron tunneling through the dot depends on the precise alignment of the electrochemical potential level of the dot with respect to $\mu_S$ and $\mu_D$. Important QD properties are revealed in a basic transport measurement. A small source-drain voltage $V_{\mathrm{SD}}$ (~100 μV) is usually applied to open up a bias window ($|\mu_S - \mu_D| > 0$). When the current is measured as function of the plunger gate voltage $V_P$, a discrete set of current peaks, called Coulomb peaks, can be observed (Fig. 2.9d). Sweeping the voltage applied to P down, moves the energy levels in the dot up. Only when a level is in between $\mu_S$ and $\mu_D$ (inside the bias window), electron transport with one electron at a time is possible, giving rise to the current peak. Otherwise this transport is blocked, also called the Coulomb blockade regime. From a simple charge transport measurement, we can extract the distance between successive energy levels, which is exactly $E_{\mathrm{add}}$ (Eq. 2.38). Moreover, the width of these Coulomb peaks are broadened by both electron temperature and tunnel coupling [46]. In order to observe well-resolved Coulomb peaks, two conditions need to be met. First, the charging energy needs to be much larger than the thermal energy of the electrons in the reservoir, $E_C \gg k_B T_e$. This condition implies the need to work at cryogenic temperatures, typically below 4 K. Second, the tunnel barriers surrounding the dot have to be sufficiently opaque to resolve quantization of charges on the island, $R_t \gg h/e^2$, with $R_t$ the tunneling resistance.

### Lever arms
We note that a useful quantity that converts gate voltages to energies is the lever arm $\alpha$. The lever arm of gate P is defined as $\alpha_P = e \frac{C_P}{C_\Sigma}$, and often expressed in meV/mV[5]. When $V_P$ is changed by $\Delta V_P$, the energy levels in the dot are moved by $\Delta E = -\alpha_P \Delta V_P$. There are several methods to obtain the lever arm of a gate. For single QDs, this can be straightforwardly extracted from Coulomb diamond measurements for instance [40].

## 2.3.3. Double quantum dots
Two QDs can be tunnel-coupled to form a double quantum dot (DQD). A simplified electric circuit representation of a DQD is shown in Fig. 2.10a. A DQD can be viewed as an artificial molecule [47]. Depending on the strength of the tunnel coupling, the

---

[5]Sometimes $e$ is taken out of the definition and $\alpha$ is reported as a dimensionless conversion factor.

**2**
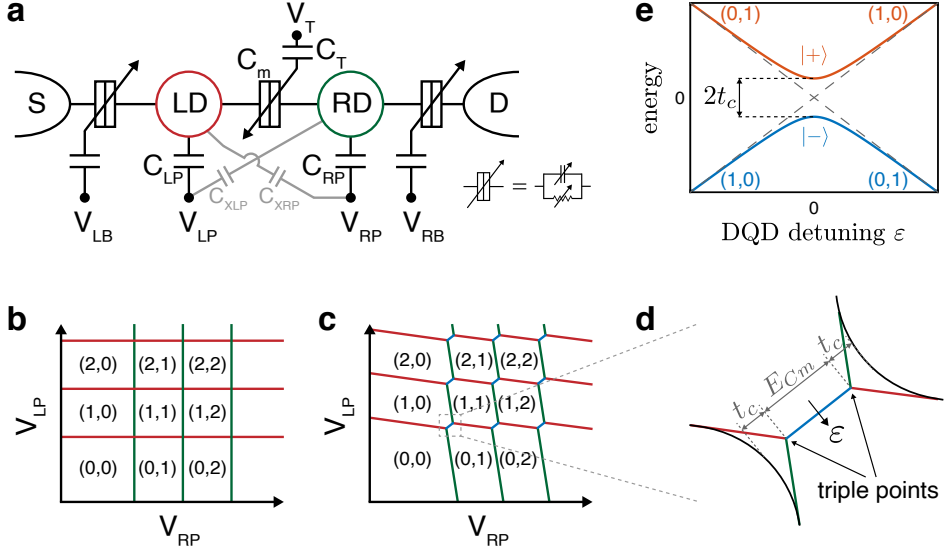


Figure 2.10: **Double quantum dot and charge stability diagrams**. **a** Electric circuit representation of a DQD. Plunger (LP, RP) and barrier (LB, T, RB) gates are capacitively coupled to the QDs (LD, RD) and tunnel barriers, respectively. In a real device, every gate is capacitively coupled, to varying degrees, to every QD and barrier. Only two parasitic capacitances ($C_{\mathrm{XLP}}$, $C_{\mathrm{XRP}}$) are depicted here for simplicity. $C_m$ is the mutual capacitance between the dots. **b, c** Schematic charge stability diagrams of the DQD system as function of the two plunger gate voltages. $(N_L, N_R)$ denote the equilibrium charge in the left (LD) and right (RD) dot. **b** depicts the case with no cross capacitances, $C_{\mathrm{XLP}} = C_{\mathrm{XRP}} = 0$, and capacitively uncoupled dots, $C_m = 0$. The horizontal red lines correspond to energy levels in LD being resonant with the source reservoir, whereas the vertical green lines correspond to energy levels of RD being resonant with the drain reservoir. **c** depicts the case with finite capacitances. The horizontal (red) and vertical (green) lines are tilted due to finite cross capacitances. Each cross point in **b** is split into two triple points, with the distance between the points (blue lines) set by $C_m$. The triple points form a typical DQD "honeycomb" pattern together. **d** Enlargement of the interdot transition line with a single excess electron. Along the blue line the energy levels of LD and RD are aligned, i.e. $\varepsilon = 0$. For a large tunnel coupling, the honeycomb lines near the triple points are bent as shown by the black lines. **e** Orbital energy levels along the black arrow that is perpendicular to the interdot transition line in **d**. The bonding $|-\rangle$ and antibonding $|+\rangle$ states can be used for a charge qubit, with the levels separated by $\sqrt{\varepsilon^2 + 4t_c^2}$.

two dots can form "ionic" (weak coupling) or "covalent" (strong coupling) bonds. In the former case, the electrons are localized in the individual dots, while in the latter case, the electrons are delocalized over both dots. The covalent binding gives rise to bonding and antibonding states, which will be discussed at the end of this section.

A very useful tool to visualize the response of two or more QDs to changes in gate voltages is called a charge stability diagram or "honeycomb" diagram. Fig. 2.10b shows a schematic stability diagram when the two dots, LD and RD, are capacitively decoupled, i.e. no mutual capacitance $C_m$. In addition, it considers the ideal case in which a plunger gate voltage only controls the electrochemical potentials of its corresponding dot. As a result, the stability diagram consists only of vertical (green) and horizontal (red) lines. Along the vertical lines the electrochemical potentials of RD are resonant with $\mu_D$, while along the horizontal lines the electrochemical potentials of LD are resonant with $\mu_S$. These lines are also called reservoir charge transition lines, because of exchange of electrons with the reservoirs. At the crossings of the vertical and horizontal lines the electrochemical potentials of LD and RD are aligned with each other and with those of the reservoirs. Within each rectangular region the number of electrons in the dots, indicated by $(N_L, N_R)$, is fixed due to Coulomb blockade.

Ideally, we would like to have independent control over each QD and tunnel barrier using dedicated gates. In reality, due to the small dimensions of the QDs and the close proximity of the gate electrodes, every gate is capacitively coupled to every nearby QD and tunnel barrier. This leads to unwanted crosstalk, where a plunger gate can affect the tunnel barriers or neighbouring dots for example. Two of these cross capacitances, $C_{\mathrm{XLP}}$ and $C_{\mathrm{XRP}}$, are shown in Fig. 2.10a. Because of this, the reservoir transition lines in a charge stability diagram are tilted, as shown in Fig. 2.10c, with the slope being a measure for the cross capacitance. This undesired effect is still manageable for single or double quantum dots, but becomes rapidly more complicated for larger systems. For this reason, so-called "virtual gates" have been developed to cancel out this crosstalk to a certain degree. A virtual gate is composed of a linear combination of several physical plunger and barrier gates. This method has been successfully employed in Ref. [48–52] for virtual plungers and Ref. [53, 54] for virtual barriers.

When the interdot capacitance $C_m$ is taken into account, the addition of an electron in one dot changes the electrochemical potential of the other dot by an amount $E_{Cm}$, called the electrostatic coupling energy. As a consequence, each crossing in Fig. 2.10b is split into two "triple points", where three different charge states are degenerate. Along a blue line connecting two triple points in Fig. 2.10c, the electrochemical potentials of LD and RD are aligned. Such a line is often called the interdot charge transition lines, because an electron moves from one dot to another dot when crossing this line.

Fig. 2.10d depicts a close-up of the interdot transition line in the single-electron regime. For a small tunnel coupling $t_c$, the length of the blue interdot transition line is mostly determined by $E_{Cm}$. When $t_c$ becomes significant, the electron is no longer localized in one of the two dots, but rather occupies molecular orbitals that span

**2**

both dots. Consequently, the reservoir transition lines near the triple points bend away from the the pure electrostatic configuration by an amount $t_c$, as indicated by the curved black lines. Although $t_c$ can in principle be extracted from the bending of the lines [55], it is in practice more conveniently and accurately done by measuring the charge distribution across the interdot charge transition line[6] [56]. Another well-known method employed to extract $t_c$ is photon-assisted tunneling (PAT) [39].

The misalignment between the electrochemical potentials of LD and RD is referred to as the DQD detuning $\varepsilon$. In a honeycomb diagram, the detuning axis is usually defined to be perpendicular to the interdot transition line (see Fig. 2.10d), and $\varepsilon = 0$ along the interdot transition line. The DQD detuning can be obtained if the relevant lever arms are known, i.e. $\varepsilon = \beta_{RP}\Delta V_{RP} - \beta_{LP}\Delta V_{LP}$, where $\beta_{RP} = \alpha_{RP} - \alpha_{XRP}$ and $\beta_{LP} = \alpha_{LP} - \alpha_{XLP}$ are differential or detuning lever arms, and $\alpha_{XRP}$ and $\alpha_{XLP}$ are cross lever arms.

The charge physics of a DQD along $\varepsilon$ is described by the following Hamiltonian in the $\{|L\rangle, |R\rangle\}$ basis:

$$H_{DQD} = \frac{\varepsilon}{2}\tau_z + t_c\tau_x, \qquad (2.39)$$

where $\tau_x$ and $\tau_z$ are Pauli operators in position space, and $|L\rangle = |(1,0)\rangle$ and $|R\rangle = |(0,1)\rangle$ represent the two charge states in which the electron is in LD and RD, respectively. At the charge degeneracy point, $\varepsilon = 0$, $|L\rangle$ and $|R\rangle$ hybridize to form molecular antibonding and bonding states $|\pm\rangle = (|L\rangle \mp |R\rangle)/\sqrt{2}$. At large detuning, $|\varepsilon| \gg t_c$, the states $|L\rangle$ and $|R\rangle$ are nearly unperturbed by tunneling. The energies of the two molecular orbital states as function of $\varepsilon$ is plotted in Fig. 2.10e. The $|L\rangle$ and $|R\rangle$ states can be used as the basis states of a charge qubit, as demonstrated in GaAs [57, 58] and in Si [59]. Fast coherent charge oscillations can be induced by a diabatic voltage pulse to $\varepsilon = 0$ for a controlled amount of time. Alternatively, the $|+\rangle$ and $|-\rangle$ states can encode a charge qubit [60] with the qubit energy splitting given by $E_{cq} = \sqrt{\varepsilon^2 + 4t_c^2}$. In this case, resonant MW pulses are applied to induce fast coherent charge oscillations.

Finally, we note that charge stability diagrams can be acquired in a few ways. The most straightforward one is from a basic charge transport measurement. However, when lateral gate-defined QDs are in the few-electron regime, the tunnel couplings to the reservoirs tend to be so small that the current is too low to be detected by our instruments. Therefore, one has to resort to other techniques instead. For example, nearby electrometers that detect displacements of single charges. This is called charge sensing [61], and charge stability diagrams taken by these charge detectors can reveal charge transitions down to the last electron [62]. Charge sensing will be discussed more in Sec. 2.5.

### 2.3.4. Valley splitting in silicon
QDs in silicon have another important energy scale, called the valley splitting [41], which has not been discussed so far. Bulk silicon has six degenerate valleys in its

---

[6]This method also works for reservoir transition lines in order to extract the tunnel rate to the reservoir or the electron temperature of reservoir.

conduction band. In silicon nanodevices, this degeneracy is usually broken. Confining electrons in a plane, as in the case of a 2DEG, lifts four of the six states to much higher energies and can therefore be disregarded. In Si/SiGe heterostructures, the in-plane strain of the silicon quantum well contributes significantly to this energy gap. The remaining two-fold degeneracy is lifted by the sharp potential step at the top Si/SiGe quantum well interface or Si/SiO$_2$ interface against which the 2DEG is pushed in the presence of a strong out-of-plane electric field (see energy diagram in Fig. 2.8a). The energy difference between the lowest two levels is called the valley splitting $E_V$, and depends on the microscopic details of the interface. In particular, atomic-scale disorder at the interface tends to suppress $E_V$ [63, 64].

The valley splitting is a very important parameter as it can negatively impact spin qubit experiments when $E_V$ is small. More specifically, if $E_V$ is not much larger than the electron temperature $k_B T_e$, the excited valley can be thermally populated, as was observed in Ref. [65]. This has negative implications for high-fidelity spin qubit operations and coherence times. In addition, having a small $E_V$ is problematic for readout relying on Pauli spin blockade, which will be discussed in Sec. 2.5.2. In Si/SiGe heterostructures, $E_V$ can be anywhere between 20 μeV and 300 μeV [65–72], with the majority of the reported values below 100 μeV. In Si-MOS this is generally higher, i.e. 200-1000 μeV (see for example Ref. [73–75]). This is likely due to the sharper potential step at the Si/SiO$_2$ interface in comparison to the quantum well top Si/SiGe interface and typically smaller Si-MOS QDs. There are still many questions regarding the valley splitting, so both theoretical and experimental studies to understand and increase $E_V$ are ongoing [76, 77].

We note that larger valley splittings enable spin qubit operations at elevated temperatures, >1 K, as recently demonstrated in a Si-MOS architecture [78, 79].

## 2.4. Silicon spin qubits

In the previous section we briefly mentioned that a single electron trapped in a DQD can encode a charge-based qubit [57–60]. However, semiconductor charge qubits have notoriously poor coherence times, 100 ps - 10 ns, due to their large electric coupling to the noisy solid-state environment. That is why the electron spin, which is more isolated and therefore has much longer coherence times, 1 μs - 100 μs, is a better quantum property to look at. The weak influence from the magnetic and electric environment stems from the very small magnetic moment of the electron spin and the fact that electric fields only affect the spin indirectly. The spin degree of freedom of one or more electrons in one or more QDs can encode a spin qubit. See Ref. [80] for a review of the current state-of-the-art spin qubits based on gate-controlled semiconductor QDs. We will only focus on one type of spin qubit in this thesis.

### 2.4.1. Loss-DiVincenzo qubits

The archetypal two-state system is the spin of an electron in a magnetic field. In the seminal work by Daniel Loss and David DiVincenzo [81], a qubit based on the two spin states of a single-electron quantum dot was proposed. Due to the Zeeman

**2**
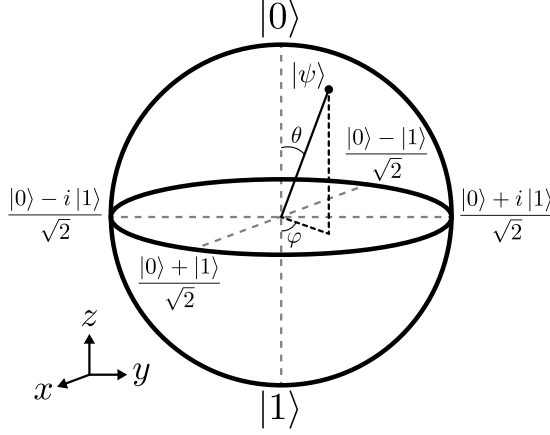


Figure 2.11: **Bloch sphere visualization of a single qubit**. The qubit state is represented by a vector $|\psi\rangle = \alpha|0\rangle + \beta|1\rangle$ pointing on the sphere. The basis states $|0\rangle$ and $|1\rangle$ lie at the poles, on the $z$-axis. Any other points on the sphere represent superposition states. When $|\psi\rangle$ lies on the equator ($\theta = \pi/2$), the qubit is said to be in an equal superposition of $|0\rangle$ and $|1\rangle$ because $|\alpha| = |\beta|$. Single-qubit logic gates correspond to controlled rotations of the state vector. A measurement of the qubit projects the state onto the $z$-axis and yields $|0\rangle$ ($|1\rangle$) with probability $|\alpha|^2$ ($|\beta|^2$).

effect, the spin-up $|\uparrow\rangle$ and spin-down $|\downarrow\rangle$ states are separated in energy in a magnet field $B$ by an amount:

$$E_Z = g\mu_B B, \tag{2.40}$$

where $g$ is the electron $g$-factor ($g \approx 2$ in silicon) and $\mu_B$ is the Bohr magneton.

The state of a single qubit is conveniently visualized on a Bloch sphere (Fig. 2.11). The qubit state is represented by a vector pointing on the sphere. The north and south poles are chosen to represent the qubit basis states $|0\rangle$ and $|1\rangle$. For a spin in silicon, the ground state $|0\rangle$ corresponds to $|\downarrow\rangle$ and excited state $|1\rangle$ to $|\uparrow\rangle$. An arbitrary spin state can be expressed as $|\psi\rangle = \cos\frac{\theta}{2}|0\rangle + e^{i\varphi}\sin\frac{\theta}{2}|1\rangle$, with $\theta$ determining the amplitudes of the two basis states and $\varphi$ setting the relative phase between them. A single-qubit gate operation rotates the state vector around the Bloch sphere. It is essential to have the ability to rotate about two axes of the Bloch sphere in order to have full control over the qubit. This, in conjunction with a two-qubit entangling gate between neighbouring qubits, constitutes a set of universal quantum logic gates. A measurement induces a collapse of $|\psi\rangle$ to either $|0\rangle$ or $|1\rangle$ with probability $\cos^2\frac{\theta}{2}$ or $\sin^2\frac{\theta}{2}$, respectively.

This type of spin qubit is often referred to as a Loss-DiVincenzo qubit, a single-spin qubit or a Zeeman qubit. Following a decade of material and technological developments, single-spin qubits were able to meet the DiVincenzo criteria [82]. They can be reliably initialized, coherently manipulated and read out. Furthermore, many experiments have been reproduced in various labs around the world. Achieving qubit operations above the fault-tolerant threshold for quantum error correction

is the topic of a major ongoing endeavour. This means achieving error rates below 1 % (or fidelities above 99 %) for initialization, readout, and single- and two-qubit gates [83]. We will briefly discuss the initialization, coherent manipulation, and relaxation and dephasing of single-spin qubits below. Readout will be covered in the next section (Sec. 2.5).

### Initialization
Initialization can in principle be achieved by waiting until the electron spin is thermalized to its ground state. However, this relaxation process is usually very slow in silicon. To speed this up by multiple orders of magnitude, on can make use of so-called relaxation "hot spots", where the exited spin state is mixed with an excited orbital or valley state via spin-orbit or spin-valley interaction, resulting in increased relaxation rates [74, 84]. Alternatively, one can make use of a reservoir by aligning the two spin states with the reservoir, such that a spin-up electron can tunnel out of the dot and a spin-down electron tunnels into the dot.

### Coherent manipulation
Magnetic and electric excitations (typically in the MW frequency domain) are used to coherently drive transitions between the Zeeman-split states of a single electron. Applying an oscillating magnetic field perpendicular to the static external magnetic field $B$ drives spin transitions directly when the frequency of the magnetic excitation matches the energy difference between the spin-up and spin-down states [85]. This well-known approach is called "electron spin resonance" (ESR). The magnetic excitation can be generated using a nearby (superconducting) ESR stripline. In contrast, an oscillating electric field drives spin transitions only indirectly, mediated through spin-orbit coupling. In this approach, called "electric dipole spin resonance" (EDSR), the electric field pushes the electron back and forth, and in the electron's frame of reference it experiences an oscillating magnetic field that rotates the spin. It is important that the electric field is applied in the direction such that the resulting effective magnetic field is perpendicular to the static magnetic field. The intrinsic spin-orbit coupling of the host material can be used for EDSR, like in GaAs [86], but this is very weak in silicon. Alternatively, a spatially inhomogeneous magnetic field produced by a nearby on-chip micromagnet can facilitate a much stronger (artificial) spin-orbit coupling [87–89]. For both ESR and EDSR holds that the rotation frequency (also called Rabi frequency) of the spin vector around the Bloch sphere is determined by the amplitude of the excitation, the rotation axis by the phase of the excitation and the rotation angle $\theta$ by the product of the amplitude and duration of the excitation. Rabi frequencies between 0.1 MHz and 30 MHz have been observed, with the higher Rabi frequencies typically driven via EDSR. Single-qubit gates with fidelities well over 99 % have already been achieved [90, 91].

   When there are two or more qubits, MW excitations need to be delivered very locally in order to address the qubits individually. This is quite challenging in dense qubit arrays. An alternative approach is to make each qubit energy unique[7]. The addressability in the latter case can arise from small differences in the electron

---

[7]Qubit energies can be reused on qubits located outside the range of a MW excitation.

**2**

$g$-factor, which a common approach in Si-MOS spin qubits with ESR lines. Alternatively, the inhomogeneous magnetic field from a micromagnet for EDSR can also give rise to different Zeeman splittings $\Delta E_Z$ between neighbouring spins when designed properly. This approach is more controlled and larger $\Delta E_Z$ can be engineered, e.g. on the order of 100 MHz.

Two-qubit logic gates are implemented via voltage pulses that control $\varepsilon$ or $t_c$ to turn on and off the exchange interaction $J$, which arises from the wave function overlap associated with the two spins. Different native two-qubit gates can be executed depending on the ratio of $J$ over $\Delta E_Z$ [92, 93]. For example, a CPHASE [94, 95] gate can be executed when $J$ is relatively small, whereas the $\sqrt{\text{SWAP}}$ [44, 48] gate is more efficiently implemented when $J$ dominates. The CROT [94, 96] gate can be executed in both regimes, but requires a single-qubit gate while the exchange interaction is on. Two-qubit gate fidelities between 91-98 % have been reported [97, 98].

### Relaxation and dephasing

A spin in a solid-state environment will inevitably interact with its environment. Although this interaction leads to the loss of quantum information (decoherence), it is not completely undesired as it also means that the spin will couple to the control and measurement apparatus. The crux of designing a qubit is to find the right balance between fast qubit control and low decoherence rate. Two timescales are commonly reported to quantify the decoherence of a qubit.

- Energy relaxation time $T_1$ : This is the typical time it takes for a qubit to relax from the excited state $|1\rangle$ to the ground state $|0\rangle$. For single spins in silicon, $T_1$ can range from milliseconds to seconds, and is usually not the limiting timescale in experiments.

- Dephasing time $T_2^*$: This is the typical time it takes before the qubit in a superposition state loses its phase information $\varphi$. This is usually a few orders of magnitude smaller than $T_1$, and therefore the limiting timescale for spin qubits.

These two timescales are heavily influenced by mainly two kinds of interaction mechanisms with the environment: spin-orbit interaction (SOI) and hyperfine interaction.

- Spin-orbit interaction: This interaction couples a particle's spin degree of freedom with its motion. In the simple picture of an electron moving in a spatially-varying electric field, it will experience a time-dependent electric field in its frame of reference, which generates an effective magnet field that affects its spin. In a solid, charged nuclei produce the spatially-varying electric field. In the presence of SOI, the eigenstates of the single-spin qubit are not pure spin states anymore, but rather admixtures of spin and orbital states [99]. Electric-field fluctuations can now couple to spin, via the electron's orbital part, and lead to spin relaxation [99–101]. Fortunately, this mechanism is indirect and not very efficient due to the weak intrinsic SOI in silicon, which

explains the long $T_1$. However, artificial SOI due to magnetic field gradients from micromagnets can be many times stronger than the intrinsic SOI, and a strong reduction of $T_1$ has been observed experimentally [102]. Electric-field fluctuations can arise from many sources, both externally (e.g. from gate electrodes) and internally. Phonons are a major internal source of electric-field fluctuations [40].

- Hyperfine interaction: This mechanism couples the electron spin in a quantum dot to the nuclear spins in the host material with which the electron wave function overlaps. The nuclear spins are orientated randomly and their collective behaviour can be described by a slowly-varying random magnet field, called the Overhauser field. The phase accumulation of the spin during free evolution depends on the total magnetic field, including the Overhauser field. As a consequence, the spin will pick up an additional random phase during free evolution, causing dephasing. In GaAs, hyperfine interction has limited $T_2^*$ to about 10 ns because every Ga and As isotope carries a nuclear spin. In natural silicon, only ~5 % of the Si nuclei carry a nuclear spin ($^{29}$Si), and $T_2^*$ improved to ~1 μs [65]. In isotopically purified silicon (800 ppm residual $^{29}$Si), this number has been extended further to 10-20 μs [91], and even 120 μs has been reported [90].

Given that spin qubits often operate in the regime $T_2^* \ll T_1$ and that the nuclear-spin bath fluctuates on a timescale much longer than that of the electron spin, dynamical decoupling (DD) techniques can be effectively applied to extend the dephasing time. DD coherence times $T_2^{\mathrm{DD}}$ of 3.1 ms in Si/SiGe [91] and 28 ms in Si-MOS [90] have been reported. In such a scheme, the qubit in a superposition state is flipped repeatedly with a train of $\pi$ pulses, so that the dephasing effect can be reversed (refocusing). This works particularly well against low-frequency noise. Moreover, by making the time between subsequent $\pi$ pulses shorter, one can effectively filter out noise at higher frequencies.

### 2.4.2. Other flavours of spin qubits

Besides the Loss-DiVincenzo qubit, which is conceptually the simplest spin qubit, other types of QD-based spin qubits have been theoretically proposed and are experimentally pursued. In contrast to the single-spin qubit, these qubits use two collective states of two or more spins. Examples include the singlet-triplet qubit [44, 103] (two electrons, two dots), quantum-dot hybrid qubit [104–106] (three electrons, two dots), exchange-only qubit [107–109] (three electrons, three dots) and quadrupolar exchange-only qubit [110] (four electrons, three dots). Each flavour comes with its pros and cons. The general idea is that, although the alternatives require more electrons and dots, they offer protection against certain types of decoherence mechanisms or alleviate experimental requirements.

## **2.5.** Spin readout techniques

The exceedingly small magnetic moment of a single spin makes its direct detection quite challenging. Consequently, the readout of an electron spin occurs rarely in a direct fashion. The signal from small displacements of an electron charge on the other hand is much stronger, and the detection of such a signal has been perfected over the years. The detection of an electron's charge degree of freedom in conjunction with a spin-to-charge mapping allows us to infer the spin state of the electron. We will first discuss charge sensing and two types of spin-to-charge conversions. We end this section by mentioning a promising alternative charge detection scheme called gate-based sensing, which is heavily relied on in our experiments.

### **2.5.1.** Charge sensing

The most common way to detect charge displacements in lateral QDs is via charge sensing [61]. In this scheme, an electrometer is placed next to the QDs and capacitively coupled to them. The current through the electrometer is monitored carefully, and an electron tunneling into or out of a QD is detected as a change in the current. No current transport through the QDs is needed for charge sensing. Several implementations of electrometers have been developed, but the most common ones are the quantum point contact (QPC) and the single-electron transistor (SET), which is also referred to as a sensing dot.

The aforementioned charge detectors provide sufficient SNR to perform real-time detection of electron tunneling in QDs [111], but it is relatively slow with measurement bandwidths around 10-100 kHz. This is mainly caused by the high resistance of the QPC or SET ($\sim$100 k$\Omega$), $RC$ filters connected to the ohmics and the parasitic capacitance of the long DC wires between the device and room temperature instruments. By embedding the QPC or SET into an $RLC$ resonant tank circuit and working with coaxial cables at high carrier frequencies, the measurement bandwidth can be dramatically increased to about 1-10 MHz. This technique is called radio-frequency (RF) reflectometry, because one measures the reflection of the RF signal from the tank circuit. Changes in the resistance or current through the QPC or SET modify the amount of reflected signal. In practice, a normal (surface-mount) or superconducting (spiral) inductor is placed closely to the QD device and wire bonded to an ohmic contact. The capacitance of the $RLC$ tank circuit comes from the parasitic capacitance of the connections between the inductor and charge sensor on the device. The resonance frequency of the tank circuit is typically on the order of $\sim$100 MHz. The RF-QPC [112] and RF-SET [113] for sensing electrons in QDs were first demonstrated in GaAs, and remain to date the most sensitive charge detectors. The performance of a charge sensor can be characterized by its charge sensitivity $\delta q$, which depends on the SNR and the integration time. RF-SETs have a charge sensitivity on the order of $10^{-4}$ e/$\sqrt{\text{Hz}}$ [113]. Note that a smaller value means a better charge sensitivity.

It is quite challenging to transfer this technique to Si devices mainly because of a large capacitance between the reservoir 2DEG and its corresponding accumulation gate through which RF signal can leak away. This capacitance is not present in GaAs devices. Only recently have there been designs introduced that
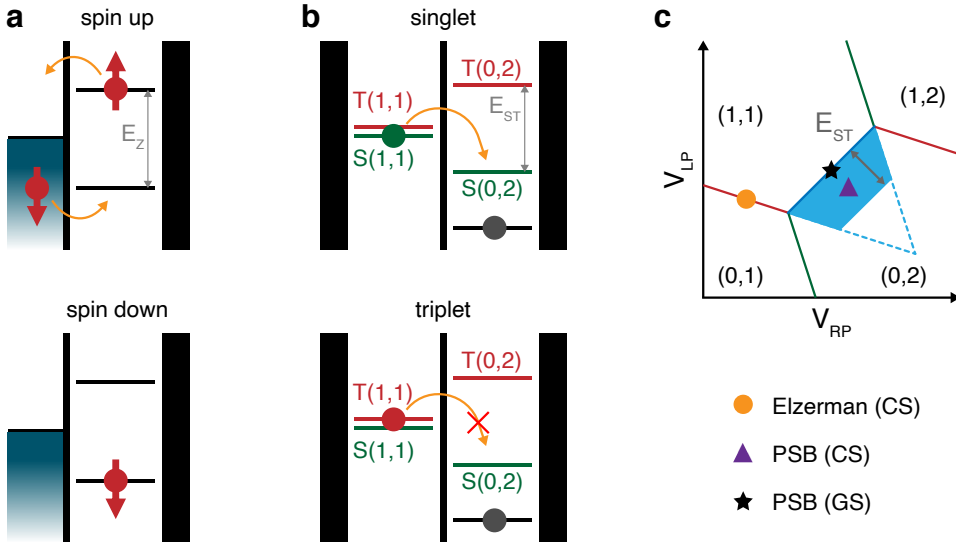
Figure 2.12: **Spin-to-charge conversions**. **a** Energy-selective (Elzerman) readout. The top drawing shows that a spin-up electron will tunnel out of the dot and after a while a spin-down electron from the reservoir tunnels into the dot. A nearby charge sensor can detect these two sequential tunneling events. The bottom drawing showcases a spin-down electron which remains in the dot during the readout. **b** Pauli spin blockade (PSB) readout. The top scenario involves electrons in a singlet state, whereas in the bottom the electrons are in one of the triplet states. **c** Schematic of the $(1,1)$-$(0,2)$ interdot and adjacent reservoir transition lines indicating the possible readout positions for various types of readout schemes. The blue area represents the spin-blockaded region, which is limited by the singlet-triplet splitting $E_{ST}$. This is mostly determined by the valley splitting $E_V$ in silicon. Charge sensing (CS) can employ both Elzerman and PSB readout, whereas gate-based sensing (GS) can only make use of PSB readout at the interdot transition.

are compatible with RF-reflectometry techniques. These designs minimize the parasitic capacitance [114, 115] or the inductor is bonded to the accumulation gate instead while the reservoir 2DEG is decoupled from the RF ground of the sample board [116].

## 2.5.2. Spin-to-charge conversion

In order to figure out the spin state of an electron from a measurement of its charge state, we make use of a so-called spin-to-charge conversion. To implement this, a charge displacement between QDs or between QD and reservoir is engineered to be dependent on the spin qubit state. Two variations are discussed below.

### Energy-selective tunneling

The most common spin-to-charge conversion, partly due to its relative ease of operation, is based on energy-selective tunneling [117] (Fig. 2.12a). In this scheme, a QD is tuned such that the Fermi reservoir lies between the two Zeeman-split spin states. An electron in the $|\uparrow\rangle$ state is able to tunnel out of the dot and into empty states of the reservoir located above the Fermi energy, which is detected by a

**2**

nearby charge sensor as a jump in the current. Subsequently, an electron in the $|\downarrow\rangle$ state tunnels back into the dot. If an electron was already in the $|\downarrow\rangle$ state, then no tunneling event to the reservoir occurs due to Coulomb blockade and no change is picked up by the sensor. Spin readout based on this conversion is often informally referred to as "Elzerman" readout. Elzerman readout is performed on a reservoir transition line, as indicated by the orange dot in Fig. 2.12c.

The reservoir is in reality broadened by temperature according to the Fermi-Dirac distribution. For a high Elzerman readout fidelity, $E_Z \gg k_B T$ is required. This is the reason why single-spin qubits are often operated at high frequencies, close to 20 GHz, with typical readout fidelities around 90 %. Operating at even higher frequencies increases the fidelity, but requires more expensive MW instrumentation. Moreover, $T_1$ decreases with magnetic field [40]. The measurement time for Elzerman readout is relatively long because one has to wait for an electron tunneling event to occur. The tunnel rate is of course tunable, but it cannot be higher than the measurement bandwidth. In practice the measurement time for Elzerman readout is on the order of 1 ms without and 10-100 µs with RF-reflectometry technique. This is long compared to the coherence times of a spin qubit, which is not ideal for quantum algorithms that require real-time feedback control. Note that this type of conversion requires a reservoir, and therefore not trivial to implement in larger and denser QD systems without resorting to electron shuttling [118] or cascading [119].

### Pauli spin blockade

Spin readout based on Pauli spin blockade (PSB) requires two electrons in a DQD. In this scheme, the dot levels are tilted to favour the $(0, 2)$ (or $(2, 0)$) charge state (Fig. 2.12b). If the two spins in the $(1, 1)$ charge state were in a (antisymmetric) singlet state, $S(1, 1)$[8], then the left electron can tunnel to the same orbital and valley occupied by the right electron to form $S(0, 2)$. This interdot tunneling is detected by a nearby charge sensor. However, if the two spins were in one of the three (symmetric) triplet states, $T(1, 1)$[9], then the left electron is not able to tunnel, unless an excited orbital or valley in the right dot can be accessed to form $T(0, 2)$. Otherwise the system remains stuck in the $(1, 1)$ charge state until $T(1, 1)$ relaxes to $S(0, 2)$. Because the Pauli exclusion principle forbids electrons to make a transition from $T(1, 1)$ to $S(0, 2)$, this blockade is also termed Pauli spin blockade. Moreover, because the readout distinguishes singlets from triplets, it is also called singlet-triplet readout.

Once the DQD detuning exceeds the singlet-triplet splitting $E_{ST}$ of the $(0, 2)$ charge state, the $T(0, 2)$ state becomes energetically accessible from the $T(1, 1)$ state and the blockade is lifted. The success of PSB readout depends heavily $E_{ST}$, which in silicon is often limited by the valley splitting. More precisely, having a large valley splitting yields a large spin-blockaded region in which PSB readout can be performed, as indicated by the blue region and the purple triangle in Fig.2.12c. In practice, it is more challenging to observe PSB in Si/SiGe than in Si-MOS due to

---

[8]$S(1, 1) = (|\uparrow_1\downarrow_2\rangle - |\downarrow_1\uparrow_2\rangle)/\sqrt{2}$, where the subscript denotes the dot in which the electron resides.
[9]$T_-(1, 1) = |\downarrow_1\downarrow_2\rangle$, $T_0(1, 1) = (|\uparrow_1\downarrow_2\rangle + |\downarrow_1\uparrow_2\rangle)/\sqrt{2}$, $T_+(1, 1) = |\uparrow_1\uparrow_2\rangle$.

the lower valley splittings.

PSB readout has many advantages compared to Elzerman readout. We will list a few here. First, in contrast to Elzerman readout, the system remains in the projected state after PSB readout, provided that the readout time is much shorter than $T_1$. Second, PSB readout does not require a reservoir, which makes it more compatible with readout of spins in dense 1D or 2D QD arrays. Third, PSB readout does not necessitate a high magnet field to maximize the readout fidelity. Therefore, it is compatible with spin qubits operating at lower frequencies (<10 GHz) and higher temperatures (>1 K) [78, 79].

PSB readout can turn into a parity readout when $T_0(1, 1)$ relaxes much faster than $T_-(1, 1)$ or $T_+(1, 1)$ due to spin-orbit coupling [120]. The readout distinguishes then parallel spin states ($|\downarrow\downarrow\rangle$, $|\uparrow\uparrow\rangle$) from antiparallel spin states ($|\downarrow\uparrow\rangle$, $|\uparrow\downarrow\rangle$).

So far, we have described the spins in the $(1, 1)$ charge state in the singlet-triplet basis, which are the eigenstates of the system when $J > \Delta E_Z$. PSB readout also works for $J < \Delta E_z$, when the spins are more conveniently described in the $\{|\downarrow\downarrow\rangle, |\uparrow\downarrow\rangle, |\downarrow\uparrow\rangle, |\uparrow\uparrow\rangle\}$ basis (also called the Zeeman basis). One considers the lowest two states, $|\downarrow\downarrow\rangle$ and, for example, $|\uparrow\downarrow\rangle$ (assuming the left spin has the smaller Zeeman splitting), and treats the right spin as a reference spin. A spin-down electron in the left dot cannot tunnel to the right dot due to spin blockade, whereas a spin-up electron is able to.

### Latched Pauli spin blockade
Recently, a scheme called latched PSB readout has been developed. This method tackles the issue that an interdot transition yields a smaller signal than a reservoir transition. Therefore, an additional mapping is introduced whereby the $(0, 2)$ charge state is mapped to $(1, 2)$. The drawback of this method is that it requires a reservoir. A readout fidelity of >99 % has been achieved in Si-MOS using this technique [121].

## 2.5.3. Gate-based sensing
Previously, we have discussed the detection of charge displacements using a nearby electrometer. To be effective, the sensor needs to be in close proximity of the QDs as charge sensing relies on capacitive coupling. This means that every few QDs needs to have a dedicated charge sensor. In a long 1D array, we can get away by adding a parallel array for charge sensors. A problem arises, however, in large and dense 2D arrays where charge sensors are too far removed from the QDs in the center and cannot detect electron tunneling. Instead, a measurement technique based on a completely different principle has been developed that makes use of the gate electrodes that are already in place to define the QDs, and is termed gate-based sensing. We discuss two implementations below: off-chip and on-chip resonators.

### Off-chip resonators
Gate-based sensing with off-chip resonators makes use of an RF-reflectometry technique similar to that of an RF-SET. The difference is that the inductor is wire bonded to a plunger or barrier gate instead. The $C$ in the resulting lumped-element $LC$

resonator stems from the parasitic capacitance to ground of the connections between the inductor and the gate electrode. The resonance frequencies range from 100 MHz to 1000 MHz, and quality factors between 10-100 with normal inductors and between 100-1000 with superconducting inductors have been achieved. The maximum detection bandwidth is determined by the linewidth of the resonator, which is typically on the order of 10 MHz. In practice, however, the effective detection bandwidth can be much smaller due to, for instance, filters in the detection chain to increase the SNR.

In early investigations of this technique, the reservoir of a DQD was used as an effective gate because of the large (differential) lever arm [122–124]. The first experiment demonstrating the feasibility of gate-based sensing using an actual gate electrode was done with GaAs QDs in 2013 [125]. Since then, this technique has been applied to many other systems, including: Si-MOS QDs [126], silicon-on-insulator QDs [127, 128] and donors in silicon [129].

In gate-based sensing, the resonator does not detect the absolute charge in a DQD as with RF-SETs, but rather charge transitions by sensing tiny changes in the polarizability or quantum admittance of the DQD when an electron tunnels in response to the alternating RF gate voltage [122, 123, 130]. Consequently, tunneling alters the capacitance and resistance of the resonator compared to when the electron is in Coulomb blockade, which in turn modifies the resonance frequency and resonance dip. By monitoring the change in phase or amplitude of the reflected RF signal from the resonator while sweeping the gate voltages, a charge stability diagrams can be constructed.

We first consider interdot charge transitions. In the adiabatic regime, $f_r \ll t_c/h$ (typically the case for devices using off-chip resonators), electron tunneling gives rise to a quantum capacitance given by [122, 131]:

$$C_q^{\pm} = -\beta^2 \frac{\partial^2 E_{\pm}}{\partial \varepsilon^2}, \tag{2.41}$$

with $\beta$ the differential lever arm and $E_{\pm} = \pm\frac{1}{2}\sqrt{\varepsilon^2 + 4t_c^2}$ the ground and excited orbital energies (see also Fig. 2.10e). We see that $C_q$ is related to the curvature of the energy level. The extrema in curvature occur at $\varepsilon = 0$, where the electron in the DQD is most readily polarizable and the quantum capacitance is given by:

$$C_q^{\pm}(\varepsilon = 0) = \mp\frac{1}{2}\frac{\beta^2}{2t_c}, \tag{2.42}$$

We see that the signal improves for smaller $t_c$ (larger curvature) and larger differential lever arm. However, if $t_c$ gets too low compared to $hf_r$, the transition will no longer be adiabatic. Another capacitance, called the tunneling capacitance, arises when diabatic processes, such as relaxations and thermal or resonant excitations, occur at a rate comparable to $f_r$ [132].

We now consider reservoir transitions. Electron tunneling between QD and reservoir can result in a resonance frequency shift as well as a reduction in the amplitude. This tunneling modifies the effective resistance ($t_r/h \approx f_r$) and capac-

itance ($t_r/h \gg f_r$) of the system, depending on the dot-reservoir tunnel rate $t_r$ in comparison to the probe frequency $f_r$ [123, 130].

The advantage of using off-chip resonators is the relative ease of implementation, i.e. bonding an inductor to a QD device. The disadvantage is that the tank circuit has a large parasitic capacitance compared to the quantum capacitance, which results typically in small frequency shifts ($\Delta f_r \ll \kappa/2\pi$), and thus small signals.

So far, we have discussed the detection of electron tunneling. In order to read out spin states, we need to incorporate the PSB spin-to-charge conversion in the readout scheme. The difference with PSB readout using charge sensing is that the readout position must be at the $(1,1)$-$(0,2)$ (or $(2,0)$-$(1,1)$) charge degeneracy point, as indicated by the black star in Fig. 2.12c. One of the electrons is able to tunnel freely between the dots when the spins are in a singlet state, giving rise to a finite $C_q$, whereas the electrons are spin blockaded in the triplet states with $C_q = 0$ as result. Gate-based sensing with off-chip resonators has advanced to the point that single-shot spin readout is now possible with fidelities of 73-98 % and measurement times of 0.2-2 ms [133–135].

### On-chip resonators

Alternatively, resonators can be placed on the same chip as the QD structures [136–139]. The main advantage of this approach is that these on-chip (distributed) resonators, with $f_r$ between 4-8 GHz, usually give a much larger change in the amplitude or phase of the transmitted or reflected MW signal than the off-chip lumped-element resonators. This is due to the higher quality factor ($Q \approx 1\,\text{k} - 10\,\text{k}$) and larger frequency shift. Furthermore, they are compatible with near-quantum-limited Josephson parametric amplifiers [20, 140]. The major drawback is that these resonators need to be integrated in the fabrication flow of the QD devices, leading to a more complicated fabrication process, and the need for relatively expensive MW equipment. Moreover, while the high $Q$ is certainly beneficial for the SNR, it limits the maximum bandwidth of the detection chain.

This approach shares a lot of similarities with the off-chip variant in terms of operation. A DQD charge stability diagram can be extracted from measurements of the amplitude and phase of the MW tone transmitted through or reflected from the resonator. Similar to the previous approach, there are two different contributions to the signal in a stability diagram. The signal at interdot charge transitions can be understood within the Jaynes-Cummings framework as the result of a dispersive shift and reduction in amplitude due to virtual exchange of photons between the resonator and DQD-based charge qubit [137]. This will be elaborated in the next section (Sec. 2.6.1). The concept of quantum capacitance starts to break down with these high-frequency resonators as the system is not strictly in the adiabatic regime ($f_r \ll t_c/h$) anymore [131].

Finally, charge tunneling between QD and reservoir results in a shift of the resonance frequency and reduction in the amplitude, similar to the case with low-frequency lumped-element resonators. This tunneling can add an effective resistance ($t_r/h \approx f_r$), capacitance ($t_r/h \gg f_r$) or inductance ($t_r/h \ll f_r$) to the resonator [123, 141].

In Chap. 5 we demonstrate fast single-shot readout of singlet-triplet spin states.

## 2.6. Putting it together: circuit QED with spins

Having discussed the superconducting cavity (Sec. 2.2) and semiconductor qubit (Sec. 2.3, 2.4, 2.5), we now focus on the most important concepts of the combined system. There are comprehensive review articles and references therein that the reader can consult for more details [142, 143].

One could naively approach the spin-photon coupling by coupling the magnetic field of the cavity directly to a single spin. However, it turns out that the magnetic dipole coupling rate is only on the order of 10-100 Hz due to the small magnetic moment of the single spin [144, 145]. This is far too small compared to the photon decay rate ($\sim 1$ MHz) and spin decoherence rate ($\sim 100$ kHz), even with a low-impedance cavity [36]. Using an ensemble of spins can enhance the coupling rate since it scales with $\sqrt{N}$, where $N \approx 10^{12}$ is the number of spins [144, 146–148].

However, coupling to single or few spins is desired as they form more promising qubits [149]. Several methods have been theoretically proposed and all of them involve some level of hybridization between the spin and charge degrees of freedom [150–158]. For a single spin in a DQD it started with Ref. [153], and was further examined in Ref. [159–161]. They use the fact that the electric dipole coupling strength, between the electric field of the cavity and the charge dipole moment of the electron in a double dot, can be six orders of magnitude larger than a typical magnetic dipole coupling strength. Combined with spin-orbit interaction (SOI), which hybridizes the spin of the electron with its charge degree of freedom, an indirect coupling of the cavity electric field to the spin degree of freedom can be obtained. This is achieved using on-chip microscale ferromagnets (micromagnets) in the work presented in this thesis. The cavity is often galvanically connected to one of the gate electrodes defining the DQD in order to maximize the electric dipole coupling strength. Although the coupling mechanism is indirect, it is predicted to be five orders of magnitude larger than than the direct magnetic coupling, making it worthwhile to experimentally investigate this.

### 2.6.1. Charge-photon coupling

The coupling between a single electron charge in a DQD and a single microwave cavity photon originates from electric dipole interactions and it is quantified by the charge-photon coupling strength [159]:

$$g_C = \frac{1}{2}\beta V_{\mathrm{rms}}^0/\hbar = \frac{1}{2}\beta \omega_r \sqrt{\frac{Z_r}{\pi\hbar}}, \tag{2.43}$$

where $\beta$ is the differential lever arm of the cavity gate. The reason for using a DQD instead of a SQD is twofold. First, the orbital energy a DQD can be tuned electrically to be on the order of 20-40 µeV, in the range of superconducting microwave resonators (5-10 GHz), whereas the smallest energy scale of a SQD, determined by the valley or orbital splitting, is usually larger and less tunable. Second, the DQD interdot spacing is typically on the order of 100 nm, which leads to a much larger larger electric dipole moment than for a SQD. The coupling strength is the product of this dipole moment with the rms vacuum electric field of the cavity. Since
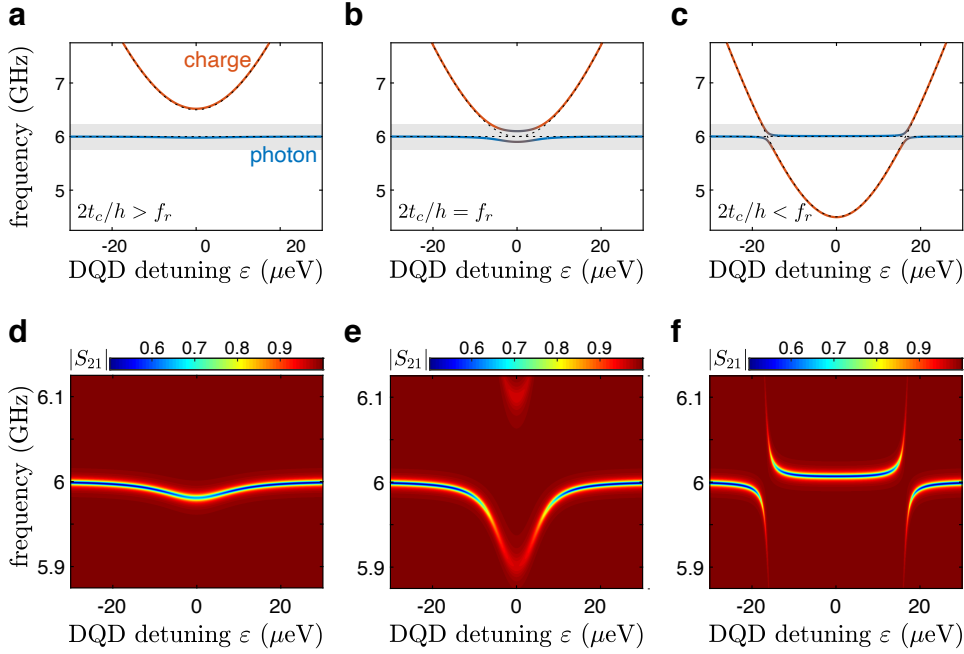
Figure 2.13: **Charge-photon interaction with a hanger style resonator**. **a** Eigenenergies of the Jaynes-Cummings Hamiltonian (Eq. 2.6, 2.7) as function of the DQD detuning parameter. Computed with $g_C/2\pi = 100\,$MHz, $f_r = 6\,$GHz and $2t_c/h = 6.5\,$GHz. **b** With $2t_c/h = 6\,$GHz. **c** With $2t_c/h = 4.5\,$GHz. The black dashed lines are computed with $g_C/2\pi = 0\,$MHz. **d**, **e** and **f** show the simulated transmission (Eq. 2.46) in the grey region around $f_r$ in **a**, **b** and **c**. **d** Dispersive shift of the cavity. **e** Vacuum Rabi splitting with the hybridized charge-photon peaks separated by $g_C/\pi = 200\,$MHz. The visibility at zero detuning is reduced because photons can now also decay through the qubit. **f** Dispersive shift of the cavity near zero detuning (in the opposite direction compared to the shift in **d**) and vacuum Rabi splittings near $\pm 16\,\mu$eV. The other parameters are $\kappa/2\pi = 5\,$MHz, $\kappa_{\text{int}}/2\pi = 2.5\,$MHz and $\gamma_C/2\pi = 25\,$MHz.

the field strength scales linearly with $\sqrt{Z_r}$, it is beneficial to use resonators with an impedance beyond the standard $50\,\Omega$. Eq. 2.43 describes the charge-photon coupling strength at zero DQD detuning, where the electron dipole moment is largest. The charge-photon coupling strength at nonzero DQD detuning is described by:

$$g_{\text{eff}} = g_C \sin\theta_{cp} = g_C \frac{2t_c}{\hbar\omega_{cq}} \tag{2.44}$$

with $\theta_{cp}$ the charge-photon mixing angle and $\omega_{cq} = \sqrt{4t_c^2 + \varepsilon^2}/\hbar$ the charge qubit angular frequency.

The charge-photon interaction can be probed via the transmission through the cavity (Fig. 2.13). The complex transmission for a transmission and hanger style resonator can be calculated using input-output theory [138, 142]:

$$S_{21}^T = \frac{-i\sqrt{\kappa_1\kappa_2}}{\Delta_0 - i\frac{\kappa}{2} + g_{\text{eff}}\chi}, \tag{2.45}$$

$$S_{21}^H = \frac{\Delta_0 - i\frac{\kappa_{\text{int}}}{2} + g_{\text{eff}}\chi}{\Delta_0 - i\frac{\kappa}{2} + g_{\text{eff}}\chi}, \tag{2.46}$$

with $\Delta_0 = \omega_d - \omega_r$ the detuning of the driving (probe) field from the cavity frequency and:

$$\chi = \frac{g_{\text{eff}}}{\Delta + i\gamma_C}, \tag{2.47}$$

the single-electron DQD electrical susceptibility, where $\Delta = \omega_{cq} - \omega_d$ is the detuning of the charge qubit frequency from the driving (probe) field and $\gamma_C = \frac{\gamma_1}{2} + \gamma_\phi$ is the charge qubit decoherence rate, and is related to the charge qubit linewidth as FWHM $= 2\gamma_C$. Here, $\gamma_1$ is the charge relaxation rate and $\gamma_\phi$ is the dephasing rate due to charge noise. It is important to emphasize that a more realistic model should include a $\gamma_C$ that depends on the DQD detuning $\varepsilon$ [162], with a minimum $\gamma_C$ at zero detuning where the qubit is to first order insensitive to charge noise [60]. Note that Eq. 2.45 and 2.46 simplify to expressions for a Lorentzian curve (Eq. 2.26, 2.27) for $g_{\text{eff}} = 0$.

Hybrid quantum devices comprising semiconductor DQDs coupled to microwave cavities have been demonstrated in a multitude of material systems, including InAs nanowires [138], graphene [163, 164], carbon nanotubes [165], GaAs/AlGaAs [137, 166, 167] and Si/SiGe heterostructures [31]. However, reaching the strong charge-photon coupling regime is a nontrivial task. The bottleneck is usually $\gamma_C > g_C$, which can be $\gamma_C/2\pi \approx 0.1 - 1$ GHz. Charge noise from fluctuating two-level systems in the dielectric and at interfaces is likely the dominant noise source contributing to $\gamma_C$ [168]. Only recently have three groups independently demonstrated the strong charge-photon coupling $g_C > \kappa/2, \gamma_C$ [162, 169, 170].

### Dispersive regime
It is insightful to group the terms in the denominator of $S_{21}^T$ (Eq. 2.45) and $S_{21}^H$ (Eq. 2.46) in a real part and an imaginary part to highlight different effects of the charge qubit on the cavity. The resulting loaded cavity frequency and linewidth are:

$$\omega_r^* = \omega_r - \text{Re}\left(g_{\text{eff}}\chi\right) = \omega_r - \frac{g_{\text{eff}}^2\Delta}{\Delta^2 + \gamma_C^2}, \tag{2.48}$$

$$\kappa^* = \kappa - 2\text{Im}\left(g_{\text{eff}}\chi\right) = \kappa + \frac{2g_{\text{eff}}^2\gamma_C}{\Delta^2 + \gamma_C^2}. \tag{2.49}$$

Fig. 2.14 shows the calculated cavity response in the dispersive charge-photon regime for three different values of $\gamma_C$ and fixed $t_c$. The dispersive shift, $-\text{Re}\left(g_{\text{eff}}\chi\right)$,
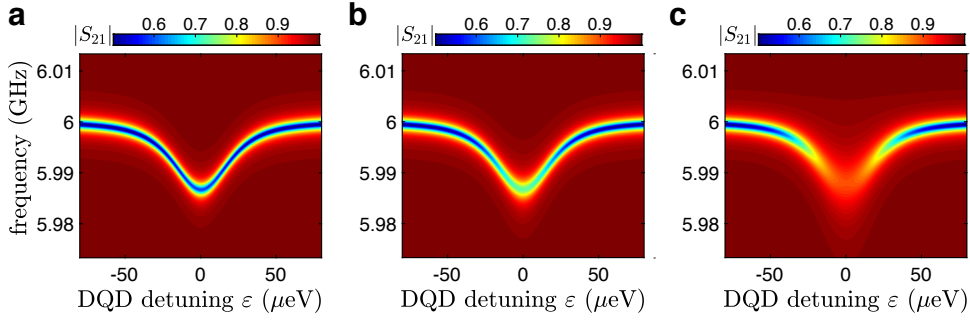
Figure 2.14: **The effect of charge qubit decoherence on the dispersively shifted cavity. a** Cavity transmission calculated with $g_C/2\pi = 200$ MHz, $f_r = 6$ GHz, $2t_c/h = 9$ GHz, $\kappa/2\pi = 2$ MHz, $\kappa_{\rm int}/2\pi = 1$ MHz and $\gamma_C/2\pi = 50$ MHz. **b** With $\gamma_C/2\pi = 200$ MHz. **c** With $\gamma_C/2\pi = 1$ GHz.

as function of the DQD detuning parameter can be well approximated by $\frac{g_{\rm eff}^2}{\Delta}$ when $\gamma_C \ll \Delta$. Since the dispersive shift is uniquely determined by $g_C$ and $t_c$ within this approximation, fitting its shape allows those parameters to be extracted, provided that the differential lever arm is known. In the regime $\gamma_C > \kappa$, which is typically true in experiments, the qubit forms a loss channel for photons, resulting in an increase of the cavity linewidth and a reduction of the visibility. This will have a negative impact on the spin-photon coupling experiment because the measurements are mostly done at zero detuning with the probe signal frequency centered at the dispersively shifted cavity frequency.

### Two-tone spectroscopy

Microwave two-tone spectroscopy is a very powerful technique in circuit QED that can unveil the energy dispersion relation of a qubit in the dispersive regime. This is done by monitoring the cavity response at a fixed probe frequency $\omega_d = 2\pi f_d$ while applying a continuous second microwave signal (tone) of which the frequency $\omega_{d2} = 2\pi f_{d2}$ is swept. The second tone drives the qubit continuously when $\omega_{d2}$ matches the qubit frequency, thereby changing the steady-state population $\langle \tau_z \rangle$. Since $\tau_z = -1$ ($\tau_z = +1$) when the qubit is in its ground (excited) state, $\langle \tau_z \rangle = -1$ when there is no drive. In the stationary regime, the cavity response is given by [165]:

$$S_{21}^T = \frac{-i\sqrt{\kappa_1 \kappa_2}}{\Delta_0 - i\frac{\kappa}{2} - g_{\rm eff}\chi\langle \tau_z \rangle}, \tag{2.50}$$

$$S_{21}^H = \frac{\Delta_0 - i\frac{\kappa_{\rm int}}{2} + g_{\rm eff}\chi}{\Delta_0 - i\frac{\kappa}{2} - g_{\rm eff}\chi\langle \tau_z \rangle}, \tag{2.51}$$

$$\langle \tau_z \rangle = \frac{-1}{1 + \frac{4g_{\rm eff}^2 n_{\rm drive}}{\gamma_1} \frac{\gamma_C}{\Delta_2^2 + \gamma_C^2}}, \tag{2.52}$$
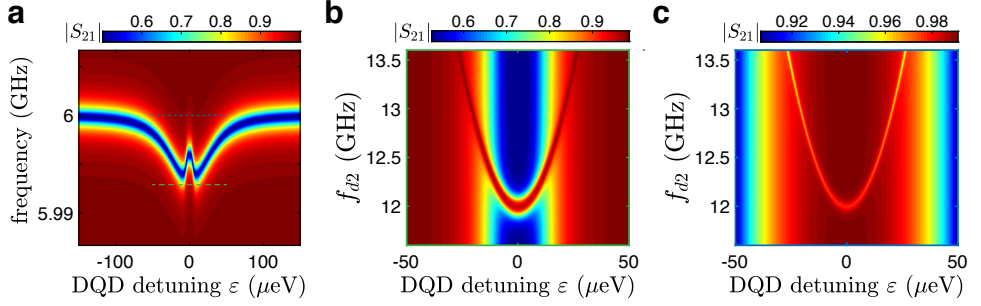
**2**



Figure 2.15: **Microwave two-tone spectroscopy of a DQD charge qubit**. **a** Cavity transmission as function of the probe frequency and DQD detuning in the presence of a second continuous microwave tone at $f_{d2} = 2t_c/h$. The cavity frequency shift at $\varepsilon = 0$ is partially canceled because the charge qubit is on average not in its ground state anymore due to the continuous driving, which leads to $\langle \tau_z \rangle > -1$. Calculated with $g_C/2\pi = 200\,\text{MHz}$, $f_r = 6\,\text{GHz}$, $2t_c/h = 12\,\text{GHz}$, $\kappa/2\pi = 2\,\text{MHz}$, $\kappa_{\text{int}}/2\pi = 1\,\text{MHz}$, $\gamma_C/2\pi = 50\,\text{MHz}$, $\gamma_1/2\pi = 50\,\text{MHz}$, $f_{d2} = 12\,\text{GHz}$ and $n_{\text{drive}} = 0.01$. **b** Cavity transmission as function of the second tone driving frequency and DQD detuning. Simulated with the probe frequency fixed at the dispersively shifted cavity frequency $f_r^* = f_r - \text{Re}\,(g_{\text{eff}}\chi)\,/2\pi$ (dashed green line in **a**). **c** Similar to **b**, but with the the probe frequency fixed at the bare resonance frequency $f_r$ (dotted blue line in **a**). The simulations do not include a $\gamma_C$ that depends on the DQD detuning, which would otherwise reduce the visibility of the charge qubit signal away from $\varepsilon = 0$.

where $n_{\text{drive}}$ is a measure of the second tone driving strength and $\Delta_2 = \omega_{cq} - \omega_{d2}$ is the detuning of the charge qubit frequency from the second microwave tone frequency. Fig. 2.15 shows the simulated cavity response in the presence of a second tone. The charge qubit dispersion relation can be efficiently mapped out close to $\varepsilon = 0$. In addition, this information can be exploited to calibrate the differential lever arm $\beta$ of a gate electrode. Furthermore, we have direct access to the charge qubit linewidth $\gamma_C$ using this technique when the drive amplitude is sufficiently low.

## 2.6.2. Spin-photon coupling

Although the charge-photon interaction provides plenty of intriguing physics by itself, it is used as a stepping stone towards the more desired spin-photon coupling in this thesis. Since the electron spin does not couple directly to the electric field of the cavity, one needs to hybridize spin and charge degrees of freedom of the electron. A mechanism that works for single electrons is the spin-orbit interaction. However, the intrinsic SOI in silicon is very weak. Therefore, microscale ferromagnets are placed close to the dots to produce a strong transverse magnetic field gradient $\partial B_x/\partial z$ that facilitates a synthetic SOI [87–89] (Fig. 2.16). The system in Fig. 2.16a can be described by the following Hamiltonian:

$$H_{\text{DQD}} = \frac{1}{2}\left(\varepsilon\tau_z + 2t_c\tau_x + g\mu_B B_z\sigma_z + g\mu_B\delta B_x\sigma_x\tau_z\right), \tag{2.53}$$

with $\tau_{x,z}$ and $\sigma_{x,z}$ the Pauli operators in position and spin space, respectively, $g$ the electron $g$-factor ($g \approx 2$ in silicon) and $\mu_B$ the Bohr magneton. $B_z = B_z^{\text{ext}} +$
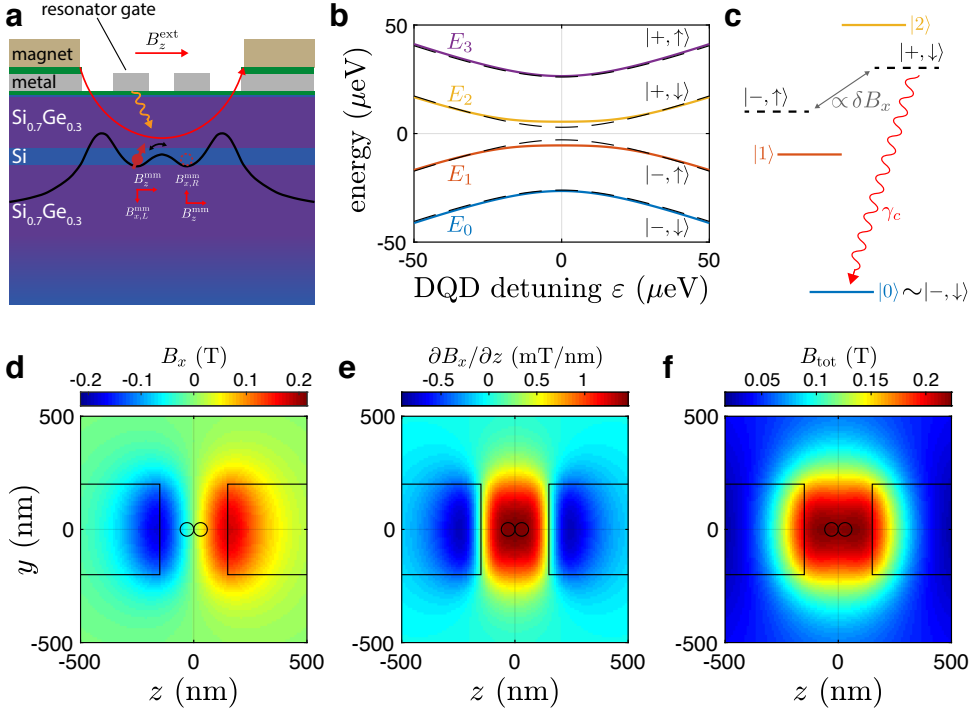
Figure 2.16: **Spin-charge hybridization via on-chip microscale ferromagnets**. **a** Schematic of a gate-defined DQD in a Si/SiGe heterostructure in a homogeneous external magnet field $B_z^{\text{ext}}$ and an inhomogeneous magnetic field with components $B_z^{\text{mm}}(\vec{r})$ and $B_x^{\text{mm}}(\vec{r})$ created by the micromagnets. The micromagnets produce a transversal field gradient with $B_{x,L}^{\text{mm}}$ and $B_{x,R}^{\text{mm}}$ the out-of-plane fields in the left and right dot, respectively, and they point in opposite directions which leads to a position-dependent quantization axis of the electron spin. The black solid line represents the potential landscape in the quantum well defined by the metallic gates at the surface. The DQD is electric-dipole-coupled to the resonator via one of the gates. **b** DQD energy levels as a function of the DQD detuning parameter (Eq. 2.54). The black dashed lines represent the bonding ($|-\rangle$) and antibonding ($|+\rangle$) orbitals in the absence of a transverse magnetic field gradient ($\delta B_x = (B_{x,R}^{\text{mm}} - B_{x,L}^{\text{mm}})/2 = 0$), and with spin $|\downarrow\rangle$, $|\uparrow\rangle$ in the $z$-direction. The colored solid lines are with finite $\delta B_x$, causing the level repulsion between $|-,\uparrow\rangle$ and $|+,\downarrow\rangle$ near $\varepsilon = 0$. The following parameters were chosen for this plot: $2t_c/h = 7\,\text{GHz}$, $B_z = 200\,\text{mT}$ and $\delta B_x = 80\,\text{mT}$. **c** Schematic of the effective three-level system that captures the important dynamics near $\varepsilon = 0$. The levels $|-,\uparrow\rangle$ and $|+,\downarrow\rangle$ hybridize into the states $|1\rangle$ and $|2\rangle$, respectively, due to a transverse field gradient. The ground state $|0\rangle \approx |-,\downarrow\rangle$ is left mostly unperturbed. Adapted from Ref. [160]. **d** Numerical simulation of $B_x(\vec{r}) = B_x^{\text{mm}}(\vec{r})$ in the Si quantum well, 110 nm below the micromagnets. The straight solid black lines outline part of the rectangular micromagnets, which are magnetized in the $z$-direction. The solid black circles represent the approximate DQD location. **e** The gradient of $B_x(\vec{r})$ along the $z$-direction, which is parallel to the external magnetic field direction and also the DQD axis. **f** The total magnet field $B_{\text{tot}} = |\vec{B}_{\text{tot}}| = \sqrt{B_z^2 + B_x^2}$, where $B_z = B_z^{\text{ext}} + B_z^{\text{mm}}$. The calculation assumes micromagnets with dimensions $400\,\text{nm} \times 1500\,\text{nm} \times 200\,\text{nm}$ ($W \times L \times H$) separated by 300 nm and a total polarization of 1.8 T, and $B_z^{\text{ext}} = 50\,\text{mT}$.
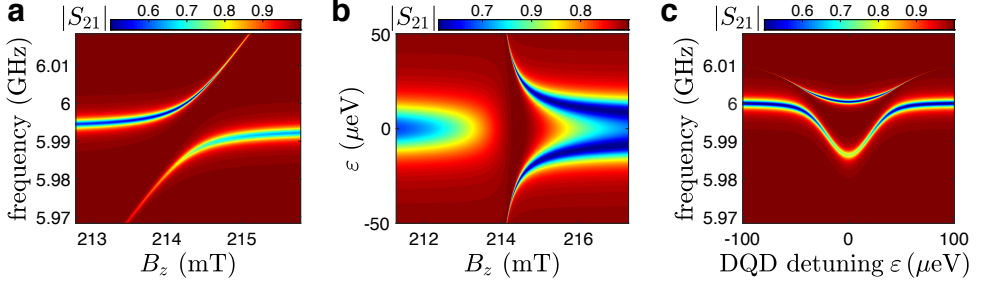
Figure 2.17: **Spin-photon interaction with a hanger style resonator**. **a** Cavity transmission as function of the probe frequency and the magnetic field in $z$-direction. The vacuum Rabi splitting is $2g_S/2\pi \approx 14\,\text{MHz}$. Simulated with $g_C/2\pi = 200\,\text{MHz}$, $f_r = 6\,\text{GHz}$, $2t_c/h = 12\,\text{GHz}$, $\delta B_x = 15\,\text{mT}$, $\kappa/2\pi = 2\,\text{MHz}$, $\kappa_{\text{int}}/2\pi = 1\,\text{MHz}$ and $\gamma_C/2\pi = 250\,\text{MHz}$. **b** Cavity response as function of the DQD detuning parameter and $B_z$ at a fixed probe frequency, which is set to the dispersively shifted cavity frequency, $f_r^* = f_r - \text{Re}\,(g_{\text{eff}}\chi)\,/2\pi$. **c** Transmission as function of the probe frequency and DQD detuning with $B_z$ fixed at the resonance condition $B_z^{\text{res}}$ (Eq. 2.67).

$B_z^{\text{mm}}$ is the total magnetic field in the $z$-direction and consists of contributions from the external magnet and on-chip micromagnets. Here, $\delta B_x = (B_{x,R}^{\text{mm}} - B_{x,L}^{\text{mm}})/2$ is half the difference in magnetic field between the two dots in the $x$-direction. For simplicity we assume $B_{x,R}^{\text{mm}} = -B_{x,L}^{\text{mm}}$, which is reasonable for a symmetric device design. Fig. 2.16e,f,d show numerical simulations of the perpendicular magnetic field component $B_x$, its gradient $\partial B_x/\partial z$ and the total magnetic field $|\vec{B}_{\text{tot}}|$ in the plane of the qubits. $|\vec{B}_{\text{tot}}|$ needs to be the same in the two dots in order to minimize the spin dephasing rate due to charge noise. The field gradient causes the two dots to have different quantization axes for the spin. When the oscillating cavity electric field pushes the electron back and forth between the dots, the electron will see an oscillating magnetic field, allowing for electric dipole spin resonance. The Hamiltonian can be expressed in the basis $|L,\uparrow\rangle$, $|R,\uparrow\rangle$, $|L,\downarrow\rangle$, $|R,\downarrow\rangle$ as:

$$H_{\text{DQD}} = \frac{1}{2} \begin{pmatrix} \varepsilon + g\mu_B B_z & 2t_c & g\mu_B \delta B_x & 0 \\ 2t_c & -\varepsilon + g\mu_B B_z & 0 & -g\mu_B \delta B_x \\ g\mu_B \delta B_x & 0 & \varepsilon - g\mu_B B_z & 2t_c \\ 0 & -g\mu_B \delta B_x & 2t_c & -\varepsilon - g\mu_B B_z \end{pmatrix}, \qquad (2.54)$$

with eigenstates:

$$|0\rangle \approx |-,\downarrow\rangle, \qquad (2.55)$$

$$|1\rangle = \cos\frac{\Phi}{2}\,|-,\uparrow\rangle + \sin\frac{\Phi}{2}\,|+,\downarrow\rangle, \qquad (2.56)$$

$$|2\rangle = \sin\frac{\Phi}{2}\,|-,\uparrow\rangle - \cos\frac{\Phi}{2}\,|+,\downarrow\rangle, \qquad (2.57)$$

$$|3\rangle \approx |+,\uparrow\rangle, \qquad (2.58)$$

where $\Phi = \arctan \frac{g\mu_B \delta B_x \cos \theta_o}{\hbar \omega_{cq} - g\mu_B B_z}$ is the spin-orbit mixing angle and $\theta_o = \arctan \frac{\varepsilon}{2t_c}$ is the orbital angle. We see that the states $|-, \uparrow\rangle$ and $|+, \downarrow\rangle$, with opposite spins, are weakly coupled due to $\delta B_x$ (Fig. 2.16c). The corresponding eigenenergies are (Fig. 2.16b):

$$E_{3,0} = \pm \sqrt{\left(\hbar\omega_{cq} + g\mu_B \sqrt{B_z^2 + \delta B_x^2 \sin^2 \theta_o}\right)^2 + (g\mu_B \delta B_x)^2 \cos^2 \theta_o}, \qquad (2.59)$$

$$E_{2,1} = \pm \sqrt{\left(\hbar\omega_{cq} - g\mu_B \sqrt{B_z^2 + \delta B_x^2 \sin^2 \theta_o}\right)^2 + (g\mu_B \delta B_x)^2 \cos^2 \theta_o}. \qquad (2.60)$$

The complex cavity transmissions are given by [160]:

$$S_{21}^T = \frac{-i\sqrt{\kappa_1 \kappa_2}}{\Delta_0 - i\frac{\kappa}{2} + g_{\text{eff}}(\chi_{01}d_{01} + \chi_{02}d_{02})}, \qquad (2.61)$$

$$S_{21}^H = \frac{\Delta_0 - i\frac{\kappa_{\text{int}}}{2} + g_{\text{eff}}(\chi_{01}d_{01} + \chi_{02}d_{02})}{\Delta_0 - i\frac{\kappa}{2} + g_{\text{eff}}(\chi_{01}d_{01} + \chi_{02}d_{02})}, \qquad (2.62)$$

with susceptibilities:

$$\chi_{01} = -\frac{g_{\text{eff}}d_{01}}{\delta_1 - i\gamma_{\text{eff}}^{(2)}}, \qquad (2.63)$$

$$\chi_{02} = -\frac{g_{\text{eff}}d_{02}}{\delta_2 - i\gamma_{\text{eff}}^{(1)}}, \qquad (2.64)$$

and electric dipole transition matrix elements:

$$d_{01} \approx -\cos\theta_o \sin\frac{\Phi}{2}, \qquad (2.65)$$

$$d_{02} \approx \cos\theta_o \cos\frac{\Phi}{2}, \qquad (2.66)$$

with detunings $\delta_{1,2} = \omega_d - (E_{1,2} - E_0)/\hbar$ and effective charge-induced decoherence rates $\gamma_{\text{eff}}^{(1,2)} = \gamma_C \left(\delta_2 \sin^2 \frac{\Phi}{2} + \delta_1 \cos^2 \frac{\Phi}{2}\right)/\delta_{1,2}$. Note that $\gamma_{\text{eff}}^{(1,2)}$ do not include spin dephasing due to fluctuations of the $^{29}$Si nuclear spin bath. The matrix element $d_{01}$ describes the primarily spin-like transition between $|0\rangle$ and $|1\rangle$, while $d_{02}$ describes the primarily charge-like transition between $|0\rangle$ and $|2\rangle$. While $H_{\text{DQD}}$ describes a four-level system, the fourth level ($|3\rangle$) is far detuned from $|0\rangle$, allowing us to model the system effectively with only the lowest three levels. The cavity response in the resonant regime is shown in Fig. 2.17. The three plots can be viewed as slices through a 3D space spanned by the probe frequency $f_d$, DQD detuning $\varepsilon$ and

**2**

magnetic field component $B_z$. The $B_z$ at which the spin qubit is resonant with the dispersively shifted cavity frequency $\omega_r^*$ for a given $\delta B_x$ is given by:

$$B_z^{\text{res}} = \frac{\hbar \omega_r^*}{g \mu_B} \sqrt{1 - \frac{g \mu_B \delta B_x^2}{\hbar \omega_r^{*2} - 4t_c^2}}. \tag{2.67}$$

In the case $2t_c > g \mu_B B_z$, the effective spin decoherence rate arising from the charge decoherence rate becomes $\gamma_S \approx \gamma_{\text{eff}}^{(2)}$. The effective spin-photon coupling strength is given by:

$$g_S = g_{\text{eff}} \frac{g \mu_B \delta B_x |\Delta_\tau| \cos \theta_o}{2 \hbar (\Delta_\tau^2 + \gamma_C^2)}, \tag{2.68}$$

with $\Delta_\tau = \frac{\omega_{cq} - g \mu_B B_z / \hbar}{2} - E_0/\hbar - \omega_r$. At $\varepsilon = 0$ and for $|\Delta_\tau| \gg \gamma_C$ the effective spin-photon coupling strength simplifies to $g_S \approx g_C \frac{g \mu_B \delta B_x}{2(2t_c - \hbar \omega_r)}$.

It is important to emphasize that strong charge-photon coupling is not a pre-requisite for strong spin-photon coupling, because $g_S$ and $\gamma_S$ scale differently with the degree of spin-charge hybridization. More specifically, $\frac{g_S}{g_C} \propto \frac{\delta B_x}{2t_c - \hbar \omega_r}$, whereas $\frac{\gamma_S}{\gamma_C} \propto \left( \frac{\delta B_x}{2t_c - \hbar \omega_r} \right)^2$, allowing for $\frac{g_S}{\gamma_S} > \frac{g_C}{\gamma_C}$ at sufficiently small $\frac{\delta B_x}{2t_c - \hbar \omega_r}$. The drawback, however, is a reduced $g_S$ that can become smaller than the cavity linewidth. Note that the condition for strong spin-photon coupling this system is $g_S > \kappa^*/2, \gamma_S$, where $\kappa^*$ is the cavity linewidth broadened by the charge qubit. In 2018, three groups, including our group (see Chap. 4), have independently reached the strong spin-photon coupling regime[10] [171–173].

The spin-charge-photon system considered here deviates from the ideal two-level system assumed within the framework of the standard Jaynes-Cummings Hamiltonian. Our system involves effectively three levels, which results in a slight asymmetry in the width and amplitude of the two vacuum Rabi split peaks or dips due to subtle interference effects between the three levels. This becomes more apparent for larger $g_C$ [160].

### Magnetic sweet spot
So far, we assumed the ideal case in which the electron spin has the same Zeeman splitting in the two dots. This leads to a minimum in the energy splitting $E_1 - E_0$ exactly at zero detuning when spin and charge are hybridized. Since $\frac{\partial (E_1 - E_0)}{\partial \varepsilon} = 0$, this is called the magnetic sweet spot, and it aligns with the electric sweet spot, $\frac{\partial (E_2 - E_0)}{\partial \varepsilon} = 0$. However, in practice the dots might not form exactly at the intented locations, so they can experience slightly different magnetic fields, causing the magnetic sweet spot to deviate from $\varepsilon = 0$. This effect can be observed as an asymmetry in the detuning in Fig. 2.17b. This may be mitigated by tuning the dots to the desired location.

---

[10]Ref. [171] was with a three-spin qubit.

# References

[1] S. Haroche and J. M. Raimond, *Exploring the Quantum: Atoms, Cavities, and Photons* (Oxford Univ. Press, Oxford, 2006).

[2] S. Haroche, *Nobel lecture: Controlling photons in a box and exploring the quantum to classical boundary,* Rev. Mod. Phys. **85**, 1083 (2013).

[3] A. Wallraff, D. I. Schuster, A. Blais, L. Frunzio, R.-S. Huang, J. Majer, S. Kumar, S. M. Girvin, and R. J. Schoelkopf, *Strong coupling of a single photon to a superconducting qubit using circuit quantum electrodynamics,* Nature **431**, 162 (2004).

[4] A. Blais, R.-S. Huang, A. Wallraff, S. M. Girvin, and R. J. Schoelkopf, *Cavity quantum electrodynamics for superconducting electrical circuits: An architecture for quantum computation,* Phys. Rev. A **69**, 062320 (2004).

[5] D. I. Schuster, *Circuit Quantum Electrodynamics*, Ph.D. thesis, Yale University (2007).

[6] *Nature Physics Focus: The ABC of cQED,* Nature Physics **16**, 233 (2020).

[7] I. I. Rabi, *On the process of space quantization,* Phys. Rev. **49**, 324 (1936).

[8] I. I. Rabi, *Space quantization in a gyrating magnetic field,* Phys. Rev. **51**, 652 (1937).

[9] Q. Xie, H. Zhong, M. T. Batchelor, and C. Lee, *The quantum rabi model: solution and dynamics,* Journal of Physics A: Mathematical and Theoretical **50**, 113001 (2017).

[10] E. T. Jaynes and F. W. Cummings, *Comparison of quantum and semiclassical radiation theories with application to the beam maser,* Proceedings of the IEEE **51**, 89 (1963).

[11] W. E. Lamb and R. C. Retherford, *Fine structure of the hydrogen atom by a microwave method,* Phys. Rev. **72**, 241 (1947).

[12] J. Majer, J. M. Chow, J. M. Gambetta, J. Koch, B. R. Johnson, J. A. Schreier, L. Frunzio, D. I. Schuster, A. A. Houck, A. Wallraff, A. Blais, M. H. Devoret, S. M. Girvin, and R. J. Schoelkopf, *Coupling superconducting qubits via a cavity bus,* Nature **449**, 443 (2007).

[13] M. A. Sillanpää, J. I. Park, and R. W. Simmonds, *Coherent quantum state storage and transfer between two phase qubits via a resonant cavity,* Nature **449**, 438 (2007).

[14] M. Tavis and F. W. Cummings, *Exact solution for an $n$-molecule—radiation-field hamiltonian,* Phys. Rev. **170**, 379 (1968).

**2**

[15] A. Blais, J. Gambetta, A. Wallraff, D. I. Schuster, S. M. Girvin, M. H. Devoret, and R. J. Schoelkopf, *Quantum-information processing with circuit quantum electrodynamics,* Phys. Rev. A **75**, 032329 (2007).

[16] B. A. Mazin, P. K. Day, H. G. LeDuc, A. Vayonakis, and J. Zmuidzinas, *Superconducting kinetic inductance photon detectors,* in *Highly Innovative Space Telescope Concepts*, Vol. 4849, edited by H. A. MacEwen, International Society for Optics and Photonics (SPIE, 2002) pp. 283 – 293.

[17] P. K. Day, H. G. LeDuc, B. A. Mazin, A. Vayonakis, and J. Zmuidzinas, *A broadband superconducting detector suitable for use in large arrays,* Nature **425**, 817 (2003).

[18] B. A. Mazin, M. E. Eckart, B. Bumble, S. Golwala, P. K. Day, J. Gao, and J. Zmuidzinas, *Optical/uv and x-ray microwave kinetic inductance strip detectors,* Journal of Low Temperature Physics **151**, 537 (2008).

[19] E. A. Tholén, A. Ergül, E. M. Doherty, F. M. Weber, F. Grégis, and D. B. Haviland, *Nonlinearities and parametric amplification in superconducting coplanar waveguide resonators,* Applied Physics Letters **90**, 253509 (2007).

[20] M. A. Castellanos-Beltran and K. W. Lehnert, *Widely tunable parametric amplifier based on a superconducting quantum interference device array resonator,* Applied Physics Letters **91**, 083509 (2007).

[21] A. Endo, C. Sfiligoj, S. J. C. Yates, J. J. A. Baselmans, D. J. Thoen, S. M. H. Javadzadeh, P. P. van der Werf, A. M. Baryshev, and T. M. Klapwijk, *On-chip filter bank spectroscopy at 600–700 ghz using nbtin superconducting resonators,* Applied Physics Letters **103**, 032601 (2013).

[22] L. Frunzio, A. Wallraff, D. Schuster, J. Majer, and R. Schoelkopf, *Fabrication and characterization of superconducting circuit qed devices for quantum computation,* IEEE Transactions on Applied Superconductivity **15**, 860 (2005).

[23] M. Göppl, A. Fragner, M. Baur, R. Bianchetti, S. Filipp, J. M. Fink, P. J. Leek, G. Puebla, L. Steffen, and A. Wallraff, *Coplanar waveguide resonators for circuit quantum electrodynamics,* Journal of Applied Physics **104**, 113904 (2008).

[24] R. E. Collin, *Foundations for Microwave Engineering* (Wiley-IEEE Press, 2001).

[25] D. M. Pozar, *Microwave Engineering* (Wiley, 2011).

[26] J. Gao, *The Physics of Superconducting Microwave Resonators*, Ph.D. thesis (2008).

[27] R. Barends, *Photon-detecting superconducting resonators*, Ph.D. thesis, Delft University of Technology (2009).

[28] J. Gao, M. Daal, A. Vayonakis, S. Kumar, J. Zmuidzinas, B. Sadoulet, B. A. Mazin, P. K. Day, and H. G. Leduc, *Experimental evidence for a surface distribution of two-level systems in superconducting lithographed microwave resonators,* Applied Physics Letters **92**, 152505 (2008).

[29] A. D. O᾿ Connell, M. Ansmann, R. C. Bialczak, M. Hofheinz, N. Katz, E. Lucero, C. McKenney, M. Neeley, H. Wang, E. M. Weig, A. N. Cleland, and J. M. Martinis, *Microwave dielectric loss at single photon energies and millikelvin temperatures,* Applied Physics Letters **92**, 112903 (2008).

[30] A. Bruno, G. de Lange, S. Asaad, K. L. van der Enden, N. K. Langford, and L. DiCarlo, *Reducing intrinsic loss in superconducting resonators by surface treatment and deep etching of silicon substrates,* Applied Physics Letters **106**, 182601 (2015).

[31] X. Mi, J. V. Cady, D. M. Zajac, J. Stehlik, L. F. Edge, and J. R. Petta, *Circuit quantum electrodynamics architecture for gate-defined quantum dots in silicon,* Applied Physics Letters **110**, 043502 (2017).

[32] P. Harvey-Collard, G. Zheng, J. Dijkema, N. Samkharadze, A. Sammak, G. Scappucci, and L. M. K. Vandersypen, *On-chip microwave filters for high-impedance resonators with gate-defined quantum dots,* Phys. Rev. Applied **14**, 034025 (2020).

[33] U. Fano, *Effects of configuration interaction on intensities and phase shifts,* Phys. Rev. **124**, 1866 (1961).

[34] M. S. Khalil, M. J. A. Stoutimore, F. C. Wellstood, and K. D. Osborn, *An analysis method for asymmetric resonator transmission applied to superconducting devices,* Journal of Applied Physics **111**, 054510 (2012).

[35] N. Samkharadze, A. Bruno, P. Scarlino, G. Zheng, D. P. DiVincenzo, L. DiCarlo, and L. M. K. Vandersypen, *High-kinetic-inductance superconducting nanowire resonators for circuit qed in a magnetic field,* Phys. Rev. Applied **5**, 044004 (2016).

[36] C. Eichler, A. J. Sigillito, S. A. Lyon, and J. R. Petta, *Electron spin resonance at the level of $10^4$ spins using low impedance superconducting resonators,* Phys. Rev. Lett. **118**, 037701 (2017).

[37] A. J. Annunziata, D. F. Santavicca, L. Frunzio, G. Catelani, M. J. Rooks, A. Frydman, and D. E. Prober, *Tunable superconducting nanoinductors,* Nanotechnology **21**, 445202 (2010).

[38] *Sonnet Software Inc. .*

[39] W. G. van der Wiel, S. De Franceschi, J. M. Elzerman, T. Fujisawa, S. Tarucha, and L. P. Kouwenhoven, *Electron transport through double quantum dots,* Rev. Mod. Phys. **75**, 1 (2002).

2

**2**

[40] R. Hanson, L. P. Kouwenhoven, J. R. Petta, S. Tarucha, and L. M. K. Vandersypen, *Spins in few-electron quantum dots,* Rev. Mod. Phys. **79**, 1217 (2007).

[41] F. A. Zwanenburg, A. S. Dzurak, A. Morello, M. Y. Simmons, L. C. L. Hollenberg, G. Klimeck, S. Rogge, S. N. Coppersmith, and M. A. Eriksson, *Silicon quantum electronics,* Rev. Mod. Phys. **85**, 961 (2013).

[42] T. Ihn, *Semiconductor Nanostructures: Quantum states and electronic transport* (Oxford University Press, 2009).

[43] G. Scappucci, C. Kloeffel, F. A. Zwanenburg, D. Loss, M. Myronov, J.-J. Zhang, S. De Franceschi, G. Katsaros, and M. Veldhorst, *The germanium quantum information route,* Nature Reviews Materials (2020), 10.1038/s41578-020-00262-z.

[44] J. R. Petta, A. C. Johnson, J. M. Taylor, E. A. Laird, A. Yacoby, M. D. Lukin, C. M. Marcus, M. P. Hanson, and A. C. Gossard, *Coherent manipulation of coupled electron spins in semiconductor quantum dots,* Science **309**, 2180 (2005).

[45] S. Tarucha, D. G. Austing, T. Honda, R. J. van der Hage, and L. P. Kouwenhoven, *Shell filling and spin effects in a few electron quantum dot,* Phys. Rev. Lett. **77**, 3613 (1996).

[46] J. M. Thijssen and H. S. J. Van der Zant, *Charge transport and single-electron effects in nanoscale systems,* physica status solidi (b) **245**, 1455 (2008).

[47] T. H. Oosterkamp, T. Fujisawa, W. G. van der Wiel, K. Ishibashi, R. V. Hijman, S. Tarucha, and L. P. Kouwenhoven, *Microwave spectroscopy of a quantum-dot molecule,* Nature **395**, 873 (1998).

[48] K. C. Nowack, M. Shafiei, M. Laforest, G. E. D. K. Prawiroatmodjo, L. R. Schreiber, C. Reichl, W. Wegscheider, and L. M. K. Vandersypen, *Single-shot correlations and two-qubit gate of solid-state spins,* Science **333**, 1269 (2011).

[49] T. Hensgens, T. Fujita, L. Janssen, X. Li, C. J. Van Diepen, C. Reichl, W. Wegscheider, S. Das Sarma, and L. M. K. Vandersypen, *Quantum simulation of a fermi–hubbard model using a semiconductor quantum dot array,* Nature **548**, 70 (2017).

[50] C. Volk, A. M. J. Zwerver, U. Mukhopadhyay, P. T. Eendebak, C. J. van Diepen, J. P. Dehollain, T. Hensgens, T. Fujita, C. Reichl, W. Wegscheider, and L. M. K. Vandersypen, *Loading a quantum-dot based "qubyte" register,* npj Quantum Information **5**, 29 (2019).

[51] A. R. Mills, D. M. Zajac, M. J. Gullans, F. J. Schupp, T. M. Hazard, and J. R. Petta, *Shuttling a single charge across a one-dimensional array of silicon quantum dots,* Nature Communications **10**, 1063 (2019).

[52] S. F. Neyens, E. MacQuarrie, J. Dodson, J. Corrigan, N. Holman, B. Thorgrimsson, M. Palma, T. McJunkin, L. Edge, M. Friesen, S. Coppersmith, and M. Eriksson, *Measurements of capacitive coupling within a quadruple-quantum-dot array,* Phys. Rev. Applied **12**, 064049 (2019).

[53] T.-K. Hsiao, C. van Diepen, U. Mukhopadhyay, C. Reichl, W. Wegscheider, and L. Vandersypen, *Efficient orthogonal control of tunnel couplings in a quantum dot array,* Phys. Rev. Applied **13**, 054018 (2020).

[54] H. Qiao, Y. P. Kandel, K. Deng, S. Fallahi, G. C. Gardner, M. J. Manfra, E. Barnes, and J. M. Nichol, *Coherent multispin exchange coupling in a quantum-dot spin chain,* Phys. Rev. X **10**, 031006 (2020).

[55] A. K. Hüttel, S. Ludwig, H. Lorenz, K. Eberl, and J. P. Kotthaus, *Direct control of the tunnel splitting in a one-electron double quantum dot,* Phys. Rev. B **72**, 081310 (2005).

[56] L. DiCarlo, H. J. Lynch, A. C. Johnson, L. I. Childress, K. Crockett, C. M. Marcus, M. P. Hanson, and A. C. Gossard, *Differential charge sensing and charge delocalization in a tunable double quantum dot,* Phys. Rev. Lett. **92**, 226801 (2004).

[57] T. Hayashi, T. Fujisawa, H. D. Cheong, Y. H. Jeong, and Y. Hirayama, *Coherent manipulation of electronic states in a double quantum dot,* Phys. Rev. Lett. **91**, 226804 (2003).

[58] K. D. Petersson, J. R. Petta, H. Lu, and A. C. Gossard, *Quantum coherence in a one-electron semiconductor charge qubit,* Phys. Rev. Lett. **105**, 246804 (2010).

[59] Z. Shi, C. B. Simmons, D. R. Ward, J. R. Prance, R. T. Mohr, T. S. Koh, J. K. Gamble, X. Wu, D. E. Savage, M. G. Lagally, M. Friesen, S. N. Coppersmith, and M. A. Eriksson, *Coherent quantum oscillations and echo measurements of a si charge qubit,* Phys. Rev. B **88**, 075416 (2013).

[60] P. Scarlino, D. J. van Woerkom, A. Stockklauser, J. V. Koski, M. C. Collodo, S. Gasparinetti, C. Reichl, W. Wegscheider, T. Ihn, K. Ensslin, and A. Wallraff, *All-microwave control and dispersive readout of gate-defined quantum dot qubits in circuit quantum electrodynamics,* Phys. Rev. Lett. **122**, 206802 (2019).

[61] M. Field, C. G. Smith, M. Pepper, D. A. Ritchie, J. E. F. Frost, G. A. C. Jones, and D. G. Hasko, *Measurements of coulomb blockade with a noninvasive voltage probe,* Phys. Rev. Lett. **70**, 1311 (1993).

[62] J. M. Elzerman, R. Hanson, J. S. Greidanus, L. H. Willems van Beveren, S. De Franceschi, L. M. K. Vandersypen, S. Tarucha, and L. P. Kouwenhoven, *Few-electron quantum dot circuit with integrated charge read out,* Phys. Rev. B **67**, 161308 (2003).

**2**

[63] M. Friesen, M. A. Eriksson,  and S. N. Coppersmith, *Magnetic field dependence of valley splitting in realistic si□sige quantum wells,* Applied Physics Letters **89**, 202106 (2006).

[64] M. Friesen, S. Chutia, C. Tahan,  and S. N. Coppersmith, *Valley splitting theory of* SiGe / Si / SiGe *quantum wells,* Phys. Rev. B **75**, 115318 (2007).

[65] E. Kawakami, P. Scarlino, D. R. Ward, F. R. Braakman, D. E. Savage, M. G. Lagally, M. Friesen, S. N. Coppersmith, M. A. Eriksson,  and L. M. K. Vandersypen, *Electrical control of a long-lived spin qubit in a si/sige quantum dot,* Nature Nanotechnology **9**, 666 (2014).

[66] M. G. Borselli, R. S. Ross, A. A. Kiselev, E. T. Croke, K. S. Holabird, P. W. Deelman, L. D. Warren, I. Alvarado-Rodriguez, I. Milosavljevic, F. C. Ku, W. S. Wong, A. E. Schmitz, M. Sokolich, M. F. Gyure,  and A. T. Hunter, *Measurement of valley splitting in high-symmetry si/sige quantum dots,* Applied Physics Letters **98**, 123118 (2011).

[67] M. G. Borselli, K. Eng, E. T. Croke, B. M. Maune, B. Huang, R. S. Ross, A. A. Kiselev, P. W. Deelman, I. Alvarado-Rodriguez, A. E. Schmitz, M. Sokolich, K. S. Holabird, T. M. Hazard, M. F. Gyure,  and A. T. Hunter, *Pauli spin blockade in undoped si/sige two-electron double quantum dots,* Applied Physics Letters **99**, 063109 (2011).

[68] Z. Shi, C. B. Simmons, J. R. Prance, J. King Gamble, M. Friesen, D. E. Savage, M. G. Lagally, S. N. Coppersmith,  and M. A. Eriksson, *Tunable singlet-triplet splitting in a few-electron si/sige quantum dot,* Applied Physics Letters **99**, 233108 (2011).

[69] J. R. Prance, Z. Shi, C. B. Simmons, D. E. Savage, M. G. Lagally, L. R. Schreiber, L. M. K. Vandersypen, M. Friesen, R. Joynt, S. N. Coppersmith,  and M. A. Eriksson, *Single-shot measurement of triplet-singlet relaxation in a* Si/SiGe *double quantum dot,* Phys. Rev. Lett. **108**, 046808 (2012).

[70] D. M. Zajac, T. M. Hazard, X. Mi, K. Wang,  and J. R. Petta, *A reconfigurable gate architecture for si/sige quantum dots,* Applied Physics Letters **106**, 223507 (2015).

[71] X. Mi, C. G. Péterfalvi, G. Burkard,  and J. R. Petta, *High-resolution valley spectroscopy of si quantum dots,* Phys. Rev. Lett. **119**, 176803 (2017).

[72] A. Hollmann, T. Struck, V. Langrock, A. Schmidbauer, F. Schauer, T. Leonhardt, K. Sawano, H. Riemann, N. V. Abrosimov, D. Bougeard,  and L. R. Schreiber, *Large, tunable valley splitting and single-spin relaxation mechanisms in a* Si/si$_x$ ge$_{1-x}$ *quantum dot,* Phys. Rev. Applied **13**, 034068 (2020).

[73] C. H. Yang, W. H. Lim, N. S. Lai, A. Rossi, A. Morello,  and A. S. Dzurak, *Orbital and valley state spectra of a few-electron silicon quantum dot,* Phys. Rev. B **86**, 115319 (2012).

[74] C. H. Yang, A. Rossi, R. Ruskov, N. S. Lai, F. A. Mohiyaddin, S. Lee, C. Tahan, G. Klimeck, A. Morello, and A. S. Dzurak, *Spin-valley lifetimes in a silicon quantum dot with tunable valley splitting,* Nature Communications **4**, 2069 (2013).

[75] L. Petit, J. M. Boter, H. G. J. Eenink, G. Droulers, M. L. V. Tagliaferri, R. Li, D. P. Franke, K. J. Singh, J. S. Clarke, R. N. Schouten, V. V. Dobrovitski, L. M. K. Vandersypen, and M. Veldhorst, *Spin lifetime and charge noise in hot silicon quantum dot qubits,* Phys. Rev. Lett. **121**, 076801 (2018).

[76] S. F. Neyens, R. H. Foote, B. Thorgrimsson, T. J. Knapp, T. McJunkin, L. M. K. Vandersypen, P. Amin, N. K. Thomas, J. S. Clarke, D. E. Savage, M. G. Lagally, M. Friesen, S. N. Coppersmith, and M. A. Eriksson, *The critical role of substrate disorder in valley splitting in si quantum wells,* Applied Physics Letters **112**, 243107 (2018).

[77] A. Hosseinkhani and G. Burkard, *Electromagnetic control of valley splitting in ideal and disordered si quantum dots,* (2020), arXiv:2007.00332 [cond-mat.mes-hall] .

[78] L. Petit, H. G. J. Eenink, M. Russ, W. I. L. Lawrie, N. W. Hendrickx, S. G. J. Philips, J. S. Clarke, L. M. K. Vandersypen, and M. Veldhorst, *Universal quantum logic in hot silicon qubits,* Nature **580**, 355 (2020).

[79] C. H. Yang, R. C. C. Leon, J. C. C. Hwang, A. Saraiva, T. Tanttu, W. Huang, J. Camirand Lemyre, K. W. Chan, K. Y. Tan, F. E. Hudson, K. M. Itoh, A. Morello, M. Pioro-Ladrière, A. Laucht, and A. S. Dzurak, *Operation of a silicon quantum processor unit cell above one kelvin,* Nature **580**, 350 (2020).

[80] A. Chatterjee, P. Stevenson, S. D. Franceschi, A. Morello, N. de Leon, and F. Kuemmeth, *Semiconductor qubits in practice,* (2020), arXiv:2005.06564 [cond-mat.mes-hall] .

[81] D. Loss and D. P. DiVincenzo, *Quantum computation with quantum dots,* Phys. Rev. A **57**, 120 (1998).

[82] D. P. DiVincenzo, *The physical implementation of quantum computation,* Fortschritte der Physik **48**, 771 (2000).

[83] A. G. Fowler, M. Mariantoni, J. M. Martinis, and A. N. Cleland, *Surface codes: Towards practical large-scale quantum computation,* Phys. Rev. A **86**, 032324 (2012).

[84] V. Srinivasa, K. C. Nowack, M. Shafiei, L. M. K. Vandersypen, and J. M. Taylor, *Simultaneous spin-charge relaxation in double quantum dots,* Phys. Rev. Lett. **110**, 196803 (2013).

**2**

[85] F. H. L. Koppens, C. Buizert, K. J. Tielrooij, I. T. Vink, K. C. Nowack, T. Meunier, L. P. Kouwenhoven, and L. M. K. Vandersypen, *Driven coherent oscillations of a single electron spin in a quantum dot,* Nature **442**, 766 (2006).

[86] K. C. Nowack, F. H. L. Koppens, Y. V. Nazarov, and L. M. K. Vandersypen, *Coherent control of a single electron spin with electric fields,* Science **318**, 1430 (2007).

[87] Y. Tokura, W. G. van der Wiel, T. Obata, and S. Tarucha, *Coherent single electron spin control in a slanting zeeman field,* Phys. Rev. Lett. **96**, 047202 (2006).

[88] M. Pioro-Ladrière, Y. Tokura, T. Obata, T. Kubo, and S. Tarucha, *Micromagnets for coherent control of spin-charge qubit in lateral quantum dots,* Applied Physics Letters **90**, 024105 (2007).

[89] M. Pioro-Ladrière, T. Obata, Y. Tokura, Y.-S. Shin, T. Kubo, K. Yoshida, T. Taniyama, and S. Tarucha, *Electrically driven single-electron spin resonance in a slanting zeeman field,* Nature Physics **4**, 776 (2008).

[90] M. Veldhorst, J. C. C. Hwang, C. H. Yang, A. W. Leenstra, B. de Ronde, J. P. Dehollain, J. T. Muhonen, F. E. Hudson, K. M. Itoh, A. Morello, and A. S. Dzurak, *An addressable quantum dot qubit with fault-tolerant control-fidelity,* Nature Nanotechnology **9**, 981 (2014).

[91] J. Yoneda, K. Takeda, T. Otsuka, T. Nakajima, M. R. Delbecq, G. Allison, T. Honda, T. Kodera, S. Oda, Y. Hoshi, N. Usami, K. M. Itoh, and S. Tarucha, *A quantum-dot spin qubit with coherence limited by charge noise and fidelity higher than 99.9%,* Nature Nanotechnology **13**, 102 (2018).

[92] T. Meunier, V. E. Calado, and L. M. K. Vandersypen, *Efficient controlled-phase gate for single-spin qubits in quantum dots,* Phys. Rev. B **83**, 121403 (2011).

[93] L. Petit, M. Russ, H. G. J. Eenink, W. I. L. Lawrie, J. S. Clarke, L. M. K. Vandersypen, and M. Veldhorst, *High-fidelity two-qubit gates in silicon above one kelvin,* (2020), arXiv:2007.09034 [cond-mat.mes-hall] .

[94] M. Veldhorst, C. H. Yang, J. C. C. Hwang, W. Huang, J. P. Dehollain, J. T. Muhonen, S. Simmons, A. Laucht, F. E. Hudson, K. M. Itoh, A. Morello, and A. S. Dzurak, *A two-qubit logic gate in silicon,* Nature **526**, 410 (2015).

[95] T. F. Watson, S. G. J. Philips, E. Kawakami, D. R. Ward, P. Scarlino, M. Veldhorst, D. E. Savage, M. G. Lagally, M. Friesen, S. N. Coppersmith, M. A. Eriksson, and L. M. K. Vandersypen, *A programmable two-qubit quantum processor in silicon,* Nature **555**, 633 (2018).

[96] D. M. Zajac, A. J. Sigillito, M. Russ, F. Borjans, J. M. Taylor, G. Burkard, and J. R. Petta, *Resonantly driven cnot gate for electron spins,* Science **359**, 439 (2018).

[97] X. Xue, T. F. Watson, J. Helsen, D. R. Ward, D. E. Savage, M. G. Lagally, S. N. Coppersmith, M. A. Eriksson, S. Wehner, and L. M. K. Vandersypen, *Benchmarking gate fidelities in a* $\mathrm{Si/SiGe}$ *two-qubit device,* Phys. Rev. X **9**, 021011 (2019).

[98] W. Huang, C. H. Yang, K. W. Chan, T. Tanttu, B. Hensen, R. C. C. Leon, M. A. Fogarty, J. C. C. Hwang, F. E. Hudson, K. M. Itoh, A. Morello, A. Laucht, and A. S. Dzurak, *Fidelity benchmarks for two-qubit gates in silicon,* Nature **569**, 532 (2019).

[99] A. V. Khaetskii and Y. V. Nazarov, *Spin-flip transitions between zeeman sublevels in semiconductor quantum dots,* Phys. Rev. B **64**, 125316 (2001).

[100] A. V. Khaetskii and Y. V. Nazarov, *Spin relaxation in semiconductor quantum dots,* Phys. Rev. B **61**, 12639 (2000).

[101] L. M. Woods, T. L. Reinecke, and Y. Lyanda-Geller, *Spin relaxation in quantum dots,* Phys. Rev. B **66**, 161318 (2002).

[102] F. Borjans, D. Zajac, T. Hazard, and J. Petta, *Single-spin relaxation in a synthetic spin-orbit field,* Phys. Rev. Applied **11**, 044063 (2019).

[103] J. Levy, *Universal quantum computation with spin-*$1/2$ *pairs and heisenberg exchange,* Phys. Rev. Lett. **89**, 147902 (2002).

[104] Z. Shi, C. B. Simmons, J. R. Prance, J. K. Gamble, T. S. Koh, Y.-P. Shim, X. Hu, D. E. Savage, M. G. Lagally, M. A. Eriksson, M. Friesen, and S. N. Coppersmith, *Fast hybrid silicon double-quantum-dot qubit,* Phys. Rev. Lett. **108**, 140503 (2012).

[105] D. Kim, Z. Shi, C. B. Simmons, D. R. Ward, J. R. Prance, T. S. Koh, J. K. Gamble, D. E. Savage, M. G. Lagally, M. Friesen, S. N. Coppersmith, and M. A. Eriksson, *Quantum control and process tomography of a semiconductor quantum dot hybrid qubit,* Nature **511**, 70 (2014).

[106] D. Kim, D. R. Ward, C. B. Simmons, D. E. Savage, M. G. Lagally, M. Friesen, S. N. Coppersmith, and M. A. Eriksson, *High-fidelity resonant gating of a silicon-based quantum dot hybrid qubit,* npj Quantum Information **1**, 15004 (2015).

[107] D. P. DiVincenzo, D. Bacon, J. Kempe, G. Burkard, and K. B. Whaley, *Universal quantum computation with the exchange interaction,* Nature **408**, 339 (2000).

[108] J. Medford, J. Beil, J. M. Taylor, E. I. Rashba, H. Lu, A. C. Gossard, and C. M. Marcus, *Quantum-dot-based resonant exchange qubit,* Phys. Rev. Lett. **111**, 050501 (2013).

**2**

[109] K. Eng, T. D. Ladd, A. Smith, M. G. Borselli, A. A. Kiselev, B. H. Fong, K. S. Holabird, T. M. Hazard, B. Huang, P. W. Deelman, I. Milosavljevic, A. E. Schmitz, R. S. Ross, M. F. Gyure, and A. T. Hunter, *Isotopically enhanced triple-quantum-dot qubit,* Science Advances **1** (2015), 10.1126/sciadv.1500214.

[110] M. Russ, J. R. Petta, and G. Burkard, *Quadrupolar exchange-only spin qubit,* Phys. Rev. Lett. **121**, 177701 (2018).

[111] L. M. K. Vandersypen, J. M. Elzerman, R. N. Schouten, L. H. Willems van Beveren, R. Hanson, and L. P. Kouwenhoven, *Real-time detection of single-electron tunneling using a quantum point contact,* Applied Physics Letters **85**, 4394 (2004).

[112] D. J. Reilly, C. M. Marcus, M. P. Hanson, and A. C. Gossard, *Fast single-charge sensing with a rf quantum point contact,* Applied Physics Letters **91**, 162101 (2007).

[113] C. Barthel, D. J. Reilly, C. M. Marcus, M. P. Hanson, and A. C. Gossard, *Rapid single-shot measurement of a singlet-triplet qubit,* Phys. Rev. Lett. **103**, 160503 (2009).

[114] A. Noiri, K. Takeda, J. Yoneda, T. Nakajima, T. Kodera, and S. Tarucha, *Radio-frequency-detected fast charge sensing in undoped silicon quantum dots,* Nano Letters **20**, 947 (2020), pMID: 31944116.

[115] E. J. Connors, J. Nelson, and J. M. Nichol, *Rapid high-fidelity spin-state readout in* $Si/Si\text{-}Ge$ *quantum dots via rf reflectometry,* Phys. Rev. Applied **13**, 024019 (2020).

[116] C. Volk, A. Chatterjee, F. Ansaloni, C. M. Marcus, and F. Kuemmeth, *Fast charge sensing of si/sige quantum dots via a high-frequency accumulation gate,* Nano Letters **19**, 5628 (2019), pMID: 31339321.

[117] J. M. Elzerman, R. Hanson, L. H. Willems van Beveren, B. Witkamp, L. M. K. Vandersypen, and L. P. Kouwenhoven, *Single-shot read-out of an individual electron spin in a quantum dot,* Nature **430**, 431 (2004).

[118] T. A. Baart, M. Shafiei, T. Fujita, C. Reichl, W. Wegscheider, and L. M. K. Vandersypen, *Single-spin ccd,* Nature Nanotechnology **11**, 330 (2016).

[119] C. J. van Diepen, T. K. Hsiao, U. Mukhopadhyay, C. Reichl, W. Wegscheider, and L. M. K. Vandersypen, *Electron cascade for spin readout,* (2020), arXiv:2002.08925 [cond-mat.mes-hall] .

[120] A. Seedhouse, T. Tanttu, R. C. C. Leon, R. Zhao, K. Y. Tan, B. Hensen, F. E. Hudson, K. M. Itoh, J. Yoneda, C. H. Yang, A. Morello, A. Laucht, S. N. Coppersmith, A. Saraiva, and A. S. Dzurak, *Parity readout of silicon spin qubits in quantum dots,* (2020), arXiv:2004.07078 [quant-ph] .

**2**

[121] P. Harvey-Collard, B. D'Anjou, M. Rudolph, N. T. Jacobson, J. Dominguez, G. A. Ten Eyck, J. R. Wendt, T. Pluym, M. P. Lilly, W. A. Coish, M. Pioro-Ladrière,  and M. S. Carroll, *High-fidelity single-shot readout for a spin qubit via an enhanced latching mechanism,* Phys. Rev. X **8**, 021046 (2018).

[122] K. D. Petersson, C. G. Smith, D. Anderson, P. Atkinson, G. A. C. Jones,  and D. A. Ritchie, *Charge and spin state readout of a double quantum dot coupled to a resonator,* Nano Letters **10**, 2789 (2010), pMID: 20698590.

[123] S. J. Chorley, J. Wabnig, Z. V. Penfold-Fitch, K. D. Petersson, J. Frake, C. G. Smith,  and M. R. Buitelaar, *Measuring the complex admittance of a carbon nanotube double quantum dot,* Phys. Rev. Lett. **108**, 036802 (2012).

[124] M. D. Schroer, M. Jung, K. D. Petersson,  and J. R. Petta, *Radio frequency charge parity meter,* Phys. Rev. Lett. **109**, 166804 (2012).

[125] J. I. Colless, A. C. Mahoney, J. M. Hornibrook, A. C. Doherty, H. Lu, A. C. Gossard,  and D. J. Reilly, *Dispersive readout of a few-electron double quantum dot with fast rf gate sensors,* Phys. Rev. Lett. **110**, 046805 (2013).

[126] A. Rossi, R. Zhao, A. S. Dzurak,  and M. F. Gonzalez-Zalba, *Dispersive readout of a silicon quantum dot with an accumulation-mode gate sensor,* Applied Physics Letters **110**, 212101 (2017).

[127] M. F. Gonzalez-Zalba, S. Barraud, A. J. Ferguson,  and A. C. Betz, *Probing the limits of gate-based charge sensing,* Nature Communications **6**, 6084 (2015).

[128] A. C. Betz, R. Wacquez, M. Vinet, X. Jehl, A. L. Saraiva, M. Sanquer, A. J. Ferguson,  and M. F. Gonzalez-Zalba, *Dispersively detected pauli spin-blockade in a silicon nanowire field-effect transistor,* Nano Letters **15**, 4622 (2015).

[129] M. G. House, T. Kobayashi, B. Weber, S. J. Hile, T. F. Watson, J. van der Heijden, S. Rogge,  and M. Y. Simmons, *Radio frequency measurements of tunnel couplings and singlet-triplet spin states in si:p quantum dots,* Nature Communications **6**, 8848 (2015).

[130] A. Cottet, C. Mora,  and T. Kontos, *Mesoscopic admittance of a double quantum dot,* Phys. Rev. B **83**, 121311 (2011).

[131] S. Park, C. Metzger, L. Tosi, M. F. Goffman, C. Urbina, H. Pothier,  and A. L. Yeyati, *From adiabatic to dispersive readout of quantum circuits,* Phys. Rev. Lett. **125**, 077701 (2020).

[132] R. Mizuta, R. M. Otxoa, A. C. Betz,  and M. F. Gonzalez-Zalba, *Quantum and tunneling capacitance in charge and spin qubits,* Phys. Rev. B **95**, 045414 (2017).

[133] P. Pakkiam, A. V. Timofeev, M. G. House, M. R. Hogg, T. Kobayashi, M. Koch, S. Rogge,  and M. Y. Simmons, *Single-shot single-gate rf spin readout in silicon,* Phys. Rev. X **8**, 041032 (2018).

[134] A. West, B. Hensen, A. Jouan, T. Tanttu, C.-H. Yang, A. Rossi, M. F. Gonzalez-Zalba, F. Hudson, A. Morello, D. J. Reilly,  and A. S. Dzurak, *Gate-based single-shot readout of spins in silicon,* Nature Nanotechnology **14**, 437 (2019).

[135] M. Urdampilleta, D. J. Niegemann, E. Chanrion, B. Jadot, C. Spence, P.-A. Mortemousque, C. Bäuerle, L. Hutin, B. Bertrand, S. Barraud, R. Maurand, M. Sanquer, X. Jehl, S. De Franceschi, M. Vinet,  and T. Meunier, *Gate-based high fidelity spin readout in a cmos device,* Nature Nanotechnology **14**, 737 (2019).

[136] M. R. Delbecq, V. Schmitt, F. D. Parmentier, N. Roch, J. J. Viennot, G. Fève, B. Huard, C. Mora, A. Cottet,  and T. Kontos, *Coupling a quantum dot, fermionic leads, and a microwave cavity on a chip,* Phys. Rev. Lett. **107**, 256804 (2011).

[137] T. Frey, P. J. Leek, M. Beck, A. Blais, T. Ihn, K. Ensslin,  and A. Wallraff, *Dipole coupling of a double quantum dot to a microwave resonator,* Phys. Rev. Lett. **108**, 046807 (2012).

[138] K. D. Petersson, L. W. McFaul, M. D. Schroer, M. Jung, J. M. Taylor, A. A. Houck,  and J. R. Petta, *Circuit quantum electrodynamics with a spin qubit,* Nature **490**, 380 (2012).

[139] J. Stehlik, Y.-Y. Liu, C. M. Quintana, C. Eichler, T. R. Hartke,  and J. R. Petta, *Fast charge sensing of a cavity-coupled double quantum dot using a josephson parametric amplifier,* Phys. Rev. Applied **4**, 014018 (2015).

[140] C. Macklin, K. O'Brien, D. Hover, M. E. Schwartz, V. Bolkhovsky, X. Zhang, W. D. Oliver,  and I. Siddiqi, *A near–quantum-limited josephson traveling-wave parametric amplifier,* Science **350**, 307 (2015), https://science.sciencemag.org/content/350/6258/307.full.pdf .

[141] T. Frey, P. J. Leek, M. Beck, J. Faist, A. Wallraff, K. Ensslin, T. Ihn,  and M. Büttiker, *Quantum dot admittance probed at microwave frequencies with an on-chip resonator,* Phys. Rev. B **86**, 115303 (2012).

[142] G. Burkard, M. J. Gullans, X. Mi,  and J. R. Petta, *Superconductor-semiconductor hybrid-circuit quantum electrodynamics,* Nature Reviews Physics  (2020), 10.1038/s42254-019-0135-2.

[143] M. Benito and G. Burkard, *Hybrid superconductor-semiconductor systems for quantum technology,*  (2020), arXiv:2005.00030 [cond-mat.mes-hall] .

[144] A. Imamoğlu, *Cavity qed based on collective magnetic dipole coupling: Spin ensembles as hybrid two-level systems,* Phys. Rev. Lett. **102**, 083602 (2009).

[145] A. Bienfait, J. J. Pla, Y. Kubo, X. Zhou, M. Stern, C. C. Lo, C. D. Weis, T. Schenkel, D. Vion, D. Esteve, J. J. L. Morton,  and P. Bertet, *Controlling spin relaxation with a cavity,* Nature **531**, 74 (2016).

[146] D. I. Schuster, A. P. Sears, E. Ginossar, L. DiCarlo, L. Frunzio, J. J. L. Morton, H. Wu, G. A. D. Briggs, B. B. Buckley, D. D. Awschalom, and R. J. Schoelkopf, *High-cooperativity coupling of electron-spin ensembles to superconducting cavities,* Phys. Rev. Lett. **105**, 140501 (2010).

[147] Y. Kubo, F. R. Ong, P. Bertet, D. Vion, V. Jacques, D. Zheng, A. Dréau, J.-F. Roch, A. Auffeves, F. Jelezko, J. Wrachtrup, M. F. Barthe, P. Bergonzo, and D. Esteve, *Strong coupling of a spin ensemble to a superconducting resonator,* Phys. Rev. Lett. **105**, 140502 (2010).

[148] R. Amsüss, C. Koller, T. Nöbauer, S. Putz, S. Rotter, K. Sandner, S. Schneider, M. Schramböck, G. Steinhauser, H. Ritsch, J. Schmiedmayer, and J. Majer, *Cavity qed with magnetically coupled collective spin states,* Phys. Rev. Lett. **107**, 060502 (2011).

[149] L. M. K. Vandersypen and M. A. Eriksson, *Quantum computing with semiconductor spins,* Physics Today **71**, 38 (2019).

[150] L. Childress, A. S. Sørensen, and M. D. Lukin, *Mesoscopic cavity quantum electrodynamics with quantum dots,* Phys. Rev. A **69**, 042302 (2004).

[151] M. Trif, V. N. Golovach, and D. Loss, *Spin dynamics in inas nanowire quantum dots coupled to a transmission line,* Phys. Rev. B **77**, 045434 (2008).

[152] A. Cottet and T. Kontos, *Spin quantum bit with ferromagnetic contacts for circuit qed,* Phys. Rev. Lett. **105**, 160502 (2010).

[153] X. Hu, Y.-x. Liu, and F. Nori, *Strong coupling of a spin qubit to a superconducting stripline cavity,* Phys. Rev. B **86**, 035314 (2012).

[154] G. Burkard and A. Imamoglu, *Ultra-long-distance interaction between spin qubits,* Phys. Rev. B **74**, 041307 (2006).

[155] P.-Q. Jin, M. Marthaler, A. Shnirman, and G. Schön, *Strong coupling of spin qubits to a transmission line resonator,* Phys. Rev. Lett. **108**, 190506 (2012).

[156] M. Russ and G. Burkard, *Long distance coupling of resonant exchange qubits,* Phys. Rev. B **92**, 205412 (2015).

[157] V. Srinivasa, J. M. Taylor, and C. Tahan, *Entangling distant resonant exchange qubits via circuit quantum electrodynamics,* Phys. Rev. B **94**, 205421 (2016).

[158] J. C. Abadillo-Uriel, M. A. Eriksson, S. N. Coppersmith, and M. Friesen, *Enhancing the dipolar coupling of a s-t0 qubit with a transverse sweet spot,* Nature Communications **10**, 5641 (2019).

[159] F. Beaudoin, D. Lachance-Quirion, W. A. Coish, and M. Pioro-Ladrière, *Coupling a single electron spin to a microwave resonator: controlling transverse and longitudinal couplings,* Nanotechnology **27**, 464003 (2016).

**2**

[160] M. Benito, X. Mi, J. M. Taylor, J. R. Petta, and G. Burkard, *Input-output theory for spin-photon coupling in si double quantum dots,* Phys. Rev. B **96**, 235434 (2017).

[161] M. Benito, J. R. Petta, and G. Burkard, *Optimized cavity-mediated dispersive two-qubit gates between spin qubits,* Phys. Rev. B **100**, 081412 (2019).

[162] A. Stockklauser, P. Scarlino, J. V. Koski, S. Gasparinetti, C. K. Andersen, C. Reichl, W. Wegscheider, T. Ihn, K. Ensslin, and A. Wallraff, *Strong coupling cavity qed with gate-defined double quantum dots enabled by a high impedance resonator,* Phys. Rev. X **7**, 011030 (2017).

[163] G.-W. Deng, D. Wei, J. R. Johansson, M.-L. Zhang, S.-X. Li, H.-O. Li, G. Cao, M. Xiao, T. Tu, G.-C. Guo, H.-W. Jiang, F. Nori, and G.-P. Guo, *Charge number dependence of the dephasing rates of a graphene double quantum dot in a circuit qed architecture,* Phys. Rev. Lett. **115**, 126804 (2015).

[164] G.-W. Deng, D. Wei, S.-X. Li, J. R. Johansson, W.-C. Kong, H.-O. Li, G. Cao, M. Xiao, G.-C. Guo, F. Nori, H.-W. Jiang, and G.-P. Guo, *Coupling two distant double quantum dots with a microwave resonator,* Nano Letters **15**, 6620 (2015).

[165] J. J. Viennot, M. R. Delbecq, M. C. Dartiailh, A. Cottet, and T. Kontos, *Out-of-equilibrium charge dynamics in a hybrid circuit quantum electrodynamics architecture,* Phys. Rev. B **89**, 165404 (2014).

[166] J. Basset, D.-D. Jarausch, A. Stockklauser, T. Frey, C. Reichl, W. Wegscheider, T. M. Ihn, K. Ensslin, and A. Wallraff, *Single-electron double quantum dot dipole-coupled to a single photonic mode,* Phys. Rev. B **88**, 125312 (2013).

[167] A. Stockklauser, V. F. Maisi, J. Basset, K. Cujia, C. Reichl, W. Wegscheider, T. Ihn, A. Wallraff, and K. Ensslin, *Microwave emission from hybridized states in a semiconductor charge qubit,* Phys. Rev. Lett. **115**, 046802 (2015).

[168] E. J. Connors, J. Nelson, H. Qiao, L. F. Edge, and J. M. Nichol, *Low-frequency charge noise in si/sige quantum dots,* Phys. Rev. B **100**, 165305 (2019).

[169] X. Mi, J. V. Cady, D. M. Zajac, P. W. Deelman, and J. R. Petta, *Strong coupling of a single electron in silicon to a microwave photon,* Science **355**, 156 (2017).

[170] L. E. Bruhat, T. Cubaynes, J. J. Viennot, M. C. Dartiailh, M. M. Desjardins, A. Cottet, and T. Kontos, *Circuit qed with a quantum-dot charge qubit dressed by cooper pairs,* Phys. Rev. B **98**, 155313 (2018).

[171] A. J. Landig, J. V. Koski, P. Scarlino, U. C. Mendes, A. Blais, C. Reichl, W. Wegscheider, A. Wallraff, K. Ensslin, and T. Ihn, *Coherent spin-photon coupling using a resonant exchange qubit,* Nature **560**, 179 (2018).

[172] N. Samkharadze, G. Zheng, N. Kalhor, D. Brousse, A. Sammak, U. C. Mendes, A. Blais, G. Scappucci,  and L. M. K. Vandersypen, *Strong spin-photon coupling in silicon,* Science **359**, 1123 (2018).

[173] X. Mi, M. Benito, S. Putz, D. M. Zajac, J. M. Taylor, G. Burkard,  and J. R. Petta, *A coherent spin-photon interface in silicon,* Nature **555**, 599 (2018).

**2**

# 3

# Device architecture and experimental methods

*The uglier the device,*
*the better it performs.*

Guoji Zheng

*The first part of this chapter describes the design and fabrication of the devices measured in Chap. 4 and 5. The second part elaborates on the room temperature and cryogenic experimental setups, as well as the measurement techniques used to obtain the experimental results presented in the subsequent chapters.*

## **3.1.** Device design

The devices reported in Chap. 4 and 5 are from the same fabrication batch. Images of one of those devices are shown and explained in Fig. 3.1.

### **3.1.1.** Device functionality

We work with a silicon/silicon-germanium (Si/SiGe) heterostructure in conjunction with a single-layer gate architecture. This architecture offers full control over the DQD confinement potential, while greatly simplifying the fabrication process (at least for the part concerning the DQD). The dots are formed in the quantum well underneath the resonator (Res) gates as indicated by the black dotted circles in Fig. 3.1c. The paddle shape at the end of the Res gates is there with the intention to increase the lever arm to the dots[1]. The Fermi reservoirs that function as source and drain of electrons for the DQD are accumulated underneath accumulation gates LAcc and RAcc (white crossed boxes). Placing the accumulation gates there enables the DQD to have simultaneously high interdot and reservoir tunnel couplings. Here, high tunnel coupling means that it is within the detection range of the resonator (typically from a few to tens of GHz). Previous designs where the accumulation gates were placed left and right of the DQD showed either high interdot or high reservoir tunnel coupling, but not both at the same time. The left and right plungers (LP and RP) are used to control the electron occupation[2]. The tunnel rates to the Fermi reservoirs are controlled by the left and right barriers (LB and RB), while the T and TT gates control the interdot tunnel rate. The gates LResD and RResD act as depletion gates to prevent electrons accumulating underneath the long arms of the resonator gates. It is worth mentioning that we have not observed any device failures due to electrostatic discharge (ESD) of the gates with the single-layer architecture, possibly because there is no (intentional) gate dielectric underneath the gates outside the DQD region. This way, the gates are shorted to each other at room temperature through the Si/SiGe heterostructure, albeit with some resistance.

We use a high-impedance resonator based on the kinetic inductance of a nanowire made of a highly disordered superconductor. Nanowire resonators have been tested separately in Ref. [1], and their design is shown in Fig. 3.1g,h,i,j. The connection between the resonator and the DQD fine gates is made via large Au pads that bridge a mesa etched region (Fig. 3.1b). The large contact area between the NbTiN and Au is to reduce the contact resistance which could degrade the resonator's performance.

### **3.1.2.** Device fabrication

The device was fabricated on an undoped Si/SiGe heterostructure grown by reduced-pressure chemical vapour on a n-type Si(100) substrate. The Si/SiGe heterostructure comprises a 900 nm thick linearly graded $Si_{1-x}Ge_x$ layer, followed by a 300 nm

---

[1]The lever arm of a Res gate to its dot underneath and the differential lever arm are $\alpha_{\mathrm{Res}} \approx 200\,\mu eV\,mV^{-1}$ and $\beta_{\mathrm{Res}} \approx 115\,\mu eV\,mV^{-1}$, respectively. These lever arms were estimated using bias triangles in later devices with independent control of the two Res gates.

[2]The lever arm of the LP (RP) gate to the left (right) dot and the differential lever arm are typically $\alpha_{\mathrm{LP/RP}} \approx 30\,\mu eV\,mV^{-1}$ and $\beta_{\mathrm{LP/RP}} \approx 15\,\mu eV\,mV^{-1}$, respectively.

**3**
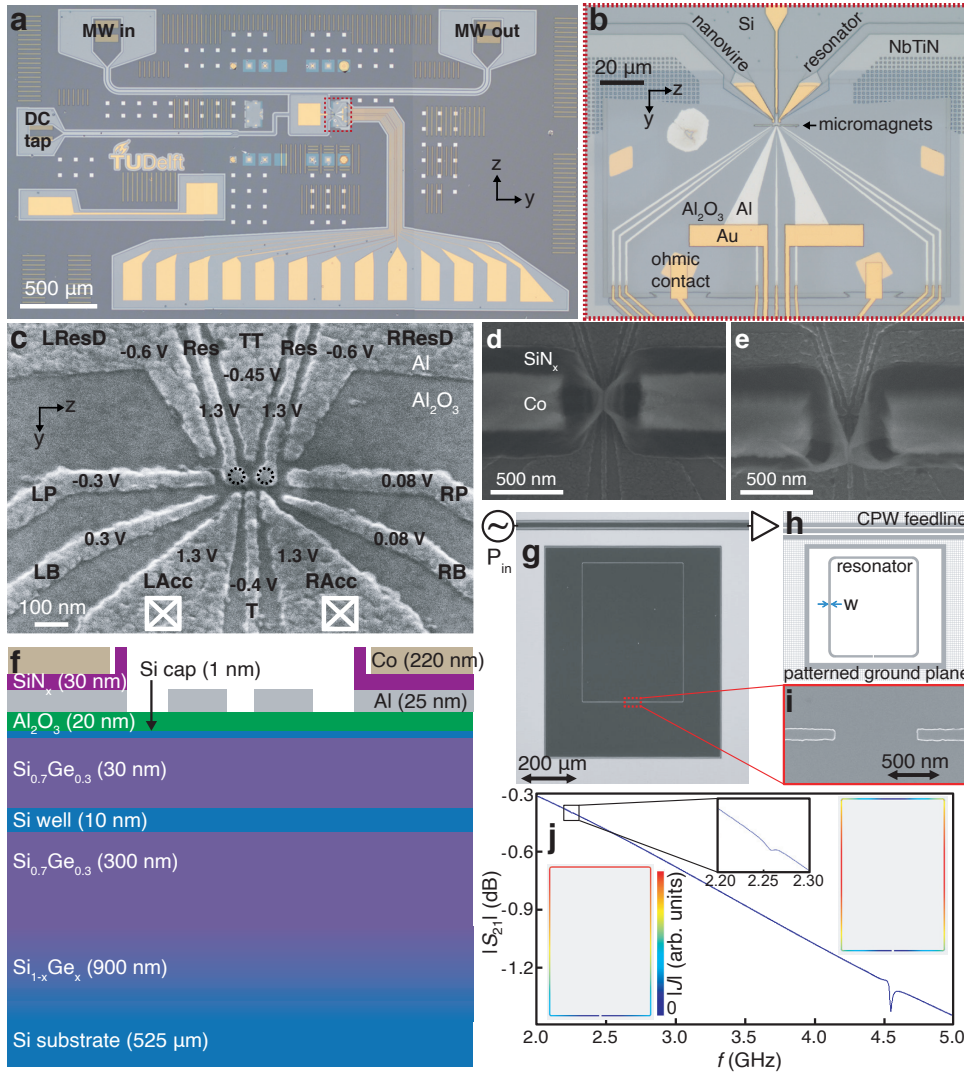
Figure 3.1: **Device images and resonator design**. **a** Optical micrograph of the entire device showing a microwave feedline (top), superconducting resonator (center), a double quantum dot with bond pads (right and bottom) and a line to apply a DC bias to the resonator (left). Dark grey areas are NbTiN, light grey the exposed Si surface, and yellow Au pads and lines. **b** Enlargement of the DQD region showing the nanowire resonator on Si connected to Al gates on $Al_2O_3$ via Au pads. Note that the orientation of the image is rotated clockwise by 90° compared to **a**. **c** Scanning electron microscope (SEM) image of the DQD region before the deposition of micromagnets. The grainy material is Al on top of smooth $Al_2O_3$ gate dielectric. The DQD is formed underneath the gates connected to the resonator (Res), indicated by the black dotted circles. Fermi reservoirs of electrons are formed underneath LAcc and RAcc. Typical voltages applied to the gates in the single electron regime are shown. **d** SEM image of a finished device with Co micromagnets on top of $SiN_x$. **e** Angled SEM image of the device showing the position of the micromagnets with respect to the Res gates. **f** Material stack schematic of the device near the DQD region. **g**, **h**, **i** and **j** are adapted from Ref. [1], and show the design and simulation of a test resonator (without DQD). **g** Dark-field image of a typical bare nanowire resonator. **h** Schematic (not to scale) showing the nanowire resonator, CPW feedline, and patterned ground plane. Here, NbTiN is shown in gray and Si substrate is white. **i** SEM enlargement of the ends of the resonator. **j** Simulated feedline transmission for the device in **f**. The insets show the absolute current distributions along the nanowire for the fundamental and second resonance modes, as well as an enlargement of the feedline transmission near the fundamental resonance.

thick relaxed $Si_{0.7}Ge_{0.3}$ layer, a 10 nm thick strained natural Si quantum well, a 30 nm thick $Si_{0.7}Ge_{0.3}$ spacer, and a 1 nm thick Si cap. Ohmic contacts to the quantum well were made by implanting $^{31}P$ donors at certain locations. A mesa etch was performed to isolate the quantum well in the DQD area from that in the rest of the sample. To insulate the gates used to define the quantum dots, 20 nm of $Al_2O_3$ was grown in the dot region with atomic-layer-deposition. Subsequently, the gates were fabricated using electron beam lithography, evaporation and a lift-off process of 25 nm of Al. The Ti/Co (5 nm/220 nm thick) micromagnets were insulated from the gates with a 30 nm thick sputtered $SiN_x$. The micromagnets are 360 nm wide, 10 μm long and separated by 500 nm. The superconducting nanowire resonator (∼100 nm wide), coplanar waveguide feedline and ground planes were fabricated by sputtering a 14 nm thick layer of NbTiN, followed by reactive ion etching in a $SF_6$/He plasma. The gate oxide is removed everywhere except in the DQD area prior to reactive ion etching to reduce dielectric loss. A sheet inductance of $L_S \approx 9.1\,pH/\square$ for the film was estimated.

## 3.2. Measurement setup

### 3.2.1. Printed circuit boards and wire bonding

A printed circuit board (PCB) is used to electrically contact the device to the control and measurement lines in a refrigerator. The two types of PCBs that were used in the experiments as well as how the devices were attached the PCB are discussed below.

#### Resonator PCB

The resonator PCB[3] in Fig. 3.2a was used for quick characterization of resonators. This PCB was originally designed for circuit QED devices with superconducting qubits. It contains eight CPW lines that can be connected to SMP connectors. The sample is placed in the hole in the center of the PCB and glued directly to the copper piece underneath using concentrated PMMA. The PCB consists of three layers, namely a dielectric layer separating the top and bottom copper layers. Vias distributed across the entire PCB connect the two copper layers to ensure a good ground potential. The PCB is usually covered with a copper lid before mounting it in the refrigerator in order to suppress spurious resonances.

#### Hybrid PCB

The hybrid PCB[4] in Fig. 3.2b allows us to operate the DQD while measuring the resonator response. The sample is glued directly on copper in the square hole in the center of the PCB. There are 48 DC lines available on the PCB for applying voltages to the gates and reservoirs. The DC lines are connected to two 51-pin nano-D connectors (Omnetics) on the back of the PCB. The two connectors are shorted to each other and needed to keep the gates on the device shorted during

---

[3]This PCB was designed in the Dicarlo lab at QuTech.
[4]This PCB was designed in collaboration with Raymond Schouten, Rogier van den Berg and Hans van der Does.
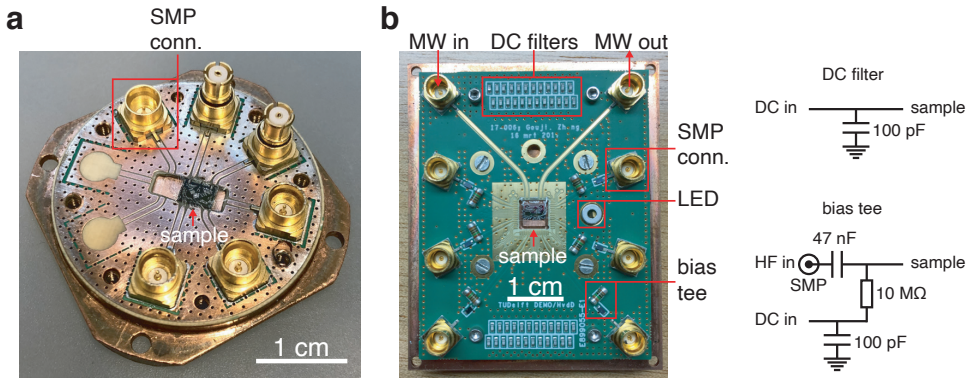
Figure 3.2: **Printed circuit boards**. **a** The resonator PCB with in total eight CPWs (six of them connected to SMP connectors here). This PCB is used to quickly characterize resonators. It sits on top of a copper piece. There is a hole in the center in which the sample is fitted and glued to the copper underneath. Most of the data presented in Chap. 6 were acquired using this type of PCB. **b** The hybrid PCB used in the measurements reported in Chap. 4 and 5. It is also screwed onto a copper plate. The sample is fitted in the hole in the center of the PCB and glued to the copper underneath. The PCB contains 48 DC and 8 HF lines in total. The DC lines are connected to two 51-pin nano-D connectors from Omnetics soldered onto the back of the PCB (roughly at the locations of the top and bottom DC filters). Each DC wire has a 100 pF capacitor to ground. Each HF line, except for the top two that are used for the resonator, is connected to a DC line via a bias tee consisting of a 47 nF capacitor and 10 MΩ resistor. An LED is soldered next to the sample on the right side. The green surface is solder mask.

the loading of the device into the refrigerator, i.e. one connector is only used to keep the gates grounded while the other connector is used to connect the gates to the DC wires in the fridge.

In addition to the DC lines, there are eight high-frequency (HF) lines in the form of CPWs with non-magnetic SMP connectors on the board. Two of them are dedicated to measuring the resonator (top two SMP connectors), while the others are combined with DC lines via bias tees with an $RC$ time constant of 0.47 s. Fast voltage pulses and microwave excitations can be applied to selected gates on the sample using these lines. In order to minimize the cross talk between HF and DC lines, each DC line is filtered with a 100 pF capacitor to ground.

The PCB is equipped with a light-emitting diode (LED) that can be used to shine light on the sample while it is cold at base temperature. The emitted light has an energy larger than the band gap energy of silicon and it can release charges from potential traps, which could influence the potential landscape in the quantum well. We use an LED that can emit light at 780 nm with a maximum optical output power of 5 mW (US-Lasers D780-5). Typically ~20 mA is sent through the diode for a few seconds (via unfiltered DC lines). As a result, the MC plate warms up to ~1 K. The LED is commonly used for (disordered) Si/SiGe devices as a quicker alternative to a thermal cycle of the sample.

Since the hybrid PCB combines DC and HF lines in a single board, its design is more complicated than the previously discussed resonator PCB, i.e. it comprises four copper layers separated by dielectric layers. Again, vias are used to uniformly
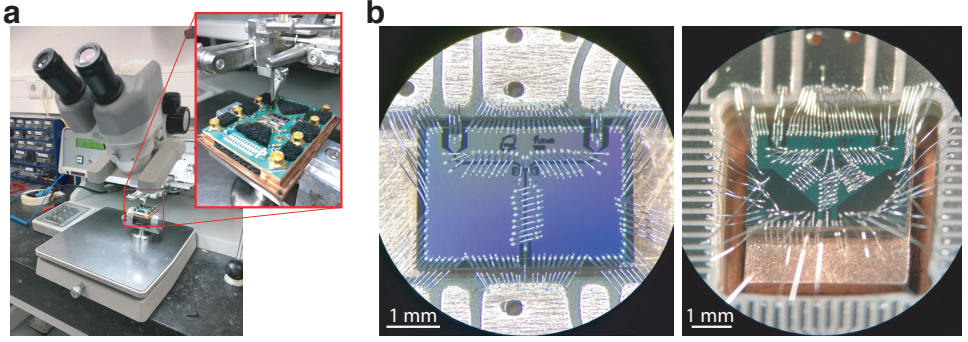
Figure 3.3: **Wire bonding**. **a** The Westbond wire bonder that is used to bond all the samples with Al wires to the PCB. **b** Examples of samples wire bonded to the resonator PCB (left) and hybrid PCB (right).

distribute the ground potential between the layers.

### Wire bonding

The bond pads on the device are electrically contacted to the DC lines on the PCB via Al wire bonds with a diameter of 25 µm. The *Westbond* wedge wire bonder in Fig. 3.3a is used to make the bonds. The bonder utilizes ultrasonic energy to attach Al wires to the sample or PCB. Examples of wire bonded devices on the resonator (left) and hybrid (right) PCBs are displayed in Fig. 3.3b. Due to the holes in the PCBs for the samples, the surface of the device is about the same height as the PCB surface. This allows for short wire bonds, which is important to efficiently transmit high-frequency signal because of the finite inductance of the wire bonds. It is good practice to connect all the interrupted ground planes together with cross overs such as airbridges [2, 3] or wire bonds to suppress spurious (odd) modes which can degrade the performance of the resonator.

## 3.2.2. Cryogenic setups

As the relevant energy scales of QDs and resonators are much lower than the thermal energy at room temperature ($k_B T$), we must cool down the samples in cryogenic systems to low enough temperatures such that thermal excitations are strongly suppressed. First of all, in order to trap electrons in QDs, $k_B T \ll E_C$ needs to be satisfied. This regime can be attained when the temperature is on the order of 1 K and lower in Si/SiGe (10 K in Si-MOS). For high-fidelity qubit operation and read-out, the valley and orbital energy splittings impose an even lower temperature on the sample. In addition, thermal photons in the cavity need to be suppressed. For example, the energy of a 6 GHz photon corresponds to a temperature of ~300 mK. Therefore, samples are cooled down in dilution refrigerators with base temperatures of ~10 mK for advanced measurements. Before moving on to the dilution refrigerator that was used for the experiments reported in this thesis, we will first discuss a different indispensable cryogenic tool that allowed us to rapidly measure resonators.
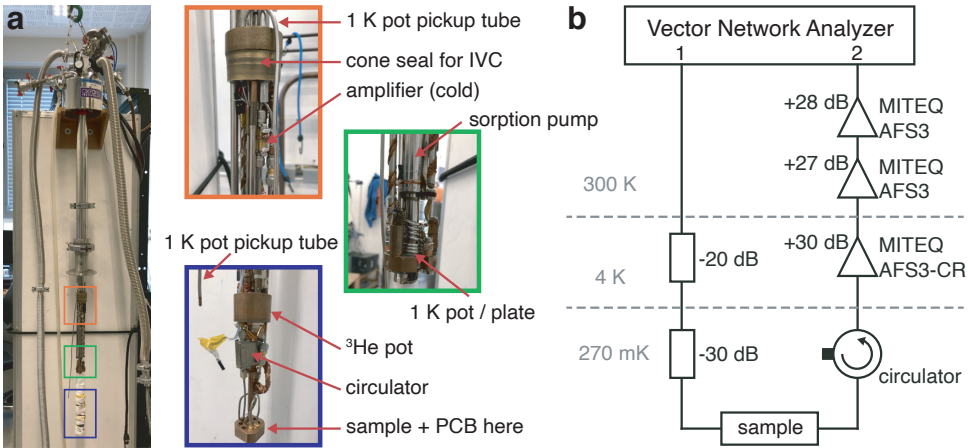
Figure 3.4: **Heliox sorption pumped** $^3$**He refrigerator**. **a** Photo showing the *Heliox* insert with enlargements at three different stages. **b** Schematic overview of the electrical circuit inside and outside the insert.

## Heliox sorption pumped $^3$He refrigerator

Fig. 3.4a shows the *Heliox* cryogenic insert[5] used for fast characterization of resonators. It is a product of *Oxford Instruments* [4]. The insert is shown without the inner vacuum can (IVC), which would otherwise enclose the bottom part of the insert up to the cone seal. The insert is dipped into a liquid $^4$He dewar and has a 1 K pot system, which is used to condense the $^3$He gas that is contained in a closed reservoir. Once condensed, the temperature of the liquid $^3$He is further reduced to ∼270mK by pumping the vapour above the liquid surface using a sorption pump (evaporative cooling). This is a single-shot system, because there is only a finite amount of $^3$He that can be condensed. Nevertheless, the base temperature can be maintained over tens of hours. The cooling process from room temperature to the base temperature takes about 1.5 hours.

The insert is equipped with two semi-rigid HF lines going from top to bottom. There is 50 dB attenuation on the signal input line (Fig. 3.4b). In the return line, the signal passes through a circulator (with a 50 Ω termination on one of the ports) before amplification at the 4 K stage. The circulator here prevents any reflected signal and noise from the amplifier to reach the sample. The signal is amplified further at room temperature using two amplifiers in series. We use a vector network analyzer (R&S ZNB40) to probe the resonator response. Most of the devices in Chap. 6 were measured in this system.

## Triton dilution refrigerator

The experiments described in Chap. 4 and 5 were conducted in a *Triton 400* dilution refrigerator manufactured by *Oxford Instruments* (see Fig. 3.5). The system has a cooling power of ∼1mW at the PT2 plate at 4 K, ∼400 µW at the mixing chamber

---

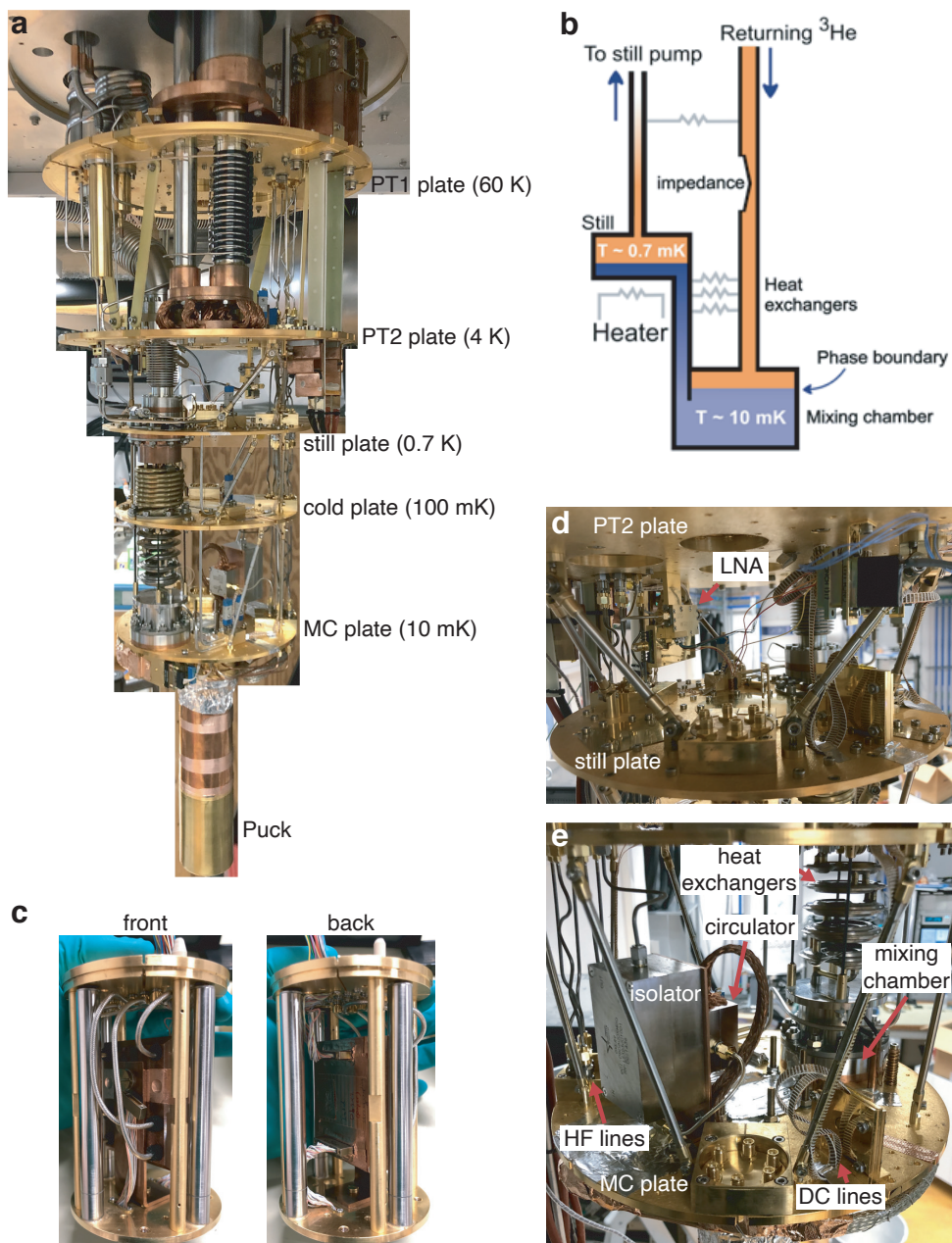[5]Property of the DiCarlo lab at QuTech.

Figure 3.5: **Triton dilution refrigerator**. **a** Photo of the *Oxford Triton 400* system without vacuum and shielding canisters, magnet and bottom loader. The puck is mounted at the bottom. **b** Schematic diagram of the key components of a dry dilution refrigerator. The arrows represent the flow direction of $^3$He. Adapted from Ref. [5]. **c** Photo of an open fast sample exchange puck showing the front (left) and back (right) of the enclosed PCB with control and measurement lines attached. **d** Photo of the PT2 plate showing the cryogenic amplifier. **e** Photo of the MC plate showing the mixing chamber, DC and HF lines, isolator and circulator.

(MC) plate at 100 mK, and is capable of reaching a base temperature of ~10 mK. In contrast to wet dilution refrigerators, this type of refrigerator does not require a continuous external supply of liquid nitrogen or helium to function properly[6], hence it is called a 'dry' dilution refrigerator. This *Triton* model has a bottom-loading system which enables fast sample exchange while the refrigerator remains cold. To do so, a sample is placed in a cylindrical enclosure called a puck, and the puck is inserted into the fridge using the bottom loader. A sample can be cooled down to base temperature within 15 hours owing to this feature. An open puck is shown in Fig. 3.5c. The enclosed PCB is fixed to an L-bracket, and connected to HF lines in the front and DC lines in the back.

The fridge contains 48 DC lines going from the top plate to the puck and ends with a 51-pin nano-D connector inside the puck. Furthermore, 24 DC lines go from the top plate to the PT2 plate to power electronics on that plate. The 24 DC lines are split at the PT2 plate and end with two 25-pin micro-D connectors, one at the top and one at the bottom of the plate. There are 6 HF lines going from the top plate to the puck. There is room for 6 more lines as can be seen from the empty SMA ports in Fig. 3.5e. The fridge is equipped with a superconducting vector magnet which is capable of providing 6 T along the $z$-axis (vertical) and 1 T along the other two orthogonal axes.

The PT1 and PT2 plates are cooled by a two-stage pulse tube (PT) cooler to 60 K and 4 K, respectively. The cooling mechanism of a dilution refrigerator is based on a mixture of $^3$He and $^4$He isotopes. The pre-cooled mixture flows through an impedance and condenses in the mixing chamber (Fig. 3.5b). At a sufficiently low temperature, the liquefied mixture separates into a $^3$He-rich phase and a $^4$He-rich phase. As the $^3$He vapour from the liquid inside the still is pumped, the $^3$He concentration in the liquid will decrease. The difference in $^3$He concentration between the still and the MC leads to an osmotic pressure gradient along the connecting tube, which draws $^3$He from the MC. As a result of the reduced $^3$He concentration in the $^4$He-rich phase in the MC, $^3$He from the $^3$He-rich phase will cross the phase boundary to the $^4$He-rich phase, where energy is absorbed via the enthalpy of mixing, thereby cooling the MC and MC plate in the process [5]. As opposed to a single-shot system, the cooling process in this fridge can continue indefinitely by circulating the $^3$He through the system with a pump.

Note that when the MC plate reaches the base temperature of 10 mK, the lattice phonons in the semiconductor are thermalized to the base temperature, but not necessarily the electrons in the 2DEG. They can have an electron temperature much higher than that, e.g. 100 mK, due to the electrical and thermal contact of the 2DEG with warmer parts of the fridge through the DC and HF lines. This is why proper filtering and thermal anchoring of these lines is of utmost importance to achieve a low electron temperature and noise.

### 3.2.3. Control and measurement electronics

The control and measurement electronics form an essential part in performing proper experiments. The challenge is to design and combine electronics with high

---

[6]Dry dilution refrigerators still need a one-time supply of the $^3$He/$^4$He mixture.

bandwidth - fast enough to manipulate and detect qubits before decohering - while limiting the noise from those electronics that could affect the qubits. Here, we divide the electronics into a DC part and an HF part. Fig. 3.6 summarizes this in a simplified schematic.

### DC electronics

The DC electronics serve mainly two purposes in the experimental setup. Firstly, to apply voltages to the gates on the device to create QDs. Secondly, to measure DC transport currents between Fermi reservoirs, possibly going through QDs. Most of the DC electronics were developed in-house[7] by Raymond Schouten and DEMO (the electronics workshop of TU Delft). The IVVI rack contains several modules, each designed with a different functionality. The gates on the device are biased using 16bit digital-to-analog converter (DAC) modules[8]. These modules have a voltage output range of $\pm 2$ V centered around -2, 0 and 2 V (set manually) and have a resolution of $\sim 60\,\mu$V. DC currents are measured using a current-to-voltage (IV) converter module by connecting it to one reservoir, while a bias (typically $\sim 100\,\mu$V) is applied to the other reservoir. The converted voltage is measured using a commercial digital multimeter (Keithley 2000). The IVVI rack with modules is battery powered and galvanically isolated from other instruments that are powered by the 50 Hz power line, including the measurement computer. Communication between the DAC modules and the computer occurs through an optical fibre.

The 48 DC wires going from the two matrix modules at room temperate to the sample inside the fridge are filtered at several stages, except for 3 lines that are dedicated to the LED. Proper filtering is very important for reducing noise and electron temperature. At room temperature, the wires go through filters inside the matrix modules[9], our in-house developed breakout boxes. Each wire goes through either a Pi-filter (for a gate) or a capacitive feedthrough (for an ohmic contact). The voltage sources in the IVVI rack are connected to the matrix modules via MCX coaxial cables. Next, the lines go to the cryostat using a shielded 24-pin Fischer cable from each matrix module. Inside the cryostat, the wires are further filtered at the MC plate. First they go through a series of four Pi-filters[10] that filter out noise up to 5 GHz. Then, they go through either a second-order $RC$-filter with a cut-off frequency of $\sim 30$ Hz for wires connected to the gates, or a first-order $RC$-filter with a cut-off frequency of $\sim 1.3$ MHz for wires connected to ohmic contacts. Part of the filtering has been sacrificed here for a higher measurement bandwidth. After the last stage of filtering, the wires are carefully shielded on the way to the PCB, where they connect via nano-D connectors from Omnetics. The DC lines are thermally anchored at every temperature plate and fixed where possible to minimize vibration-induced (triboelectric effect) and flux-induced noises.

---

[7]For more details, see: http://qtwork.tudelft.nl/ schouten/
[8]For more details, see: http://qtwork.tudelft.nl/ schouten/ivvi/doc-d5/index-d5.htm
[9]For more details, see: http://qtwork.tudelft.nl/ schouten/matrix/index-matrix.htm
[10]LFCN5000, LFCN2750, LFCN80, LFCN1450 from Mini-Circuits.

### HF electronics

The HF electronics are mainly used for the following three purposes. Firstly, to apply either continuous or pulsed microwave (MW) excitation up to 20 GHz (limited by hardware) to the sample. This is to manipulate the qubit or to probe the resonator. Secondly, to apply rapid voltage pulses that modify the chemical potentials of the dots with nanosecond time resolution. Thirdly, to ramp gate voltages with a time period of a few milliseconds or shorter for fast mapping of charge stability diagrams. The last two objectives were realized using an arbitrary waveform generator (AWG) Tektronix 5014C with a maximum sampling rate of 1.2 GS/s. Two of the four analog output channels are connected to the LP and RP gates. The output signal is filtered at room temperature using low-pass filters with a 120 MHz cut-off frequency (SBLP-200+ Mini-Circuits), and then attenuated by 23 dB inside the cryostat. The Keysight E8267D vector signal generator with a frequency range of 100 kHz - 20 GHz was used to perform two-tone spectroscopy, and can also be used to drive spin states via EDSR. The microwave signal is attenuated at room temperature by typically 50 dB and 40 dB inside the cryostat before reaching one of the gates (usually the LB gate). An inner/outer DC block is attached to all MW source outputs in order to prevent ground loops and block low frequency noise from the generator.

The fridge has 6 HF semi-rigid coaxial lines with SMA connectors installed. They are broken into four different parts. First, from the top plate to the 4 K plate we use UT085 SSS/SS (outer diameter: 2.2 mm, inner conductor: silver-plated stainless steel, outer conductor: stainless steel). Second, from the 4 K plate to the MC plate we use UT085 NT/NT (outer diameter: 2.2 mm, inner and outer conductor: superconducting NbTi). Third, from the MC plate to the puck we use UT085 CU/CU (outer diameter: 2.2 mm, inner and outer conductor: copper) with SMP connectors at the puck. Fourth, inside the puck we use flexible non-magnetic coaxial cables with SMP connectors (see Fig. 3.5c). The HF lines for the gates have either 23 dB or 40 dB attenuation due to attenuators distributed over different plates. This is done for two reasons. First, the attenuators thermally anchor the inner conductor of the coax cables via the galvanic connection between inner and outer conductors inside attenuators. Second, they reduce the thermal noise coming from room temperature to the Johnson noise at the plate. Typically 20 dB of attenuation is needed for a temperature change of two order of magnitude. The amount of attenuation in the fridge is a trade-off between low noise and large signal at the sample. The resonator input line is more heavily attenuated, i.e. 70 dB of attenuation in order to go down to the single-photon regime. We typically apply $-120$ dBm at the sample. Note that we use cryogenic attenuators from XMA inside the cryostat. The resonator return line has a circulator and an isolator from QuinStar (see Fig. 3.6 for the model numbers) in series at the MC plate to block any reflected signal and noise from the cryogenic microwave amplifier (LNF-LNC4_8A from Low Noise Factory) at the PT2 plate. The rest of the HF electronics at room temperature for the resonator will be discussed next.
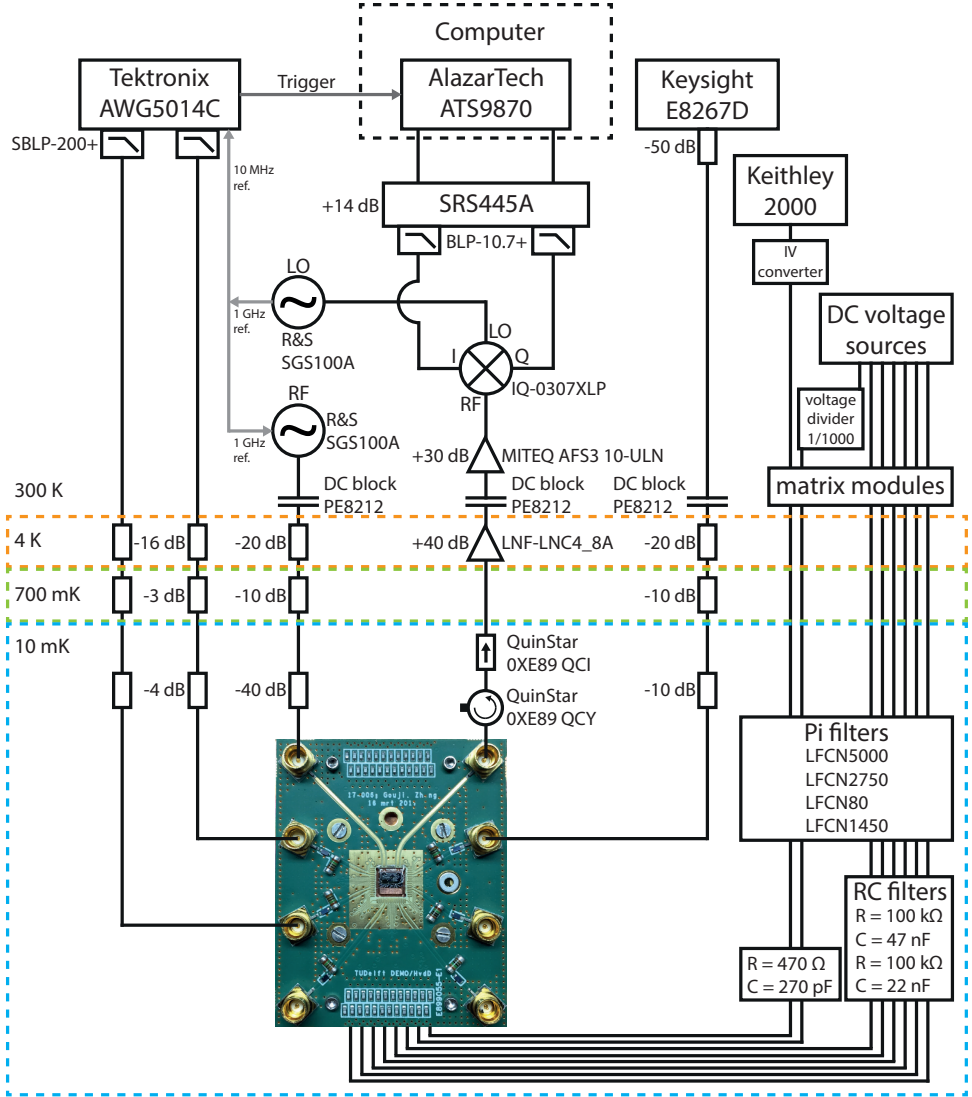
**3**

Figure 3.6: **Schematic overview of the electrical circuit of the Triton measurement setup.** See main text for details.

### **3.2.4.** Heterodyne detection

A heterodyne detection scheme is often employed to extract the amplitude and phase information contained in the transmission signal of the resonator. We use two MW generators (R&S SGS100A) with a frequency range of 1 MHz - 12.75 GHz. One is for probing the resonator (RF), while the other functions as the local oscillator (LO). The sources are usually 10 MHz detuned (homodyne detection for zero detuning). The RF tone is sent to the resonator and is amplified after coming out of the fridge. Subsequently, the RF signal is multiplied with the LO signal in an IQ mixer in order to downconvert it to an IF (intermediate frequency) of 10 MHz. This is necessary because we cannot directly digitize a ~6 GHz signal due to the limited sampling rate of our analog-to-digital converter (ADC). The IQ mixer outputs an in-phase (I) component and a quadrature (Q) component that is shifted by 90° in phase. They pass through a 11 MHz low-pass filter (BLP-10.7+ Mini-Circuits) and an amplifier (SRS445A) before being recorded by our 2-channel digitizer (AlazarTech ATS9870) in the measurement computer with a sampling rate of 1 GS/s. One of the channels on the AWG is used to trigger the digitizer. The two digitized signals are further digitally demodulated down to baseband in order to reconstruct the complex transmission. The in-phase component is proportional to the real part of the transmission and the quadrature component is proportional to the imaginary part.

## References

[1] N. Samkharadze, A. Bruno, P. Scarlino, G. Zheng, D. P. DiVincenzo, L. DiCarlo, and L. M. K. Vandersypen, *High-kinetic-inductance superconducting nanowire resonators for circuit qed in a magnetic field,* Phys. Rev. Applied **5**, 044004 (2016).

[2] Y. J. Y. Lankwarden, A. Endo, J. J. A. Baselmans, and M. P. Bruijn, *Development of nbtin-al direct antenna coupled kinetic inductance detectors,* Journal of Low Temperature Physics **167**, 367 (2012).

[3] Z. Chen, A. Megrant, J. Kelly, R. Barends, J. Bochmann, Y. Chen, B. Chiaro, A. Dunsworth, E. Jeffrey, J. Y. Mutus, P. J. J. O'Malley, C. Neill, P. Roushan, D. Sank, A. Vainsencher, J. Wenner, T. C. White, A. N. Cleland, and J. M. Martinis, *Fabrication and characterization of aluminum airbridges for superconducting microwave circuits,* Applied Physics Letters **104**, 052602 (2014).

[4] *Heliox Sorption Pumped $^3$He Refrigerator Systems - Principles of Operation and Control (Oxford Instruments),* (2013).

[5] G. Batey and G. Teleberg, *Principles of dilution refrigeration - A brief technology guide (Oxford Instruments),* (2015).

# 4

# Strong spin-photon coupling in silicon

*Anybody who has been seriously engaged in scientific work of any kind realizes that over the entrance to the gates of the temple of science are written the words: 'Ye must have faith.'*

Max Planck

N. Samkharadze[*], **G. Zheng**[*], N. Kalhor, D. Brousse, A. Sammak, U. C. Mendes, A. Blais, G. Scappucci, L. M. K. Vandersypen

*Long coherence times of single spins in silicon quantum dots make these systems highly attractive for quantum computation, but how to scale up spin qubit systems remains an open question. As a first step to address this issue, we report the strong coupling of a single electron spin and a single microwave photon. The electron spin is trapped in a silicon double quantum dot and the microwave photon is stored in an on-chip high-impedance superconducting resonator. The electric field component of the cavity photon couples directly to the charge dipole of the electron in the double dot, and indirectly to the electron spin, through a strong local magnetic field gradient from a nearby micromagnet. Our results provide a route to realizing large networks of quantum dot-based spin qubit registers.*

## **4.1.** Introduction

Light-matter interaction has had profound impact on the development of quantum theory starting from the discovery of the photo-electric effect [1]: one single photon can release one single electron from a solid provided the photon energy exceeds the electron binding energy of the material. This observation demonstrates that light consists of quanta, but does not rely on a coherent interaction between light and matter. In cavity quantum electrodynamics, a photon is stored in a cavity so that its interaction with a resonant atom or other two-level system in the cavity is enhanced to the point where a single quantum of energy is exchanged coherently between the cavity photon mode and the atom [2]. This regime of strong coupling has been achieved across a wide range of experimental platforms, from atoms to superconducting qubits and self-assembled quantum dots, using either optical or microwave photons [3–8]. Given that cavities extend over macroscopic distances, the coherent cavity-atom interaction can be used to indirectly couple well-separated atoms coherently, offering a path to scalable quantum computing.

This prospect has motivated extensive theoretical and experimental work to achieve the strong-coupling regime with gate-defined semiconductor quantum dots, one of the leading platform for the realization of quantum circuits [9–12]. Recently, strong coupling has been reported between a microwave photon and a charge qubit formed in a double quantum dot, an impressive achievement given the small electric dipole of a double dot and the short-lived charge qubit coherence [13–15]. Even more challenging, but also more desirable, is the strong coupling to a spin qubit [16, 17]. Compared to the electron charge, the electron spin has far superior coherence properties, but its direct interaction with the cavity magnetic field is exceedingly small [18]. Therefore, one must resort to indirect interaction of the electron spin to the cavity electric field by hybridization of the spin with the electron charge degree of freedom, without compromising spin coherence too severely in the process [19–24]. For a single spin, spin-charge hybridization can be achieved in a controlled way via a transverse magnetic field gradient [24–29].

We report the observation of vacuum Rabi splitting of a single electron spin resonant with an on-chip microwave cavity, the telltale sign of strong coupling. The spin-photon coupling strength is controlled by the charge qubit settings and we can extract all the relevant coupling strengths and decay rates. At a spin-photon coupling strength of 10 MHz, we observe cavity decay and spin decoherence rates of 4.1 MHz and 1.8 MHz, respectively.

## **4.2.** Device design and operation

The superconducting cavity consists of a NbTiN half-wavelength coplanar resonator with a narrow center conductor and remote ground planes (Fig. 4.1A,B), capacitively coupled to a feed line. The cavity resonator is wrapped in a square shape and its two ends are connected to two Al gates that extend over the quantum dot locations. The resonator materials choice and dimensions give it a high characteristic impedance of about 1 kΩ that enhances the coupling $g_c$ to the double dot charge dipole [14, 31], and make it resilient to in-plane magnetic fields of over 6 T [31]. The double
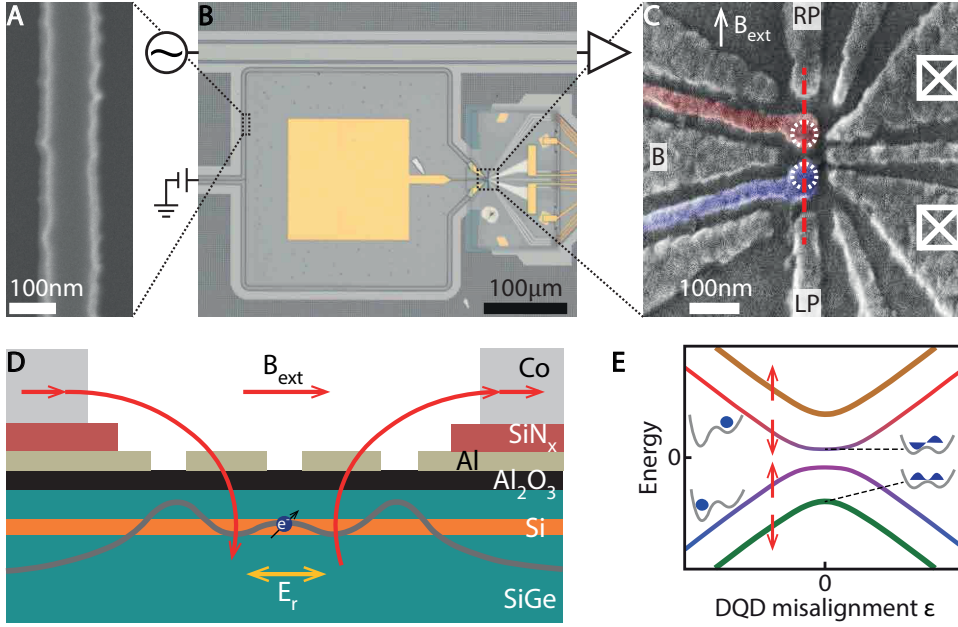
Figure 4.1: **Device images and schematic.** (**A**) Scanning electron micrograph of a segment of the NbTiN resonator center conductor. (**B**) Optical micrograph of the resonator (square shape) adjacent to the feed line (top) and double dot (right). The yellow square in the center is a bond pad to bias gate B. (**C**) Scanning electron micrograph showing the gates used to form the double quantum dot (white dotted circles indicate dot positions). The purple and red colored gates are connected to the resonator ends. (**D**) Schematic cross-section of the quantum dot along the red dashed line in panel (C), showing the Si quantum well with SiGe buffer and barrier layers, and the $Al_2O_3$ and $SiN_x$ dielectrics separating the substrate from the Al gates and Co micromagnets. In the experiment, a single electron moves in the double dot potential landscape (grey line) in response to the resonator electric field, $E_r$. A magnetic field is applied in the plane of the quantum well. The Co micromagnets create an additional magnetic field component (red curves with arrows), with a different orientation between the two dots. (**E**) The DQD energy levels as a function of DQD misalignment $\varepsilon$. Near $\varepsilon = 0$, the left and right dot levels hybridize, forming bonding and anti-bonding states that define a charge qubit [30]. Each of the DQD levels is split by the Zeeman energy. The micromagnets cause spin and orbital levels to hybridize as well, as reflected in the color gradients near $\varepsilon = 0$ for the middle two energy levels.

quantum dot (DQD) is formed electrostatically in an undoped Si/SiGe quantum well (natural isotopic abundance), using a single layer of Al gates [32] (Fig. 4.1C). A positive bias on a gate accumulates electrons in the quantum well underneath, a negative bias repels electrons. An in-plane magnetic field $B_{ext}$ induces a Zeeman splitting on an electron in the DQD. Two Cobalt micromagnets placed near the quantum dots produce a local gradient in the static magnetic field. As a result, when an electron oscillates between the two dots, it experiences an oscillating transverse magnetic field, providing the necessary (indirect) spin-charge hybridization that allows an electric field to couple to the spin [25, 26, 28] (Fig. 4.1E).

We apply a probe tone to the feed line at frequency $f_p$ and record the transmission through the feed line (unless indicated, all transmission plots show the normalised amplitude of the transmission through the feed line). With the DQD tuned to keep the electron fixed in one of the dots, the transmission shows a dip for $f_p$ near 6.051 GHz, the bare resonance frequency $f_r$ of the NbTiN resonator (Fig. 4.2B square symbol). From the linewidth, we find the bare resonator decay rate $\kappa_r/2\pi = 2.7$ MHz, with an internal loss rate $\kappa_{int}/2\pi = 1.5$ MHz. We monitor the transmission through the feed line at low probe power (below $-125$ dBm, corresponding to $< 1$ photon in the resonator) to tune up the DQD, characterize the charge-photon interaction, and study spin-photon coupling.

To characterize the charge-photon interaction, we tune the DQD to a regime where the electron can move back and forth between the two dots in response to the cavity electric field, setting $B_{ext} = 110$ mT, well above the spin resonance condition. Such motion is possible whenever the electrochemical potentials of the two dots are aligned, i.e. where it costs equal energy for an electron to be in either dot. This occurs for specific combinations of gate voltages, seen as the short bright lines in Fig. 4.2A, where the charge-photon interaction modifies the transmission [33]. We focus on the lower left line, which corresponds to the last electron in the DQD.

## 4.3. Dispersive charge-photon interaction

In order to place the charge-photon interaction in the dispersive regime, the gate voltages are adjusted to set $2t_c$ in the range of 8 to 15 GHz, so that the charge qubit splitting $hf_c = \sqrt{4t_c^2 + \varepsilon^2}$ is always well above $hf_r$, with $t_c$ the interdot tunnel coupling and $h$ Planck's constant. We measure $f_c$ using two-tone spectroscopy. In the dispersive regime, the charge-photon interaction results in a frequency shift of the resonator (Fig. 4.2F). In Fig. 4.2B, the characteristic dependence of this dispersive shift on the DQD misalignment $\varepsilon$ is observed. At $\varepsilon = 0$, the electron can most easily move between the dots, hence the electrical susceptibility is the highest and the dispersive shift the largest (triangle). At $\varepsilon = 0$, the magnitude of the dispersive shift is approximated by $(g_c/2\pi)^2/(f_c - f_r)$, where the charge-photon coupling strength $g_c$ is mostly fixed by design and the detuning between $f_c$ and $f_r$ can be adjusted. From a fit based on input-output theory [34], a charge-photon coupling strength $g_c/2\pi$ of $\sim 200$ MHz is extracted.
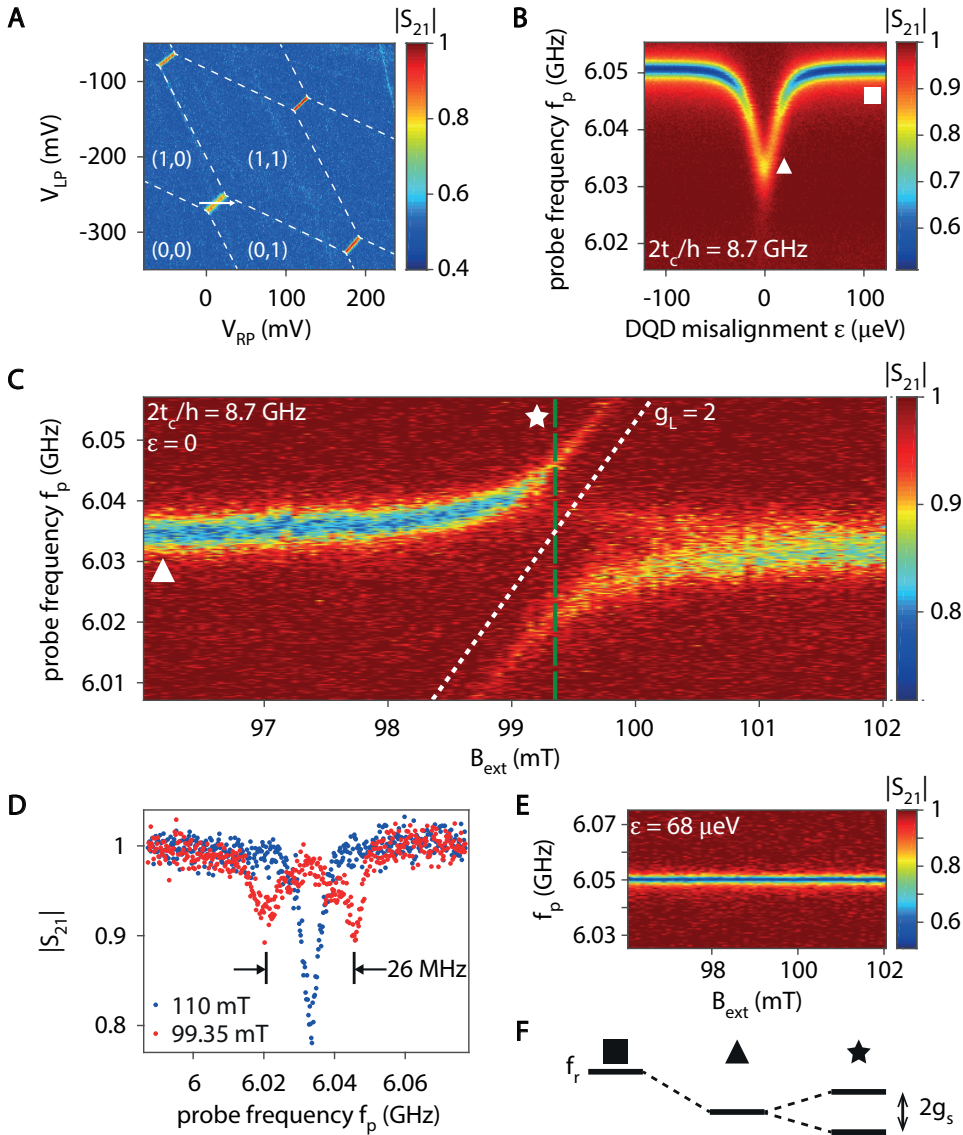
Figure 4.2: **Strong spin-photon coupling.** (**A**) Transmission as a function of two gate voltages that control the potential of the two dots. At the four bright lines, the electron can move between the dots. The dashed lines connecting the short lines indicate alignment of a dot with a reservoir electrochemical potential. Labels indicate the electron number in the two dots. The DQD misalignment $\varepsilon$ is varied along the direction of the white arrow causing an inconsequential uniform shift in the DQD potential as well. (**B**) Transmission as a function of $\varepsilon$ and $f_p$. At large $|\varepsilon|$, we measure the bare resonator transmission (square symbol). Near $\varepsilon = 0$, the DQD charge qubit interacts dispersively with the cavity frequency, leading to a characteristic frequency shift (triangle symbol). (**C**) Transmission as a function of $B_{ext}$ and $f_p$. When $B_{ext}$ makes the spin splitting resonant with the resonator frequency (star symbol), a clear avoided crossing occurs, which we attribute to the strong coupling of a single spin and a single photon. The white dotted line shows the expected spin splitting for a spin in silicon. (**D**) Line cut through panel (C) at the position of the green dashed vertical line (red data points) and line cut at 110 mT (blue points). The red data shows clear vacuum Rabi splitting. (**E**) Similar to (C) but with the DQD misaligned, so the electron cannot move between the two dots. The spin-photon coupling is no longer visible. (**F**) Schematic representation of the transmission resonance of the superconducting cavity. The bare transmission resonance (square) is shifted dispersively by its interaction with the charge qubit (triangle), and splits when it is resonant with the spin qubit (star).

## **4.4.** Resonant spin-photon interaction

To probe coherent spin-photon coupling, the charge sector parameters are kept constant so that the interaction with charge remains dispersive. By varying $B_{\text{ext}}$, the spin splitting is controlled such that the interaction with the spin goes from dispersive to resonant. On resonance, spin and photon hybridize (Fig. 4.2F star). In Fig. 4.2C, the transmission through the feed line is recorded as a function of the strength of an in-plane magnetic field $B_{\text{ext}}$ (the total field is the vector sum of external field and the micromagnet stray field) and the probe frequency $f_p$ applied to the feed line. As expected, the cavity resonance seen in transmission is (nearly) independent of $B_{\text{ext}}$ at large spin-resonator detuning. When the spin splitting approaches resonance with the resonator frequency, we observe a strong response in the form of an anti-crossing (Fig. 4.2C star). The slope $f_p/B_{\text{ext}}$ of the slanted branch corresponds to $g_L \mu_B/h$, with $\mu_B$ the Bohr magneton and $g_L \approx 2$ the Landé $g$-factor of an electron spin in Si. The observed avoided crossing is thus a clear signature of the coherent hybridization of the spin qubit with a single microwave photon.

The line cut, indicated by the dashed green line in Fig. 4.2C and shown in Fig. 4.2D, reveals two well separated peaks. This feature is known as the vacuum Rabi splitting and is expected for strong coherent spin-photon coupling. The peak separation is about 26 MHz, corresponding to a spin-photon coupling strength $g_s/2\pi$ of 13 MHz. The cavity decay rate can be extracted independently from the linewidth away from spin-photon resonance, here $\kappa/2\pi = 5.4$ MHz (the cavity dispersively interacts with the charge, so $\kappa > \kappa_r$ [33]). The spin dephasing rate $\gamma_s/2\pi = 2.5$ MHz is independently obtained from two-tone spectroscopy of the spin transition (discussed next). We observe that $g_s > \kappa, \gamma_s$, satisfying the condition for strong coupling of a single electron spin to a single microwave photon.

## **4.5.** Two-tone microwave spectroscopy

Two-tone spectroscopy of the charge and spin qubits allows us to independently extract the respective qubit splittings and dephasing rates. In Fig. 4.3A,B the second tone is resonant with the charge qubit splitting around 11.1 GHz, with a dependence on $\varepsilon$ described by $hf_c = \sqrt{4t_c^2 + \varepsilon^2}$, see the white dashed line (neglecting spin-charge hybridization). In this case, a charge qubit dephasing rate $\gamma_c/2\pi$ of 52 MHz is extracted from the linewidth. In Fig. 4.3C,D the second tone is swept through the spin resonance condition while keeping the spin-cavity system in the dispersive regime. A linear dependence of the spin splitting on $B_{\text{ext}}$ is observed, with a slope corresponding to $g_L \approx 2$. At $2t_c/h = 12.6$ GHz, we extract $\gamma_s/2\pi = 1.4$ MHz from the linewidth. This is somewhat larger than the ~0.3 MHz single-spin dephasing rates observed in a single Si/SiGe quantum dot [11, 12, 26], as can be expected given that an electron in a DQD at $\varepsilon = 0$ is more susceptible to charge noise, which affects spin coherence through the magnetic field gradient [24, 27, 29].
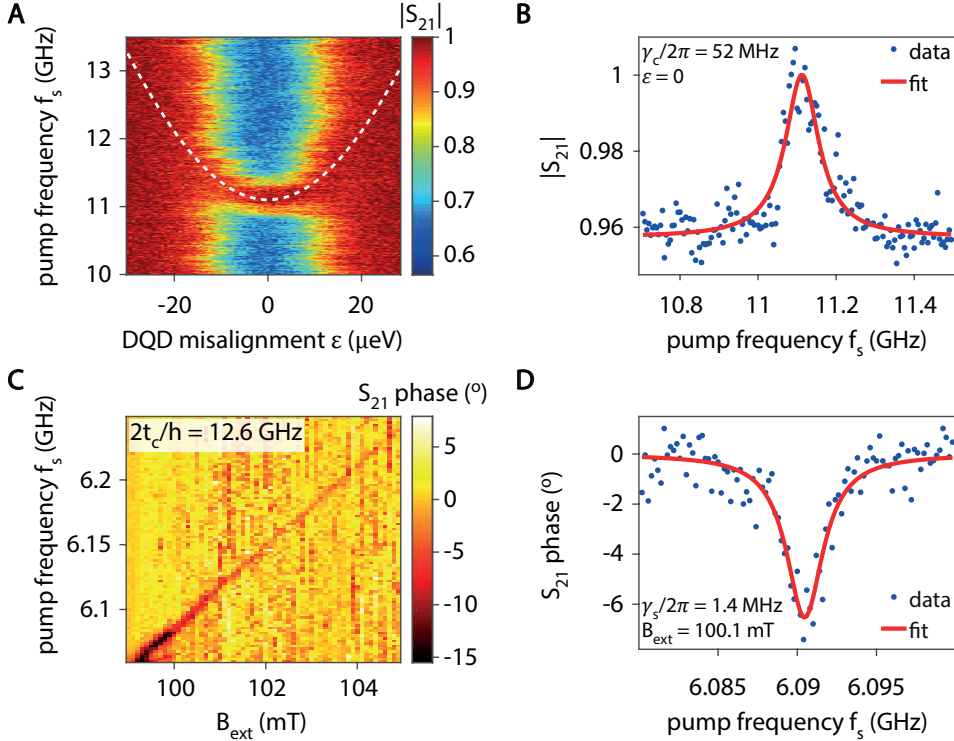
**Figure 4.3: Two-tone spectroscopy of the charge and spin qubit.** (**A**) Transmission at $f_p = 6.041$ GHz as a function of DQD misalignment $\varepsilon$ and the frequency $f_s$ of a second tone (pump frequency) that is applied to gate LP. When the second tone is in resonance with the charge qubit splitting (white dashed line), the steady-state occupation of the charge qubit is changed, and due to the charge-photon coupling, this is reflected in a modified dispersive shift of the resonator. (**B**) Line cut at $\varepsilon = 0$, from which we extract a charge qubit dephasing rate of 52 MHz. (**C**) Transmission (phase response) at $f_p = 6.043$ MHz as a function of $B_{\text{ext}}$ and the pump frequency applied to gate LP. When the pump frequency is in resonance with the spin qubit splitting, the steady-state occupation of the spin qubit is changed, and due to the spin-photon coupling, this is reflected in a modified response of the resonator. The slope of the response corresponds to a spin with $g_L \approx 2$. (**D**) Line cut at $B_{\text{ext}} = 100.1$ mT, from which we extract a spin qubit dephasing rate of 1.4 MHz.

## **4.6.** Control of the spin-photon hybridization

The spin-photon hybridization can be controlled with gate voltages. Indeed, by moving away from $\varepsilon = 0$, the photon and charge no longer hybridize, and then also the spin-photon coupling vanishes (Fig. 4.2E). Furthermore, at $\varepsilon = 0$ the spin-photon coupling strength can be approximated as $g_s = \frac{1}{4} g_c g_L \mu_B \Delta B_x / (2t_c - hf_r)$ (provided the magnetic field profile is symmetric relative to the DQD) [24, 27, 29]. Here $\Delta B_x$ is the difference in the transverse field between the two dots. Starting from large $t_c$, reducing $t_c$ increases charge-photon admixing, and thus indirectly spin-photon coupling as well, as seen experimentally in Figs. 4.4B-D. With increased charge-photon admixing, the asymmetry in the intensity of the two branches also increases, which is understood as a result of quantum interference in the one-excitation manifold of photon, charge and spin [29]. Furthermore an additional feature (Fig. 4.4D white arrow) appears close to the lower branch (discussed in the Supplementary Materials). The variation of $g_s$ with $t_c$ is summarised in Fig. 4.4A, along with the theoretical approximation for $g_s$ versus $t_c$. However, as seen in the same figure, with lower $t_c$ the spin dephasing rate $\gamma_s$ increases as well, as does the cavity decay rate $\kappa$ [29]. Ultimately, we wish to maximize the peak separation over linewidth, $2g_s/(\gamma_s + \kappa/2)$. In this respect, there is an optimal choice of tunnel coupling, as seen from Fig. 4.4A.

## **4.7.** Charge and spin sweet spots

Finally, we study how close together the charge and spin sweet spots occur, where the relevant frequency (charge or spin) is to first order insensitive to the DQD misalignment. The charge sweet spot is seen in Fig. 4.2B, at $\varepsilon = 0$ and $f_p = 6.032$ MHz. If the micromagnets are placed symmetrically with respect to the DQD (as in Fig. 4.1D), the total magnetic field magnitude is symmetric around the center of the DQD. In this case, the spin splitting has no first order dependence on $\varepsilon$ at $\varepsilon = 0$ and the charge and spin sweet spots coincide. For asymmetrically placed magnets, the spin sweet spot occurs away from $\varepsilon = 0$. To find the spin sweet spot, we vary $\varepsilon$ and $B_{\text{ext}}$ at $f_p = 6.040$ GHz (Fig. 4.4E). Throughout the blue band, $f_p$ is resonant with the cavity frequency (in the dispersive charge-photon regime). Where the blue band is interrupted, the magnetic field brings the spin on resonance with the cavity photon, spin and photon hybridize, and the transmission is modified. This spin-photon resonance condition shifts down in magnetic field as a function of $\varepsilon$ [28]. The value of $\varepsilon$ where this shift has no first order dependence on $\varepsilon$ occurs close to $\varepsilon = 0$, i.e. the spin sweet spot lies close to the charge sweet spot.

## **4.8.** Conclusion

The strong coupling of spin and photon not only opens up a new range of physics experiments, but is also the crucial requirement for coupling spin qubits at a distance via a superconducting resonator. Given the large dimensions of the resonators compared to the double dot dimensions, multiple spin qubits can interact to and via the same resonator, enabling scalable networks of interconnected spin qubit
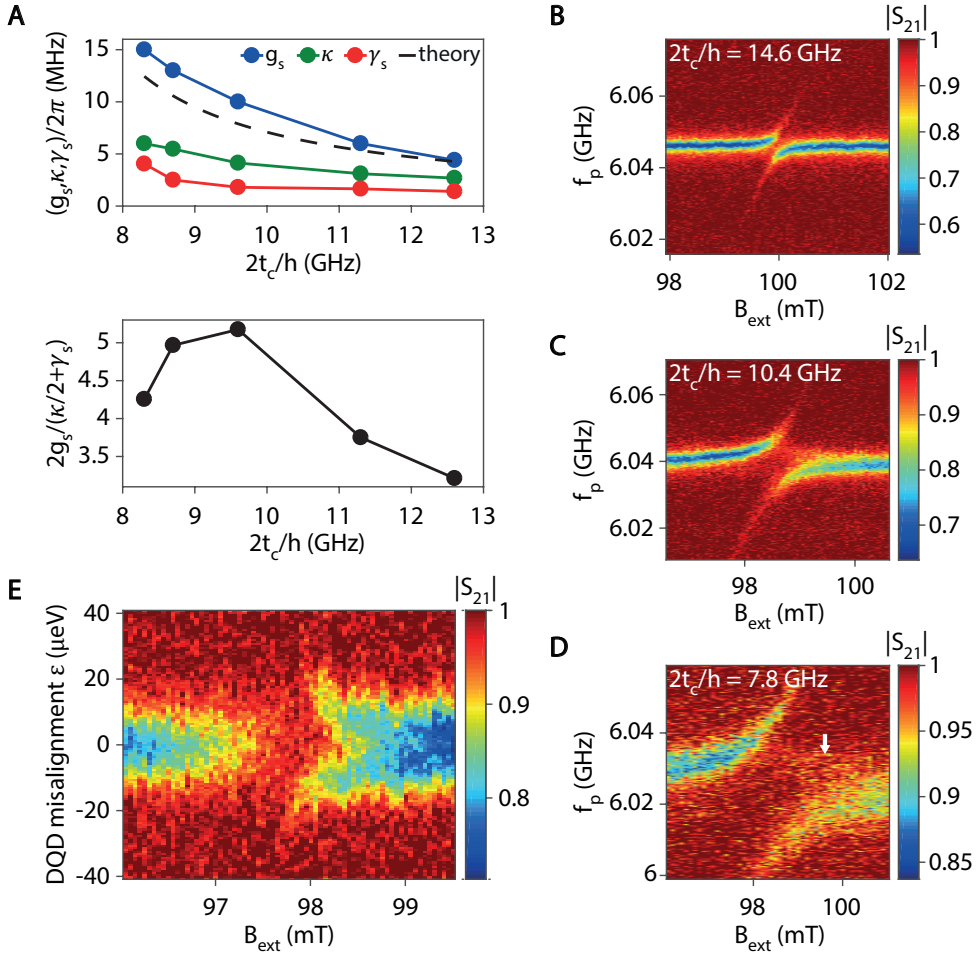
**Figure 4.4: Control of the spin-photon coupling. (A)** The dependence on DQD tunnel coupling of $g_s$, $\kappa$, $\gamma_s$ (upper panel) and the ratio of peak splitting to linewidth $2g_s/(\gamma_s + \kappa/2)$ (lower panel) for $\varepsilon = 0$. While all three separate quantities increase with lower $2t_c$, the ratio $2g_s/(\gamma_s + \kappa/2)$, which is the most relevant quantity, shows an optimum value around $f_c = 9.5$ GHz. The black dashed line shows $g_s$ approximated as $\frac{1}{4}g_c g_L \mu_B \Delta B_x/(2t_c - h f_r)$ [29], taking $\Delta B_x = 20$ mT (which translates to an estimated interdot distance of 45 nm given the 0.45 mT/nm simulated transverse gradient). **(B-D)** Similar data to Fig. 4.2C for three different values of DQD tunnel coupling, as indicated. The small differences in the resonant magnetic field are mostly due to different magnetic field sweep histories and hysteresis in the micromagnet. **(E)** Transmission as a function of $B_{ext}$ and $\varepsilon$ for $2t_c/h = 10.3$ MHz, $f_p = 6.040$ MHz. Where the blue band is interrupted, the Zeeman splitting is resonant with the (dispersively shifted) resonator.

registers [35]. Importantly, the spin-photon coupling can be switched on or off on nanosecond timescales using gate voltage pulses that control the double dot misalignment and tunnel coupling, facilitating on-demand coupling of one or more spins to a common resonator.

## Acknowledgments

## Data availability

Data contained in this paper are archived at `http://doi.org/10.4121/uuid: 1483c28e-c1d5-45d5-971c-8e660f01f768`.

## 4.9. Supplementary materials

### Bare cavity resonance
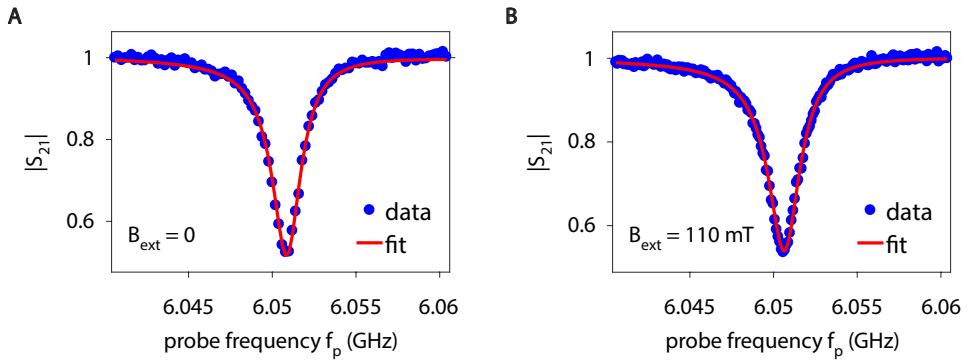


Figure 4.5: (**A**) Cavity resonance before the formation of the DQD and in the absence of an external magnetic field. (**B**) Similar data to (A), but after the formation of the DQD with a single electron confined in one of the dots and with $B_{\text{ext}} = 110\,\text{mT}$.

### Additional structure in the avoided crossing

A small additional structure located between the two well resolved vacuum Rabi splitting peaks can be observed in Fig. 4.2C and Fig. 4.4C,D. We note that this peak has an asymmetric behavior with respect to the external magnetic field. To eliminate the possibility that this structure is due to magnetic hysteresis effects in the Co micromagnets, we compared the feed line transmission for the spin qubit

in the configuration corresponding to the avoided crossing (with $2t_c/h \approx 10.4\,\text{GHz}$) when ramping up or down the magnetic field. The observed anti-crossing is unchanged for both directions, as can be seen in Fig. 4.6. Moreover, increasing the measurement power by 20 dB did not reveal a change in this additional structure, suggesting that it is not due to stray photon population. Finally, we computed the transmission spectrum using an input-output model including the spin, charge and photon using the theory from Ref. [29]. Using the measured spin qubit parameters, this theoretical result, shown in Fig. 4.7, did not show any feature similar to the one observed in Fig. 4.2C and Fig. 4.4C,D. To conclude, while the origin of this small additional structure remains to be clarified, the avoided crossing of the spin qubit and to the resonator responds fully as expected to changes in DQD detuning, DQD tunnel coupling, and magnetic field. Also the two-tone spectroscopy data appears not to be affected by this small feature.
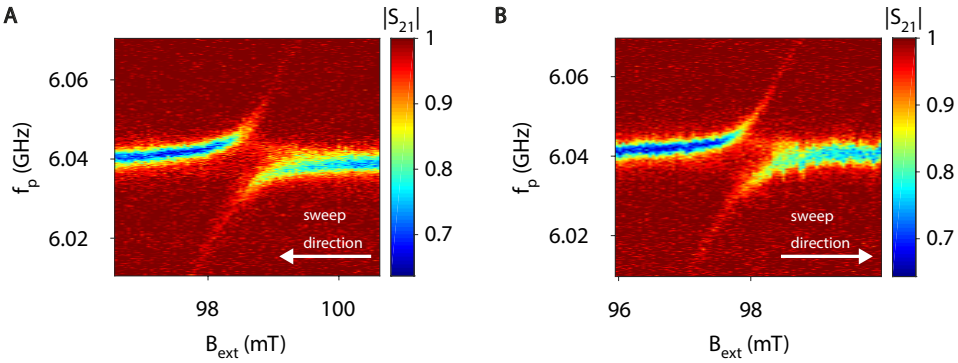


Figure 4.6: (**A**) Copy of Fig. 4.4C in the main text where the sweep direction of $B_{\text{ext}}$ is from high to low field. (**B**) Similar data to (A), but with $B_{\text{ext}}$ swept in the opposite direction.
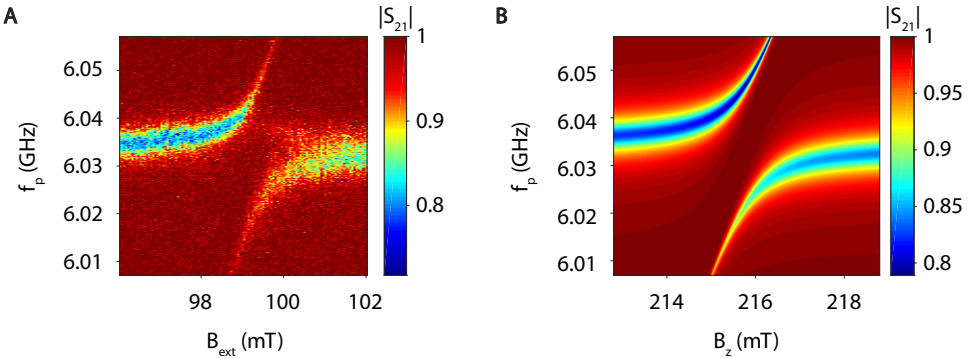


Figure 4.7: (**A**) Copy of Fig. 4.2C in the main text. (**B**) Simulation of the transmission using the following parameters: $\varepsilon = 0$, $2t_c/h = 8.7\,\text{GHz}$, $g_c/2\pi = 210\,\text{MHz}$, $\Delta B_x = 23\,\text{mT}$, $\gamma_c/2\pi = 52\,\text{MHz}$, $f_r = 6.0507\,\text{GHz}$, $\kappa_r/2\pi = 2.7\,\text{MHz}$, $\kappa_{\text{int}}/2\pi = 1.46\,\text{MHz}$. Here, $B_z = B_{\text{ext}} + B_z^{\text{mm}}$, with $B_z^{\text{mm}}$ the stray field of the micromagnets in the direction of the external magnetic field.

# References

[1] A. Einstein, *Über einen die erzeugung und verwandlung des lichtes betref-fenden heuristischen gesichtspunkt,* Annalen der Physik **322**, 132 (1905).

[2] S. Haroche and J. M. Raimond, *Exploring the Quantum: Atoms, Cavities, and Photons* (Oxford Univ. Press, Oxford, 2006).

[3] R. J. Thompson, G. Rempe, and H. J. Kimble, *Observation of normal-mode splitting for an atom in an optical cavity,* Phys. Rev. Lett. **68**, 1132 (1992).

[4] M. Brune, F. Schmidt-Kaler, A. Maali, J. Dreyer, E. Hagley, J. M. Raimond, and S. Haroche, *Quantum rabi oscillation: A direct test of field quantization in a cavity,* Phys. Rev. Lett. **76**, 1800 (1996).

[5] A. Wallraff, D. I. Schuster, A. Blais, L. Frunzio, R.-S. Huang, J. Majer, S. Kumar, S. M. Girvin, and R. J. Schoelkopf, *Strong coupling of a single photon to a superconducting qubit using circuit quantum electrodynamics,* Nature **431**, 162 (2004).

[6] I. Chiorescu, P. Bertet, K. Semba, Y. Nakamura, C. J. P. M. Harmans, and J. E. Mooij, *Coherent dynamics of a flux qubit coupled to a harmonic oscillator,* Nature **431**, 159 (2004).

[7] J. P. Reithmaier, G. Sek, A. Löffler, C. Hofmann, S. Kuhn, S. Reitzenstein, L. V. Keldysh, V. D. Kulakovskii, T. L. Reinecke, and A. Forchel, *Strong coupling in a single quantum dot-semiconductor microcavity system,* Nature **432**, 197 (2004).

[8] T. Yoshie, A. Scherer, J. Hendrickson, G. Khitrova, H. M. Gibbs, G. Rupper, C. Ell, O. B. Shchekin, and D. G. Deppe, *Vacuum rabi splitting with a single quantum dot in a photonic crystal nanocavity,* Nature **432**, 200 (2004).

[9] M. D. Shulman, O. E. Dial, S. P. Harvey, H. Bluhm, V. Umansky, and A. Yacoby, *Demonstration of entanglement of electrostatically coupled singlet-triplet qubits,* Science **336**, 202 (2012).

[10] M. Veldhorst, C. H. Yang, J. C. C. Hwang, W. Huang, J. P. Dehollain, J. T. Muhonen, S. Simmons, A. Laucht, F. E. Hudson, K. M. Itoh, A. Morello, and A. S. Dzurak, *A two-qubit logic gate in silicon,* Nature **526**, 410 (2015).

[11] T. F. Watson, S. G. J. Philips, E. Kawakami, D. R. Ward, P. Scarlino, M. Veldhorst, D. E. Savage, M. G. Lagally, M. Friesen, S. N. Coppersmith, M. A. Eriksson, and L. M. K. Vandersypen, *A programmable two-qubit quantum processor in silicon,* Nature **555**, 633 (2018).

[12] D. M. Zajac, A. J. Sigillito, M. Russ, F. Borjans, J. M. Taylor, G. Burkard, and J. R. Petta, *Resonantly driven cnot gate for electron spins,* Science **359**, 439 (2018).

[13] X. Mi, J. V. Cady, D. M. Zajac, P. W. Deelman, and J. R. Petta, *Strong coupling of a single electron in silicon to a microwave photon,* Science **355**, 156 (2017).

[14] A. Stockklauser, P. Scarlino, J. V. Koski, S. Gasparinetti, C. K. Andersen, C. Reichl, W. Wegscheider, T. Ihn, K. Ensslin, and A. Wallraff, *Strong coupling cavity qed with gate-defined double quantum dots enabled by a high impedance resonator,* Phys. Rev. X **7**, 011030 (2017).

[15] L. E. Bruhat, T. Cubaynes, J. J. Viennot, M. C. Dartiailh, M. M. Desjardins, A. Cottet, and T. Kontos, *Circuit qed with a quantum-dot charge qubit dressed by cooper pairs,* Phys. Rev. B **98**, 155313 (2018).

[16] X. Mi, M. Benito, S. Putz, D. M. Zajac, J. M. Taylor, G. Burkard, and J. R. Petta, *A coherent spin-photon interface in silicon,* Nature **555**, 599 (2018).

[17] A. J. Landig, J. V. Koski, P. Scarlino, U. C. Mendes, A. Blais, C. Reichl, W. Wegscheider, A. Wallraff, K. Ensslin, and T. Ihn, *Coherent spin-photon coupling using a resonant exchange qubit,* Nature **560**, 179 (2018).

[18] P. Haikka, Y. Kubo, A. Bienfait, P. Bertet, and K. Mølmer, *Proposal for detecting a single electron spin in a microwave resonator,* Phys. Rev. A **95**, 022306 (2017).

[19] L. Childress, A. S. Sørensen, and M. D. Lukin, *Mesoscopic cavity quantum electrodynamics with quantum dots,* Phys. Rev. A **69**, 042302 (2004).

[20] G. Burkard and A. Imamoglu, *Ultra-long-distance interaction between spin qubits,* Phys. Rev. B **74**, 041307 (2006).

[21] M. Trif, V. N. Golovach, and D. Loss, *Spin dynamics in inas nanowire quantum dots coupled to a transmission line,* Phys. Rev. B **77**, 045434 (2008).

[22] A. Cottet and T. Kontos, *Spin quantum bit with ferromagnetic contacts for circuit qed,* Phys. Rev. Lett. **105**, 160502 (2010).

[23] C. Kloeffel, M. Trif, P. Stano, and D. Loss, *Circuit qed with hole-spin qubits in ge/si nanowire quantum dots,* Phys. Rev. B **88**, 241405 (2013).

[24] F. Beaudoin, D. Lachance-Quirion, W. A. Coish, and M. Pioro-Ladrière, *Coupling a single electron spin to a microwave resonator: controlling transverse and longitudinal couplings,* Nanotechnology **27**, 464003 (2016).

[25] M. Pioro-Ladrière, Y. Tokura, T. Obata, T. Kubo, and S. Tarucha, *Micromagnets for coherent control of spin-charge qubit in lateral quantum dots,* Applied Physics Letters **90**, 024105 (2007).

[26] E. Kawakami, P. Scarlino, D. R. Ward, F. R. Braakman, D. E. Savage, M. G. Lagally, M. Friesen, S. N. Coppersmith, M. A. Eriksson, and L. M. K. Vandersypen, *Electrical control of a long-lived spin qubit in a si/sige quantum dot,* Nature Nanotechnology **9**, 666 (2014).

**4**

[27] X. Hu, Y.-x. Liu, and F. Nori, *Strong coupling of a spin qubit to a superconducting stripline cavity,* Phys. Rev. B **86**, 035314 (2012).

[28] J. J. Viennot, M. C. Dartiailh, A. Cottet, and T. Kontos, *Coherent coupling of a single spin to microwave cavity photons,* Science **349**, 408 (2015).

[29] M. Benito, X. Mi, J. M. Taylor, J. R. Petta, and G. Burkard, *Input-output theory for spin-photon coupling in si double quantum dots,* Phys. Rev. B **96**, 235434 (2017).

[30] T. Hayashi, T. Fujisawa, H. D. Cheong, Y. H. Jeong, and Y. Hirayama, *Coherent manipulation of electronic states in a double quantum dot,* Phys. Rev. Lett. **91**, 226804 (2003).

[31] N. Samkharadze, A. Bruno, P. Scarlino, G. Zheng, D. P. DiVincenzo, L. DiCarlo, and L. M. K. Vandersypen, *High-kinetic-inductance superconducting nanowire resonators for circuit qed in a magnetic field,* Phys. Rev. Applied **5**, 044004 (2016).

[32] S. Rochette, M. Rudolph, A.-M. Roy, M. J. Curry, G. A. T. Eyck, R. P. Manginell, J. R. Wendt, T. Pluym, S. M. Carr, D. R. Ward, M. P. Lilly, M. S. Carroll, and M. Pioro-Ladrière, *Quantum dots with split enhancement gate tunnel barrier control,* Applied Physics Letters **114**, 083101 (2019).

[33] T. Frey, P. J. Leek, M. Beck, A. Blais, T. Ihn, K. Ensslin, and A. Wallraff, *Dipole coupling of a double quantum dot to a microwave resonator,* Phys. Rev. Lett. **108**, 046807 (2012).

[34] K. D. Petersson, L. W. McFaul, M. D. Schroer, M. Jung, J. M. Taylor, A. A. Houck, and J. R. Petta, *Circuit quantum electrodynamics with a spin qubit,* Nature **490**, 380 (2012).

[35] L. M. K. Vandersypen, H. Bluhm, J. S. Clarke, A. S. Dzurak, R. Ishihara, A. Morello, D. J. Reilly, L. R. Schreiber, and M. Veldhorst, *Interfacing spin qubits in quantum dots and donors–hot, dense, and coherent,* npj Quantum Information **3**, 34 (2017).

# 5

# Rapid gate-based spin readout in silicon using an on-chip resonator

**G. Zheng**, N. Samkharadze, M. L. Noordam, N. Kalhor, D. Brousse, A. Sammak, G. Scappucci, L. M. K. Vandersypen

*A critical requirement for any qubit implementation is the ability to read out the qubit rapidly, with high fidelity, and in a scalable manner. While single-electron transistors embedded in radio-frequency reflectometry circuits are the most sensitive detectors to date, they come with additional resources that occupy space near the quantum dots (gate electrodes, electron reservoirs), which makes scaling up to two-dimensional spin qubit arrays difficult. More efficiently, gate-based sensing connects gates that are already in place for defining quantum dots to a resonant circuit. This method has been developed using off-chip resonators, and only very recently reached the sensitivity necessary for single-shot readout of spins in silicon. Here, we use an on-chip superconducting microwave resonator to improve the sensitivity. With this approach, we achieve a signal-to-noise ratio (SNR) of about six within an integration time of $1\,\mu s$. Using Pauli's exclusion principle for spin-to-charge conversion, we demonstrate single-shot readout of a two-electron spin state with an average fidelity of $>98\,\%$ in $6\,\mu s$. This result may form the basis of frequency multiplexed readout in dense spin qubit systems without external electrometers, therefore simplifying the system architecture.*

## **5.1.** Introduction

As with any qubit implementation, a crucial requirement is the ability to measure individual quantum states rapidly and with high fidelity. Since the signal from a single electron spin is minute, the different spin states are converted to different charge states [1, 2]. Charge detection, so far, mostly relied on external electrometers [3–5], which hinders scaling to two-dimensional spin qubit arrays [6–8]. Alternatively, gate-based dispersive readout based on off-chip lumped element resonators were introduced [9–12], but integration times of 0.2 to 2 ms were required to achieve single-shot readout [13–15]. Here, we connect an on-chip superconducting resonant circuit to two of the gates that confine electrons in a double quantum dot (DQD). Measurement of the power transmitted through a feedline coupled to the resonator probes the charge susceptibility, distinguishing whether or not an electron can oscillate between the dots in response to the probe power. In conjunction with Pauli spin blockade, we demonstrate rapid single-shot readout of a two-electron spin state.

Single-shot readout is required for implementing quantum error correcting schemes, where the measurement and correction should be performed with high fidelity and well within the qubit coherence times (that is, with high bandwidth). In gate-based sensing, a technique using radio-frequency reflectometry [5] is applied to a single gate that is already in place to define the quantum dot [16–18]. However, resonant circuits, so far, have made use of commercial or superconducting inductors mounted on a printed circuit board adjacent to the quantum dot chip. These circuits are quite lossy and contain large parasitic capacitances, masking the useful signal from the capacitive response of the quantum dots. Although single-shot readout of spin states could be achieved thanks to long spin relaxation timescales, the effective detection bandwidths were limited by the SNR to a few kilohertz [13–15].

On-chip superconducting resonators can be used for dispersive readout of single spins directly, as we have seen in Chap. 4 (Fig. 4.3, see also Ref. [19]). However, the dispersive signal from the spin is rather weak, which makes single-shot detection in this fashion very challenging. The dispersive signal from the charge is many times larger on the other hand, making it worthwhile to read out the spin indirectly via a spin-to-charge conversion scheme.

## **5.2.** Device design and operation

Here, we fully integrate an on-chip superconducting microwave resonator into a Si/SiGe DQD device [21] (similar to the device in Chap. 4) to perform single-shot singlet-triplet readout (Fig. 5.1a,c). Two gates are galvanically connected to the NbTiN nanowire resonator with a high characteristic impedance of ~1 kΩ [22]. The resonator is probed through a capacitively coupled planar transmission line (feedline) with an average population of three photons. The observed dip in the normalized transmission amplitude of the probe signal reveals the resonance frequency $f_0 = 5.7116\,\text{GHz}$, as well as the total linewidth $\kappa/2\pi \approx 2.2\,\text{MHz}$ (Fig. 5.1b), which sets the maximum measurement bandwidth. The high quality factor ($Q \approx 2600$) and large impedance of the resonator enable fast high-fidelity charge detection.
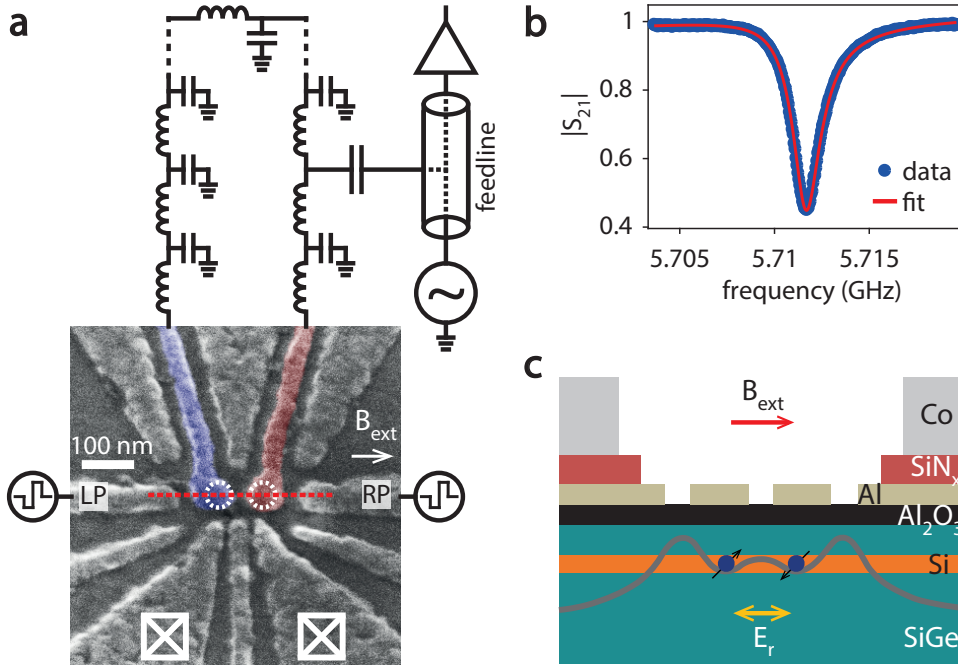
Figure 5.1: **Device schematics. a** Scanning electron micrograph of a device nominally identical to that used in the experiment, showing a single layer of Al gate electrodes for accumulation and confinement of electrons, with a schematic of the superconducting resonator. The circuit consists of a NbTiN thin wire with a $\lambda/2$ resonance mode. The ends of the wire - the purple and red shaded gates - extend towards and overlap with the location of the two dots (white dashed circles). The left and right plunger gates (LP and RP, respectively) are used to adjust the electrochemical potentials of the dots. Voltage pulses are also sent to these gates, through bias tees. White crossed boxes at the bottom indicate the location of Fermi reservoirs of electrons that are connected to source and drain electrodes outside the image. **b** Normalized transmission amplitude through the superconducting feedline, prior to the formation of dots. The applied microwave power is $P = -110\,$dBm. From a Lorentzian fit (red solid line) the resonance frequency $f_0 = 5.7116\,$GHz, loaded quality factor $Q \approx 2600$, internal quality factor $Q_i \approx 5780$ and coupling quality factor $Q_c \approx 4730$ are extracted [20]. **c** Schematic cross-section of the device along the red dashed line in **a**. The double dot confining the electrons is formed in the strained Si quantum well layer by applying appropriate gate voltages to create a double-well potential. The resonator gates produce a tiny oscillating electric field $E_r$ to which the electron in the DQD responds. Co micromagnets are located on top of the gate stack, isolated from the gates by a layer of SiN dielectric, and provide a transverse field gradient after they are magnetized by an external magnetic field $B_{\mathrm{ext}}$. The gradient is not used intentionally in this experiment.

The resonator is a sensitive probe that can detect tiny changes in the charge susceptibility of the DQD [23–27]. The susceptibility is largest at zero detuning, $\varepsilon = 0$, where the electrochemical potentials of the left and right dots align and an electron is able to tunnel freely between the two dots. In this case, the DQD damps the resonator and shifts its frequency. Away from zero detuning, the electron(s) can only move within a quantum dot, and the electrical susceptibility is negligible in comparison. By recording the transmitted signal at the resonance frequency $f_0$ while varying the voltages on the plunger gates, LP and RP, one can map out the charge stability diagram of the DQD. A typical diagram in the few-electron regime is shown in Fig. 5.2a, where $(N_L, N_R)$ indicates the charge occupation, with $N_L$ $(N_R)$ the number of electrons in the left (right) dot (see Fig. 5.4 for a larger stability diagram). A bright yellow line appears at the transition between the (1,1) and (0,2) charge states. Because the probe frequency of ~5.7 GHz is above the interdot tunnel coupling $t_c/h \approx 2$ GHz, measured using two-tone spectroscopy [28], the system is not in the adiabatic limit where quantum capacitance arising from the curvature of the dispersion relation dominates the response [29]. Instead, there is also a significant contribution from the tunnelling capacitance, whereby charges non-adiabatically redistribute in the double dot at a rate comparable to the probe frequency.

## 5.3. Charge sensitivity

We first quantify the sensitivity of the resonator to changes in the DQD susceptibility due to electron tunnelling. We scan over the interdot transition by sweeping the voltage on RP (red dashed line in Fig. 5.2a). Fig. 5.2b shows two examples of the resulting line traces, with an integration time of 1.28 μs (blue) and 2.56 μs (red) per point. The power SNR is defined as $\mathrm{SNR} = (A/B)^2$. The signal $A$ is the difference between the transmitted amplitude at the interdot transition ($V_{\mathrm{RP}} \approx -162$ mV) and the amplitude in the Coulomb blockaded region, where no electrons are allowed to tunnel. This difference is obtained from a Gaussian fit to data such as that in Fig. 5.2b. The noise $B$ is the r.m.s. noise amplitude measured with the electrons in Coulomb blockade ($V_{\mathrm{RP}} \approx -170$ mV). We expect $A^2$ to increase linearly with probe power, and $B^2$ to decrease linearly with integration time. Fig. 5.2c shows the SNR as a function of the integration time for three different probe powers. The data points follow $\mathrm{SNR}(t_{\mathrm{int}}) = t_{\mathrm{int}}/t_{\mathrm{min}}$, with $t_{\mathrm{min}}$ the integration time for an SNR of unity. We find $t_{\mathrm{min}} \approx 170$ ns at $-110$ dBm input power, and it is ~3.3 times longer at $-115$ dBm, which is expected from the 5 dB difference in power. At higher power ($-105$ dBm) $t_{\mathrm{min}}$ begins to saturate, presumably since the electron displacement in the DQD reaches a maximum. The inverse resonator linewidth imposes a constraint on the minimum measurement time of $0.35(\kappa/2\pi)^{-1} \approx 160$ ns. Using the following definition of the charge sensitivity, we get $\delta q = e\sqrt{t_{\mathrm{min}}} = (4.1 \pm 0.3) \times 10^{-4} \ e/\sqrt{\mathrm{Hz}}$ at $P = -110$ dBm (with 1 s.d. uncertainty). This is an order of magnitude higher than reported for a microwave resonator probed with a quantum-limited Josephson parametric amplifier, but two orders of magnitude lower compared to the value reported without the parametric amplifier [30]. In the following experiment we set $P = -110$ dBm, where we have SNR $\approx 6$ at 1 μs integration time, corresponding to
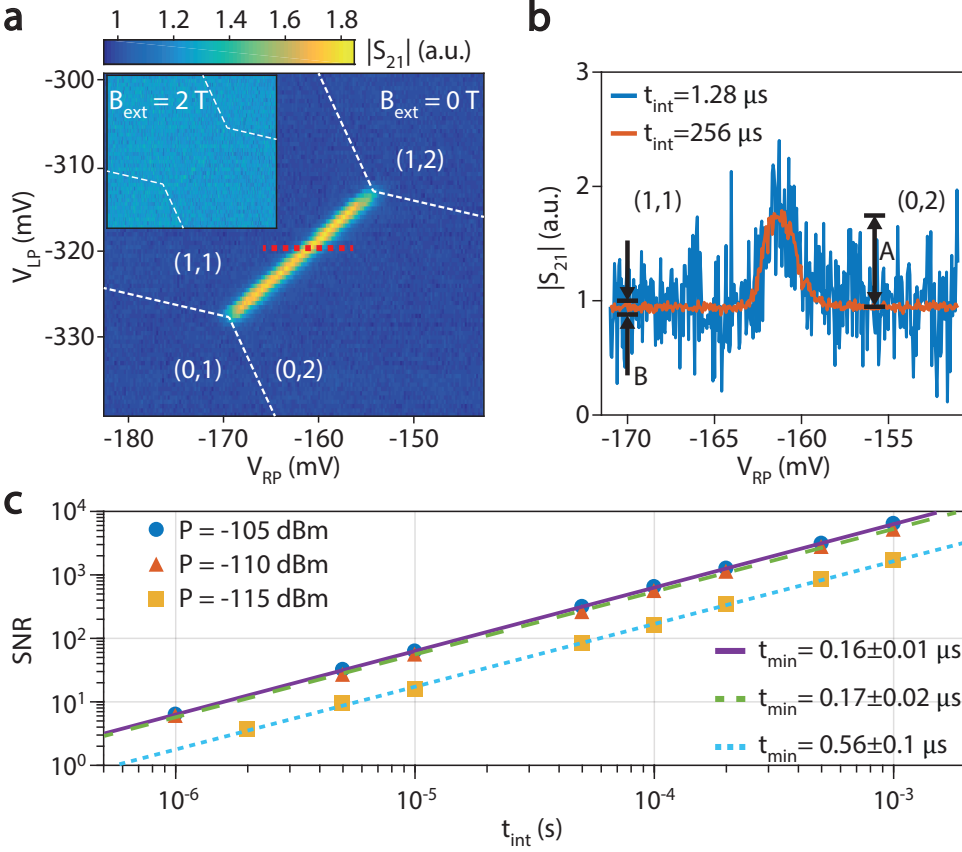
Figure 5.2: **Characterization of the charge sensitivity. a** The transmitted amplitude at 5.7116 GHz and −110 dBm as a function of the voltages applied to LP and RP. The yellow bright line defines the zero detuning axis, along which one electron can tunnel freely between the left and right dots while a second electron remains in the right dot. White dashed lines indicate the boundaries of the charge stability diagrams, where electrons can be added to or removed from the dots. The tunnelling rates to the reservoirs were set well below $f_0$ (making these transitions undetectable by the resonator) to minimize effects from co-tunnelling [11]. The scan was taken by repeatedly applying a 500 Hz sawtooth wave to RP and stepping $V_{LP}$ every 200 ms. Each pixel in the plot has an effective integration time of 1 ms. Inset: exactly the same scan in the presence of an external in-plane magnetic field of 2 T. Here, the probe frequency was set to 5.6930 GHz, to account for a shift of the resonance frequency with magnetic field. The overall transmission in the new frequency range is higher. White dashed lines in the inset are copied from the main plot. **b** Transmitted amplitude versus the voltage on RP around zero detuning (red dashed line in **a**). Data are collected point by point in $V_{RP}$, with integration times of 1.28 μs (blue trace) and 256 μs (red trace). **c** SNR as a function of the integration time. Three sets of data are shown, corresponding to a power of −105 dBm (blue dots), −110 dBm (red triangles) and −115 dBm (yellow squares) through the feedline. Red data points were taken in a slightly different charge configuration from the blue and yellow data points. Each data set is fitted well by a straight line, from which we extrapolate $t_{min}$. The root-mean-square (r.m.s.) noise amplitude $B$ was obtained from time traces containing 1,000 points for each integration time. Errors in $A$ and $B$ translate to uncertainties (standard deviations, s.d.) in SNR that are smaller than the size of the data points.

a ~350 kHz bandwidth. The coupling strength between the DQD and resonator is ~175 MHz. We note that, in general, a larger coupling strength is beneficial for the charge sensitivity provided that the frequency shift is smaller than half the resonator linewidth. Beyond that, the signal saturates (for a fixed power).

## 5.4. Single-shot spin readout

Having characterized the charge sensitivity, we move on to detecting spin states. At $\varepsilon = 0$, the S(1,1) and S(0,2) singlet states hybridize due to a finite interdot tunnel coupling $t_c$. Thus, when the system is in a singlet state, one electron is allowed to tunnel between the dots, loading the resonator as a result. When the system is in one of the triplet states, there is negligible hybridization of the (1,1) and (0,2) states at $\varepsilon = 0$ (the valley splitting is estimated to be ~85 µeV from magnetospectroscopy), so tunnelling is now prohibited and the resonator remains unaffected. At zero magnetic field the two electrons form a spin singlet ground state and a strong signal is observed at zero detuning, as discussed (Fig. 5.2a). When we apply an external in-plane magnetic field $B_{\text{ext}}$ of 2 T, the triplet state T_(1,1) becomes the ground state (Fig. 5.3a). As expected, this suppresses the signal from the S(1,1)-S(0,2) tunnelling significantly (inset, Fig. 5.2a). Here, we benefit from the resiliency of our resonator to high magnetic fields [22].

We probe the spin dynamics of our system by applying voltage pulses to gates LP and RP (Fig. 5.3a), first to empty the left quantum dot at point E (100 µs), then to load an electron with a random spin orientation into the left dot at point L (10 µs), and finally to measure the response of the resonator at point R. We perform 10,000 repetitions of this single-shot cycle, and record time traces of the transmitted signal with an integration time of 1 µs. The traces start 50 µs before to pulsing to point R. The results from 100 cycles are shown in Fig. 5.3b (top panel) with an additional 9 µs integration time set in post-processing of the experimental data. We perform threshold detection, declaring singlet (triplet) when the signal exceeds (does not exceed) a predefined threshold, $|S_{21}|_{\text{th}}$. Two examples of single traces are shown separately in the bottom panel. The blue trace reflects the case in which the two electrons form a spin triplet state; that is, the signal remains low during the entire trace. The red trace corresponds to loading a spin singlet state, which here decays to a T_(1,1) state after ~150 µs. When averaged over all traces, we obtain a characteristic decay with a relaxation time $T_1$ from the singlet to the triplet ground state of 159 µs (Fig. 5.3c). This value of $T_1$ is smaller than typical values for spins in silicon dots, possibly because it is measured at the charge degeneracy point and there is a strong transverse field gradient present along the interdot axis (see also Ref. [19]). We expect that removing the transverse field gradient or orienting it perpendicular to the interdot axis would increase the $T_1$. We note that the spin relaxation rate from the Purcell effect would be several orders of magnitude smaller [32]. Despite the short $T_1$, we can achieve high-fidelity single-shot readout thanks to the high sensitivity and bandwidth of our resonator.

To characterize the spin readout fidelity, we create a histogram of the signal integrated over the first 9 µs in point R. A clear bimodal distribution is visible in Fig. 5.3d. We fit the data to a model that is based on two noise-broadened Gaussian
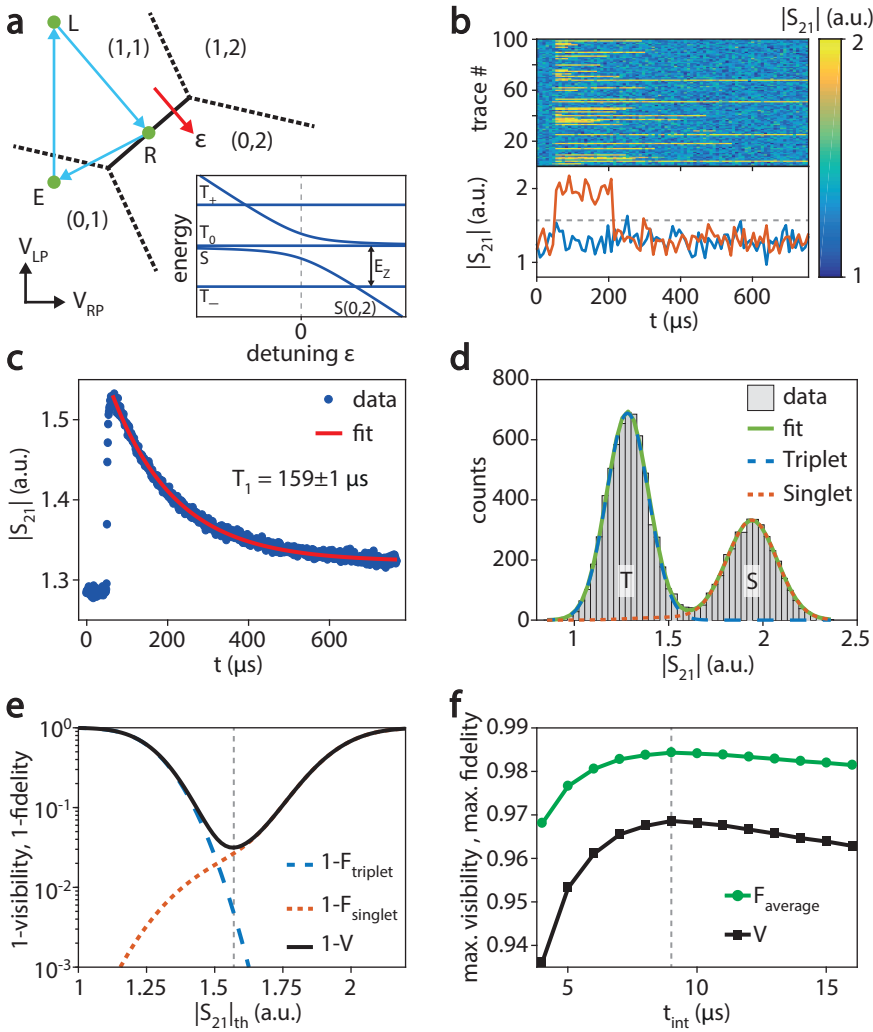
Figure 5.3: **Single-shot spin readout and fidelity analysis. a** Schematic of a typical charge stability diagram with a three-stage pulse sequence. The d.c. voltages on LP and RP are set to point R. Voltage pulses are applied to LP and RP as well. A two-electron energy level diagram as a function of the detuning $\varepsilon$ (red arrow) in a finite magnetic field is shown in the lower half. The $T_{\pm}$ states are separated from $T_0$ by $E_Z = g\mu_B B_{\text{tot}}$, where $g$ is the $g$ factor and $\mu_B$ is the Bohr magneton and $B_{\text{tot}}$ consists of $B_{\text{ext}}$ and the field from the micromagnets. Valley-orbit states are neglected in this diagram for simplicity. **b** A total of 100 single-shot traces with 9 µs averaging time per data point are shown in the top panel as a function of time. The traces start 50 µs before to pulsing to point R. The bright yellow lines correspond to the signal from the spin singlet state. Two traces are shown separately in the bottom panel. For the blue (red) line the electron was loaded into either $T_0(1,1)$ or $T_-(1,1)$ ($S(1,1)$) at point L. The grey dashed line is the optimum threshold $|S_{21}|_{\text{th}} \approx 1.57$. **c** Transmitted amplitude as a function of time shows a typical $T_1$ decay (blue dots). The error in $T_1$ corresponds to the s.d. of the exponential fit (red solid line). Data are taken at 2 T. **d** Measured histogram of the single-shot traces with 9 µs integration time. A model adapted from Ref. [31] was fitted to the data (green solid line) to extract the triplet (blue dashed line) and singlet (red dotted line) distributions. See main text for details. **e** The calculated spin readout fidelities and visibility as a function of threshold amplitude for 9 µs integration. The maximum visibility is found by setting the threshold at $|S_{21}|_{\text{th}} \approx 1.57$. **f** Maximum average fidelity and visibility as a function of the integration time. For each $t_{\text{int}}$, an analysis similar to that in **e** was performed.

distributions with an additional term taking into account the relaxation of the singlet state during the measurement [31]:

$$N(|S_{21}|) = N_{\text{tot}}[P_S n_S + (1 - P_S)n_T]|S_{21}|_{\text{bin}}, \tag{5.1}$$

with

$$n_T = \frac{1}{\sqrt{2\pi}\sigma_T} e^{-\frac{(|S_{21}|-\mu_T)^2}{2\sigma_T^2}} \tag{5.2}$$

the triplet probability density and

$$n_S = \frac{1}{\sqrt{2\pi}\sigma_S} e^{-\frac{(|S_{21}|-\mu_S)^2}{2\sigma_S^2}} e^{-\frac{t_{\text{int}}}{T_1}} +$$

$$\frac{1}{\sqrt{2\pi}\sigma_S} \frac{t_{\text{int}}}{T_1} \int_{\mu_T}^{\mu_S} \frac{1}{\mu_S - \mu_T} e^{-\frac{x-\mu_T}{\mu_S-\mu_T}\frac{t_{\text{int}}}{T_1}} e^{-\frac{(|S_{21}|-x)^2}{2\sigma_S^2}} \, \mathrm{d}x \tag{5.3}$$

the singlet probability density. Here, $\mu_T$ ($\mu_S$) is the average triplet (singlet) signal amplitude, $\sigma_T$ ($\sigma_S$) is the standard deviation of the triplet (singlet) peak, $P_S$ is the probability of loading into S(1,1) and $|S_{21}|_{\text{bin}}$ is the bin size. We note that the singlet peak has a slightly larger spread than the triplet peak. This could be explained by the fact that in addition to the measurement noise that broadens the triplet signal, the singlet signal is also prone to effects of charge noise.

We use the following definition of the readout fidelities: $F_{\text{triplet}} = 1 - \int_{|S_{21}|_{\text{th}}}^{\infty} n_T d|S_{21}|$ and $F_{\text{singlet}} = 1 - \int_{-\infty}^{|S_{21}|_{\text{th}}} n_S d|S_{21}|$. The visibility is defined as $V = F_{\text{triplet}} + F_{\text{singlet}} - 1$. The maximum visibility for 9 µs averaging is 96.9 % (Fig. 5.3e). The corresponding readout fidelity for the singlet (triplet) is 97.3 % (99.5 %), with an average readout fidelity of 98.4 %. We repeat this analysis for various integration times (Fig. 5.3f). The average readout fidelity is above 98 % for $t_{\text{int}}$ greater than 6 µs.

## 5.5. Discussion

Extrapolating our results assuming a $T_1$ of 4.5 ms and $t_{\text{int}} = 16$ µs, a spin readout fidelity of 99.9 % is possible, well above the fault-tolerance threshold. This integration time compares favourably to the millisecond coherence times of dynamically decoupled single spin qubits [33, 34], even taking into account the duration of error correction pulses. Further improvements both in the duration and fidelity of spin readout can be achieved by using quantum-limited amplifiers, such as a Josephson parametric amplifier or a traveling wave parametric amplifier. We expect an order of magnitude shorter readout time to be feasible, assuming the amplifier noise remains the dominant noise source.

Although the readout of singlet-triplet spin states is demonstrated here, this technique can also be applied to detecting addressable single spins provided that there is a reference spin. Manipulation of a single spin can be performed using a separate gate [19], so that the qubit frequency can be far detuned from the

resonator frequency, minimizing the Purcell effect. Unwanted excitations due to a high probe frequency should be negligible provided that the frequency is far detuned from splittings such as the valley and Zeeman splittings.

The range of $t_c$ that gives maximal resonator response (for a fixed power) depends on the DQD-resonator coupling strength. For the present tuning of the sample, a value of $t_c/h$ below ~2 GHz would yield a resonator frequency shift of less than half the resonator linewidth, and would thus not achieve the maximum signal. The $t_c/h$ can be tuned up to ~18 GHz while retaining full signal. However, for spin detection, the valley splitting in our device imposes in practice a much lower upper limit on $t_c$. An increased $t_c$ leads to an increased intervalley tunnel coupling (between T$_-$(1,1) and T$_-$(0,2)), which can also be detected by the resonator when sufficiently large [10], giving the same signal as the singlet state for small valley splittings. A larger valley splitting could mitigate this effect.

## 5.6. Conclusion

In conclusion, we have used a high-$Q$ and high-impedance on-chip superconducting resonator to demonstrate single-shot gate-based spin readout in silicon within a few microseconds. Despite the relatively short $T_1$ in our system, we achieve a spin readout fidelity up to 98.4 % in less than 10 μs. The demonstration of single-shot gate-based spin readout is a crucial step towards readout in dense spin qubit arrays where it is not possible to integrate electrometers and accompanying reservoirs adjacent to the qubit dots. In contrast, multiple qubits on the inside of an array can be probed using a single resonator coupled to a word or bit line in a cross-bar architecture. Furthermore, a single feedline can be used for probing multiple resonators using frequency multiplexing. Moreover, this on-chip superconducting resonator is compatible with other implementations of silicon quantum dot qubits in a magnetic field.

## Acknowledgments

## Author contributions

G.Z., N.S. and L.M.K.V. conceived and planned the experiments. G.Z. and M.L.N. carried out the experiments. A.S. grew the heterostructure with G.S.'s supervision. N.S. designed and fabricated the device. D.B. and N.K. contributed to sample fabrication. G.Z., M.L.N. and L.M.K.V. analysed the results. G.Z. and L.M.K.V. wrote the manuscript with input from all co-authors. L.M.K.V. supervised the project.

## Data availability

The data reported in this paper are archived at `https://doi.org/10.4121/uuid:8df1a6fa-9230-400f-a790-1b7714b1aad5`.

## 5.7. Supplementary materials

### Methods

The microwave response of the resonator was measured using standard heterodyne detection. One of the two microwave sources was used to send a signal with frequency 5.7117 GHz (5.6930 GHz at 2 T) to the feedline, through heavily attenueated semi-rigid coaxial cables. The transmitted response was first amplified at ~4 K using a commercial cryogenic amplifier, then amplified a second time at room temperature using another commercial amplifier. The signal was demodulated using an IQ mixer, with a reference signal from the second microwave source (5 MHz offset). The in-phase and quadrature components were filtered and amplified before being recorded by a giga-sample waveform digitizer to extract the transmitted signal amplitude and phase. The 500 Hz sawtooth wave used for producing the stability diagram as well as the voltage pulses used for unloading and loading an electron were generated by an arbitrary waveform generator.

### Charge stability diagram



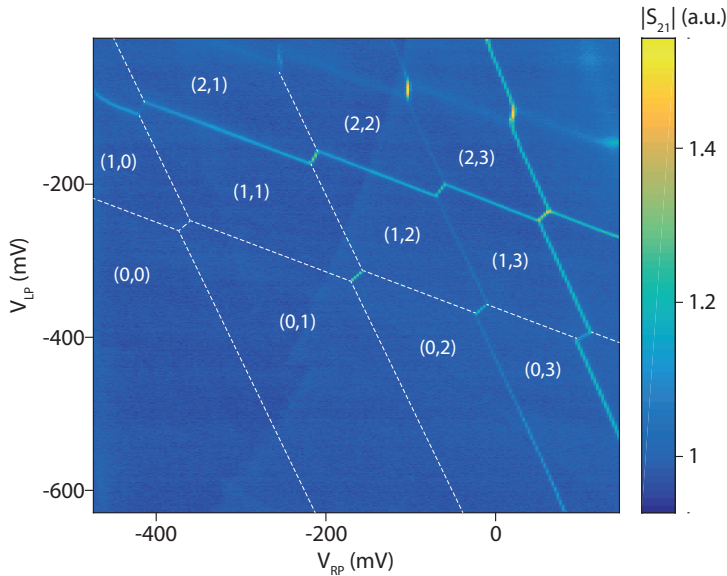Figure 5.4: **DQD stability diagram.** Similar to Fig. 5.2a, with a larger range in $V_{LP}$ and $V_{RP}$. White dashed lines indicate the expected reservoir and interdot transition lines, which are not visible here because the tunnel rates are too low compared to the resonator's resonance frequency. In contrast, the transitions at more positive voltages have a smaller signal because the tunnel rates are too high.

# References

[1] K. Ono, D. G. Austing, Y. Tokura, and S. Tarucha, *Current rectification by pauli exclusion in a weakly coupled double quantum dot system,* Science **297**, 1313 (2002).

[2] J. M. Elzerman, R. Hanson, L. H. Willems van Beveren, B. Witkamp, L. M. K. Vandersypen, and L. P. Kouwenhoven, *Single-shot read-out of an individual electron spin in a quantum dot,* Nature **430**, 431 (2004).

[3] R. Hanson, L. P. Kouwenhoven, J. R. Petta, S. Tarucha, and L. M. K. Vandersypen, *Spins in few-electron quantum dots,* Rev. Mod. Phys. **79**, 1217 (2007).

[4] M. Field, C. G. Smith, M. Pepper, D. A. Ritchie, J. E. F. Frost, G. A. C. Jones, and D. G. Hasko, *Measurements of coulomb blockade with a noninvasive voltage probe,* Phys. Rev. Lett. **70**, 1311 (1993).

[5] C. Barthel, D. J. Reilly, C. M. Marcus, M. P. Hanson, and A. C. Gossard, *Rapid single-shot measurement of a singlet-triplet qubit,* Phys. Rev. Lett. **103**, 160503 (2009).

[6] L. M. K. Vandersypen, H. Bluhm, J. S. Clarke, A. S. Dzurak, R. Ishihara, A. Morello, D. J. Reilly, L. R. Schreiber, and M. Veldhorst, *Interfacing spin qubits in quantum dots and donors–hot, dense, and coherent,* npj Quantum Information **3**, 34 (2017).

[7] M. Veldhorst, H. G. J. Eenink, C. H. Yang, and A. S. Dzurak, *Silicon cmos architecture for a spin-based quantum computer,* Nature Communications **8**, 1766 (2017).

[8] R. Li, L. Petit, D. P. Franke, J. P. Dehollain, J. Helsen, M. Steudtner, N. K. Thomas, Z. R. Yoscovits, K. J. Singh, S. Wehner, L. M. K. Vandersypen, J. S. Clarke, and M. Veldhorst, *A crossbar network for silicon quantum dot qubits,* Science Advances **4** (2018), 10.1126/sciadv.aar3960.

[9] J. I. Colless, A. C. Mahoney, J. M. Hornibrook, A. C. Doherty, H. Lu, A. C. Gossard, and D. J. Reilly, *Dispersive readout of a few-electron double quantum dot with fast rf gate sensors,* Phys. Rev. Lett. **110**, 046805 (2013).

[10] A. C. Betz, R. Wacquez, M. Vinet, X. Jehl, A. L. Saraiva, M. Sanquer, A. J. Ferguson, and M. F. Gonzalez-Zalba, *Dispersively detected pauli spin-blockade in a silicon nanowire field-effect transistor,* Nano Letters **15**, 4622 (2015).

[11] M. G. House, T. Kobayashi, B. Weber, S. J. Hile, T. F. Watson, J. van der Heijden, S. Rogge, and M. Y. Simmons, *Radio frequency measurements of tunnel couplings and singlet-triplet spin states in si:p quantum dots,* Nature Communications **6**, 8848 (2015).

5

[12] A. Crippa, R. Ezzouch, A. Aprá, A. Amisse, R. Laviéville, L. Hutin, B. Bertrand, M. Vinet, M. Urdampilleta, T. Meunier, M. Sanquer, X. Jehl, R. Maurand, and S. De Franceschi, *Gate-reflectometry dispersive readout and coherent control of a spin qubit in silicon,* Nature Communications **10**, 2776 (2019).

[13] P. Pakkiam, A. V. Timofeev, M. G. House, M. R. Hogg, T. Kobayashi, M. Koch, S. Rogge, and M. Y. Simmons, *Single-shot single-gate rf spin readout in silicon,* Phys. Rev. X **8**, 041032 (2018).

[14] A. West, B. Hensen, A. Jouan, T. Tanttu, C.-H. Yang, A. Rossi, M. F. Gonzalez-Zalba, F. Hudson, A. Morello, D. J. Reilly, and A. S. Dzurak, *Gate-based single-shot readout of spins in silicon,* Nature Nanotechnology **14**, 437 (2019).

[15] M. Urdampilleta, D. J. Niegemann, E. Chanrion, B. Jadot, C. Spence, P.-A. Mortemousque, C. Bäuerle, L. Hutin, B. Bertrand, S. Barraud, R. Maurand, M. Sanquer, X. Jehl, S. De Franceschi, M. Vinet, and T. Meunier, *Gate-based high fidelity spin readout in a cmos device,* Nature Nanotechnology **14**, 737 (2019).

[16] M. F. Gonzalez-Zalba, S. Barraud, A. J. Ferguson, and A. C. Betz, *Probing the limits of gate-based charge sensing,* Nature Communications **6**, 6084 (2015).

[17] A. Rossi, R. Zhao, A. S. Dzurak, and M. F. Gonzalez-Zalba, *Dispersive readout of a silicon quantum dot with an accumulation-mode gate sensor,* Applied Physics Letters **110**, 212101 (2017).

[18] D. de Jong, J. van Veen, L. Binci, A. Singh, P. Krogstrup, L. P. Kouwenhoven, W. Pfaff, and J. D. Watson, *Rapid detection of coherent tunneling in an* InAs *nanowire quantum dot through dispersive gate sensing,* Phys. Rev. Applied **11**, 044061 (2019).

[19] X. Mi, M. Benito, S. Putz, D. M. Zajac, J. M. Taylor, G. Burkard, and J. R. Petta, *A coherent spin-photon interface in silicon,* Nature **555**, 599 (2018).

[20] M. S. Khalil, M. J. A. Stoutimore, F. C. Wellstood, and K. D. Osborn, *An analysis method for asymmetric resonator transmission applied to superconducting devices,* Journal of Applied Physics **111**, 054510 (2012).

[21] N. Samkharadze, G. Zheng, N. Kalhor, D. Brousse, A. Sammak, U. C. Mendes, A. Blais, G. Scappucci, and L. M. K. Vandersypen, *Strong spin-photon coupling in silicon,* Science **359**, 1123 (2018).

[22] N. Samkharadze, A. Bruno, P. Scarlino, G. Zheng, D. P. DiVincenzo, L. DiCarlo, and L. M. K. Vandersypen, *High-kinetic-inductance superconducting nanowire resonators for circuit qed in a magnetic field,* Phys. Rev. Applied **5**, 044004 (2016).

[23] A. Cottet, C. Mora, and T. Kontos, *Mesoscopic admittance of a double quantum dot,* Phys. Rev. B **83**, 121311 (2011).

[24] K. D. Petersson, L. W. McFaul, M. D. Schroer, M. Jung, J. M. Taylor, A. A. Houck, and J. R. Petta, *Circuit quantum electrodynamics with a spin qubit,* Nature **490**, 380 (2012).

[25] T. Frey, P. J. Leek, M. Beck, A. Blais, T. Ihn, K. Ensslin, and A. Wallraff, *Dipole coupling of a double quantum dot to a microwave resonator,* Phys. Rev. Lett. **108**, 046807 (2012).

[26] S. J. Chorley, J. Wabnig, Z. V. Penfold-Fitch, K. D. Petersson, J. Frake, C. G. Smith, and M. R. Buitelaar, *Measuring the complex admittance of a carbon nanotube double quantum dot,* Phys. Rev. Lett. **108**, 036802 (2012).

[27] A. J. Landig, J. V. Koski, P. Scarlino, U. C. Mendes, A. Blais, C. Reichl, W. Wegscheider, A. Wallraff, K. Ensslin, and T. Ihn, *Coherent spin-photon coupling using a resonant exchange qubit,* Nature **560**, 179 (2018).

[28] D. I. Schuster, A. Wallraff, A. Blais, L. Frunzio, R.-S. Huang, J. Majer, S. M. Girvin, and R. J. Schoelkopf, *ac stark shift and dephasing of a superconducting qubit strongly coupled to a cavity field,* Phys. Rev. Lett. **94**, 123602 (2005).

[29] R. Mizuta, R. M. Otxoa, A. C. Betz, and M. F. Gonzalez-Zalba, *Quantum and tunneling capacitance in charge and spin qubits,* Phys. Rev. B **95**, 045414 (2017).

[30] J. Stehlik, Y.-Y. Liu, C. M. Quintana, C. Eichler, T. R. Hartke, and J. R. Petta, *Fast charge sensing of a cavity-coupled double quantum dot using a josephson parametric amplifier,* Phys. Rev. Applied **4**, 014018 (2015).

[31] C. Barthel, D. J. Reilly, C. M. Marcus, M. P. Hanson, and A. C. Gossard, *Rapid single-shot measurement of a singlet-triplet qubit,* Phys. Rev. Lett. **103**, 160503 (2009).

[32] A. Bienfait, J. J. Pla, Y. Kubo, X. Zhou, M. Stern, C. C. Lo, C. D. Weis, T. Schenkel, D. Vion, D. Esteve, J. J. L. Morton, and P. Bertet, *Controlling spin relaxation with a cavity,* Nature **531**, 74 (2016).

[33] M. Veldhorst, J. C. C. Hwang, C. H. Yang, A. W. Leenstra, B. de Ronde, J. P. Dehollain, J. T. Muhonen, F. E. Hudson, K. M. Itoh, A. Morello, and A. S. Dzurak, *An addressable quantum dot qubit with fault-tolerant control-fidelity,* Nature Nanotechnology **9**, 981 (2014).

[34] J. Yoneda, K. Takeda, T. Otsuka, T. Nakajima, M. R. Delbecq, G. Allison, T. Honda, T. Kodera, S. Oda, Y. Hoshi, N. Usami, K. M. Itoh, and S. Tarucha, *A quantum-dot spin qubit with coherence limited by charge noise and fidelity higher than 99.9%,* Nature Nanotechnology **13**, 102 (2018).

**5**

# 6

# On-chip microwave filters for high-impedance resonators with gate-defined quantum dots

P. Harvey-Collard, **G. Zheng**, J. Dijkema, N. Samkharadze, A. Sammak, G. Scappucci, L. M. K. Vandersypen

*In circuit QED with semiconductor quantum-dot-based qubits, increasing the resonator impedance is desirable as it enhances the coupling to the typically small charge dipole moment of these qubits. However, the gate electrodes necessary to form quantum dots in the vicinity of a resonator inadvertently lead to a parasitic port through which microwave photons can leak, thereby reducing the quality factor of the resonator. This is particularly the case for high-impedance resonators, as the ratio of their total capacitance over the parasitic port capacitance is smaller, leading to larger microwave leakage than for $50\,\Omega$ resonators. Here, we introduce an implementation of on-chip filters to suppress the microwave leakage. The filters comprise a high-kinetic-inductance nanowire inductor and a thin-film capacitor. The filter has a small footprint and can be placed close to the resonator, confining microwaves to a small area of the chip. The inductance and capacitance of the filter elements can be varied over a wider range of values than their typical spiral inductor and interdigitated capacitor counterparts. We demonstrate that the total linewidth of a $6.4\,\mathrm{GHz}$ and $\sim 3\,\mathrm{k\Omega}$ resonator can be improved down to $540\,\mathrm{kHz}$ using these filters.*

## **6.1.** Introduction

The gate electrodes necessary to form quantum dots in the vicinity of a resonator inadvertently lead to a parasitic capacitance through which microwave photons can leak, thereby reducing the quality factor of the resonator significantly [1]. This effect is more pronounced for high-impedance resonators, i.e. with impedance in the kiloohm range, as the ratio of their total capacitance over the parasitic capacitance is smaller, leading to larger microwave leakage than for $50\,\Omega$ resonators. To mitigate this leakage, symmetric [2] and dipolar[1] [3] mode resonators have been developed that reduce the mode coupling to the gates, while gate filters [1] have been employed for popular half- and quarter-wave coplanar resonators with monopolar modes. Until now, the efficiency of gate filters has not been demonstrated in combination with high-impedance resonators that require heavy filtering. Furthermore, current designs have a problematic footprint, including a large interdigitated capacitor and a spiral inductor looping around a bondpad. In this work, we develop on-chip filters, consisting of a high-kinetic-inductance nanowire serving as a compact inductor and a small thin-film capacitor, to mitigate leakage from a high-impedance half-wave resonator with silicon DQDs at each end. The resonator and inductors are patterned from the same high-kinetic-inductance NbTiN film on a [28]Si/SiGe heterostructure. We use prototyping chips to mimic the parasitic losses by the QD gates with faster fabrication and measurement turnaround than full devices, while minimizing the other lossy mechanisms like dielectric and resistive losses. Finally, we compare thin-film capacitor filters with interdigitated capacitor filters on the aspects of performance, footprint and integrability.

## **6.2.** Methods

The full device being optimized in this work is shown in Fig. 6.1a. A high-impedance superconducting resonator is etched from a thin, high-kinetic-inductance NbTiN film. At each end of the resonator with angular frequency $\omega_r$ and impedance $Z_r$, a DQD gate structure is fabricated with one accumulation gate attached to the resonator's end, similarly to the device of Ref. [4]. The charge displacement in the DQD is then linked to the zero-point root-mean-square voltage swing $V_{rms} \propto \omega_r\sqrt{Z_r}$ at the resonator end through the gate lever arm $\alpha$, allowing a dot-resonator interaction of strength $g_C \propto \alpha V_{rms}$ [5]. Maximizing this interaction can help reach the strong spin-photon coupling regime [4, 6, 7] and increases the sensitivity of the resonator for readout [8].

This work focuses on reducing the linewidth $\kappa/2\pi$, or improving the quality factor $Q = \omega_r/\kappa$, of the high-impedance resonator using on-chip filters. We model the behavior of this device using the electrical circuit shown in Fig. 6.1b. The resonator can be roughly approximated as an interrupted coplanar waveguide [9], with a half-wave mode $\lambda/2$ and a quarter-wave mode $\zeta/4$. The quarter-wave mode arises from the "T"-shaped section of the resonator direct current (DC) biasing line terminated by an alternating current (AC) ground provided by the filter (Fig. 6.1b). With a frequency roughly half of the $\lambda/2$ mode, it is used as a diagnostics tool

---

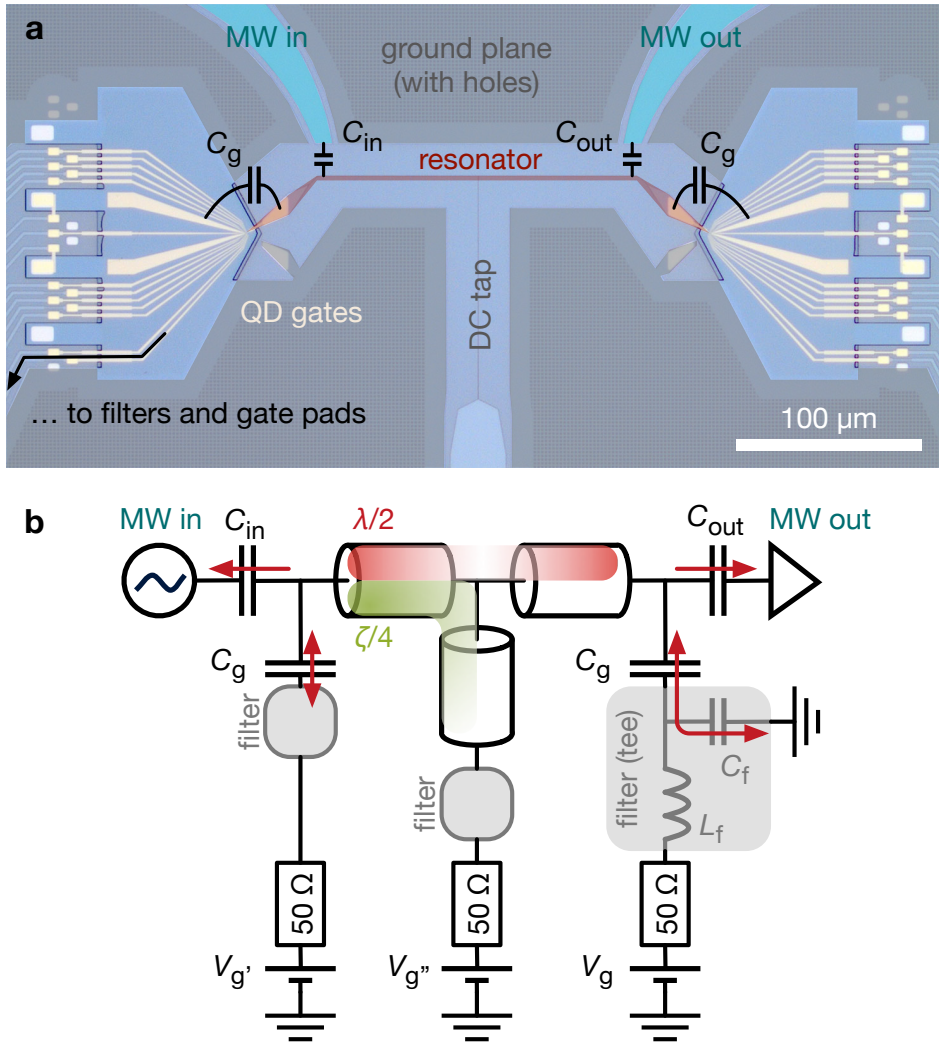[1]Such as the resonator design in Chap. 4 and 5.

Figure 6.1: **a** Optical image with false-color shading of the central area of the device, showing the superconducting high-impedance nanowire resonator (in red) and the QD gates of a full device (in yellow). **b** Simplified electrical circuit of the resonator and its surrounding components. The resonance modes of this device can be understood using three sections of coplanar waveguides with appropriate capacitance and inductance per unit length, $\tilde{c}_r$ and $\tilde{l}_r$, respectively. A half-wave mode $\lambda/2$ couples the DQDs at each end of the resonator in antiphase, whereas a quarter-wave mode $\zeta/4$ also exists where both DQDs are coupled in phase (only one side of the mode is shown for simplicity). The resonator is probed in transmission through the "in" and "out" ports with coupling capacitances $C_{in}$ and $C_{out}$. Because of the physical footprint of the DQD gates at each end, an extra capacitance $C_g \gg \{C_{in}, C_{out}\}$ causes the microwave energy to escape from the resonator primarily through the gate fanout lines. To prevent irreversible loss, modelled here by $50\,\Omega$ resistors, low-loss microwave filters are fabricated on-chip to reflect the microwaves back into the resonator. Filters act as AC grounds through a bias tee effect. The path of energy escaping the $\lambda/2$ mode is represented by red arrows, with double-ended arrows representing a reflection back into the resonator.

for the work that follows. The inductance per unit length $\tilde{L}_r$ is dominated by the kinetic inductance contribution of the NbTiN film section near the current antinode, with nominal sheet inductance 115 pH/□. The nanowire width, in the range 100 to 200 nm, serves to adjust the frequency [3]. The kinetic inductance is almost 1000 times larger than the geometric inductance. The effective capacitance per unit length $\tilde{C}_r$ is influenced to a large extent by the end sections of the resonator near the voltage antinodes. A typical frequency is $\omega_{\lambda/2}/2\pi = 6.4$ GHz and $Z_r \sim 3$ kΩ. The end-to-end length is $l_r = 250$ μm, which is much smaller than the ~9 mm of a coplanar resonator without kinetic inductance. A numerical circuit model and additional details can be found in Sec. 6.5.2.

We now illustrate why the losses through the gates are increasingly problematic as the resonator impedance increases. We first note that the coupling losses can be approximated in our regime by [10]

$$\kappa_g = \frac{2}{\pi}\omega_r^3 Z_r Z_g C_g^2, \tag{6.1}$$

which shows that the losses through a gate fanout $\kappa_g$, with fixed fanout impedance $Z_g$, scale as $Z_r$. For a 3 kΩ resonator, the coupling loss is about 60 times worse than for an equivalent 50 Ω resonator, or 10 times worse than for a 300 Ω one. We use this ideal waveguide formula to get insights into the scaling of leakage but do not rely on quantitative predictions since the gate fanout lines are not simple waveguides. The resonator is probed in transmission, with input and output capacitance $C_{in} = C_{out} = 0.28$ fF. The capacitance between each resonator end and the DQD gate ensemble is found to be $C_g = 1.8$ fF using numerical simulations with COMSOL. Using an equivalent lumped-element parallel $LCR$ oscillator [9], we estimate a resonator capacitance of $\tilde{C}_r l_r/2 \approx 8$ fF before gate loading. Hence, the gates contribute a significant fraction of the total capacitance, which is a direct side effect of the large bare impedance $Z_r' = (\tilde{L}_r/\tilde{C}_r)^{1/2} \approx 4$ kΩ at fixed $\omega_r$. Given the large contribution of the gates, improved mitigation strategies need to be devised compared with previous work [1]. The benefit of this large impedance is a large charge-photon coupling strength $g_c/2\pi \sim 200$ MHz [4]. Other work with high-impedance resonators has so far been limited to linewidths $\kappa/2\pi > 10$ MHz [7, 11], with the exception of Ref. [4] where the resonator geometry is not suitable for the coupling of distant qubits. Meanwhile, a reasonable target to achieve two-qubit gates in the dispersive regime would be $\kappa/2\pi < 1$ MHz [12]. This target value is comparable to other ~50 Ω resonators used for spin-photon coupling experiments [1, 13], and is also lower than current spin dephasing rates in current silicon devices with strong coupling [4, 14].

We propose and demonstrate two models of gate filters to suppress leakage of photons through the gates, which are shown in Fig. 6.2. Previous implementations have relied on spiral inductors that loop around bondpads [1]. Their drawback is that they have a footprint at least as large as a bond pad, and that the inductance values are typically in the tens of nH. The capacitor therefore needs to be large to maintain the $LC$ filter angular cutoff frequency $2\pi f_f = (L_f C_f)^{-1/2}$. We advantageously use the high kinetic inductance of the NbTiN film to etch low-loss and
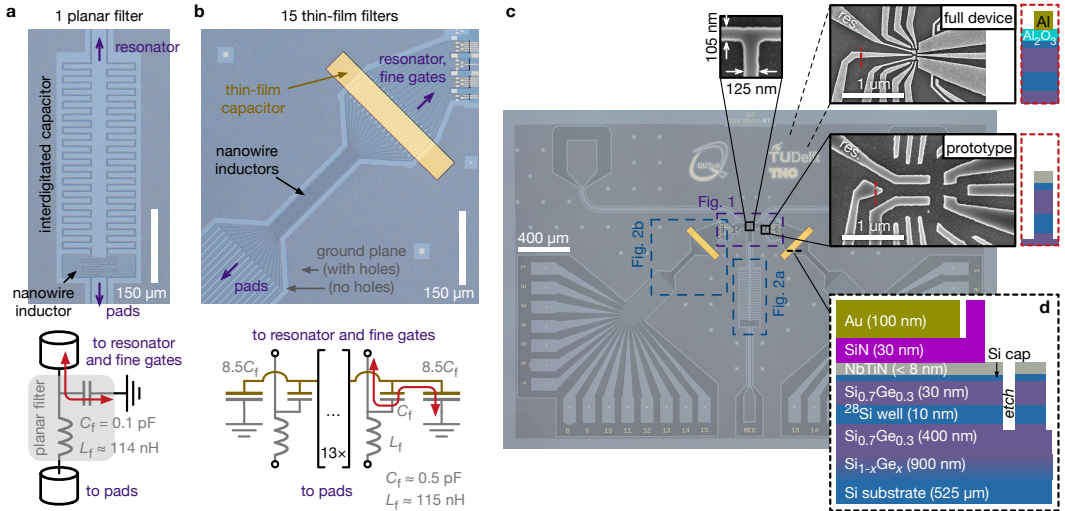
Figure 6.2: **a** Optical image of a planar filter with one line. Each filter can be thought of as an LC microwave bias tee. The inductor $L_f$ consists of a superconducting high-kinetic-inductance nanowire made from the same film as the resonator. The capacitor $C_f$ has an interdigitated geometry. Both components are low-loss, thanks to superconducting metals and the absence of amorphous dielectrics. The nanowire inductor is much smaller than an equivalent spiral inductor and does not require looping around a bondpad, allowing the filter to be placed closer to the active area. The interdigitated capacitor is still relatively large. **b** Optical image of a thin-film filter with 15 gate lines (with the same scale as **a**). The thin-film capacitor can be made a lot smaller than its interdigitated equivalent and straddles multiple gate lines at once, thereby dramatically reducing the footprint and simplifying the microwave hygiene. In this implementation, the top capacitor plate is electrically floating to further simplify the integration. The large $8.5C_f$ series capacitance of the capacitor plate to the ground plane acts as a short for the relevant frequencies. **c** Stitched optical image of a full device chip (4 mm by 2.8 mm) with thin-film filters. To single out the effects from the capacitive loading of the resonator by the gates while minimizing any other loss mechanisms, we used prototyping chips built from the same processed wafers as the full devices, but the quantum dot areas do not include any of the implanted regions, the gate oxide, or the implant contact pads. The insets show electron microscope images of the nanowire resonator DC tap intersection, the prototyping fine gates mockup and full device fine gates. The mockup and full devices have identical capacitive load, 1.8 fF per DQD. **d** Material stack of a thin-film capacitor prototyping chip. See Sec. 6.5.1 for details.

compact nanowire inductors. Given a target sheet inductance of 115 pH/□, and a nanowire of length 380 µm and width 380 nm, an inductance of 115 nH can easily be achieved. The resulting planar filter with $f_f \approx 1.5$ GHz is shown in Fig. 6.2a. Still, the footprint of typical interdigitated capacitors remains problematic due to their large size, and since extra space has to be allocated between bond pads to allow the ground plane access in-between each line. Our target is 15 gate lines per DQD. We therefore also test a thin-film capacitor with SiN dielectric that straddles 15 gate lines at once, and contacts with the ground plane through a larger series capacitor that acts as a short at the frequencies of interest, as shown in Fig. 6.2b. Floating the capacitor top plate is not necessary, but it allows for a single-step liftoff of both the SiN dielectric and the Au metal top plate. As a result, capacitors in the 0.1 to 1 pF range can be produced with small footprints. Combining the nanowire inductors and the thin-film capacitor, the entire set of filters for 15 lines can fit in the footprint required for a single planar filter. This design also allows us to limit the microwaves to an area much closer to the resonator, simplifying its integration.

6

In order to test the efficacy of the filters, we use a prototyping chip which is a simplified version of the full device, as shown in Fig. 6.2c. This prototyping chip is made from the same wafers that are used for full devices. All the linewidths reported in this work come from these prototypes. The 100 mm $^{28}$Si/SiGe wafers have been processed with the ion-implanted regions, the 5-to-7-nm-thin NbTiN film, the $Al_2O_3$ gate dielectric, and the Ti/Pt contacts to the implanted regions and the NbTiN film; then diced in 20 mm coupons. Each coupon is further processed with one electron beam lithography and SF$_6$He reactive ion etching step to define the superconducting elements; optionally one electron beam lithography and liftoff step to pattern the SiN/Au thin-film capacitor stack (Fig. 6.2d); followed by dicing into 4 mm by 2.8 mm individual devices. The pattern is offset such that there is none of the $Al_2O_3$ gate dielectric or the Ti/Pt contacts used in full devices while using the same starting pieces. Further fabrication details can be found in Sec. 6.5.1. To accurately capture the effects of the resonator capacitive loading by the gate structure, a simplified version of the gates is patterned directly into the supercon-ducting film, as shown in Fig. 6.2c. This structure has the same capacitance to the resonator as the real gates, according to numerical simulations with COMSOL. Hence, the resonator losses should be dominated by microwave leakage into the gate fanout, as opposed to dielectric or resistive losses. The devices are then mea-sured in a $^3$He refrigerator with a base temperature of ~270 mK, unless otherwise specified. Setup details can be found in Sec. 6.5.3. The gate pads of each DQD are wirebonded to each other, and then to a common port with a 50 Ω termination (one line per DQD side) on a five ports printed circuit board (PCB). This simulates the irreversible loss of microwaves in a dilution refrigerator with resistive-capacitive filters and instruments attached to each gate line. Linewidth analysis details can be found in Sec. 6.5.4.

## **6.3.** Results

### **6.3.1.** Planar filters

We now turn to the results for devices with planar filters, which are summarized in Fig. 6.3. We first validated the experimental protocol with various consistency checks. We have verified that the devices measured in our $^3$He system have similar linewidths, both the good and poor ones, to the ones obtained in our dilution refrigerator setup with all gate lines connected individually to real instruments. Second, we measured "no filters" devices and found that the linewidth is so broad that the resonances can barely be found, and at times cannot be seen at all. This usually means that the linewidth is $\gtrsim 15$ MHz. This is to be compared with the coupling linewidths $\kappa_{\zeta/4}^{\text{ext}}/2\pi \sim 0.03$ MHz and $\kappa_{\lambda/2}^{\text{ext}}/2\pi \sim 0.2$ MHz, estimated from numerical simulations. As the resonator is usually undercoupled, the improvements in linewidths are also visible in the larger transmission amplitude. A "no gates" variant, not shown in the figure, is meant as a control experiment to measure frequencies and linewidths in the absence of gate loading. Typical values yield $\kappa_{\zeta/4}/2\pi = 0.3$ MHz and $\kappa_{\lambda/2}/2\pi = 0.9$ MHz for the two modes. Because of the device-to-device variability in resonance frequency, it is difficult to precisely measure the gate loading (the difference in frequency between the "no gates" and "with gates" prototypes). The variability is due partly to the thicker superconducting film in the wafer center, and partly to the lithographic variability of long narrow features. Nevertheless, we usually see a 0.5 to 1 GHz frequency difference between the "no gates" and "with gates" prototypes, in line with our estimates from numerical simulations. Finally, a very useful consistency check is the "wirebond surgery" technique. This consists of adding extra wirebonds to a previously measured device to diagnose the cause of the failure or suboptimal linewidth. It is usually possible to short the gate lines directly to the ground plane before the filters, and even a few hundreds of microns from the resonator, to effectively remove the gate fanout losses. This useful technique allows us to confidently identify failure mechanisms due to filters, as opposed to an accidental failure of the resonator for example, with minimal work.

Next, we look at the various prototypes shown in Fig. 6.3. The experimental splits are designed to separate the problems caused by insufficient or defective filtering from those caused by poor microwave hygiene. Because of the large kinetic inductance of the superconducting film, certain waveguides or parts of the gate fanout lines can have associated wavelengths that are problematic at the frequencies of interest, effectively causing spurious resonances at a scale that would be otherwise unexpected. Another potential problem can be the finite inductance between different ground plane sections causing out-of-phase return currents that hinder the functioning of components. These problems are generically referred to as microwave hygiene problems. To keep the fabrication process simple and maintain magnetic field compatibility, we opted not to locally deposit a thicker ground plane, and to avoid the use of air bridges. The different ground plane sections are always connected with crossbonds, as is common practice. In the case of the "few pads" prototypes, we specifically test extra crossbonds between the capacitors.

The most striking feature seen in the top row of Fig. 6.3 is that the filters seem

| No filters | | |
|---|---|---|


| $\kappa_{\zeta/4}/2\pi$ | $\kappa_{\lambda/2}/2\pi$ | Expected |
|---|---|---|
| X | X | X |

| **With wirebond surgery** | 0.37 MHz | 0.44 MHz | ✓ |
|---|---|---|---|

| Filters (0.5 $L_f$ and 1 $L_f$) | | |
|---|---|---|

| $\kappa_{\zeta/4}/2\pi$ | $\kappa_{\lambda/2}/2\pi$ | Expected | |
|---|---|---|---|
| 0.69 MHz | X | **0.5$L_f$** | ✓ |
| 0.40 MHz | X | **1$L_f$** | ✓ |
| 0.24 MHz | 0.48 MHz | **0.5$L_f$** | ✓ |
| 0.42 MHz | 0.31 MHz | **1$L_f$** | ✓ |

| Few pads (*with/without extra crossb.*) | | |
|---|---|---|

| $\kappa_{\zeta/4}/2\pi$ | $\kappa_{\lambda/2}/2\pi$ | Expected | |
|---|---|---|---|
| 0.36 MHz | X | **without** | ✓ |
| 0.21 MHz | 0.56 MHz | **with** | ✓ |

| One pad (0.5 $C_f$) | | |
|---|---|---|

| $\kappa_{\zeta/4}/2\pi$ | $\kappa_{\lambda/2}/2\pi$ | Expected |
|---|---|---|
| 1.25 MHz | 3.61 MHz | ✓ |

| One pad (1 $C_f$) | | |
|---|---|---|

| $\kappa_{\zeta/4}/2\pi$ | $\kappa_{\lambda/2}/2\pi$ | Expected |
|---|---|---|
| 0.31 MHz | 0.24 MHz | ✓ |

| One pad, *long narrow lines* | | |
|---|---|---|

| $\kappa_{\zeta/4}/2\pi$ | $\kappa_{\lambda/2}/2\pi$ | Expected |
|---|---|---|
| 0.51 MHz | 0.98 MHz | ✓ |

Figure 6.3: Summary for planar filter prototypes. The $\zeta/4$ mode frequencies lie between 3 and 4 GHz, while the $\lambda/2$ mode frequencies lie between 6 and 7.5 GHz. The experimental splits were designed to separate the problems caused by insufficient or defective filtering from those caused by poor microwave hygiene. For each prototype, up to three variants were tested. A "no gates" variant, not shown in the table, is meant as a control experiment to measure frequencies and linewidths in absence of gate loading. Typical values yield $\kappa_{\zeta/4}/2\pi = 0.3$ MHz and $\kappa_{\lambda/2}/2\pi = 0.9$ MHz for the two modes. The "with gates" variant mimics the full devices. In certain cases, after initial measurements, extra wirebonds shorting the gates to the ground plane are added close to the resonator area and chips are then remeasured, resulting in the "with wirebond surgery" variant. This sanity check procedure is useful to verify that the failure of chips is due to insufficient filtering or poor microwave hygiene, and not due to other problems like a resonator defect. The color coding is a subjective assessment of whether or not the linewidth was optimal, with green being very close to ideal ($\lesssim 0.5$ MHz), yellow being not ideal but still $\lesssim 4$ MHz, and red being >10 MHz. For this set, $L_f \approx 114$ nH and $C_f \approx 0.1$ pF. The 'expected' column is a binary assessment of whether the linewidth should be narrow (✓) or broad (X) based on the presence or absence of filtering. See main text for discussion.

to be somewhat effective for the quarter-wave mode, but not for the half-wave mode. We attribute this to a microwave hygiene problem, where the filters are only effective for the quarter-wave mode because of its lower frequency. The "one pad" prototypes in the second row mean to test the design of a single planar filter while ensuring proper microwave hygiene. Therefore, all gates are attached to the same filter unit and surrounded by a well connected ground plane. Here, we find that the prototype with $0.5C_f$ has larger linewidths than the prototype with $1C_f$, which we attribute to a difference in filtering efficacy. To further our understanding, we also test a variant that has longer sections of narrow gate lines before the filter ("one pad, long narrow lines"). We find that the linewidths are not as small as our best performing "one pad" device, but still considered acceptable. We think it is possibly due to the distance between the resonator and filter that interferes with the filtering. Notably, the linewidths of good prototypes with gates are consistently smaller than those without gates, an effect that we attribute to the larger total capacitance, hence lower impedance and frequency, of gated prototypes.

The first row "few pads" prototype means to test the microwave hygiene further in the case where a bigger chip size would ultimately be adopted. The hypothesis is that the failure of the "filters" prototypes from the first row comes from the insufficient space between the gate pads. Because of the high kinetic inductance, the sections connecting the interdigitated capacitors to the rest of the ground plane act as inductors, hindering their action. Results show that the extra space allowed between the pads in the "few pads" prototype does not help. However, adding crossbonds to further distribute the ground plane potential improves the linewidth of the high frequency mode to a good level. This seems an acceptable design with efficient filters, with the caveat that the footprint allowed a maximum of 5 or 6 gate lines per DQD given our chip size.

Finally, we note that the results for the quarter-wave mode linewidths in the $0.5$ and $1L_f$ variants are in qualitative agreement with those of the $0.5$ and $1C_f$ variants, but they are convoluted with the microwave hygiene issue aforementioned.

### 6.3.2. Thin-film filters

In order to find a more extensible solution to the filtering problem, we turn to a thin-film capacitor design, shown in Fig. 6.4a. This design reaches the target of 15 gate lines per DQD. An example device is shown in Fig. 6.2c, and the filter operation is described in Fig. 6.2b. For experimental splits, we change the area of the $C_f$ capacitor, as well as the deposition conditions for the SiN film. We also cool down several instances of each prototype. One reason for this extensive testing is to verify whether there is a critical area beyond which the dielectric losses in the thin-film capacitor would degrade the quality of the filtering. From a simple lumped-element circuit model perspective, the larger the capacitance is, the more efficient the filtering should be. In practice however, it is useful to only use the minimum amount of filtering (i.e. highest $f_f$ possible), since this allows control signals to the DQDs with less distortion. We find that the size of the capacitor does not have a large effect on the linewidth. Most devices perform acceptably with linewidths $<1.25\,\text{MHz}$. However, a few devices have linewidths that are significantly
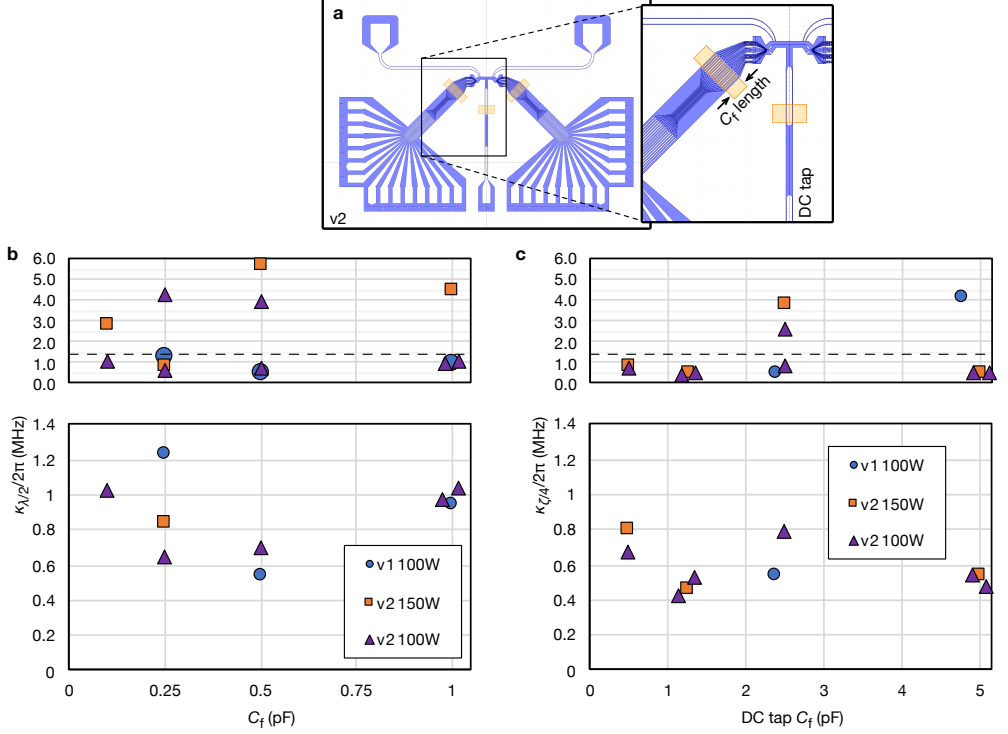
Figure 6.4: Summary for thin-film filter prototypes. **a** The experimental splits were designed to test the impact of the capacitor area, by changing the length of the capacitor (as shown in the inset), and include results from two very slightly different designs (v1 and v2) and SiN deposition powers (100 W and 150 W). The capacitor $C_f = 1$ pF has a width of 6 μm (top plate width of 320 μm) and length of 100 μm, while the SiN thickness is 30 nm. **b** The $\lambda/2$ mode frequencies lie between 6 and 7.5 GHz. Two groups are observed: good devices with $\kappa_{\lambda/2}/2\pi < 1.25$ MHz, and poor devices with $\kappa_{\lambda/2}/2\pi > 2$ MHz. The reason for their failure is unknown, but in two cases we have verified that the resonance is recovered using wirebond surgery with linewidths 1.1 MHz and 0.7 MHz. The best performing device achieved $\kappa_{\lambda/2}/2\pi = 0.540$ MHz, or a quality factor of 11900. **c** Linewidths for the $\zeta/4$ mode. The DC tap capacitor for this mode is scaled up in size compared with the gate line capacitors to improve the AC grounding of the mode (see main text). While the half-wave mode is insensitive to losses through the DC tap because of its symmetry, the quarter-wave mode can lose energy through both the gate lines and the DC tap, making the contributions from the different filters convoluted for this mode. In all plots, some points are slightly offset horizontally for clarity.

broader than this. In two of those devices, wirebond surgery successfully recovered a linewidth comparable to the best devices. This seems to indicate a problem with the filters. This type of failure was not observed in later fabrication rounds, but we included the results here for completeness. The detailed results are shown in Fig. 6.4b. There seems to be an optimal point at $C_f = 0.5\,\text{pF}$ where the best devices have the narrowest linewidths, but considering the spread of the results, we cannot be certain that this is a systematic effect.

The $\zeta/4$ mode performs similarly to the $\lambda/2$ mode with $\sim 30\,\%$ narrower linewidths, as shown in Fig. 6.4c. For the v2 design, shown in Fig. 6.4a, the capacitor on the DC tap is larger by a factor 5 than the gate line ones. This is done to improve the AC grounding of the mode. The ratio is 9.5 for the v1 design (not shown). While the half-wave mode is insensitive to losses through the DC tap because of its symmetry, the quarter-wave mode can lose energy through both the gate lines and the DC tap, making the contributions from the different filters convoluted. Therefore, the linewidth results for this mode are provided for completeness, but are not factored into the optimization process.

Given that the thin-film solution produces devices with <1 MHz linewidths with the right number of gate lines, we are satisfied with these results. It is worth noting that the cutoff frequency of each line can be adjusted individually, by changing the capacitance or the nanowire inductance, simply by adjusting the widths of the gate line sections.

## **6.4.** Conclusion

In summary, we have demonstrated compact on-chip filters for high-impedance resonators that prevent the losses of microwave energy through the gate lines of the coupled QD structure. The inductors are made of the same high-kinetic-inductance superconductor as the resonator. This produces small inductors of large inductance that can be placed anywhere on the chip, as opposed to spiral inductors. We compared two approaches to implement the filter capacitor: one with a planar interdigitated capacitor and one with an overlapping thin-film capacitor. The planar filters performed well when used with sufficient crossbonds; however, their footprint is relatively large, making the solution inconvenient as the number of gate lines increases. The thin-film capacitors are fabricated with a single additional lithography step and dramatically reduce the total footprint of the filter. Our implementation has one capacitor plate overlapping 15 gate lines, effectively producing a very compact filter unit. When combined with the nanowire inductors, this simplifies the microwave engineering by confining the resonator energy to a small area of the chip. We demonstrate that the total linewidth of a 6.4 GHz resonator can be improved down to 540 kHz using these filters, therefore achieving a loaded quality factor of 11900. It is understood that the best solution depends on the combination of footprint and linewidth requirements. For us, the thin-film solution was the only one to satisfy both. With these filters in place, the biggest source of loss in full devices is then dominated by the gate resistance and dielectric losses of the QD area, which will be addressed in future work. Since the resonator and its ground plane have been shown to be compatible with in-plane magnetic fields

6. On-chip microwave filters for high-impedance resonators with
gate-defined quantum dots
130

up to 6 T [3], we do not expect a different behavior in the current case. These low-loss resonators with large coupling to quantum dots could allow more sensitive hybrid spin-superconducting devices to realize long-range two-qubit gates, high-speed gate-based readout, circuit QED experiments with single spins, as well as more fundamental experiments in the device and materials fields.

## Acknowledgments

## Author contributions

P.H.-C and G.Z. conceived and planned the experiments. G.Z. and J.D. performed the electrical cryogenic measurements. J.D. performed numerical simulations. P.H.-C designed the devices, and N.S. provided advice. P.H.-C and J.D. fabricated the devices. A.S. contributed to sample fabrication. A.S. grew the heterostructure with G.S.'s supervision. P.H.-C, G.Z., J.D. and L.M.K.V. analyzed the results. P.H.-C wrote the manuscript with input from all co-authors. L.M.K.V. supervised the project.

## Data availability

The data reported in this paper are archived online at `https://dx.doi.org/10.4121/uuid:913e3aaf-71ac-4a00-b191-0ab8df56280c`.

## 6.5. Supplementary information

### 6.5.1. Device fabrication

The ²⁸Si/SiGe quantum well heterostructure is grown on a 100 mm Si wafer via reduced-pressure chemical vapor deposition, as per Fig. 6.2d. Photolithography alignment markers are plasma etched into the surface with a Cl/HBr chemistry. Doped contacts to the quantum well are formed by ³¹P implantation and activated with a 700 °C rapid thermal anneal. The 5-7 nm superconducting NbTiN film is deposited via magnetron sputtering, preceded by a hydrofluoric acid dip and Marangoni drying, and followed by liftoff of the resist-covered quantum dot areas. The sheet inductance is targeted to be around 115 pH/□. The 10 nm $Al_2O_3$ gate oxide is grown by atomic layer deposition, followed by wet etching with buffered hydrofluoric acid everywhere except for the resist-covered quantum dot areas. Contacts to implants, contacts to the NbTiN film and electron beam lithography alignment markers are patterned with Ti/Pt evaporation preceded with buffered hy-
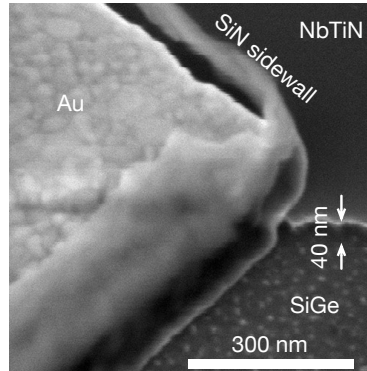
Figure 6.5: Angled-view scanning electron microscope image of the thin-film capacitor structure overlapping a step and the NbTiN film.

drofluoric acid dip and followed by liftoff. The wafer is diced into pieces for further electron beam lithography steps. The NbTiN film is etched via $SF_6$/He reactive ion etching to define the resonator, inductors, capacitors, and gate lines in a single electron beam lithography step, leaving a 40 nm step after the etch. The thin-film capacitor is patterned by first sputtering 30 nm of silicon nitride in a conformal deposition, then evaporating 5 nm of Ti and 100 nm of Au in a directional deposition, allowing for a single patterning and liftoff step. The SiN conformal deposition covers the 40 nm steps created during the etch of the NbTiN film. The resulting structure is shown in Fig. 6.5. The SiN relative dielectric constant was not measured, and is estimated to be ~6 based on typical values for sputtered SiN. The top-plate metal is chosen sufficiently thick to cover the steps and have low electrical resistance. Pieces are diced into individual device chips for electrical characterization.

### 6.5.2. Numerical resonator model

In this section, we present a numerical method to model the resonator's half-wave and quarter-wave modes, together with the effect of the filters, as shown in Fig. 6.1. The model can easily be adapted with different levels of complexity to better capture the effects of the various impedances of the different waveguide and resonator sections, while remaining computationally fast by avoiding three-dimensional (3D) microwave simulations. Simulations with Sonnet have also been performed on individual components (like the resonator or a planar filter) as a consistency check, but the results are not presented in this work. As seen from the optical image in Fig. 6.1a, the resonator doesn't have a simple coplanar waveguide geometry. However, we can get a good (yet still relatively simple) model of it by using combinations of coplanar waveguide sections. These sections then account, to a better degree, for the spatially inhomogeneous capacitance and inductance per unit length of the system.

The model is implemented using the open source software QUCS (`https://sourceforge.net/projects/qucs/`, v0.0.19). It makes use of a mixture of
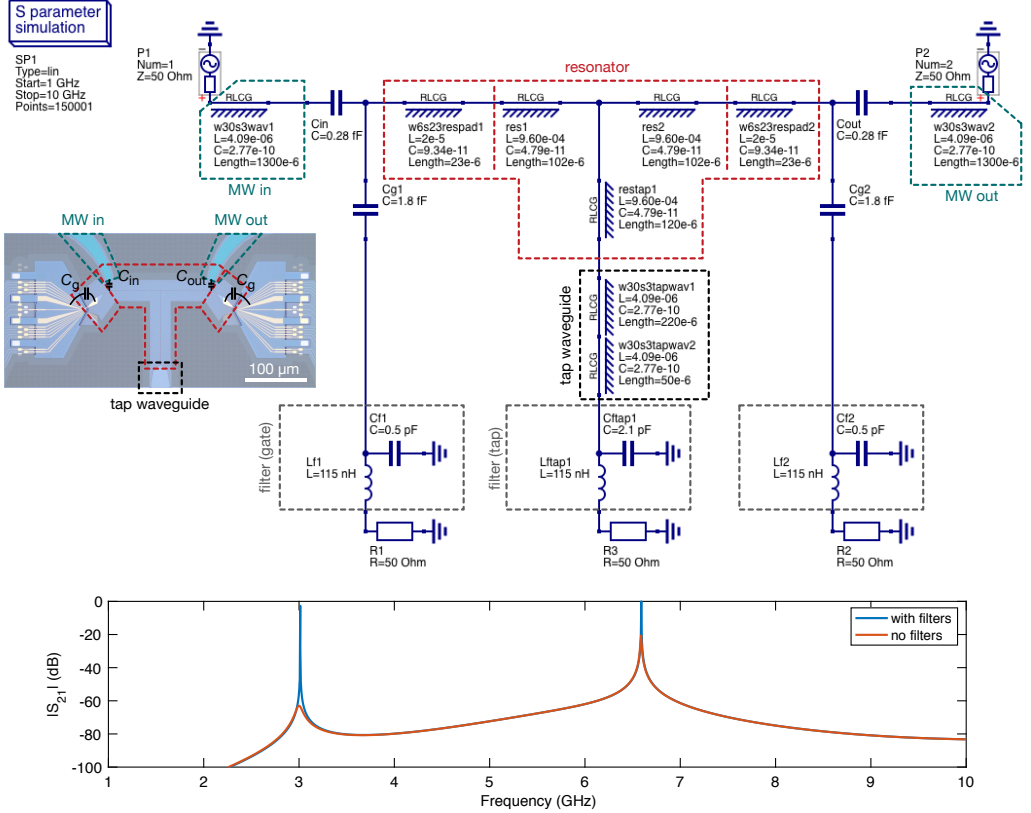
Figure 6.6: Numerical model of the resonator and gate filters implemented using the software QUCS. RLCG elements represent waveguides with arbitrary inductance per unit length `L` and capacitance per unit length `C` (in SI units). The corresponding device elements are delimited by dashed boxes. The model includes effects from the diamond-shaped pads at the end of the resonator narrow section, capacitive loading by the gates, and various waveguide impedances. In some cases, the waveguide dimensions $w$ and $s$ are indicated in the element name in units of microns for convenience. The narrow resonator sections `res1`, `res2` and `restap1` have $w = 120$ nm and $s = 17$ µm. The diamond-shaped pad `w6s23respad1` has $w = 6$ µm and $s = 23$ µm. While the bare impedance of the narrow resonator section consisting of `res1` and `res2` is quite high at about 4.5 kΩ, the resonator is so small that the capacitive loading by the surrounding elements brings the effective impedance down to about ∼3.2 kΩ. This last value is obtained by replacing the `w6s23respad1`, `res1` and `Cg1` elements, and their symmetric counterparts, with a single RLCG element of the same total length, fixing `L` = 9.60e-4 and yielding `C` = 9.4e-11.

lumped components, RLCG waveguide components, and performs a S-parameter simulation. The circuit is shown in Fig. 6.6. To calculate the inductance per unit length $\tilde{L}$ and capacitance per unit length $\tilde{C}$ of the different coplanar waveguide sections, we use the analytical formulae

$$\tilde{L} = \frac{\mu_0}{4}\frac{K(k')}{K(k)} + \frac{L_k}{w},\tag{6.2}$$

$$\tilde{C} = 4\epsilon_0\epsilon_{\text{eff}}\frac{K(k)}{K(k')},\tag{6.3}$$

where $\mu_0$ is the permeability of free space, $\epsilon_0$ is the permittivity of free space, $\epsilon_{\text{eff}} = (11.7+1)/2$, $K$ is the complete elliptic integral of the first kind, $k = w/(w+2s)$, $k' = \sqrt{(1 - k^2)}$, $L_k$ is the sheet inductance, and $w$ and $s$ are the center conductor width and gap width, respectively.

In a real use case, the capacitances in the model are determined either by COMSOL simulations or by the waveguide geometry Eq. 6.3. The resonator width is measured with a scanning electron microscope. The only free parameter is then $L_k$, on which the different values for $\tilde{L}$ depend. We determine $L_k$ by adjusting its value so that the two resonance frequencies match the experimental ones. $L_k$ varies from wafer to wafer, and also from center to edge within one wafer. The model accurately describes the two resonance frequencies simultaneously. However the linewidths show only qualitative agreement with the measured ones. This could be due to unaccounted factors: for example, to dielectric or resistive losses in the resonator and filters, to the overly simplistic description of the ports' impedances [see Eq. 6.1], or to other 3D microwave effects.

The model presented in Fig. 6.6 can be further refined with little computational overhead to include many gate channels per DQD, to describe the floating top capacitor plate in the thin-film filter implementation, to change lumped elements into distributed RLCG ones, or to attempt to model the effect of the finite impedance of the gate lines on the filtering efficacy. We have tried various combinations of these refinements. They sometimes help identify undesirable features, like resonances in gate fanout lines or in other waveguides. The outcomes serve as a quick design starting point. However, we have found that chip-scale effects can significantly degrade the predicted performance, as explained in the main text.

### 6.5.3. Measurement setup
The measurement setup is shown in Fig. 6.7.

### 6.5.4. Data analysis
We generally observe a slight power dependence of the linewidths. The narrower linewidths are typically 5 % to 30 % broader at −110 dBm power than at higher powers. Since we are interested in the low photon number regime, all linewidths are measured with −110 dBm delivered at the PCB, except for some of the broadest ones where the signal-to-noise ratio is too small. Although a Lorentzian lineshape
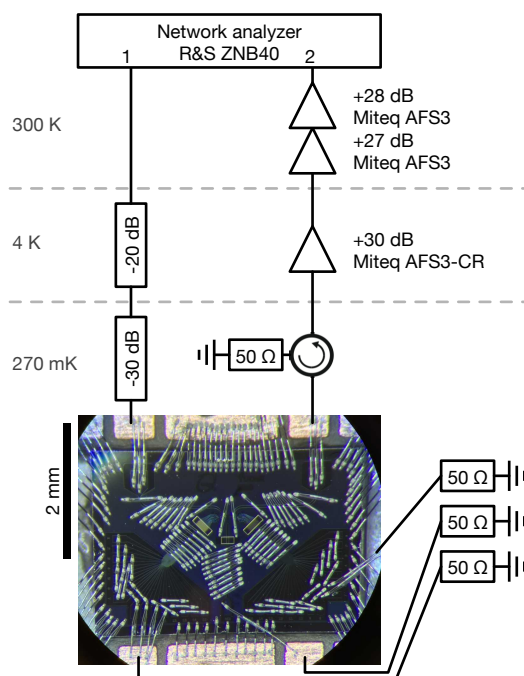
Figure 6.7: Measurement setup for the $^3$He system. The picture shows a wire bonded device with cross bonds mounted on the PCB.

typically yields acceptable fits for $\kappa/2\pi \lesssim 1\,\mathrm{MHz}$, the broader resonances are better captured by a Fano lineshape:

$$|S_{21}|^2 = a \left| \frac{(\omega - \omega_\mathrm{r})/q + \kappa_\mathrm{ext}/2}{i(\omega - \omega_\mathrm{r}) + \kappa/2} \right|^2, \tag{6.4}$$

where $a$ is an arbitrary parameter, $q$ is a complex Fano factor, and $\kappa = \kappa_\mathrm{ext} + \kappa_\mathrm{int}$. The fits do not allow to independently determine the external and internal losses, $\kappa_\mathrm{ext}$ and $\kappa_\mathrm{int}$, respectively.

# References

[1] X. Mi, J. V. Cady, D. M. Zajac, J. Stehlik, L. F. Edge, and J. R. Petta, *Circuit quantum electrodynamics architecture for gate-defined quantum dots in silicon,* Applied Physics Letters **110**, 043502 (2017).

[2] M.-L. Zhang, G.-W. Deng, S.-X. Li, H.-O. Li, G. Cao, T. Tu, M. Xiao, G.-C. Guo, H.-W. Jiang, I. Siddiqi, and G.-P. Guo, *Symmetric reflection line resonator and its quality factor modulation by a two-dimensional electron gas,* Applied Physics Letters **104**, 083511 (2014).

[3] N. Samkharadze, A. Bruno, P. Scarlino, G. Zheng, D. P. DiVincenzo, L. DiCarlo, and L. M. K. Vandersypen, *High-kinetic-inductance superconducting nanowire resonators for circuit qed in a magnetic field,* Phys. Rev. Applied **5**, 044004 (2016).

[4] N. Samkharadze, G. Zheng, N. Kalhor, D. Brousse, A. Sammak, U. C. Mendes, A. Blais, G. Scappucci, and L. M. K. Vandersypen, *Strong spin-photon coupling in silicon,* Science **359**, 1123 (2018).

[5] F. Beaudoin, D. Lachance-Quirion, W. A. Coish, and M. Pioro-Ladrière, *Coupling a single electron spin to a microwave resonator: controlling transverse and longitudinal couplings,* Nanotechnology **27**, 464003 (2016).

[6] X. Mi, M. Benito, S. Putz, D. M. Zajac, J. M. Taylor, G. Burkard, and J. R. Petta, *A coherent spin-photon interface in silicon,* Nature **555**, 599 (2018).

[7] A. J. Landig, J. V. Koski, P. Scarlino, U. C. Mendes, A. Blais, C. Reichl, W. Wegscheider, A. Wallraff, K. Ensslin, and T. Ihn, *Coherent spin-photon coupling using a resonant exchange qubit,* Nature **560**, 179 (2018).

[8] G. Zheng, N. Samkharadze, M. L. Noordam, N. Kalhor, D. Brousse, A. Sammak, G. Scappucci, and L. M. K. Vandersypen, *Rapid gate-based spin read-out in silicon using an on-chip resonator,* Nature Nanotechnology **14**, 742 (2019).

[9] M. Göppl, A. Fragner, M. Baur, R. Bianchetti, S. Filipp, J. M. Fink, P. J. Leek, G. Puebla, L. Steffen, and A. Wallraff, *Coplanar waveguide resonators for circuit quantum electrodynamics,* Journal of Applied Physics **104**, 113904 (2008).

[10] B. A. Mazin, *Microwave Kinetic Inductance Detectors*, Ph.D. thesis, California Institute of Technology (2005).

[11] P. Scarlino, D. J. van Woerkom, A. Stockklauser, J. V. Koski, M. C. Collodo, S. Gasparinetti, C. Reichl, W. Wegscheider, T. Ihn, K. Ensslin, and A. Wallraff, *All-microwave control and dispersive readout of gate-defined quantum dot qubits in circuit quantum electrodynamics,* Phys. Rev. Lett. **122**, 206802 (2019).

[12] M. Benito, J. R. Petta, and G. Burkard, *Optimized cavity-mediated dispersive two-qubit gates between spin qubits,* Phys. Rev. B **100**, 081412 (2019).

[13] T. Cubaynes, M. R. Delbecq, M. C. Dartiailh, R. Assouly, M. M. Desjardins, L. C. Contamin, L. E. Bruhat, Z. Leghtas, F. Mallet, A. Cottet, and T. Kontos, *Highly coherent spin states in carbon nanotubes coupled to cavity photons,* npj Quantum Information **5**, 47 (2019).

[14] F. Borjans, X. G. Croot, X. Mi, M. J. Gullans, and J. R. Petta, *Resonant microwave-mediated interactions between distant electron spins,* Nature **577**, 195 (2020).

**6**

# 7

# Conclusion and outlook

*Everything happens for a reason.*

Old quote

## **7.1.** Conclusion

The goal of my research for the past four years was to establish a hybrid circuit quantum electrodynamics (QED) architecture with single electron spins in silicon and set up the necessary infrastructure to observe the relevant quantum effects. These entail spin-photon coupling, spin readout and cavity-mediated spin-spin coupling. In this section, we summarize the research progress and key findings so far.

We introduced a device design and fabrication procedure in chapter 3 that enabled us to reliably integrate superconducting circuits with semiconductor QDs in a single chip. The superconducting cavity trapping microwave photons consisted of a high-impedance (>1 kΩ) NbTiN resonator, which had been tested thoroughly and validated in the early stage of the project [1]. High-impedance resonators are desirable since their small capacitance produces large electric fields that enhance the coupling to systems with a small charge dipole moment. The use of a single-layer gate design made it possible to reduce the complexity of the fabrication process for QDs, while retaining precise control over the DQD parameters in the few-electron regime. This was extremely beneficial for the fabrication yield and fabrication time. The QDs were formed in the strained Si quantum well of a Si/SiGe heterostructure comprising natural silicon. The quantum well can be improved by using isotopically purified $^{28}$Si.

Using this hybrid device, we were able to observe a vacuum Rabi splitting in the cavity transmission when the electron spin was brought into resonance with the cavity by sweeping the magnet field in chapter 4. This gave preliminary evidence for a highly coherent spin-photon interaction. We observed both the charge and the spin in the dispersive regime using two-tone spectroscopy, and extracted their linewidths. When we compared the spin-photon coupling strength to the independently extracted loaded cavity and spin decoherence rates, we found that we indeed reached the strong coupling regime between a single photon and a single electron spin. The mechanism behind the spin-photon interaction here is not a direct one, but an indirect one that involves the electric dipole moment of the electron. The cavity electric field is coupled to the electron charge, which in turn is coupled to the electron spin via a transverse magnetic field gradient. The field gradient hybridizes the spin and charge degrees of freedom, and we were able to control the level of hybridization by adjusting the interdot tunnel coupling strength. The spin-photon coupling strength, spin decoherence rate as well as the cavity decay rate depend on this spin-charge hybridization. We observed that there is an optimal degree of hybridization that maximizes the expected number of vacuum Rabi oscillations. The results summarized so far were obtained at the charge degeneracy point. We also showed that there is no measurable spin-photon coupling strength when the electron is pushed into a Coulomb-blockaded region. This suggests that the spin-photon coupling can be turned on and off on a nanosecond timescale in our device.

The cavity response from the spin in the dispersive regime depends directly on the state of the spin. In this sense, the cavity can function as an efficient detector

without the need for a spin-to-charge conversion mechanism. However, given the modest ratio of the spin-photon coupling strength to the loaded cavity linewidth that we have observed in our devices, performing single-shot dispersive readout of the spin proved to be quite challenging. Motivated by the much larger charge-photon coupling strength, and thus much larger dispersive shift of the resonator due to the electron charge when it is allowed to tunnel between the dots, we started benchmarking the charge sensitivity and bandwidth of the detector in chapter 5, and found that we were able to perform rapid charge detection with high SNR. Subsequently, using Pauli spin blockade as the spin-to-charge conversion mechanism in the two-electron regime, we were able to detect singlet states in a high-fidelity single-shot fashion.

We described a new generation of device design that included two distant DQDs coupled to a single cavity in chapter 6. In the new design, the square loop geometry of the nanowire resonator has been opened up by pulling the two ends of the nanowire apart. In addition, the feedline has been modified accordingly to transform the cavity from a hanger style to transmission style resonator. DQD gates were placed at each end of the nanowire. In parallel, the heterostructures have been upgraded with quantum wells comprising isotopically purified $^{28}$Si (800 p.p.m. residual $^{29}$Si). Although the new design of the cavity allows for long-distance connectivity between DQDs and eventually spins, it contains several drawbacks. First, we expected a reduced charge-photon coupling strength as each DQD has only one of its gates connected to the cavity in the new configuration, whereas in the older generation two of the DQD gates were connected to the cavity. To compensate for this reduction, the impedance of the resonator was increased by a factor 3 to 4. Second, microwave photon leakage from the cavity to the gates has become more severe as the single resonator gate is able to extend its cavity electric field lines to all the surrounding gates. In contrast, the old cavity design had the two out-of-phase voltage antinodes next to each other, which confined most of the field lines between the resonator gates, thereby suppressing the photon leakage to nearby gates. Microwave leakage through the gates is a known problem, but high-impedance resonators are in particular more susceptible to this type of loss due to the necessarily small capacitance for a 4-8 GHz resonance frequency. We countered the leakage in the new cavity design with on-chip low-pass filters. Two filter variations, with the same nanowire inductor but different capacitor, were tested: planar and thin-film filters. All the data presented in Chap. 6 came from simplified devices that mimicked the full devices with the correct parasitic capacitance to the gates. This was done to isolate the microwave leakage from other losses and simplify the fabrication. We found that both filter designs were effective against microwave leakage. However, given the large footprint of the planar filter, fitting ~30 of these filters on our chip leaves little to no space for well-defined ground planes surrounding to the interdigitated capacitors, rendering them ineffective. Therefore, even though it requires an extra fabrication step, the thin-film capacitor with its much smaller footprint is better suited for our devices.

**7**

Based on the results reported in this thesis, we can reach the following conclusions. The single-layer gate architecture is an encouraging platform for gate-defined DQDs that offers a fair balance between control and fabrication. High-impedance resonators based on disordered nanowires do provide an enhanced coupling to charge qubits, thereby clearly demonstrating that these resonators are excellent for coupling to small electric dipole moments. Previously, they were only characterized separately without DQDs. On-chip micromagnets can provide a local and controlled synthetic SOI that is many orders of magnitude larger than the intrinsic SOI in Si. Owing to the enhanced charge-photon coupling and SOI, we were able to convincingly achieve strong spin-photon coupling, which is the first step towards cavity-mediated spin-spin interaction. Moreover, on-chip superconducting resonators are a powerful tool for gate-based sensing of the charge dynamics of DQDs. As an alternative to conventional charge sensors with sensing dots or quantum point contacts that require additional gates, they can map out charge stability regions using gate electrodes that are already present for defining the QDs. They can further be utilized as very sensitive detectors to perform fast and high-fidelity single-shot spin readout. This can be an important asset for readout in 2D arrays of QDs. Moreover, nanowire inductors based on kinetic inductance can act as proper inductors when designed well, and they have a smaller footprint and larger inductance compared to conventional spiral inductors. Combined with an interdigitated or thin-film capacitor, they form a highly tunable on-chip low-pass filter in the microwave regime.

The major bottleneck that currently impedes our progress towards entanglement between distant spins is charge noise. Most of our devices suffer from both low-frequency and high-frequency charge noise. The low-frequency charge noise (<Hz) is responsible for sizeable changes in the electrostatic environment of the DQD, causing interdot transitions to move around in voltage space during a measurement. The high-frequency charge noise contributes to $\gamma_C$, which in turn can severely affect $\gamma_S$ and $\kappa$ due to substantial spin-charge and charge-photon hybridizations. Charge noise is a more common problem that also occurs in other spin qubit devices. Therefore, it is important to study charge noise in order to identify and possibly eliminate their sources. Nevertheless, taking everything into consideration, we conclude that the circuit QED architecture presented in this thesis shows potential for long-range spin-spin coupling. A more quantitative analysis on this can be found in the outlook section. In the near-term, this hybrid architecture might also be useful for readout of spin qubits in 1D or 2D arrays. Achieving these will enhance the prospects for using solid-state spins in QDs for quantum information processing.

## 7.2. Outlook

The research towards long-distance spin-spin entanglement and beyond is still ongoing. Here, we will report some of the unpublished progress and discuss a few unexplored avenues, along with challenges and possible solutions, that one could take to build upon our research.

### 7.2.1. Improving the cooperativity

The cooperativity $C = \frac{g_S^2}{\kappa^* \gamma_S}$ is an important figure of merit in circuit QED systems, and can be physically interpreted as the ratio of the coherent coupling rate ($g_S$) to the incoherent coupling rates ($\kappa^*$ and $\gamma_S$). As might be expected, improving this quantity will enable higher fidelity quantum logic gates. There are several possible ways to go about this. It was mentioned in section 2.6 how the three parameters determining the cooperativity depend on other parameters: $g_S(g_C, \delta B_x)$, $\kappa^*(\gamma_C)$ and $\gamma_S(\gamma_C)$.

- $g_S(g_C, \delta B_x)$: Two different routes can be pursued in order to increase $g_S$. First, the design and fabrication of the micromagnets can be optimized to give a larger transversal gradient $\delta B_x$. The micromagnets on the device in Chap. 4 came out of the fabrication smaller than intended. Second, $g_C$ can be enhanced by increasing the resonator impedance. One can optimize the geometry of the resonator structure or use a different material with higher sheet inductance, e.g. TiN [2], disordered Al [3] or granular Al [4, 5]. Furthermore, increasing the differential lever arm $\beta$ increases $g_C$. For this reason, Si/SiGe heterostructures with shallower quantum wells or Si-MOS substrates might be interesting.

- $\kappa^*(\gamma_C)$: Reducing the loaded cavity linewidth $\kappa^*$ (Eq. 2.49) will be of benefit to the performance of the dispersive readout as it increases the cavity response, provided that the dispersive shift is not already larger than $\kappa^*$. The cavity linewidth $\kappa$ (the linewidth when the cavity is not hybridized with the charge qubit) will be discussed first. We observed that the resonators of fully functional hybrid devices with on-chip filters perform worse than the test devices in Chap. 6, i.e. $\kappa/2\pi \approx 4\,\text{MHz}$, independent of the presence of 2DEG underneath the reservoir accumulation gates. This is partially due to resistive losses from the Au fine gates for the QDs. The use of superconducting Al fine gates reduced the resistive losses, and we observed $\kappa/2\pi < 2\,\text{MHz}$. The remaining small difference compared to the test devices is tentatively attributed to dielectric losses from the gate oxide. Therefore, we expect a cavity linewidth comparable to the test devices when we remove the gate dielectrics. When the cavity hybridizes with the charge qubit, $\kappa$ broadens to $\kappa^*(\gamma_C)$. A Recent study found that charge noise, which contributes to $\gamma_C$, can be reduced by using as little $Al_2O_3$ as possible [6]. This aligns well with the previous suggestion of removing the gate dielectric. It would be interesting to measure $\gamma_C$ in such devices.

- $\gamma_S(\gamma_C)$: Reducing $\gamma_S$ will help resolve the dispersive spin-spin interaction as the condition $J > \gamma_S^{(1)}, \gamma_S^{(2)}$ needs to be fulfilled (Sec. 2.1.2). Prior to hybridizing the spin with the charge, the spin decoherence rate in natural Si is dominated by the random nuclear field from the 5 % $^{29}$Si atoms in the quantum well, which amounts to $\sim 0.3\,\text{MHz}$ for a single spin in a single SiGe QD [7]. We expect a dramatic improvement of 1 to 2 orders of magnitude in isotopically enriched $^{28}$Si quantum wells [8]. However, after spin-charge hybridization

**7**

we observed $\gamma_S/2\pi > 1$ MHz in Chap. 4 (natural Si), suggesting that our spin linewidth is dominated by charge noise. Thus reducing charge noise will have a great impact on $\gamma_S$. Although we do not know for sure yet where the charge noise originates from, one of the first things to try is to remove the gate dielectric as mentioned in the previous bullet.

On the hardware side, the readout can be improved using a Josephson traveling-wave parametric amplifier (TWPA) on the MC plate [9].

### 7.2.2. Towards coupling spin qubits in distant QD pairs

As hinted in Chap. 6, we have developed a new generation of devices containing two DQDs (Fig. 7.1a). The devices measured in that chapter were simplified in order to isolate the effect of microwave leakage, but in parallel we also made fully functional hybrid devices containing two DQDs with the single-layer gate design. The resonator linewidth has indeed improved from >15 MHz to <2 MHz owing to the on-chip filters and superconducting fine gates, with $\kappa/2\pi \approx 1.5$ MHz the best we have observed so far. Both DQDs can be tuned with gate-sensing to the few-electron regime (Fig. 7.1b,c). Moreover, we estimated a charge-photon coupling strength similar to the previous generation of devices that contained a looped resonator geometry with a single DQD ($g_C/2\pi \approx 200$ MHz), indicating that the increased impedance (now typically 3-4 k$\Omega$ instead of $\sim$1 k$\Omega$) compensated for the reduced $g_C$ in the 'open' resonator geometry. Additionally, Fig. 7.1d shows that the two charge qubits can simultaneously interact with the cavity and enhance the cavity dispersive shift compared to when only a single charge qubit is interacting with the cavity. The four different plots can be viewed as 2D slices through a 3D space spanned by the detunings of DQD1 and DQD2 and the probe frequency $f_p$. The horizontal (vertical) blue band in the first plot with $f_p = f_r$ is the (1,0)-(0,1) interdot transition of DQD1 (DQD2). In the last plot $f_p$ is offset by $-11$ MHz, which is larger than the dispersive shift due to either DQD1 or DQD2. A bright signal is still visible when both DQDs are at zero detuning, demonstrating the sum of the shifts is larger than each dispersive shift by itself.

Unfortunately, we have been experiencing instabilities in later devices that prevented us from performing long measurements. More precisely, the chemical potentials of the QDs fluctuate every second by a non-negligible amount. We believe that this is related to the device itself or its fabrication process, rather than the electronics.

A problem that arises in devices with two DQDs using the current spin-photon coupling scheme is that the micromagnets are in practice not identical. Consequently, the electron spin splitting will be different in the two DQDs for a given external magnetic field. This is undesired for cavity-mediated two-qubit gates that rely on identical qubit energies, such as the $\sqrt{i\text{SWAP}}$ gate (more on this in the next section). A neat trick that can be applied in this situation is to tilt the micromagnets in-plane (Fig. 7.1a), in a different direction in each DQD, so that the spin splitting is a result of the vector sum of the external magnetic field and stray field of the micromagnets [10]. However, this trick will not work beyond two DQDs and some
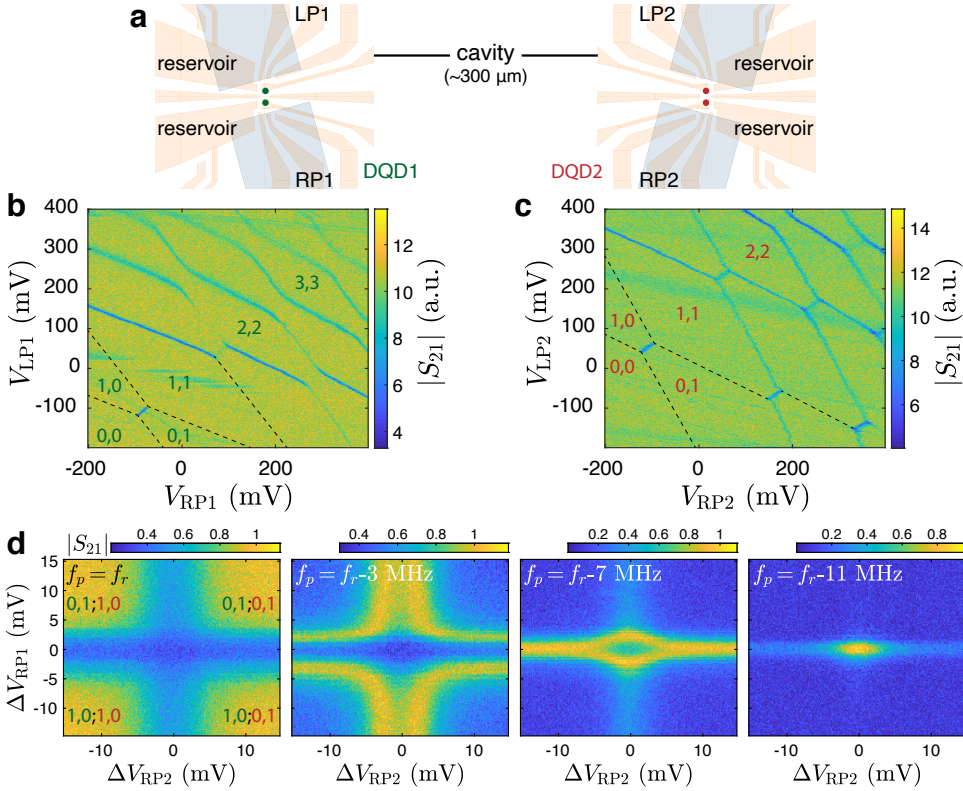
Figure 7.1: **Two DQDs interacting with a common cavity**. **a** Single-layer gate design of the two DQDs. The colored dots indicate the locations of the QDs. Each DQD gate set has one of its gates connected to the cavity. The gates LP1,2 and RP1,2 are used as plunger gates. The shaded regions mark the position and orientation of the micromagnets. The micromagnet axes are rotated by 15° from the DQD axis (in opposite directions for the two DQDs). The data shown in panels **b**, **c** and **d** are from a device without micromagnets. **b**, **c** Charge stability diagrams of DQD1 and DQD2 in the few-electron regime. The data are taken via dispersive gate-sensing. The black dashed lines indicate the approximate position of reservoir transition lines not detected by the cavity. **d** Normalized cavity transmissions as function of the voltages on RP1 and RP2, while $V_{LP1}$ and $V_{RP1}$ ($V_{LP2}$ and $V_{RP2}$) are set to the center of the (1,0)-(0,1) interdot transition of DQD1 (DQD2). $(n_1, m_1; n_2, m_2)$ indicates the electron occupation number with $n_1, m_1$ ($n_2, m_2$) corresponding to DQD1 (DQD2). The four plots are taken with different probe frequencies $f_p$ to unveil the enhanced dispersive shift of the cavity when both DQDs are at zero detuning compared to when only one DQD is at zero detuning. The dispersive shift of DQD1 is larger than that of DQD2 in this particular measurement because $t_{c,1} < t_{c,2}$. Device fabricated by P. Harvey-Collard.

kind of local (DC) magnetic field control is needed to tune. One can for example think of nearby current-carrying superconducting striplines.

### 7.2.3. Cavity-mediated two-qubit gates

Long-range $i$SWAP [11] and $\sqrt{i\text{SWAP}}$ [12] gates for spin qubits have been studied theoretically. Given the coupling strengths obtained in Chap. 4 ($\sim$10 MHz) and

assuming identical DQDs, we estimate an effective long-distance exchange interaction of $J/2\pi \approx 1\,\text{MHz}$ (Eq. 2.12) in the dispersive regime (say, $|\Delta| = 10g_S$). This is about the same order of magnitude as $\gamma_S$, making it seemingly difficult to achieve a two-qubit gate with high fidelity. Upon closer look, a quantitative analysis reveals that the approximated average fidelity of an $i\text{SWAP}$ gate, at an optimized spin-charge mixing and spin qubit-cavity detuning $\Delta$, is [11]:

$$\bar{F}_{i\text{SWAP}} \approx 1 - \frac{4\pi}{5}\sqrt{\frac{\gamma_C \kappa}{g_C^2}}, \tag{7.1}$$

and depends only on the charge qubit and cavity parameters. The decoherence due to $^{29}$Si nuclear spins is neglected in this analysis. Strikingly, the spin qubit parameters seem to be missing in the above equation, but note that $J = g_S^2/\Delta$ and $\gamma_S$ can be written in terms of the charge qubit parameters and spin-charge admixing (see Sec. 2.6.2), with the latter dropping out of the Eq. 7.1. The degree of spin-charge admixing does affect the gate time, $t_{i\text{SWAP}} = \frac{\pi}{2}\frac{|\Delta|}{g_S^2}$, and can compete with the hyperfine noise. Based on the numbers from Chap. 4 ($g_C/2\pi = 200\,\text{MHz}$, $\kappa/2\pi = 2\,\text{MHz}$, $\gamma_C/2\pi = 50\,\text{MHz}$), we estimate $\bar{F}_{i\text{SWAP}} \approx 87\,\%$. With a modest improvement of, for example, the cavity ($\kappa/2\pi = 1\,\text{MHz}$), we should be able to reach fidelities over 90 %. However, there needs to be serious improvements in $g_C$, $\gamma_C$ and $\kappa$ (e.g. $\kappa/2\pi = 0.6\,\text{MHz}$, $\gamma_C/2\pi = 1\,\text{MHz}$ or $\kappa/2\pi = 0.06\,\text{MHz}$, $\gamma_C/2\pi = 10\,\text{MHz}$ for $g_C/2\pi = 200\,\text{MHz}$) in order to achieve $\bar{F}_{i\text{SWAP}} > 99\,\%$.

Alternatively, given that we expect to see several vacuum Rabi oscillations before decaying, one could perform a long-distance SWAP gate in the resonant regime by sequential swapping with the cavity. Subsequently, the spin states can be read out dispersively using Pauli spin blockade with an ancilla spin (in a third dot). This approach offers shorter gate times, with the caveat that it is more susceptible to cavity losses.

### 7.2.4. Alternative cavity design

Hybrid superconductor-quantum dot devices seem to need on-chip gate filters in order to achieve cavity linewidths of ~1 MHz. CPW resonators are not the only type of resonator used in circuit QED systems. A half-wavelength resonator design that can potentially perform well without filters is displayed in Fig. 7.2a [13]. A pair of coupled parallel microstrip lines constitute the resonating structure. The fundamental mode can be excited by applying microwave fields of equal amplitude, but opposite phase, to the microstrip lines simultaneously (Fig. 7.2c). In doing so, the microstrip lines exhibit an out-of-phase $\lambda/2$ resonance, thereby confining most of the microwave field between the two conductors (Fig. 7.2b). A cavity linewidth of $\kappa/2\pi = \kappa_{\text{int}}/2\pi + \kappa_{\text{ext}}/2\pi = 2\,\text{MHz} + 1.1\,\text{MHz} = 3.1\,\text{MHz}$ has been demonstrated.

Each end of this cavity can be connected to two adjacent DQD gates, similar to the device in Chap. 4. The alternative cavity design offers several practical advantages. It could mitigate the problem of microwave leakage through the gates as most of the cavity electric field is confined between the adjacent resonator gates, possibly removing the need for on-chip gate filters. In addition, it yields a higher
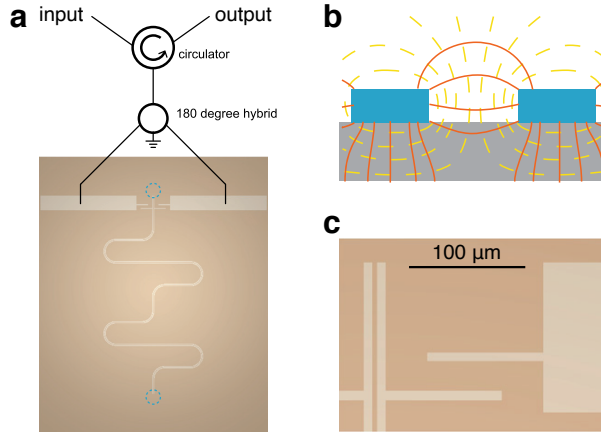
Figure 7.2: **Symmetric reflection line resonator**. **a** Optical microscope image of the reflection line resonator and schematic of part of the measurement setup showing a circulator and a 180° hybrid, which was used to change the single-ended input microwaves to a differential excitation and combine the two reflected signals into one signal. The light regions show the superconducting material (Al) and the dark region the substrate. The blue dashed circles mark the potential locations for qubits. **b** Schematic cross section of the two parallel conductors showing the electric (solid lines) and magnetic (dashed lines) fields for the fundamental mode. **c** Enlargement of the right coupling capacitor. Adapted from Ref. [13].

differential lever arm compared to the cavity shape in Chap. 6. Finally, this type of resonator does not require ground planes, thereby alleviating design constraints and removing the need for wire bonds between ground planes (Fig. 3.3).

### 7.2.5. Dedicated readout resonator

The gate-based readout in Chap. 5 was performed using an on-chip resonator that was meant for spin-photon coupling. In principle, this gives conflicting requirements, i.e. $\kappa$ should be as small as possible for a resonator quantum bus, but large for a high-bandwidth readout resonator. In an attempt to resolve this, we have explored on-chip resonator designs that are dedicated to sensing and readout. One of them is shown in Fig. 7.3a. It is a $\lambda/4$ nanowire resonator that is designed to be probed in reflection. This removes the need for a second bond pad on the chip for the output signal. By adjusting the resonance frequency down to ~1 GHz, this type of resonator becomes compatible with the standard RF reflectometry circuitry (e.g. directional coupler, <2 GHz cryogenic amplifier) for RF-SET or RF-QPC. This relieves the requirement for expensive high-frequency microwave instrumentation. One caveat, however, is that the lower resonance frequency can compromise the SNR for gate-based sensing if the dispersive shift becomes smaller than the resonator linewidth. Fig. 7.3b shows a typical DQD charge stability diagram obtained using the resonator on this device. A regular honeycomb pattern can be identified in the top right corner, but fades out closer to the center due to low tunnel rates. A single 2D scan took 2 ms of data acquisition and the plot in Fig. 7.3b is averaged 100 times, so the total data was acquired in 200 ms. This acquisition time is
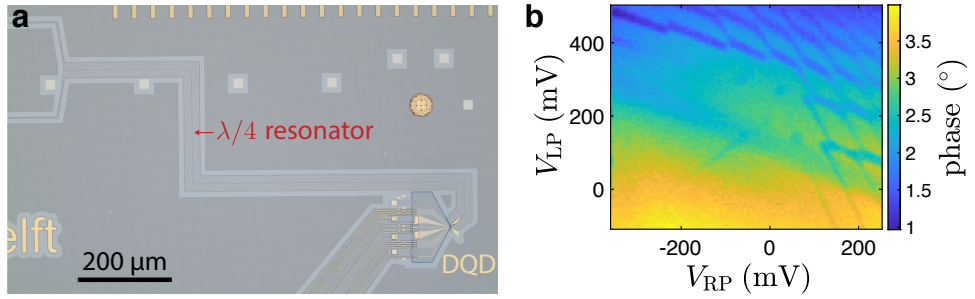
Figure 7.3: **Readout reflection resonator**. **a** Optical microscope image of a high-impedance ($\sim$4 kΩ) NbTiN quarter-wavelength resonator with a resonance frequency of $\sim$1.02 GHz. The voltage antinode is on the side of the DQD (bottom right) and the voltage node is at the impedance mismatch with the bond pad (top left). **b** Phase of the reflected microwave signal from the resonator as function of the two plunger gate voltages. A typical DQD charge stability diagram in the few-electron regime can be recognized. Some interdot transitions are elongated because of very low tunnel rates to the reservoirs. Data was taken by applying sawtooth waves to both gates, one of 50 kHz and one of 500 Hz. Total data acquisition time is 200 ms. Each pixel has an effective integration time of 20 μs. Device fabricated by N. Samkharadze and D. Brousse. M. Noordam assisted with the measurement.

many orders of magnitude shorter than that of a typical DC transport measurement through a sensing dot, and compares favourably to that of an RF-SET. This is an encouraging result suggesting that this type of resonator can be employed for fast gate-based sensing, and even allow the acquisition of charge stability diagrams in a live 'video mode', enabling real-time tuning of DQDs [14, 15]. The SNR can be improved further by making use of a <1 GHz Josephson parametric amplifier [16]. Frequency multiplexing in this design can potentially be done by placing resonators of different lengths next to each other, using the same bond pad.

### 7.2.6. Beyond DQDs

Once a reliable long-range two-qubit gate has been demonstrated, one can start to look at larger and more complex systems. As an intermediate step, it would be interesting to combine the cavity with QD structures beyond a DQD. For example, using the cavity to connect linear chains of eigth to nine QDs [15, 17]. The single-layer gate design might fall short of giving sufficient tunability for a chain of that size in silicon, in which case one can adopt the overlapping gate architecture [10, 18–21].

Alternatively, the array can be expanded to 2D, starting with a 2x2 or 3x3 array [22, 23]. This will provide an excellent testbed for the resonator as a coherent long-range qubit coupler in a sparse spin qubit architecture [24], or as a tool for gate-based readout in a crossbar network [25].

### 7.2.7. Epilogue

It is at this point in time still unclear how a large-scale quantum processor based on spin qubits will look like, and whether or not it will be that of a hybrid type that coexists with superconducting technology. This is the subject of an ongoing global

effort. In fact, scaling up a quantum system to many qubits in a useful way is currently one of the biggest challenges in the field of quantum computing [26]. A daunting challenge that applies to all qubit platforms. However, there is certainly also room for optimism in general. Even if fault-tolerant quantum computing still seems far away today, we are getting closer and closer as a community to NISQ (Noisy Intermediate-Scale Quantum) devices [27]. These are quantum computers containing 50 to 100 qubits with noisy logic gates unprotected by quantum error correction. The recent demonstration of quantum supremacy by Google is definitely a major step in the right direction [28]. More specifically, they used 53 superconducting qubits to perform a quantum computation (one with no practical use in this particular case) within 200 seconds that would otherwise take a classical computer an unreasonable amount of time to complete.

So far, only a modest number of spin qubits in silicon has been operated [29–32] and tough challenges in fabrication uniformity and control need to be overcome before spin-based NISQ devices become feasible. Nevertheless, Si spin qubits offer several attractive features that can give them an edge over other qubit platforms regarding the scaling problem [24] (see Fig. 1.4 for a possible architecture of a future spin-based quantum processor). These include the resemblance of QDs to traditional semiconductor technology, the host material being silicon and the small footprint.

Finally, there is increasing interest from industry and governments, now more than ever, in quantum information science and technology, and it has become the focus of numerous startup companies. Their efforts will certainly accelerate the progress in our field. In particular for Si spin qubits, big companies and institutes including Intel [33, 34], CEA-Leti [35–37], IMEC and HRL have joined this endeavour. Exciting times are ahead of us!

**7**

# References

[1] N. Samkharadze, A. Bruno, P. Scarlino, G. Zheng, D. P. DiVincenzo, L. DiCarlo, and L. M. K. Vandersypen, *High-kinetic-inductance superconducting nanowire resonators for circuit qed in a magnetic field,* Phys. Rev. Applied **5**, 044004 (2016).

[2] P. C. J. J. Coumou, M. R. Zuiddam, E. F. C. Driessen, P. J. de Visser, J. J. A. Baselmans, and T. M. Klapwijk, *Microwave properties of superconducting atomic-layer deposited tin films,* IEEE Transactions on Applied Superconductivity **23**, 7500404 (2013).

[3] W. Zhang, K. Kalashnikov, W.-S. Lu, P. Kamenov, T. DiNapoli, and M. Gershenson, *Microresonators fabricated from high-kinetic-inductance aluminum films,* Phys. Rev. Applied **11**, 011003 (2019).

[4] L. Grünhaupt, N. Maleeva, S. T. Skacel, M. Calvo, F. Levy-Bertrand, A. V. Ustinov, H. Rotzinger, A. Monfardini, G. Catelani, and I. M. Pop, *Loss mechanisms and quasiparticle dynamics in superconducting microwave resonators made of thin-film granular aluminum,* Phys. Rev. Lett. **121**, 117001 (2018).

[5] K. Borisov, D. Rieger, P. Winkel, F. Henriques, F. Valenti, A. Ionita, M. Wessbecher, M. Spiecker, D. Gusenkova, I. M. Pop, and W. Wernsdorfer, *Superconducting granular aluminum resonators resilient to magnetic fields up to 1 tesla,* (2020), arXiv:2006.05171 [cond-mat.supr-con] .

[6] E. J. Connors, J. Nelson, H. Qiao, L. F. Edge, and J. M. Nichol, *Low-frequency charge noise in si/sige quantum dots,* Phys. Rev. B **100**, 165305 (2019).

[7] E. Kawakami, P. Scarlino, D. R. Ward, F. R. Braakman, D. E. Savage, M. G. Lagally, M. Friesen, S. N. Coppersmith, M. A. Eriksson, and L. M. K. Vandersypen, *Electrical control of a long-lived spin qubit in a si/sige quantum dot,* Nature Nanotechnology **9**, 666 (2014).

[8] M. Veldhorst, J. C. C. Hwang, C. H. Yang, A. W. Leenstra, B. de Ronde, J. P. Dehollain, J. T. Muhonen, F. E. Hudson, K. M. Itoh, A. Morello, and A. S. Dzurak, *An addressable quantum dot qubit with fault-tolerant control-fidelity,* Nature Nanotechnology **9**, 981 (2014).

[9] C. Macklin, K. O'Brien, D. Hover, M. E. Schwartz, V. Bolkhovsky, X. Zhang, W. D. Oliver, and I. Siddiqi, *A near–quantum-limited josephson traveling-wave parametric amplifier,* Science **350**, 307 (2015), https://science.sciencemag.org/content/350/6258/307.full.pdf .

[10] F. Borjans, X. G. Croot, X. Mi, M. J. Gullans, and J. R. Petta, *Resonant microwave-mediated interactions between distant electron spins,* Nature **577**, 195 (2020).

[11] M. Benito, J. R. Petta, and G. Burkard, *Optimized cavity-mediated dispersive two-qubit gates between spin qubits,* Phys. Rev. B **100**, 081412 (2019).

[12] A. Warren, E. Barnes, and S. E. Economou, *Long-distance entangling gates between quantum dot spins mediated by a superconducting resonator,* Phys. Rev. B **100**, 161303 (2019).

[13] M.-L. Zhang, G.-W. Deng, S.-X. Li, H.-O. Li, G. Cao, T. Tu, M. Xiao, G.-C. Guo, H.-W. Jiang, I. Siddiqi, and G.-P. Guo, *Symmetric reflection line resonator and its quality factor modulation by a two-dimensional electron gas,* Applied Physics Letters **104**, 083511 (2014).

[14] J. Stehlik, Y.-Y. Liu, C. M. Quintana, C. Eichler, T. R. Hartke, and J. R. Petta, *Fast charge sensing of a cavity-coupled double quantum dot using a josephson parametric amplifier,* Phys. Rev. Applied **4**, 014018 (2015).

[15] C. Volk, A. M. J. Zwerver, U. Mukhopadhyay, P. T. Eendebak, C. J. van Diepen, J. P. Dehollain, T. Hensgens, T. Fujita, C. Reichl, W. Wegscheider, and L. M. K. Vandersypen, *Loading a quantum-dot based "qubyte" register,* npj Quantum Information **5**, 29 (2019).

**7**

[16] S. Schaal, I. Ahmed, J. A. Haigh, L. Hutin, B. Bertrand, S. Barraud, M. Vinet, C.-M. Lee, N. Stelmashenko, J. W. A. Robinson, J. Y. Qiu, S. Hacohen-Gourgy, I. Siddiqi, M. F. Gonzalez-Zalba,  and J. J. L. Morton, *Fast gate-based readout of silicon quantum dots using josephson parametric amplification,* Phys. Rev. Lett. **124**, 067701 (2020).

[17] D. M. Zajac, T. M. Hazard, X. Mi, E. Nielsen,  and J. R. Petta, *Scalable gate architecture for a one-dimensional array of semiconductor spin qubits,* Phys. Rev. Applied **6**, 054013 (2016).

[18] S. J. Angus, A. J. Ferguson, A. S. Dzurak,  and R. G. Clark, *Gate-defined quantum dots in intrinsic silicon,* Nano Letters **7**, 2051 (2007), pMID: 17567176.

[19] M. G. Borselli, K. Eng, R. S. Ross, T. M. Hazard, K. S. Holabird, B. Huang, A. A. Kiselev, P. W. Deelman, L. D. Warren, I. Milosavljevic, A. E. Schmitz, M. Sokolich, M. F. Gyure,  and A. T. Hunter, *Undoped accumulation-mode si/SiGe quantum dots,* Nanotechnology **26**, 375202 (2015).

[20] D. M. Zajac, T. M. Hazard, X. Mi, K. Wang,  and J. R. Petta, *A reconfigurable gate architecture for si/sige quantum dots,* Applied Physics Letters **106**, 223507 (2015).

[21] J. P. Dodson, N. Holman, B. Thorgrimsson, S. F. Neyens, E. R. MacQuarrie, T. McJunkin, R. H. Foote, L. F. Edge, S. N. Coppersmith,  and M. A. Eriksson, *Fabrication process and failure analysis for robust quantum dots in silicon,* (2020), arXiv:2004.05683 [physics.app-ph] .

[22] U. Mukhopadhyay, J. P. Dehollain, C. Reichl, W. Wegscheider,  and L. M. K. Vandersypen, *A 2 × 2 quantum dot array with controllable inter-dot tunnel couplings,* Applied Physics Letters **112**, 183505 (2018).

[23] P.-A. Mortemousque, E. Chanrion, B. Jadot, H. Flentje, A. Ludwig, A. D. Wieck, M. Urdampilleta, C. Bauerle,  and T. Meunier, *Coherent control of individual electron spins in a two dimensional array of quantum dots,* (2018), arXiv:1808.06180 [cond-mat.mes-hall] .

[24] L. M. K. Vandersypen, H. Bluhm, J. S. Clarke, A. S. Dzurak, R. Ishihara, A. Morello, D. J. Reilly, L. R. Schreiber,  and M. Veldhorst, *Interfacing spin qubits in quantum dots and donors–hot, dense, and coherent,* npj Quantum Information **3**, 34 (2017).

[25] R. Li, L. Petit, D. P. Franke, J. P. Dehollain, J. Helsen, M. Steudtner, N. K. Thomas, Z. R. Yoscovits, K. J. Singh, S. Wehner, L. M. K. Vandersypen, J. S. Clarke,  and M. Veldhorst, *A crossbar network for silicon quantum dot qubits,* Science Advances **4** (2018), 10.1126/sciadv.aar3960.

[26] D. Franke, J. Clarke, L. Vandersypen,  and M. Veldhorst, *Rent' s rule and extensibility in quantum computing,* Microprocessors and Microsystems **67**, 1 (2019).

**7**

[27] J. Preskill, *Quantum Computing in the NISQ era and beyond,* Quantum **2**, 79 (2018).

[28] F. Arute *et al.*, *Quantum supremacy using a programmable superconducting processor,* Nature **574**, 505 (2019).

[29] M. Veldhorst, C. H. Yang, J. C. C. Hwang, W. Huang, J. P. Dehollain, J. T. Muhonen, S. Simmons, A. Laucht, F. E. Hudson, K. M. Itoh, A. Morello, and A. S. Dzurak, *A two-qubit logic gate in silicon,* Nature **526**, 410 (2015).

[30] T. F. Watson, S. G. J. Philips, E. Kawakami, D. R. Ward, P. Scarlino, M. Veldhorst, D. E. Savage, M. G. Lagally, M. Friesen, S. N. Coppersmith, M. A. Eriksson, and L. M. K. Vandersypen, *A programmable two-qubit quantum processor in silicon,* Nature **555**, 633 (2018).

[31] D. M. Zajac, A. J. Sigillito, M. Russ, F. Borjans, J. M. Taylor, G. Burkard, and J. R. Petta, *Resonantly driven cnot gate for electron spins,* Science **359**, 439 (2018).

[32] A. Sigillito, J. Loy, D. Zajac, M. Gullans, L. Edge, and J. Petta, *Site-selective quantum control in an isotopically enriched* $^{28}$Si/si$_{0.7}$ge$_{0.3}$ *quadruple quantum dot,* Phys. Rev. Applied **11**, 061006 (2019).

[33] R. Pillarisetty, N. Thomas, H. C. George, K. Singh, J. Roberts, L. Lampert, P. Amin, T. F. Watson, G. Zheng, J. Torres, M. Metz, R. Kotlyar, P. Keys, J. M. Boter, J. P. Dehollain, G. Droulers, G. Eenink, R. Li, L. Massa, D. Sabbagh, N. Samkharadze, C. Volk, B. P. Wuetz, A. M. J. Zwerver, M. Veldhorst, G. Scappucci, L. M. K. Vandersypen, and J. S. Clarke, *Qubit device integration using advanced semiconductor manufacturing process technology,* in *2018 IEEE International Electron Devices Meeting (IEDM)* (2018) pp. 6.3.1–6.3.4.

[34] R. Pillarisetty, H. C. George, T. F. Watson, L. Lampert, N. Thomas, S. Bojarski, P. Amin, R. Caudillo, E. Henry, N. Kashani, P. Keys, R. Kotlyar, F. Luthi, D. Michalak, K. Millard, J. Roberts, J. Torres, O. Zietz, T. Krähenmann, A. M. J. Zwerver, M. Veldhorst, G. Scappucci, L. M. K. Vandersypen, and J. S. Clarke, *High volume electrical characterization of semiconductor qubits,* in *2019 IEEE International Electron Devices Meeting (IEDM)* (2019) pp. 31.5.1–31.5.4.

[35] L. Hutin, R. Maurand, D. Kotekar-Patil, A. Corna, H. Bohuslavskyi, X. Jehl, S. Barraud, S. De Franceschi, M. Sanquer, and M. Vinet, *Si cmos platform for quantum information processing,* in *2016 IEEE Symposium on VLSI Technology* (2016) pp. 1–2.

[36] M. Vinet, L. Hutin, B. Bertrand, S. Barraud, J. . Hartmann, Y. . Kim, V. Mazzocchi, A. Amisse, H. Bohuslavskyi, L. Bourdet, A. Crippa, X. Jehl, R. Maurand, Y. . Niquet, M. Sanquer, B. Venitucci, B. Jadot, E. Chanrion, P. . Mortemousque, C. Spence, M. Urdampilleta, S. De Franceschi, and T. Meunier, *Towards scalable silicon quantum computing,* in *2018 IEEE International Electron Devices Meeting (IEDM)* (2018) pp. 6.5.1–6.5.4.

[37] L. Bourdet, L. Hutin, B. Bertrand, A. Corna, H. Bohuslavskyi, A. Amisse, A. Crippa, R. Maurand, S. Barraud, M. Urdampilleta, C. Bäuerle, T. Meunier, M. Sanquer, X. Jehl, S. De Franceschi, Y. Niquet, and M. Vinet, *All-electrical control of a hybrid electron spin/valley quantum bit in soi cmos technology,* IEEE Transactions on Electron Devices **65**, 5151 (2018).

7

# Acknowledgements

As I am writing this acknowledgements, I am starting to realize that all things must come to an end and I cannot help but be a bit sentimental. My time at QuTech felt like a roller coaster. There were good times, happy times and exciting times, but also tough times, sad times and depressing times. Reflecting back, each and every one of them was a priceless experience that shaped me into the person I am today. My contributions to science were the result of numerous fun, intriguing and fruitful interactions with the people around me, both inside and outside QuTech, and I want to take a moment to thank them all.

First and foremost, I want to thank my kind promotor, **Lieven**, to whom I'm forever grateful for the opportunity to do research under his guidance in his lab. It made me very happy that you offered me a PhD position even before I obtained my Casimir PhD grant. I'm thankful that I was able to work in a new direction in your lab. We were both new to circuit QED and I'm glad that we were able to learn together along the way. I deeply respect you as a scientist and as a teacher. You never fail to amaze me with your broad knowledge and scientific breakthroughs in the field of quantum computation and simulation. You have a knack for asking the right questions and always give well-considered advices. You give us more than enough freedom to do our research, but also provide support when needed. I'll definitely miss the annual BBQ at your place! I'm very happy for you that you became the new scientific director of QuTech, and I have no doubt that your leadership will take QuTech to the next level!

I'm genuinely blessed to have **Nodar** and **Patrick** as my partners in crime. **Nodar**, you're truly a giant on whose shoulders I could rely on during my whole PhD. You're one of, if not the most, creative person I have met. You're so confident, yet humble. You have so much common sense. You're a great scientist and a wizard in the cleanroom. You have taught me so much, ranging from physics and how to do science to matters in life, how to make peace and hoarding free food :P (Yes, it started with you!). The first few years of our project were tough. We were making insane working hours, still nothing worked and we didn't know why. We must have gone through hundreds of devices together... But I'm glad that we persisted though, and eventually we shared a breakthrough. I very much enjoyed our countless lighthearted conversations about random things. I wish you nothing but the best at TNO. I'm sure you'll keep doing amazing things!

Then along came **Patrick** in the middle of my PhD. You are such a nice guy (I guess the stereotype about Canadians is true :P). Your polar opposite character to that of Nodar's made me see things from a completely new angle, which I really appreciate. You're a seasoned scientist who cares about the details. In fact, you are as thorough as one can get. I have certainly benefited from your excellent research skills, logical thinking, systematic approach and encyclopedic knowledge

of spin qubits. So it's no surprise that I have learned so much from you. We could talk about physics for hours (literally). I truly enjoyed working with you and it was reassuring to know that you always had my back (like that time in San Sebastián...). It had a slow start, but I'm very pleased to see that our project is going at full throttle at the time of writing. Good luck and tons of best wishes to you and Chloé!

I was fortunate enough to be surrounded by the best people in the spin qubit team. **Stephan**, you joined the group not long after me, so we have been on our PhD adventures mostly side by side. We have shared plenty of struggles with our samples. Brainstorming with you was always fun. You continue to amaze me with your wizard-like programming skills. I enjoyed our conference trip to Helsinki. I wish you all the best in making the first 4-qubit entangled state in silicon! **Anne-Marije**, you bring happiness to the group! I really appreciate all your efforts in bringing our group closer together. Your sense of justice is admirable. The amount of things you do in parallel is insane, yet you seem to be managing them quite well :). Good luck making the best industrial qubits! **Xiao**, I initially thought you were a Facebook scammer :P. We started hanging out together more often when you permanently joined the cool kids club in QCLab2. We realized that we had many things in common. Working late and having dinner together was always fun. You're a gifted physicist with good intuition. Good luck with your future career steps! **Sjaak**, your drive to understand every detail is respectable. I will never forget your face in Denver when I told you that the March Meeting was canceled last minute haha. All the best quantum simulating! **Jelmer**, I have never seen anyone as fanatic as you in running. You also rubbed some of that energy onto me actually. Running a marathon is now on my bucket list. Thanks for all your help during my PhD, and have fun at ASML! **Udi**, you are the embodiment of positive energy in the lab with your contagious laugh. Thanks for organizing the awesome Iceland trip together with Anne-Marije. I have made fond memories over there, but I'm sure you remember more than I do... **Alice**, you were a great office mate. Good luck finishing the final part of your PhD! **Kostas**, it was fun having you around! **Sergey**, our group is in dire need of someone like you who is so passionate and knowledgeable about fabrication. I appreciate all that you have done for us, inside and outside the cleanroom. **Tobias**, it was never awkward with you around. Somehow conversations go so smoothly with your company. You also have a talent for learning Dutch! **Max**, thanks for all your help in the hybrid project. I hope you enjoy your stay in an experimental group! **Tzu-Kan**, many thanks for the Chinese New Year gift. **Mateusz**, enjoy your time in Delft! **Delphine**, you were vital to our project. Thanks for introducing and developing the prefab for us. That was definitely a game changer! **Amir**, your help was instrumental. Thanks for supplying all those wafers! **Pieter**, **Luc** and **Sander**, your help made our lifes so much easier!

The most talented seniors were showing me the ropes when I started my PhD. **Tim**, I wish I could be as pragmatic as you. Have fun at Shell! **Toivo**, my charismatic friend. I truly miss our hallway conversations. One of our highlights definitely has to be that time when we tried so hard to get to Veldhoven. Best of luck at BCG! **Erika**, thank you for your kindness and patience. It was nice seeing you again in Denver. Good luck with your new position at RIKEN!. **Pasquale**, you were always

so positive. I wish we had more overlap together. You did amazing work on hybrid cQED at ETH and you were always excited to share new results. All the best with your own group at EPFL! **Andrea**, I am glad to have met you. You were there for me in times of need and listened to my personal struggles. That meant a lot to me. Good luck at Zurich Instruments! **Nima**, thanks for your help in the hybrid project. Have fun at Single quantum! **Tom**, it was fun hanging out with you in Seattle! **JP**, you're awesome and you know it! **Takafumi**, it was nice chatting with you. **Christian**, I could always count on you sitting across from me in the lab late at night. **Kanwal**, I will never forget your philosophy: "copy exactly". **Gabriel**, thanks for your fab contributions.

I had the honor of supervising excellent MSc and BSc students. **Marc**, you did phenomenal work in assisting with the readout project. Good luck with your PhD! **Jurgen**, you were an outstanding student. Thanks for contributing to the gate filter project. I'm glad that you decided to join the hybrid project as PhD student. Good luck with the measurements! **Friso**, all the best with your MSc!

I have great expectations for the new generation in Lieven's group. **Florian** and **Pablo**, good luck with your PhD projects. **Tobias** and **Brennan**, you're doing awesome jobs. Good luck with the remainder of your MSc projects.

**Giordano**, thanks for being my co-promotor. You're a wonderful team player. You did an astonishing job setting up the in-house growth of silicon and germanium wafers from scratch. Good luck with germanium! **Menno**, I enjoyed our occasional discussions on spin qubits. You're an incredible and sharp-minded scientist. Keep up the good work! **Brian**, thanks for inviting Liwen and me over to your place for dinner and gluhwein. I wish you and Ailin the best. **Luka**, thanks for taking over my role in the Casimir PhD platform. **Alberto**, you're an awesome office mate. To all the others in the spin qubit team: **Luca**, **Gertjan**, **Nico**, **Will**, **Floor**, **Marcel**, **Mario**, **Diego**, **LaReine**, **Roy**, **Marco**, **David**, **Mohammad**, **Slava**, **Haruki** and **Nora**, thank you all for making my time in the group so enjoyable.

To my neighbours across the street at EWI: **Bagas**, **Bishnu** and **Masoud**, thanks for the collaboration on the cryo-CMOS project. It was intense, but worth it! **Gerd**, thanks for the occasional chats during coffee breaks.

QuTech is of course much bigger than just the spin qubit team. **Alex**, **Michiel**, **Norbert**, **James**, **Fokko**, **Damaz**, **Willemijn**, **Di**, **Nick**, **Jasper**, **Jouri**, **Daniël**, **Francesco**, **David**, **Qing**, **Srijit**, **Suzanne**, **Peter**, **Mohamed**, **Sophie**, **Max**, **Bas**, **Alessandro**, **Adriaan**, **Niels**, **Florian**, **Ramiro**, **Christian**, **Thijs**, **Thorsten** and many others. Thank you all for making QuTech such an awesome place to work! I will miss the annual QuTech Uitje, BBQ, Christmas Dinner and weekly Friday beers with you all.

An experimental PhD at QuTech cannot be completed without the help of **Raymond Schouten**, **Raymond Vermeulen**, **Marijn**, **Jelle**, **Siebe**, **Mark**, **Remco**, **Olaf**, **Jason**, **Matt** and **Nico**. Thank you **Hans**, **Jack** and the rest of the DEMO staff for providing us with home-built electronics and PCBs. I'm very grateful to the all the administrative support from **Marja**, **Chantal**, **Joanna** and also **Yuki** at the beginning. Thank you all for making the life of everyone at QuTech easier!

**Julia**, **Heera**, **Leontien**, **Rianne** and **Aletta**, thank you for doing an amazing

PR job for QuTech and for all your help with the press releases. Especially **Julia** and **Heera**, I want to thank you for helping me with the Young Speakers Contest.

QuTech would not have been the stimulating and scientific environment it is today without the contributions from all its PIs. Thank you **Leo K**, **Ronald**, **Lieven** and **Leo DC** for your leadership from the start.

**Marios**, I'm glad you introduced me to the Casimir PhD Platform and asked me to follow in your footsteps. **Marije**, I don't know how you do it, but you're amazing coordinator. Thank you for being the backbone of this platform and for always having such a positive attitude. **Gesa**, **Koen**, **Kirsten**, **Nicole**, **Robbie**, **Zohre**, **Michal** and of course **Jacqueline** during Marije's leave, it was my pleasure to have worked with you all in order to organize the Casimir Spring School and to think about ways to make the life of PhD students better. **Christophe**, all the best being the Casimir scientific director.

My PhD journey was temporarily put on hold in 2018 for a wonderful internship at Intel. That was my first contact with industry, and truly a life-changing experience. I'm in many ways grateful to **Jim**, **Jeanette**, **Lester**, **Tom**, **Nicole**, **Hubert**, **Ravi**, **Dave**, **Roman**, **Stephanie**, the rest of the Quantum Team and Intel Labs. Thank you for taking good care of me!

A special mention to the people I met in Wisconsin right before I started my PhD. **Mark**, **Luke**, **Gabe**, **Tom**, **Amy**, **Nathan**, **Will**, **Marnie**, **Brandur**, **Trevor**, **Sam** and **Ryan**. Thanks for the unforgettable memories.

I'm of course indebted to the committee members who took their time reading my dissertation. So I'm grateful to prof. **Kontos**, prof. **Wallraff**, prof. **Oosterkamp**, and **Gary**. Special thanks to **Leo DC** for being my reserve member. Also, thank you for letting me use the Heliox during my PhD.

To my closest and dearest friends: **Richel**, **Arsenio**, **Rob** and **Steve**. I'm a very lucky man to be surrounded by you guys. Our friendships have stood the test of time and distance! Thank you for all the awesome parties and memorable moments. Time seems to flow so much faster when we're together! **Rob**, our trip to Japan was unforgettable! Thanks for helping me translate the propositions and summary.

**Guowei**, het leven is niet makkelijk. Zeker omdat we zijn opgegroeid in twee verschillende culturen die op menig vlak tegenstrijdige uitgangspunten hebben. Ik weet dat jij toch altijd je uiterste best doet. Ondanks onze botsende persoonlijkheden hebben we veel dingen gemeen. Mede dankzij jouw onvoorwaardelijke steun heb ik de kans gekregen om zo ver te komen. Ik ben echt trots om je grotere broer te zijn. Jouw kans komt zeker nog, het is maar een kwestie van tijd. De aanhouder wint!

**Liwen**, meeting you was one of the best things that ever happened to me. There is never a dull moment with you by my side, and at the same time I always feel at ease. Thank you for always encouraging and supporting me. You're so talented at putting things in perspective. I'm truly amazed by all the things you're capable of. You're a source of inspiration. I'm happy that we have so many things in common and share similar goals in life. We will face more obstacle in the future, but I'm confident that we can overcome them as long as we are together. I look

forward to our adventures in the future.

妈妈，爸爸，我想对你们说：你们无条件爱与支持，陪伴我一路走到这里。养大一个像我这样的儿子一定不容易。你们已经教了我永远不会忘记的重要人生课程，例如生活中没有什么是免费的，为了实现自己的梦想，人们应该努力并且坚持。你们一直聆听我的担忧并向安慰我。你们能抓住一切机会庆祝我的成就，无论成就多么小，这使我每次都很开心。你们为我牺牲了很多，对此我始终心存感激。

我还要感谢所有我的姑姑和叔叔，外公，外婆，爷爷和奶奶的爱戴和支持。由于工作，我最近一直很忙，但我没有忘记你们和你们像自己的儿子一样对我的照顾。

国伟，生活不容易，特别是因为我们在两种多方面都相抵触的文化中长大。我知道你做什么事都会尽力而为。尽管我们的性格冲突，我们仍然有许多共同点。你给我的的无条件支持，帮助我走到今天。作为你的哥哥，我为你感到自豪。我希望你耐心等待，你的机会会来的，总有一天能成功！

力文，认识你是我最好的经历之一。和你在一起我再也感受不到沉闷，而总是感到轻松自在。感谢你一直以来对我的支持。你非常擅于正确地看待事物，你所具备的多方面的能力总能让我感到惊喜。你是我的灵感之源。我很高兴我们有很多共同点，并在生活中拥有相似的目标。将来我们将面临更多考验，但是我相信，只要我们在一起，我们就能克服它们。我期待能接受未来的挑战。

*Guoji Zheng*
郑国际

# Curriculum Vitæ

## Guoji ZHENG

29-02-1992      Born in Ruian, Zhejiang, China.

## Education

2004-2010      Secondary School
*Aloysius College, Den Haag, Netherlands*

2010-2013      Bachelor of Science in Applied Physics
*Delft University of Technology*

2013-2016      Master of Science in Applied Physics
*Delft University of Technology*

Graduate research project in the group of Prof. dr. G.A. Steele
*Delft University of Technology*
"Improving the quality factor of 3D copper cavities with a superconducting layer of MoRe for cavity optomechanics"

Graduate research project in the group of Prof. dr. ir. L.M.K. Vandersypen
*Delft University of Technology*
"Towards strong coupling of a spin qubit in a Si/SiGe double quantum dot to a photon in a superconducting resonator"

Graduate research project in the group of Prof. dr. M.A. Eriksson
*University of Wisconsin-Madison, USA*
"Linear quadruple quantum dot devices"

2016-2020      PhD in Experimental Quantum Physics
*Delft University of Technology*
"Circuit Quantum Electrodynamics with Electron Spins in Silicon"
Promotor:    Prof. dr. ir. L.M.K. Vandersypen

2018      Industry internship in Quantum Computing Group, Components Research
*Intel Corporation, Hillsboro, USA*
Manager:    J.S. Clarke, PhD

## Awards & Honours

2020          Winner 26$^{th}$ NTvN (Dutch Journal of Physics) Competition
              *Nederlandse Tijdschrift voor Natuurkunde*
              *Netherlands*

2019          Young Scientist
              *69$^{th}$ Lindau Nobel Laureate Meeting*
              *Lindau, Germany*

2018          Finalist Young Speakers Contest
              *FYSICA 2018*
              *Utrecht, Netherlands*

2017          Best Poster Presentation Prize
              *QTC 2017*
              *Espoo, Finland*

2015          Casimir PhD grant, based on the proposal:
              "A spin qubit network coupled via a microwave resonator"
              *Funded by NWO Gravitation programme (NanoFront)*
              *Netherlands*
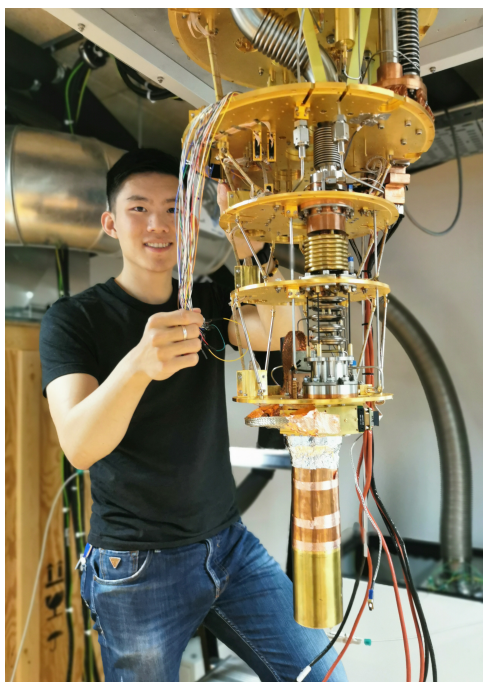
# List of Publications

## Journal Papers and Preprints

6. *On-Chip Microwave Filters for High-Impedance Resonators with Gate-Defined Quantum Dots* (**Editor's Suggestion**)
   P. Harvey-Collard, **G. Zheng**, J. Dijkema, N. Samkharadze, D. Brousse, A. Sammak, G. Scappucci, L.M.K. Vandersypen
   Physical Review Applied **14**, 034025 (2020)

5. *Van elektronen en fotonen naar quantumprocessoren: Het moderne foto-elektrisch effect op een chip* (**Cover**)
   **G. Zheng**
   Nederlands Tijdschrift voor Natuurkunde **86-04**, 10 (2020)

4. *Rapid gate-based spin read-out in silicon using an on-chip resonator*
   **G. Zheng**, N. Samkharadze, M.L. Noordam, N. Kalhor, D. Brousse, A. Sammak, G. Scappucci and L.M.K. Vandersypen
   Nature Nanotechnology **14**, 742 (2019)

3. *Strong spin-photon coupling in silicon*
   N. Samkharadze\*, **G. Zheng**\*, N. Kalhor, D. Brousse, A. Sammak, U.C. Mendes, A. Blais, G. Scappucci and L.M.K. Vandersypen
   \* These authors contributed equally
   Science **359**, 1123 (2018)

2. *High-Kinetic-Inductance Superconducting Nanowire Resonators for Circuit QED in a Magnetic Field*
   N. Samkharadze, A. Bruno, P. Scarlino, **G. Zheng**, D.P. DiVincenzo, L. DiCarlo and L.M.K. Vandersypen
   Phys. Rev. Applied **5**, 044004 (2016)

1. *Anomalous response of superconducting titanium nitride resonators to terahertz radiation*
   J. Bueno, P.C.J.J. Coumou, **G. Zheng**, P.J. de Visser, T.M. Klapwijk, E.F.C. Driessen, S. Doyle and J.J.A. Baselmans
   Appl. Phys. Lett. **105**, 192601 (2014)

## Conference Proceedings

2. *A 6-8GHz 0.17mW/qubit Cryo-CMOS Receiver for Multiple Spin Qubit Readout in 40nm CMOS Technology*
   B. Prabowo, **G. Zheng**, M. Mehrpoo, B. Patra, P. Harvey-Collard, J. Dijkema, A. Sammak, G. Scappucci, E. Charbon, F. Sebastiano, L.M.K. Vandersypen and M. Babaie
   2021 IEEE International Solid-State Circuits Conference (ISSCC), 13.3

1. *Qubit Device Integration Using Advanced Semiconductor Manufacturing Process Technology*
   R. Pillarisetty, N. Thomas, H.C. George, K. Singh, J. Roberts, L. Lampert, P. Amin, T.F. Watson, **G. Zheng**, J. Torres, M. Metz, R. Kotlyar, P. Keys, J.M. Boter, J.P. Dehollain, G. Droulers, G. Eenink, R. Li, L. Massa, D. Sabbagh, N. Samkharadze, C. Volk, B.P. Wuetz, A.-M. Zwerver, M. Veldhorst, G. Scappucci, L.M.K. Vandersypen and J.S. Clarke
   2018 IEEE International Electron Devices Meeting (IEDM), 6.3.1

## Patent Applications

2. N. Samkharadze, **G. Zheng**, in preparation.

1. **G. Zheng**, P. Harvey-Collard, *Superconducting microwave filters and filter elements for quantum devices*, patent pending (NL2025291).